ABSTRACT

Title of Dissertation: QUANTIFYING NITROUS OXIDE AND METHANE FLUXES USING THE TOWER-BASED GRADIENT METHOD ON A DRAINAGE WATER MANAGED FARM ON THE EASTERN SHORE OF MARYLAND

Qiurui Zhu, Doctor of Philosophy, 2022

Dissertation directed by: Professor Eric A. Davidson, Marine, Estuarine, and Environmental Science

Excess nitrogen resulting from agricultural fertilizer and manure applications on the Eastern Shore degrades the Chesapeake Bay's water quality and causes environmental issues such as algal blooms and "dead zones". Drainage water management (DWM) is an effective best management practice (BMP) to reduce hydrological nitrate export from croplands to surface and ground water by controlling the timing and the amount of ditch discharge and retaining water within ditches and adjacent fields using drainage control structures (DCS). While promoted denitrification in the subsurface and reduction in nitrate leaching are intended consequences of maintaining higher water table level, an unintended environmental consequence is possible production of nitrous oxide (N_2O) from denitrification and methane (CH_4) from methanogenesis, which are both potent greenhouse gases (GHGs). Whether the application of DWM leads to a "pollution swapping" concern (i.e., trading reduction of nitrate concentrations in ditch water for increases in emissions of N_2O and CH_4 to the atmosphere) is a question that must be addressed

before more widespread implementation of DWM can be endorsed. In this dissertation, I employed a micrometeorological method called the flux gradient (FG) method to a corn-soybean rotation agricultural system with DCS in eastern Maryland on the Delmarva Peninsula to answer this question. This method was chosen because it allows near-continuous measurements of soil trace gas exchanges at multiple locations with a single laser spectrometer at a fine temporal resolution without disturbing the microclimate between soils and the atmosphere. Soil N_2O and CH_4 fluxes were quantified using the FG method on this drainage water managed farm for three consecutive years when no fertilizer, synthetic fertilizer, and biosolids were applied in 2018 (soybean), 2019 (corn), and 2020 (corn), respectively. Statistical tests indicated that there were no consistent treatment effects of DWM on soil GHG emissions between DWM and non-DWM conditions, suggesting that DWM did not trade the intended consequence of reduced nitrate leaching for the unintended consequence of increased soil GHG emissions. The biosolid addition in 2020 led to the largest N_2O emissions among the three years, while the lowest N_2O emissions in the growing season were found in the unfertilized soybean year of 2018. In contrast, different fertilization regimes did not yield distinct differences between the three years for CH_4 fluxes. In addition, some potential methodological concerns associated with this tower-based micrometeorological approach were addressed and resolved, conferring confidence that the FG method can be applied simultaneously to multiple plots for N_2O and CH_4 measurements. This research adds to the existing understanding of the impacts of DWM on soil GHG emissions and suggests that this BMP could be applicable in other regions of the Chesapeake Bay as well as other watersheds. This work also contributes to the efforts of studying the impacts of soil organic amendments on soil GHG emissions and deriving improved estimates of emission factors (EFs) for organic amendments.

QUANTIFYING NITROUS OXIDE AND METHANE FLUXES USING THE TOWER-BASED GRADIENT METHOD ON A DRAINAGE WATER MANAGED FARM ON THE EASTERN SHORE OF MARYLAND

by

Qiurui Zhu

Dissertation submitted to the Faculty of the Graduate School of the
University of Maryland, College Park, in partial fulfillment
of the requirements for the degree of
Doctor of Philosophy
2022

Advisory Committee:
Professor Eric A. Davidson, Chair
Associate Professor Mark Castro
Associate Professor Xin Zhang
Associate Research Professor Dong Liang
Research Associate Dr. Shannon Brown
Professor Russell Dickerson, Dean's Representative

Acknowledgements

I would like to express my gratitude and appreciation to the individuals and groups below. Without your support and help, it would have been impossible for me to arrive at this important milestone.

I would like to give huge thanks to my advisor, Dr. Eric Davidson, for the endless guidance, support, and encouragement. You have showed me what is a great mentor about and guided me through solving complex and challenging problems in my field work, data analysis, and dissertation writing with great patience. Your support and encouragement mean a lot to me.

I want to deliver many thanks to my program committee members: Dr. Mark Castro, Dr. Xin Zhang, Dr. Dong Liang, and Dr. Shannon Brown. Dr. Mark Castro hosted me when I arrived at this small town and led me through the first few years of my field work. Dr. Xin Zhang introduced me to this program, provided a lot of feedbacks on my research topics, and hosted me on almost every festival. Dr. Dong Liang taught me basic skills in environmental statistics and offered many useful suggestions about statistical analysis for my dissertation project. I benefited so much from Dr. Shannon Brown's expertise in micrometeorology and the visit to her university in Canada. Your help and inputs are much appreciated.

Special thanks to the wonderful and lovely students and staff in the Appalachian Laboratory. Thanks to the fellow graduate students (Jacob Hagedorn, Joel Bostic, Stephanie Siemek, Claire Nemes, Srishti Vishwakarma, Juliet Nagel, and many others) for your companion, support, and encouragement. Thank you to the ladies in the administration office (Heather Johnson, Cami Martin, Kristen Harper, and others) for filling out my paperwork, coordinating my field trips, and ordering field supplies. I would like to express my special thanks to Katie Kline for teaching me to perform soil KCl extractions and to John Piasecki for his help in repairing field equipment and his great maintenance work on the lab vehicles. Thanks to the AL for providing financial supporting for my last semester.

Many thanks to the Horn Point Laboratory team: Dr. Tom Fisher, Dr. Rebecca Fox, Anne Gustafson, and Erika Koontz for your assistance in the field work, sharing of the data, and feedbacks on my research. I would like to convey my profound gratitude to Dr. Rebecca Fox for accommodating us during the field work seasons in Washington College. I appreciate the generosity of our collaborating farmer, Jim Lewis. Thanks for letting us invade your farm, accommodating our research needs, and providing key information and assistance.

I want to express my gratitude to Prof. Rodrigo Vargas's group at the University of Delaware for lending me the eddy covariance equipment and to the company Eosense for lending us the automated chambers. I want to deliver my profound gratitude to Dr. Kathleen Savage and the Woodwell Climate Research Center for lending the quantum cascade laser and helping with setup. Special thanks to the technical support from Aerodyne: Dr. Mark Zahniser, Michael Moore, Dr. David Nelson, and others.

This project would not have been possible without funding from USDA-NIFA and UMCES. Thanks to the University of Maryland for providing me with the COVID fellowship to continue my study.

Last but not least, I am deeply grateful to my family (my parents and Tan Zou). Without your love and support, I would never have had the opportunity and courage to chase my dreams.

Table of Contents

List of Tables

List of Figures

List of Abbreviations

BMP	Best Management Practice
DWM	Drainage Water Management
CH_4	Methane
CO_2	Carbon Dioxide
DCS	Drainage Control Structure
EC	Eddy Covariance
EF	Emission Factor
FG	Flux Gradient
GHG	Greenhouse Gases
IPCC	Intergovernmental Panel on Climate Change
ITC	Integral Turbulence Characteristics
KCl	Potassium Chloride
MDL	Minimum Detection Limit
N	Nitrogen
N_2	Dinitrogen Gas
N_2O	Nitrous Oxide
NH_4^+	Ammonium
NO	Nitric Oxide
NO_2^-	Nitrite
NO_3^-	Nitrate
QCL	Quantum Cascade Laser
RMSE	Root Mean Squared Error
SD	Standard Deviation
UAN	Urea Ammonium Nitrate
VWC	Volumetric Water Content
WFPS	Water Filled Pore Space

Chapter 1: Introduction

1.1 A "Pollution Swapping" Concern of Applying Agricultural Drainage Water Management

Although the Eastern Shore contains only 7 percent of the Chesapeake Bay watershed, it has contributed disproportionately large loads of excess nitrogen to the Bay in the past few decades, of which a great proportion comes from agricultural fertilizer and manure applications (Ator & Denver, 2015). Excess nitrogen degrades the Bay's water quality and causes environmental issues such as algal blooms and "dead zones" in the water. To reduce agricultural runoff into the Bay, cost-effective conservation measures, or so-called best management practices (BMPs) are needed, such as planting cover crops, installing forested buffers, and a variety of nutrient management and conservation plans.

Drainage water management (DWM) has been demonstrated as a useful BMP not only to control water levels in agricultural fields but also to reduce nitrate loads to surface waters and ground water (Drury et al., 2014; Fisher et al., 2010; Schott et al., 2017; Williams et al., 2015). The DWM structures control the timing and the amount of water leaving from agricultural lands using adjustable weirs placed at the end of drainage ditches. With more control over drainage and proper management of the structures, increased crop yields may also be possible (Cooper et al., 1991; Delbecq et al., 2012; Skaggs et al., 2012). Most importantly for this study, DWM creates more anaerobic conditions that promote denitrification in the subsurface by raising the water level and retaining water within the ditches and adjacent fields, thus reducing nitrate concentration in discharged water.

However, an unintended environmental consequence of maintaining higher water table levels is that it creates favorable conditions for possible production of nitrous oxide (N_2O) and methane

(CH_4), which are both potent greenhouse gases (GHG) with high global warming potentials (IPCC, 2014). In addition, N_2O depletes the stratospheric ozone that acts as Earth's shield to filter ultraviolet radiation from the sun, while CH_4 contributes to the photochemical production of tropospheric ozone that is harmful to ecosystem and human health (Abernethy et al., 2021; Dentener et al., 2005; Müller, 2021; Ravishankara et al., 2009; West et al., 2006).

N_2O can be formed in soils through microbial denitrification, which is a form of anaerobic respiration that reduces nitrate (NO_3^-) to a series of products: nitrite (NO_2^-), nitric oxide (NO), nitrous oxide (N_2O), and dinitrogen (N_2) (Firestone, 1982; Firestone & Davidson, 1989). The microbial conversion of agriculturally derived N to N_2O in soils increased ten times from the preindustrial period (the 1860s) to the recent decade (2007-2016), accounting for the majority of increase in global soil N_2O emissions over the same period (Tian et al., 2019). CH_4 is another potent greenhouse gas that could possibly be produced by methanogenesis when higher water table levels are maintained and increased anoxic conditions are present. Cai et al. (1997) saw that the CH_4 flux peaked when rice paddy fields were flooded and was depressed when the fields were aerated. Tyagi et al. (2010) also found that continuously flooded plots had the highest efflux of methane and mid-season drainage and multiple drainage plots had approximately 40% less efflux of methane in their irrigated paddy fields.

Therefore, applying DWM could lead to a "pollution swapping" concern: namely DWM could trade reduction of nitrate concentrations in ditch water for increases in emissions of N_2O and CH_4 to the atmosphere. This trade-off must be addressed before more widespread implementation of DWM can be endorsed.

1.2 Quantification of Greenhouse Gas Fluxes from Agricultural Soils

N_2O and CH_4 emissions from soils are highly variable in space and time due to spatial heterogeneity of soil physical and chemical properties (e.g., soil moisture, pH, nitrogen and carbon content), diel cycles and seasonality (rainfall and temperature change), and management practices (e.g., fertilization, tillage, irrigation, soil compaction), which all can influence the microbially mediated processes that produce the above two gases. For example, in a subtropical forest catchment in southern China, soil temperature and water-filled pore space were identified as the two major control factors that explained 68.9% of the temporal variability of N_2O emissions on a mesic forested hillslope (Zhu et al., 2013). In agricultural fields, N_2O emissions are highly episodic events and peak emissions typically occur after the addition of N fertilizer, triggered by wetting of soils by rain and irrigation (Y. Cai et al., 2013; Jones et al., 2011; Skiba et al., 2013; Tallec et al., 2019; Tenuta et al., 2019). Thus, continuous measurements are advantageous for quantifying annual emissions.

On-farm management practices further complicate the emission dynamics, and key factors that affect emissions include the timing of fertilizer application, the manner of fertilizer spreading, the type of fertilizer used, tillage or no-tillage, and the amount of irrigation water used. For example, Wagner-Riddle et al. (2007) found that their BMP (no-tillage + reduced fertilizer) significantly decreased mean annual N_2O emissions in comparison with conventional tillage. In contrast, Waldo et al. (2019) reported that the N_2O emission factor (EF) was larger on a no-till site than that on a paired conventional-till site. While the contradictory findings can be explained by the complex interaction of soil factors affected by no-tillage, they both highlight the need to take spatial variability of soil emissions into account.

Static (or "non-steady state") chambers have been the principal method for measuring N_2O and CH_4 fluxes from agricultural soils for the last few decades (Hensen et al., 2013) and over 95% of published N_2O emission studies employed chamber methods according to Rochette (2011). This method involves using an open-bottomed chamber to cover a small area of ground (e.g., bare soil or short canopy) and accumulating N_2O/CH_4 within the headspace. Headspace samples are taken when the chamber remains closed on the soil surface, and then analyzed by either a portable closed-path gas analyzer on site or gas chromatography (GC) in the laboratory. The main advantage of this method is that it is relatively inexpensive, versatile, and easy to adopt in the field (De Klein & Harvey, 2015; Hensen et al., 2013). However, an important limitation is that only expensive automated chamber systems can make continuous measurements and are often limited in number due to their cost, whereas manually operated chambers, while cheaper and potentially more numerous, can miss important emission events ("hot moments"). Spatial variability can be addressed through placing multiple small chambers on a plot of interest, but where to place these chambers or how to cover a sufficient surface area to ensure representative fluxes are measured from the plot requires additional consideration and intensive labor (Chadwick et al., 2014). De Klein and Harvey (2015) also pointed out the current difficulty of using chambers is "having to balance limited resources between carefully measuring individual fluxes, versus increasing the number of chambers and/or sampling occasions to account for spatial and temporal variability".

Micrometeorological methods have become popular in recent years as the laser technology advances, enabling integration of high temporal and spatial resolution measurements of soil-atmosphere trace gas exchanges at the field scale (0.1 to 1 km^2) and also at a declining price (Hargreaves et al., 1996; Shurpali et al., 2016; Smith, 1994; Wagner-Riddle et al., 1996). The eddy covariance (EC) method and the flux gradient (FG) method are two principal micrometeorological methods that involve fast-response trace gas analyzers (e.g., tunable diode laser (TDL) and quantum cascade laser (QCL) spectrometers) based on the development of laser spectroscopic techniques (Pattey et al., 2007; Rannik et al., 2015).

The EC method is currently the most widely used approach to measure trace gas exchanges between land surfaces and the atmosphere (Cowan et al., 2016; Hensen et al., 2013; Huang et al., 2014; Liang et al., 2018; Merbold et al., 2014; Neftel et al., 2010). This method requires fast-response instruments to capture high-frequency air movement and gas concentration data and calculates the vertical turbulent flux of this trace gas as covariance between the vertical wind velocity and the scalar concentration over an average period of typically 30 minutes. The advantage of the EC method is that it is a direct measure of real-time fluxes and it allows continuous measurement on a larger field scale (hectare to km^2) in different ecosystems, without disturbing the soil or the interface between the surface and the atmosphere (Chadwick et al., 2014; Huang et al., 2014; Tallec et al., 2019). However, the EC method requires the fast-response gas analyzer to be located near the measurement tower, which precludes using a single centralized gas analyzer for more than one plot/tower in an experimental design. Other limitations are: 1) the required fast-response, high-frequency, and high-precision instruments are relatively expensive; 2) considerable maintenance work is needed (depending on what instrument is used), especially at remote field sites (Liang et al., 2018); 3) it requires the area of interest to be horizontally homogeneous and the air flow should not be distorted by the installation of other instruments or structures; 4) data collection is constrained by the atmospheric stability (Hensen et al., 2013); 5) it is not easy to replicate treatments at the micrometeorological scale (0.1-1 km^2) (Chadwick et al., 2014); 6) bias and uncertainty exist because of data gaps, laser drift (Kroon et al., 2007), etc.

The flux gradient (FG) method is a micrometeorological approach based on Monin-Obukhov similarity theory. It shares with eddy covariance the use of sonic anemometers to estimate sensible heat flux, but differs from eddy covariance by measuring the difference in concentration of target trace gases at two heights on one or multiple towers. Assuming the eddy diffusivities for sensible heat and the trace gas (N_2O or CH_4) are equal, the relationship between the flux (F) and the concentration difference is expressed as:

$$F = -K\frac{\partial C}{\partial z} \quad [1]$$

where K is the eddy diffusivity (m^2s^{-1}) of the trace gas (e.g. N_2O or CH_4), and $\partial C/\partial z$ is the concentration gradient of this gas (kg m^{-4}) (details about the calculation procedures for each term can be found in Chapter 2). In addition to all the advantages mentioned above as a micrometeorological approach, the FG approach can rely on slower sensors than the EC approach (Hensen et al., 2013). Unlike EC, which requires careful matching of rapid changes in concentration at a single intake position, the concentration gradient between the two sampling heights can be averaged over a longer time interval. Hence, the FG approach permits the use of longer tubing between the tower inlets and the gas analyzer thereby allowing a centrally located instrument to be integrated with multiple towers and facilitating treatment replication in experimental designs. In other words, FG can be adapted for small plots (E. Topp & Pattey, 1997).

For this dissertation project, the FG approach was selected because it is the best-suited method for multi-plot sampling with a single laser spectrometer (McMillan et al., 2014). Besides, FG has been preferred over EC for measuring surface-atmosphere fluxes within a few meters of the surface layer (Meredith et al., 2014; N. M. Taylor et al., 1999).

1.3 Dissertation Structure

As discussed in Section 1.1, the application of DWM has the potential to reduce nitrate leaching but also increase soil greenhouse gas emissions as a possible trade-off. An earlier companion study (Hagedorn et al., 2022) demonstrated that DWM was effective to reduce nitrate leaching into ditches on the same study farm, and it has also been shown to be effective in the region (Fisher et al., 2010). In my dissertation, I employed the flux gradient method to a corn-soybean rotation system with drainage control structures (DCS) in eastern Maryland on the Delmarva Peninsula to study three major questions:

1) would DWM lead to significant increases in soil emissions of either N_2O or CH_4, thus creating a "pollution swapping" situation?

2) how does biosolids addition, which farmers of the region commonly apply about once every five years in lieu of synthetic fertilizer, affect soil N_2O and CH_4 fluxes in this agricultural setting? Because the sludge contains carbon as well as nitrogen, it could enhance N_2O and CH_4 fluxes compared to synthetic fertilizer applications if carbon is a limiting factor to denitrification and methanogenesis.

3). are there any concerns or disadvantages of this micrometeorological FG method that could possibly outweigh the aforementioned advantages of the tower-based system?

The dissertation is organized in an order according to the three objectives, with each corresponding to a respective chapter of Chapter 2-4.

In Chapter 2, I quantified soil N_2O and CH_4 emissions using the tower-based FG method for two consecutive years on a drainage water managed farm in soybean and corn on the Eastern Shore of Maryland and identified two factors (i.e., fertilization and precipitation) upon which large N_2O emissions were highly dependent. The flux results of the FG measurements were compared to simultaneous static and automated chamber measurements and general agreements were found in the comparisons. I also performed statistical tests to evaluate the effects of DWM on soil GHG emissions.

In Chapter 3, I employed the FG method on the same farm in corn in year 3 to quantify the post-biosolids N_2O and CH_4 emissions from the soil surface and compared the flux results to that of the years when no fertilizer/conventional synthetic fertilizer was applied. Effects of DWM on N_2O and CH_4 fluxes were also tested using statistical analysis but no consistent treatment effects were found, aligning with previous findings. In addition, annual soil N_2O emissions from this site were estimated and N_2O emission factors (EFs) were calculated for the years when synthetic fertilizer and biosolids were used.

In Chapter 4, I investigated sources of uncertainty in the FG method. Four potential sources of uncertainty were considered: (1) minimum resolvable concentration gradient; (2) towers' flux footprint overlap/contamination; (3) the validity of the aerodynamic method to calculate the eddy diffusivity coefficient; and (4) the choice of the gap-filling techniques for N_2O flux data.

In this study, the flux gradient method was proved capable of capturing intermittent bursts of soil N_2O emissions at a fine temporal resolution across spatial heterogeneity. This work adds to the limited number of studies comparing micrometeorological and chamber methods in trace gas flux measurements. This research also adds to the existing understanding of the impacts of DWM. It demonstrates that DWM did not result in unacceptable pollution trading at this farm and suggests that this management option could be applicable in other regions of the Chesapeake Bay as well as other watersheds or river basins. In addition, the findings concerning the effects of biosolids addition in this research contribute investigations of the impacts of biosolid or other organic soil amendments on soil GHG emissions and derivation of improved estimates of emission factors for organic amendments.

Chapter 2: Quantification of Soil N_2O and CH_4 Fluxes Using the Flux Gradient Technique on a Drainage Water Managed Farm and Evaluation of Effects of Drainage Water Management on Soil Greenhouse Gas Emissions

Abstract

Implementation of drainage water management (DWM) could trade reduction of nitrate concentrations in ditch water for increases in emissions of nitrous oxide (N_2O) and methane (CH_4) to the atmosphere. The literature evaluating effects of DWM on N_2O and CH_4 emissions from agricultural soils shows contradictory results: some studies measured larger soil emissions whereas others did not detect significant differences in N_2O or CH_4 emissions when DWM was implemented. In this chapter, soil N_2O and CH_4 emissions were quantified using the tower-based flux gradient (FG) method in a corn-soybean rotation system with drainage control structures (DCS) on the Eastern Shore of Maryland for two consecutive years. The FG measurements were also compared with static and automated chamber measurements, which were generally in good agreements, despite spatial variability in the chamber data. I found that large N_2O emissions were highly dependent on fertilization and precipitation events. Furthermore, statistical analysis assessing the effects of DWM on soil greenhouse gas (GHG) emissions indicated that no consistent treatment effects were found between DWM and non-DWM conditions. These results indicate that DWM may be employed to reduce nitrate leaching without increasing soil GHG emissions.

2.1 Introduction

Drainage ditches have been adopted widely on the Delmarva Peninsula for the past 200 years to remove excess water and create drier land for agricultural and residential uses (Bell, 2000; Fisher et al. 2010). According to the Maryland Department of Agriculture, there are over 800 miles of publicly administered drainage ditches in Maryland today helping drain 183,000 acres of land composed of agricultural land, forest land, roadways, commercial and residential areas, etc. In North America, about 50.9 million acres of cropland in the eastern and midwestern United States and about 20 million acres in Canada are artificially drained (Shedekar et al., 2020). Proper management of drainage ditches to retain partially elevated groundwater during most of the growing season not only improves water availability to crops but also promotes the denitrification process in soils and reduces nitrate leaching (Carstensen et al., 2020; Drury et al., 2014; Sunohara et al., 2014). However, the possible production of N_2O from denitrification and CH_4 from methanogenesis as a result of managing drainage ditches to reduce nitrate leaching remains as a major concern.

Previous studies regarding drainage effects on N_2O emissions showed contrasting results. Some researchers reported that a lower water table in drained soils leads to lower N_2O emissions. Hall et al. (2018) saw that N_2O emissions from poorly drained cropland soils were much higher than that from well-drained soils and could be an important part in estimates of regional bottom-up emissions. Grossel et al. (2016) found that in a cropped landscape in Central France, N_2O emission levels from the undrained soils were significantly larger than the emissions from the drained soils in both wet and dry climatic conditions. They also pointed out that drainage was the dominant factor over other soil variables explaining the spatial variability of the N_2O emissions within their study site. Similar drainage effects on N_2O emissions can be found in Fernández et al. (2016) and Kumar et al. (2014). In contrast, other studies did not detect significant differences in N_2O or CH_4 emissions when drainage water management (DWM) was implemented (Datta et al., 2013; Nangia et al., 2013; Nash et al., 2015; Van Zandvoort et al., 2017).

Most studies employed the static chamber method to assess the effects of DWM on N_2O or CH_4 emissions (Datta et al., 2013; Fernández et al., 2016; Grossel et al., 2016; Hagedorn et al., 2022; Nangia et al., 2013), whereas studies using the tower-based micrometeorological methods are scarce. The strengths and weaknesses of both methods are clarified in the first chapter of this dissertation separately. In short, the advantage of the flux gradient method is that it allows near-continuous measurements of soil-atmosphere trace gas exchanges at a finer temporal resolution and a larger scale (0.1 to 1 km^2) without disturbing the microclimate between soils and the atmosphere. This provides a better estimation of cumulative emissions at the field scale so that a more accurate estimates of N_2O and CH_4 emissions can be determined. Here I applied the flux gradient method to a corn-soybean rotation system in eastern Maryland on the Delmarva Peninsula to estimate N_2O and CH_4 emissions under DWM and non-DWM conditions and I compared flux gradient estimates with chamber based estimates from a companion study.

2.2 Materials and Methods

2.2.1 Site Description

The research site was located on a private farm in the Choptank Basin on the Eastern Shore of Maryland, where land use is dominated (60%) by agriculture, and forests and wetlands cover most of the remaining land (35%) (Fisher et al., 2021). This farm was chosen because the farmer, who is actively involved in on-farm research to test effectiveness of several types of nutrient management interventions, had already installed DWM structures and was eager to collaborate. The region has a humid subtropical climate with average annual precipitation of 114 cm and an average temperature of 24 °C in July and 2 °C in January. The soil in this field is predominantly Fallsington fine-loamy, mixed, active, mesic Typic Endoaquults. The typical crop rotation is a corn-soybean rotation with daikon radish used as the winter cover crop. Pivot irrigation is turned on every few days in the summer as needed.

2.2.2 Farm Management

In 2018, soybean was planted in June and harvested in October, with no application of any N fertilizer. In 2019, corn was planted in late April and harvested in September. Approximately 22 kg N ha^{-1} of synthetic urea-ammonium-nitrate (UAN) was knifed-in on April 25 and the other 191 kg N ha^{-1} was broadcast-applied on May 24. Herbicide was applied twice in 2019, one time in late March prior to the planting of corn and the second time in June, to remove undesired vegetation from the field. The entire research area, with and without DWM, was subject to the same crop rotation scheme, fertilization rate, and irrigation rate.

2.2.3 Experimental Design

Figure 1 is a Google Earth image with a map view of the positions of the drainage ditches, the four FG measurement towers, and the instrument trailer. The ditches were spaced about 90 meters apart and 180 meters long on average, and each of them had a drainage control structure (DCS) at the end. The DCS is capable of slowing ditch discharge and retaining more water in the ditch and its adjacent fields or draining the fields and creating a drier condition for farm activities such as planting, fertilizer application, and harvest. We used two of the DCS structures in ditches 5 and 6 to manage the water table, leaving the other three ditches (ditches 1, 2, and 4) to flow freely and unmanaged. The specific management plan was dependent on weather conditions and groundwater levels. Thus, the ditches divided the farm into a controlled drainage (DWM) site and a free drainage (non-DWM) site.

Four 3.5 m flux towers were installed at this research farm. Two of them were located in the non-DWM field and the other two were located in the DWM field, all within 61-183 m from the instrument trailer (Fig.1). Each tower contained a pair of upper and lower sampling inlets, which were attached to 3/8’’ O.D. Synflex tubing via a three-way solenoid valve. The upper and lower inlets were always kept 0.5-0.7 m apart while the entire sampling unit was raised throughout the growing season in order to be above the crop canopy. Ambient air sampling switched between the upper and lower inlets every 20 seconds for 30 minutes before it switched to the next tower. The sampling sequence was controlled by a Campbell Scientific CR1000 data logger (Campbell Scientific Inc., UT, U.S.A.) (see Fig. 2). Air samples from the towers were pulled into the instrument trailer at rates of over 20 liters per minute using two Thomas rotary vane vacuum pumps (model number: QR0100). Inside the trailer, N_2O and CH_4 mixing ratios were continuously measured by a quantum cascade laser (QCL) trace gas monitor (Aerodyne Research Inc., MA, U.S.A.) at a frequency of 1Hz. The manufacturer’s specifications indicated that the precisions (1σ) of N_2O and CH_4 mixing ratio measurements at 1270 cm^{-1} were 60 and 300 ppt, respectively on a 1-s basis. In addition, an automated auxiliary calibration valve was turned on periodically (once every two weeks approximately) during the sampling period to inject N_2O and CH_4 gas standards into the QCL for instrument validation and calibration. Thus, this sampling system allowed us to calculate the concentration gradients of N_2O and CH_4 between the upper and lower inlets at each tower for each 30-minute sampling period. These averaged 30-minute concentration gradients were then combined with the micrometeorological data collected every half hour at each tower with a Campbell Scientific CSAT3B sonic anemometer (Campbell Scientific Inc., UT, U.S.A.) to calculate the half-hourly fluxes of N_2O and CH_4. The full cycle for measuring fluxes from all four towers required two hours, thus permitting twelve flux measurements made per day for each tower. The measured fluxes were analyzed for temporal pattern, diel variation, and tower-to-tower comparison and interpolated to estimate the cumulative emissions from this field site.

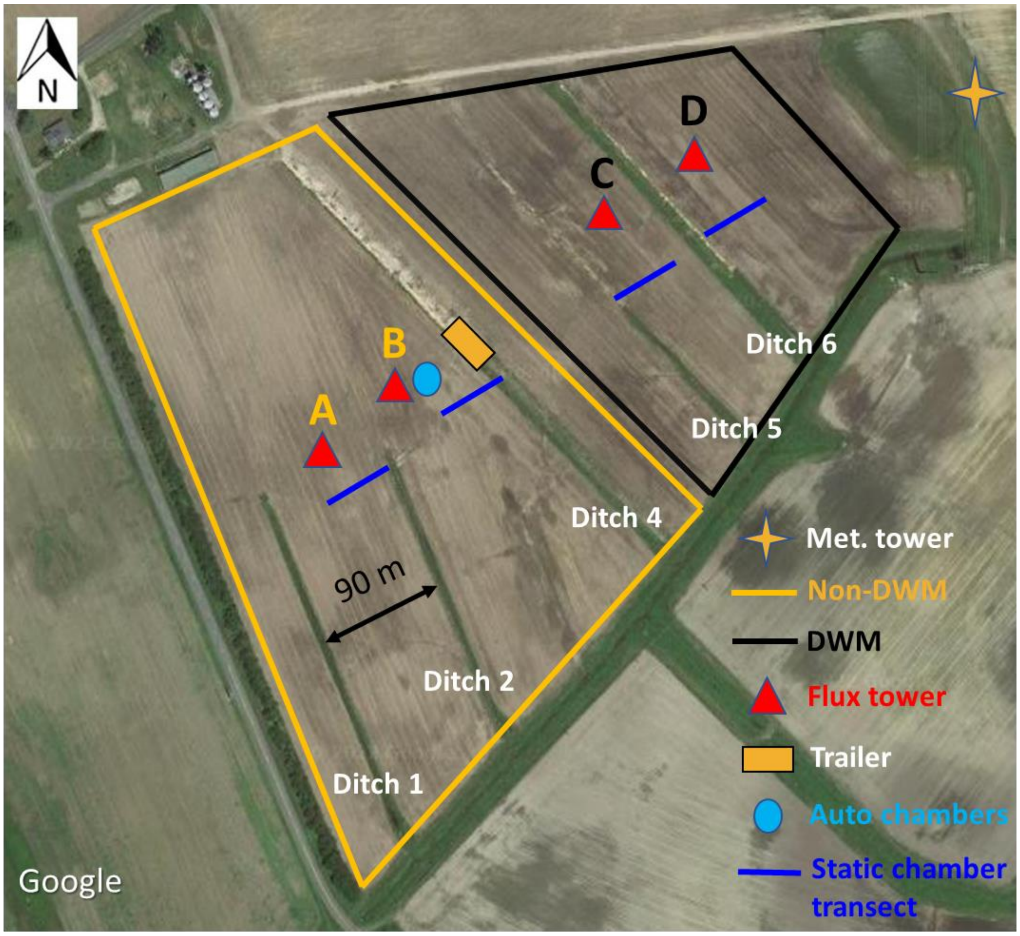

Figure 1. Google Map satellite image of the research farm with proposed siting of the DWM structures, the flux gradient measurement towers, the automated chambers, the static chamber transects, the meteorology tower, and the instrument trailer. Towers A and B were in the free drainage (non-DWM) fields; towers C and D were in the controlled drainage (DWM) fields.

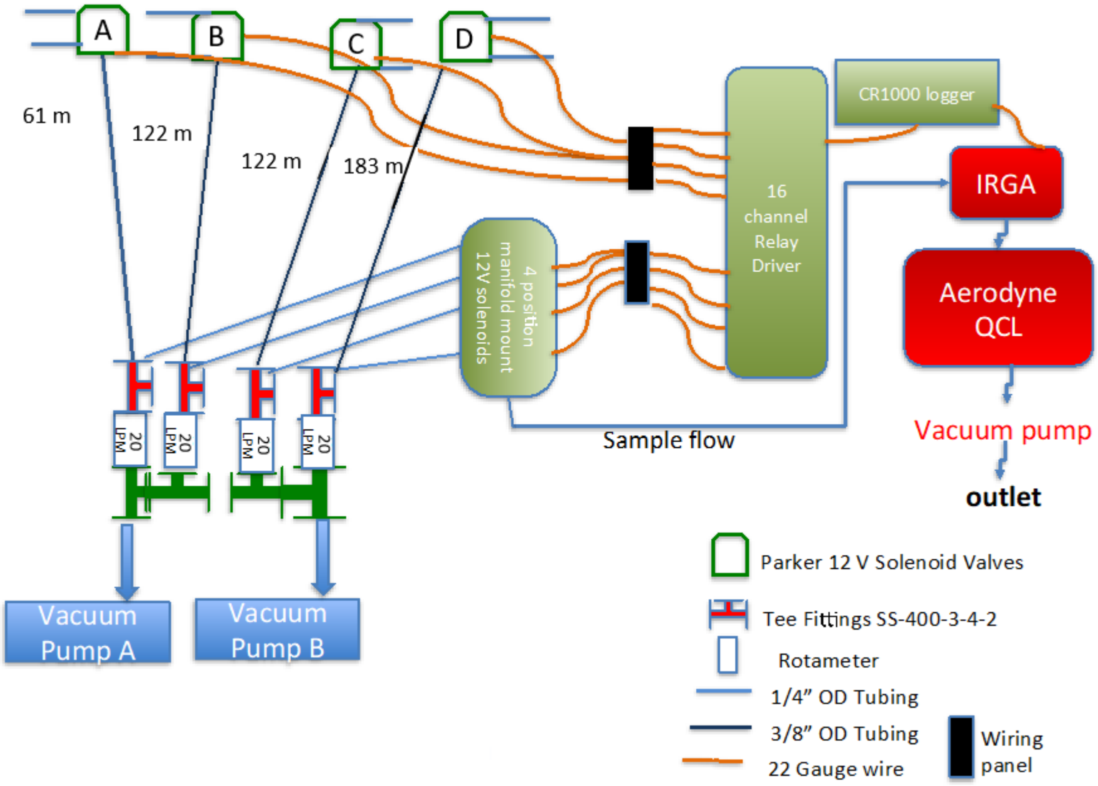

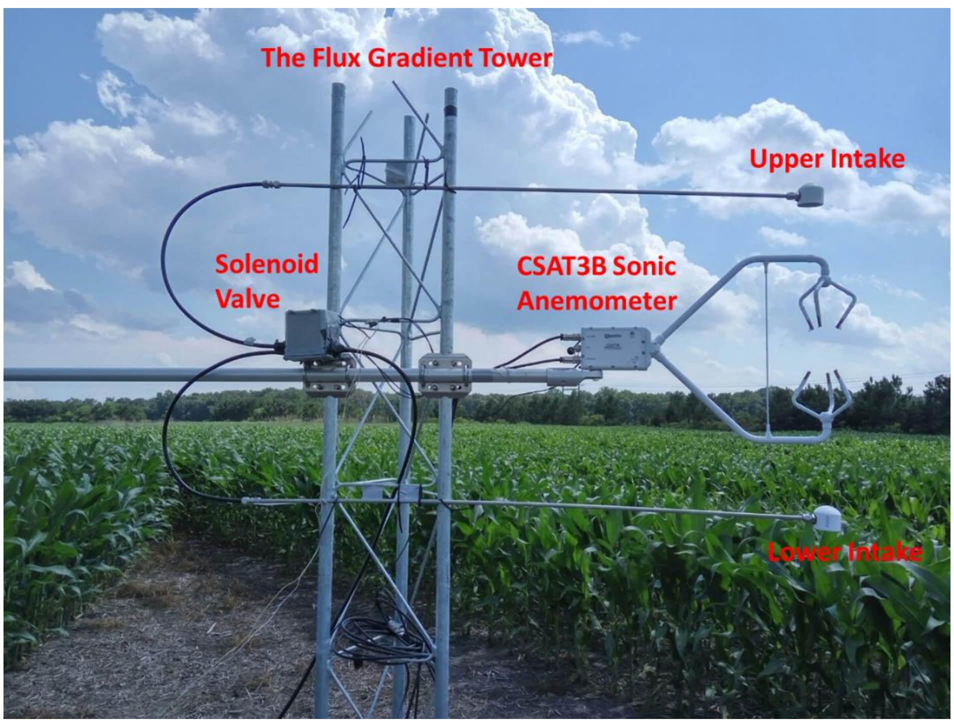

Figure 2. Diagram of the flux gradient system (top) (credit: Kathleen Savage) and a picture of the flux gradient tower (bottom). Vacuum pumps A and B were responsible for bringing air samples from towers to the instrument trailer. The Campbell Scientific CR1000 data logger and the 16-channel AC/DC relay driver were used to select air samples from towers in sequence and control switching between upper and lower intake inlets.

2.2.4 Flux Calculation

The flux gradient (FG) method is a micrometeorological approach based on the Monin-Obukhov similarity theory. It shares with the eddy covariance (EC) method the use of sonic anemometers, but differs from the EC method by measuring the differences in concentration of target trace gases at two heights on one or multiple towers. The relationship between the half-hourly flux (F) and the 30-min averaged concentration gradient is expressed as:

$$F = -K\frac{\partial C}{\partial z} \qquad [\ 1\ ]$$

where K is the eddy diffusivity ($m^2\ s^{-1}$) of the trace gas (e.g. N_2O or CH_4), and ∂C/∂z is the concentration gradient of this gas (kg m^{-4}). The introduction of the negative sign before K is to make sure positive fluxes are emissions and negative fluxes are uptakes as a convention. K is calculated as:

$$K = \frac{u_* \kappa (z_2 - z_1)}{\left[ln\left(\frac{z_2 - d}{z_1 - d}\right) - \psi_{h2} + \ \psi_{h1}\right]} \qquad [\ 2\ ]$$

$$\psi = \begin{cases} -4.7\frac{z-d}{L} & Stable \\ 2\ln\left(\frac{1+x^2}{2}\right), x = \left(1 - 15\frac{z-d}{L}\right)^{\frac{1}{4}} & Unstable \\ 0 & Neutral \end{cases} \qquad [\ 3\ ]$$

where u_* is the friction velocity measured at a half-hourly interval, κ is the von Karman constant (0.41), d is the displacement height (0.67 times canopy height), and ψ_{h1} and ψ_{h2} are the integrated Monin-Obukhov similarity functions for sensible heat at sampling heights z_1 and z_2. The similarity functions were calculated using Eq. [3], with the atmospheric stability conditions determined by the stability parameter (z-d)/L, where L is the Obukhov length (Wagner-riddle et al., 2007). For the stability parameter acquired every 30-min, the range from 0.02 to 2 was defined as “stable”; the range from -2 to -0.02 was defined as “unstable”; the range from -0.02 to 0.02 was defined as “neutral”. Here it was assumed that the eddy diffusivities for heat and the trace gas (N_2O or CH_4) were equal. The Obukhov length (L) was calculated as:

$$L = \frac{-u_*^3 T_v}{\kappa g \overline{w' T_v'}} \qquad [\,4\,]$$

where T_v is the virtual temperature, g is the acceleration due to gravity, and $\overline{w'T_v'}$ is the kinematic virtual temperature flux which is related to the sensible heat flux (H):

$$\overline{w' T_v'} = {}^{H}\!/_{\rho_a C_p} \qquad [\,5\,]$$

where ρ_a is the air density and C_p is the heat capacity of air.

The 30-min averaged concentration difference (ΔC) between the upper (even c_i) and lower (odd c_i) inlets was calculated as:

$$\Delta C = \frac{1}{n-2} \sum_{i=1,3,5,\ldots}^{n-3} c_{i+1} - \frac{c_i + c_{i+2}}{2} + \frac{c_{i+1} + c_{i+3}}{2} - c_{i+2} \qquad [\,6\,]$$

This averaging technique acted as a high-pass digital filter and removed low-frequency noise from the data (Brown & Wagner-Riddle, 2017; Wagner-Riddle et al., 2005; Waldo et al., 2019). In addition, a number of criteria were adopted to ensure data quality:

- unreasonably high or low concentration data were filtered;
- the first 6 seconds of each 20-second concentration measurement at the upper or lower inlet were discarded to allow transients in the sampling flow to stabilize following switching between inlets;
- air sample travel time lags were different for the four towers because of their different distances to the instrument trailer, which was taken into account in the calculation (the air

sample travel time lag for a tower was determined by repeatedly injecting N_2O and CH_4 gas standards at the tower and calculating the average elapsed time until the injected gas samples were detected by the QCL instrument);

- the maximum difference in analyzer pressure between the upper and lower inlets was restricted to ±2 torr;
- the number of samples collected every 30 minutes was required to be ≥ 80% of the maximum possible number of data points;
- any measurements disrupted by field work were discarded;
- half-hourly sonic anemometer data with a non-zero diagnostic word flag were discarded;
- friction velocity was ≥ 0.1 m/s;
- the stability parameter (z-d)/L was constrained to the range from -2 to 2;
- concentration data were omitted when the wind was coming from behind the tower (170-190°);
- the distance from the tower to the edge of the field was at least 50 times the height of the tower to assure that > 80% of the observed flux originated within the experimental fields.

Flux units of ng m^{-2} s^{-1} were used for the 30-min N_2O and CH_4 fluxes, and the units were converted to g N_2O-N ha^{-1} day^{-1} and g CH_4-C ha^{-1} day^{-1} for N_2O and CH_4, respectively, when daily flux means and annual emissions were calculated. Daily flux means were calculated by averaging the 30-min flux values of each day. Daily fluxes were reported only when there were at least two half-hourly values recorded.

2.2.5 Chamber Measurements

In a companion study (Hagedorn et al., 2022), soil gas fluxes of N_2O and CH_4 were also measured using manual static chambers with a Picarro G2308 cavity ringdown spectrometer

(Picarro Inc., CA, U.S.A.), connected to a low-flow (~0.23 L/min) pump circulatory system. This Picarro analyzer measured real-time, in-situ headspace gas concentrations at a frequency of 1 Hz, and the sampling time for small fluxes was approximately 5 minutes. Transects of 8 chambers were installed perpendicular to each ditch (except for D1, see Fig. 1). The length of each transect was approximately 12 m and the soil chamber collars were equally spaced. The chamber measurements were made approximately monthly, but more frequent sampling was conducted around agricultural practices such as planting, fertilization, and harvest to better capture the dynamics of N_2O and CH_4 fluxes during those periods. Fluxes were measured between 8:00 EST and 17:00 EST, and the sampling order was randomized to ensure the same field was not sampled at the same time of day to minimize the effects of diel variation.

In addition to the static chamber measurements of N_2O and CH_4 fluxes, four Eosense closed dynamic automated chambers (model: eosAC) and a multiplexer (model: eosMX) (Eosense Inc., NS, Canada) were installed next to tower B (Fig. 1) and connected to the Picarro G2308 gas analyzer from April to June in the 2019 corn-growing season.

Further details about the chamber measurements can be found in the companion study (Hagedorn et al., 2022) of this project.

2.2.6 Supporting Environmental Data

A 3.5 m meteorological tower was installed approximately 120 m from the research site, equipped with sensors to continuously measure air temperature and relative humidity (using Campbell Scientific CS215 temperature and relative humidity sensor), barometric pressure (using CS105 Vaisala PTB101B Barometer), precipitation (using Texas Electronics TE525WS tipping rain gauge), and wind speed and direction (using RM Young 05103 wind monitor). These sensors were located approximately 3 m high (except the barometric pressure sensor was at 1 m high) above the soil surface. The data were stored on a Campbell Scientific CR10X data logger inside a weather-proof enclosure attached to the tower and output at a 30-minute interval in order to match the measurement interval of N_2O and CH_4 fluxes. Gaps in the precipitation data were filled using historical precipitation data from two nearby weather stations at Greensboro, MD (GHCND:US1MDCL0009) and Denton, MD (GHCND: US1MDCL0010).

The vertical profile of soil temperature and volumetric water content (VWC) was acquired from two continuously recording systems, one installed next to tower A in the non-DWM field and the other one installed next to tower C in the DWM field. By horizontally inserting the Decagon 5TE water content, EC, and temperature sensors (METER Group Inc., WA, U.S.A.) at five depths (5 cm, 10 cm, 20 cm, 30 cm, and 50 cm) below the soil surface, soil temperature and moisture data were stored on the Campbell Scientific CR10X data loggers at 30-minute intervals. The Topp equation (G. C. Topp et al., 1980) was used to convert raw dielectric permittivity measured by the 5TE sensors into soil VWC data. Manufacturer's tests showed that data from a properly installed 5TE sensor in a normal mineral soil applied to the Topp equation resulted in measurements within ±3% VWC of the actual soil VWC. Cross-calibration of the 5TE sensors can be found in the supplementary materials.

In 2018 and 2019, analyses of soil ammonium and nitrate concentration were part of the companion study; details can be found in Hagedorn et al. (2022). In brief, samples of the 0-5 cm soil depth were taken approximately monthly using a 2.2 cm diameter soil push probe, transported back to the laboratory in a refrigerated cooler and processed within 48 hours. Triplicate soil samples were composited at each of eight locations on each of the four fields at each date. At the lab, each field moist sample was sifted using a 2 mm opening sieve to remove rocks, fine roots, etc. Six grams of the sieved soil were extracted in 30 mL of 2M potassium chloride (KCl) in an Ehrlenmeyer flask, placed on a shaker table on low speed for at least 2 hours, and vacuum filtered through a Whatman No.42 filter paper. The filtered extracts were analyzed for nitrate and ammonium concentrations by a Lachat autoanalyzer (Maynard et al., 1993).

2.2.7 Statistical Analyses

To test the effects of DWM on trace gas fluxes, a one-way repeated measures ANOVA test was used to detect whether there were significant differences in the flux measurements between the four towers when all of them were functioning. A logarithm transformation (log10) was applied when the data were non-normal or skewed to meet the required assumptions of normality and homogeneity of variances for all groups. A small positive offset was added to make all values positive before log transformation. After the logarithmic transformation, not all of the towers' data were normally distributed (Fig. 3 and Fig. 4), but the assumption of homogeneity of variances across groups (towers) was satisfied (Table 1). The one-way repeated measures ANOVA was followed up by multiple pairwise t-tests using a Bonferroni multiple testing correction method for p-value adjustment to test differences between towers. In addition, a Friedman test was used when the assumption of normality was relaxed/violated (see Appendix A). Pairwise Wilcoxon signed-rank tests were the post hoc tests for the Friedman test. Because the alternative Friedman test showed nearly identical results to the one-way repeated measures ANOVA, only the comparisons using the latter were presented in the following section. Gap-filled flux values were not used in the statistical tests to avoid bias in the comparisons. Statistical analyses were performed in R (R Core Team, 2022).

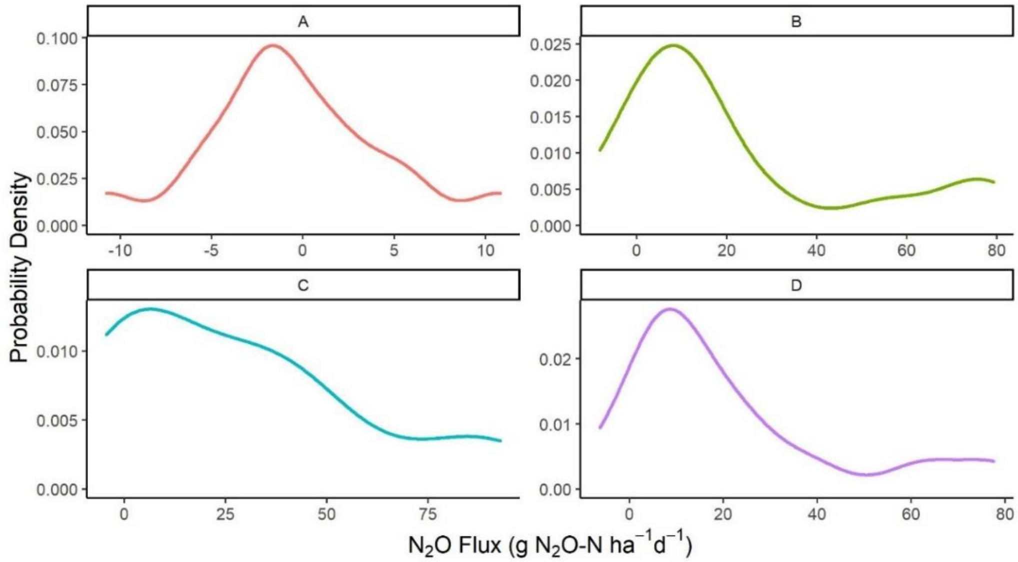

Figure 3. The density distributions of the daily N_2O fluxes measured in July 2018 when all of the four towers were functioning. Each tower contains 14 daily values. Notice the differences in scale on the x- and y-axes.

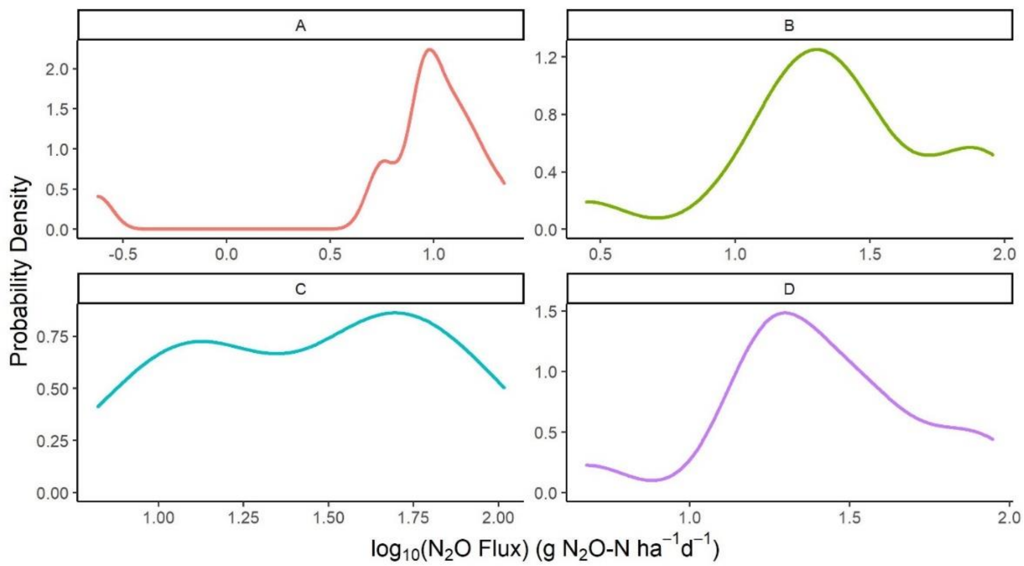

Figure 4. The density distributions of the log-transformed daily N_2O fluxes measured in July 2018 when all of the four towers were functioning. Each tower contains 14 daily values. Notice the differences in scale on the x- and y-axes.

Table 1. The Levene's test and the Fligner-Killeen's test to check the homogeneity of variances across groups (towers) for the daily N_2O fluxes measured in July 2018. The Levene's test is not sensitive to departures from normality and the Fligner-Killeen's test is very robust against departures from normality. A p-value less than 0.05 indicates significant differences between variances across groups (towers).

Test	Before log-transformation	After log-transformation
Levene's test	p = 0.023	p = 0.823
Fligner-Killeen's test	p = 0.004	p = 0.460

2.3 Results

2.3.1 Environmental Data

2.3.1.1 Precipitation and Air Temperature

Daily precipitation and irrigation amounts during the 2018-2019 experimental period are shown in Fig. 5a. The highest daily rainfall amount was 7.46 cm, recorded on October 12, 2018. The total annual precipitation was 157 cm in 2018 and 109 cm in 2019. The driest month was November 2019 with 1.62 cm precipitation and the wettest month was September 2018 with 8.57 cm precipitation. The daily average air temperature over two years was 13.4 ºC and ranged from -13.0 to 30.1 ºC (Fig. 5b). Mean monthly air temperature varied between -0.2 ºC in January 2018 and 25.5 ºC in July 2019.

2.3.1.2 Soil Temperature and Moisture

Daily averaged soil temperature at 5 cm depth followed the seasonal trends observed in the air temperature data (Fig. 5c), ranging from -1.5 to 31.1 ºC over the two-year period. In the DWM field, the daily mean of the soil volumetric water content (VWC) measured at 5 cm depth ranged from 0.140 to 0.416 $m^3 m^{-3}$ over the course of the two-year measurement; in the non-DWM field, the daily mean of the soil VWC at 5 cm depth varied from 0.127 to 0.316 $m^3 m^{-3}$ (Fig. 5d). The figure shows that the daily averaged surface soil VWC followed the same pattern in the DWM and non-DWM fields following precipitation events and both sites had drier soil conditions in the summer than in other seasons of the year. Comparing the non-DWM site to the DWM site, the soil VWC at 5 cm depth was 0.087 m^3 m^{-3} lower on average. Data gaps existed for both the soil temperature and moisture data because of the malfunction of the data loggers (such as dead batteries) and gaps were more common for the non-DWM site.

2.3.1.3 Soil Nitrogen Concentration

The soil extractable nitrate in the top 5 cm ranged from 0.70 to 28.31 mg N kg^{-1} in the DWM field and from 0.55 to 22.66 mg N kg^{-1} in the non-DWM field (Fig. 5e). Fertilization events occurred two times following the planting of corn in 2019, as indicated by the arrows in the figure. Soil nitrate concentrations increased immediately after the applications of the UAN fertilizer and decreased through the remainder of the year in both the DWM and non-DWM fields. The N fertilizer applications in the growing season of 2019 did not result in significant changes in soil extractable ammonium concentrations. In 2018, soil nitrate concentrations were elevated after the planting of soybean but did not increase as high as the concentrations in the corn year when synthetic fertilizer was used. However, there was one measurement in June 2018 showing high ammonium values compared to other measurements during this study period.

2.3.2 The FG Measurements

Over the two years (2018-2019), 6752 individual half-hourly flux measurements were made with the four FG towers, which had been converted into 337 daily mean values for the DWM site and 324 daily mean values for the non-DWM site (Fig. 5g and Fig. 5h). Due to some instrument issues, there was only approximately one-month of flux measurements in 2018.

For N_2O, both sites showed the same general trend over time: significant emissions were observed following the application of N fertilizer in the May-July period of 2019, coinciding with precipitation events. After the second fertilization in 2019, maximum daily N_2O emission values measured from the DWM site and the non-DWM sites were 963 and 236 g N_2O-N ha^{-1} day^{-1} on June 30, respectively. N_2O emissions then decreased to close to zero throughout the remaining months of the year. During the one-month measurements in soybean from June 29 to August 3 in 2018, both sites had measurable N_2O emissions, but those emissions were low compared to the 2019 N_2O flux data in corn.

For CH_4, there were no such trends in the daily mean time series as I found in the N_2O data following N fertilization, with the CH_4 fluxes ranging from -83 to 85 g CH_4-C ha^{-1} day^{-1} in the DWM field and -93 to 53 g CH_4-C ha^{-1} day^{-1} in the non-DWM field.

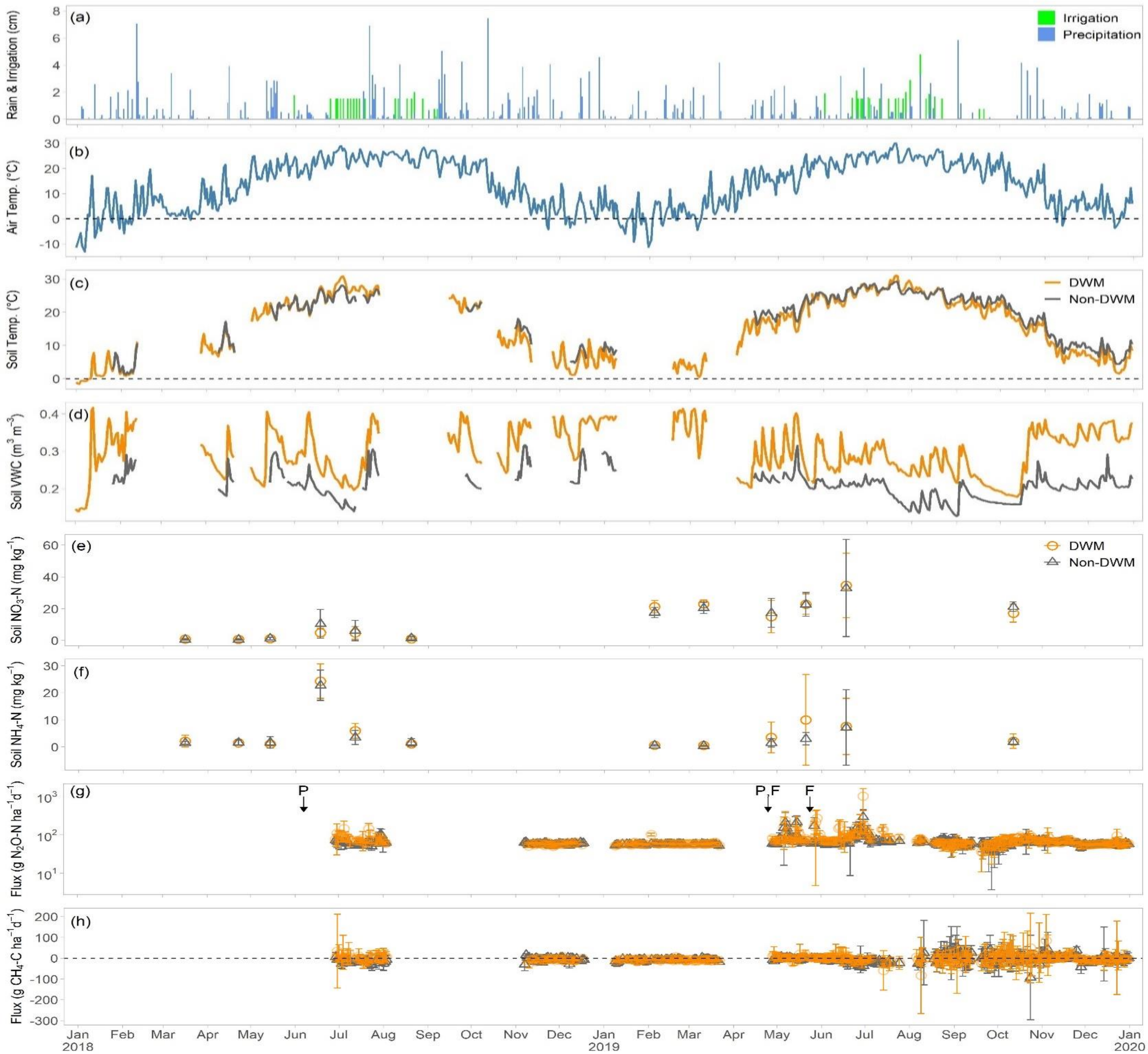

Figure 5. Time series of environmental, soil, and flux variables measured in the 2018 soybean and 2019 corn years. (a) Precipitation and irrigation events, (b) daily averaged air temperature, (c) daily averaged soil temperature at 5 cm depth, (d) daily averaged soil volumetric water content (VWC) at 5 cm depth, (e) soil extractable nitrate, (f) soil extractable ammonium, (g) daily averaged N_2O fluxes (in log scale, a small positive offset (60 g N_2O-N ha^{-1} d^{-1}) was added to make all values positive before log transformation), and (h) daily averaged CH_4 fluxes aggregated by treatment. Black arrows denote planting (P) and fertilization (F) events. Whiskers in panels (e) and (f) represent the standard deviation of the replicated samplings of the field soil (spatial heterogeneity) and whiskers in panels (g) and (h) represent the standard deviation of the daily mean calculated from half-hourly flux values (temporal heterogeneity).

2.3.2.1 Comparisons between the FG Towers

During the one-month flux measurements in the growing season of 2018, all of the FG towers measured N_2O fluxes that significantly exceeded the minimum detection limit (MDL)[1] of the FG system (Fig. 6 and Fig. 7), except for tower A. These emission events were triggered by frequent irrigation and heavy rainfalls, given sufficient reactive nitrogen was contained in the soil, which was shown by the somewhat elevated soil nitrate concentrations during the summer of 2018 in Fig. 5e. The lack of emission pulses at tower A was most likely due to drier conditions on the plot where tower A was installed, which was reflected by the soil VWC at 5 cm depth in Fig. 5d. From mid-June to mid-July of 2018, the soil VWC dropped to almost the lowest level in the 2-year study period. Hagedorn et al. (2022) also reported a particularly dry period when the lowest soil moisture content was recorded in July 2018 by using a manual Decagon 5TM soil moisture probe. Later in the winter, no emission events were observed by towers A and C (only two towers were deployed for sampling to save on maintenance costs and labor). For CH_4, most fluxes measured in this year were within the minimum detection limit of the FG system, except for some mild emission pulses showed at towers C and D in the summer. In general, no clear pattern was discernible in the CH_4 flux data.

In contrast to 2018, more vigorous N_2O production by soil in the growing season of 2019 was detected at all of the four FG towers (Fig. 8 and Fig. 9). Tower C had the most intense emission events among all of the towers, with both the maximum half-hourly and daily N_2O fluxes (3383 ng m^{-2} s^{-1} and 963 g N_2O-N ha^{-1} day^{-1} (not shown in the figure because it is off the scale of the Y axis), respectively) being observed on the same day (June 30). N_2O emissions increased

[1] The minimum detection limit (MDL) for N_2O/CH_4 concentration gradients is determined in Chapter 4. To calculate the MDL for N_2O/CH_4 fluxes, replace the concentration gradient term (ΔC) in Eq. [1] with the MDL for N_2O/CH_4 gradients.

moderately in late October and early November (observed in all data sets), which was driven by frequent heavy rainfall events that took place on October 16 (4.17 cm), 20 (3.61 cm), 22 (1.78 cm), 27 (3.81 cm), and 31 (1.47 cm). This can be ascribed to the potential post-harvest release of some mineralized soil N that was not taken up by the crop. At other times of the year, there were scarcely any N_2O emission events apart from baseline fluxes that were within the system's detection limit. In the case of the CH_4 flux measurements, similar to 2018, no distinct differences were found among the four FG towers, except for some emission spikes detected in September at tower B and in October and November at tower D. Below Table 2 and Table 3 provides summary statistics of the half-hourly and the mean daily N_2O and CH_4 fluxes measured by the four towers in the 2018-2019 experimental period.

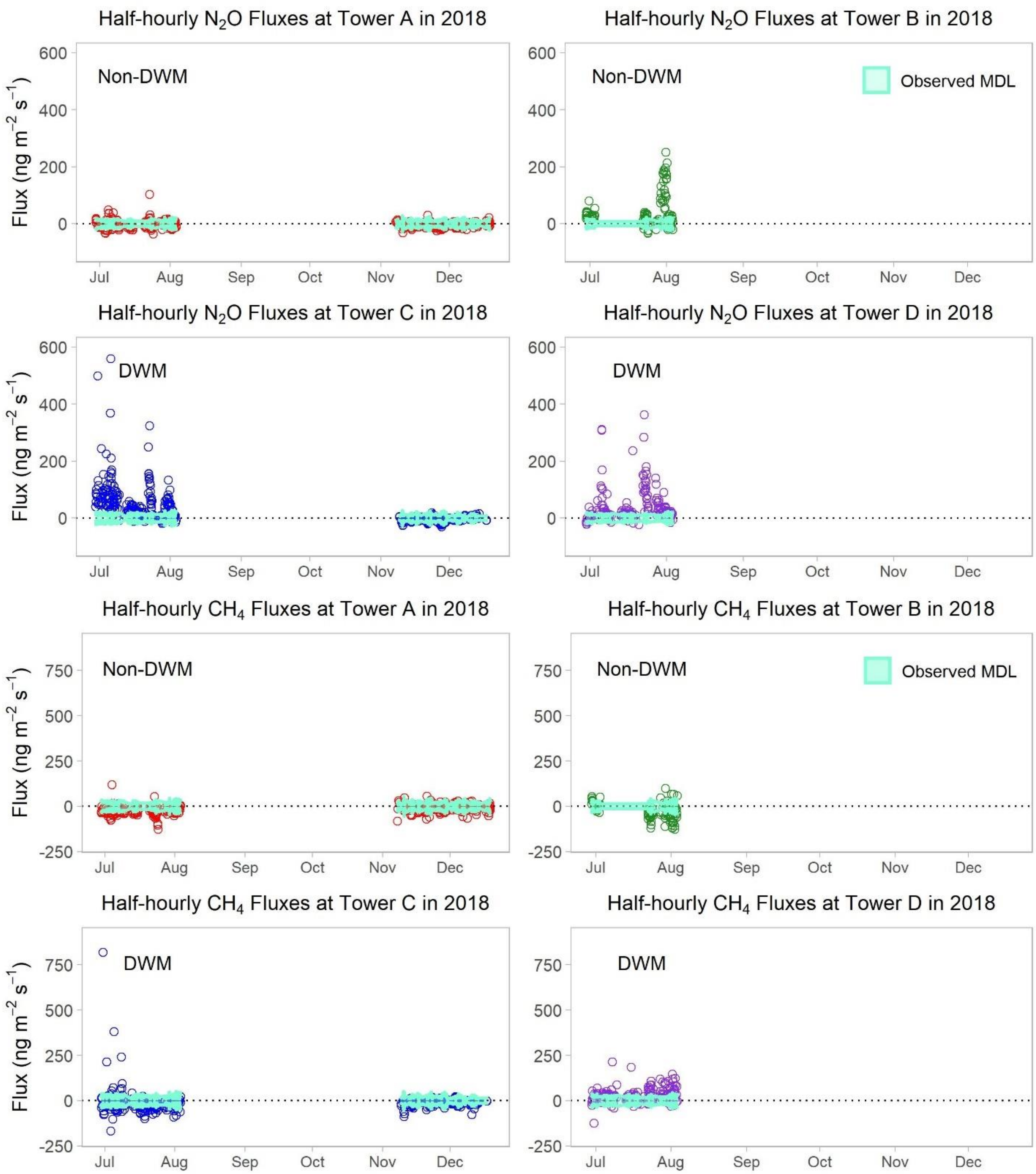

Figure 6. Half-hourly N_2O and CH_4 fluxes (in units of ng m^{-2} s^{-1}) measured at each of the four FG towers in 2018. Due to instrument failure, no N_2O/CH_4 mixing ratio data were available from early August to November. Only tower A and tower C were used for sampling in the winter. The shaded aquamarine areas represent the observed minimum detection limit (MDL) using the zero-gradient test for the flux data (see Chapter 4 for more details regarding the determination of the MDL).

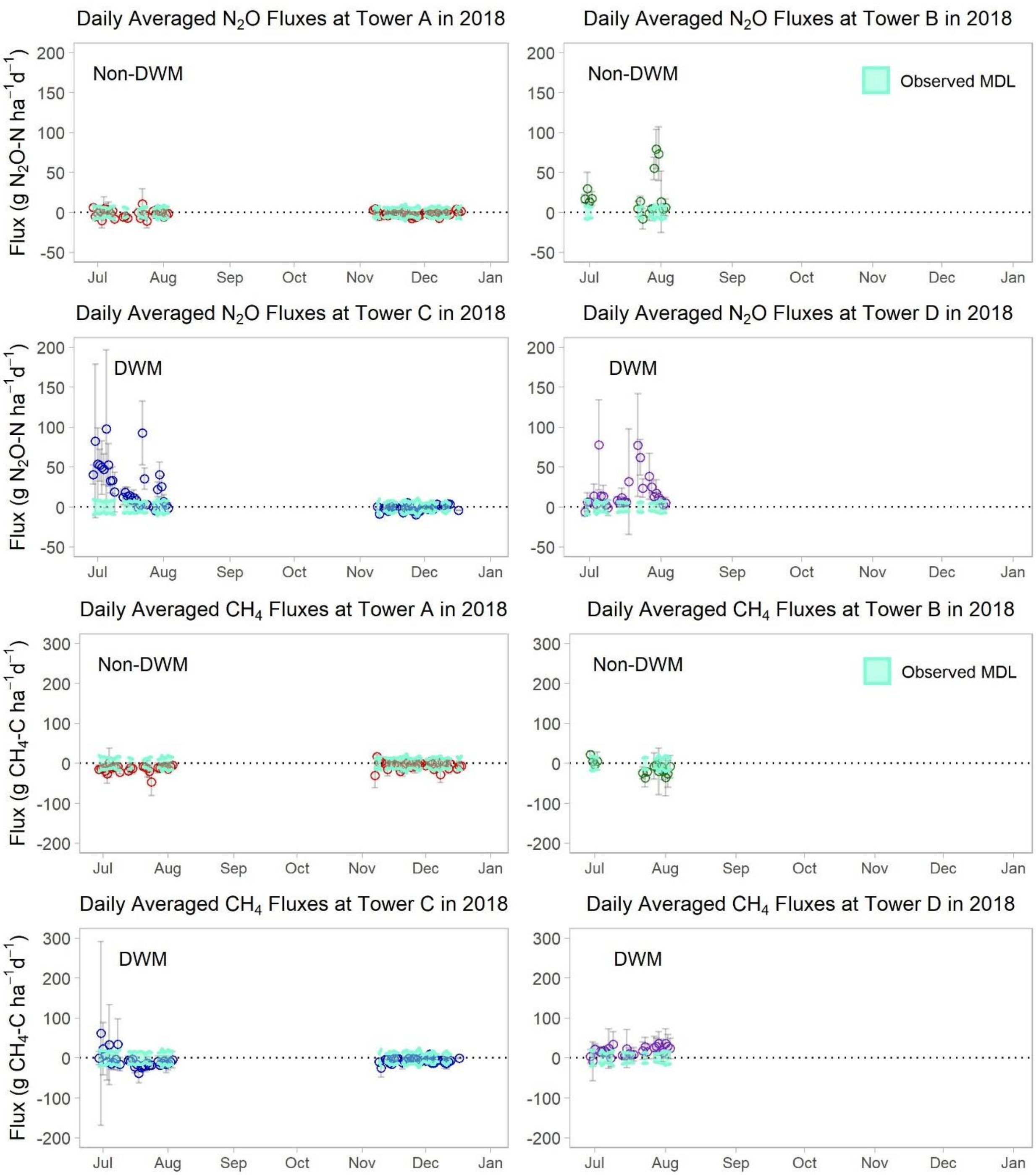

Figure 7. Mean daily N_2O and CH_4 fluxes (in units of g N_2O-N ha^{-1} d^{-1} and g CH_4-C ha^{-1} d^{-1}, respectively) at each of the four FG towers in 2018. Due to instrument failure, no N_2O/CH_4 mixing ratio data were available from early August to November. Only tower A and tower C were used for sampling in the winter. The shaded aquamarine areas represent the observed minimum detection limit (MDL) using the zero-gradient test for the flux data (see Chapter 4 for more details regarding the determination of the MDL).

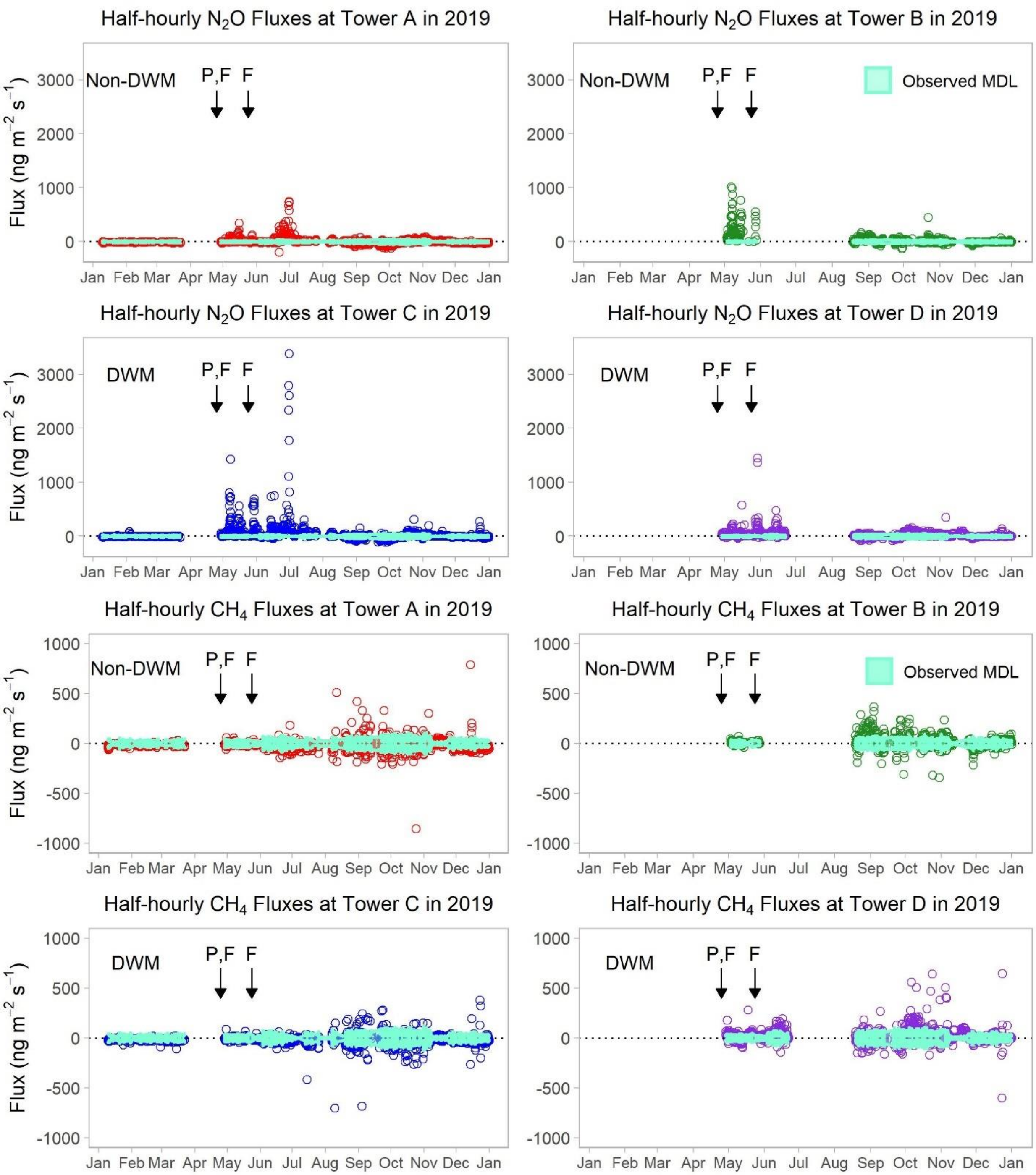

Figure 8. Half-hourly N_2O and CH_4 fluxes (in units of ng m^{-2} s^{-1}) measured at each of the four FG towers in 2019. Only tower A and tower C were used for sampling in the spring. The shaded aquamarine areas represent the observed minimum detection limit (MDL) using the zero-gradient test for the flux data (see Chapter 4 for more details regarding the determination of the MDL). The black arrows denote corn planting (P) and fertilization (F) with UAN.

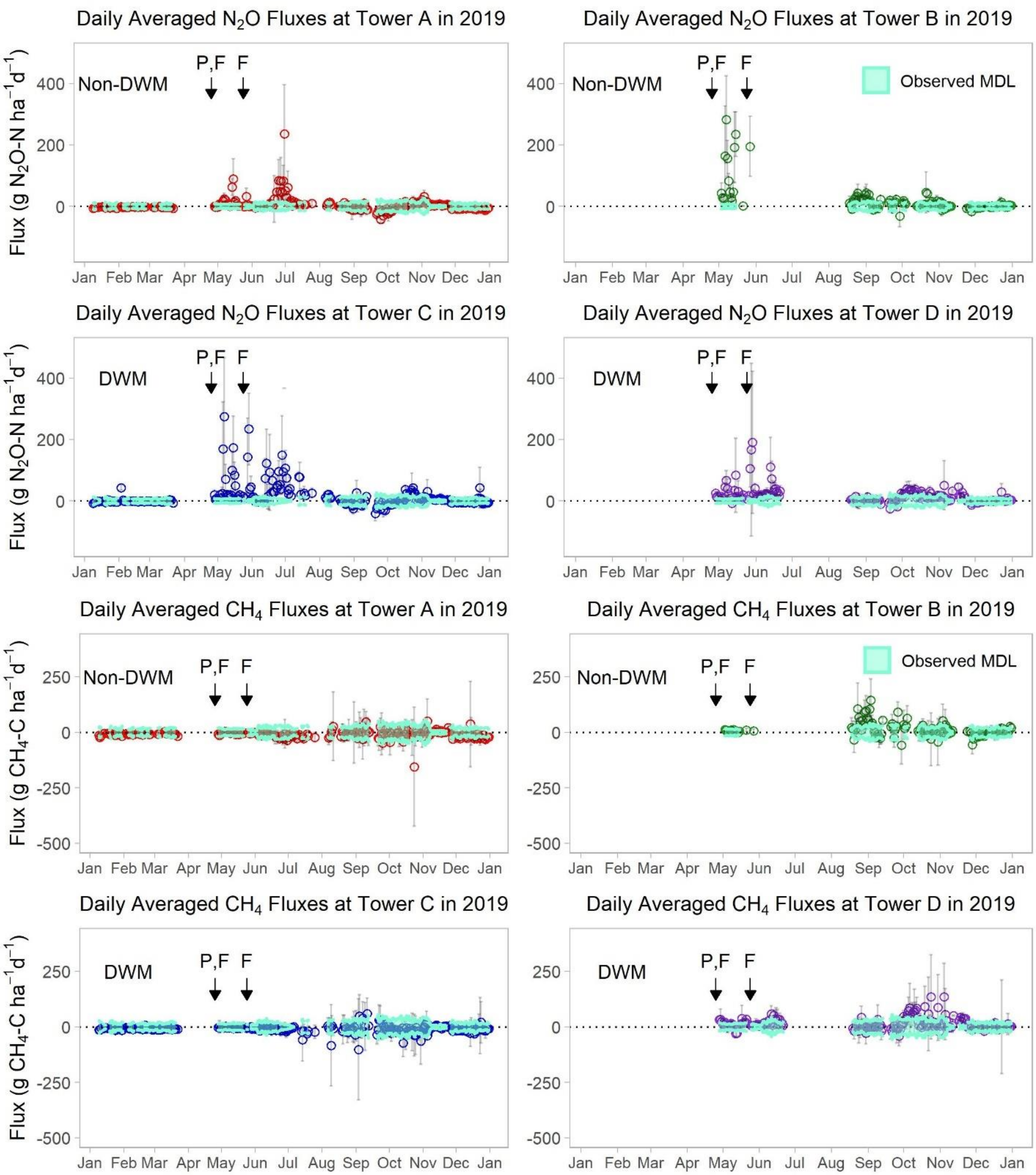

Figure 9. Mean daily N_2O and CH_4 fluxes (in units of g N_2O-N ha^{-1} d^{-1} and g CH_4-C ha^{-1} d^{-1}, respectively) at each of the four FG towers in 2019. Only tower A and tower C were used for sampling in the spring. The shaded aquamarine areas represent the observed minimum detection limit (MDL) using the zero-gradient test for the flux data (see Chapter 4 for more details regarding the determination of the MDL). For tower C, the maximum mean daily N_2O flux (963 ± 596 g N_2O-N ha^{-1} d^{-1} on June 30) was not included in the figure in order to have a consistent y-axis scale among the figures. The black arrows denote corn planting (P) and fertilization (F) with UAN.

Table 2. Summary statistics (minimum, maximum, 25th and 75th percentiles, median, mean, and number of observations (n)) of the half-hourly N_2O and CH_4 fluxes measured by the four FG towers in 2018 and 2019.

Year		2018				2019			
Tower		A	B	C	D	A	B	C	D
Day of year		180-215, 311-352	180-183, 203-215	180-215, 313-351	180-190, 194-215	9-81, 118-206, 219-256, 263-365	122-147, 230-256, 263-315, 328-365	9-81, 118-187, 194-206, 218-256, 263-365	118-173, 231-256, 263-365
Half-hourly N_2O flux	min.	-36.58	-32.36	-29.59	-23.18	-192.97	-135.80	-113.26	-81.69
($ng\ m^{-2}\ s^{-1}$)	25th%	-8.73	8.63	-4.36	8.30	-8.33	-4.64	-6.03	1.48
	75th%	2.57	55.42	44.27	36.60	8.86	35.06	21.73	38.91
	max.	103.83	250.67	559.27	363.44	744.13	1019.88	3383.27	1453.04
	median	-2.67	26.37	5.20	17.73	-1.28	5.08	0.86	16.07
	mean	-2.46	45.03	28.25	38.00	5.51	37.83	33.10	28.41
	n	419	98	399	182	1770	788	1814	1282
Half-hourly CH_4 flux	min.	-125.93	-127.31	-167.63	-123.32	-852.33	-342.35	-703.99	-599.04
($ng\ m^{-2}\ s^{-1}$)	25th%	-23.72	-51.28	-26.94	5.46	-26.45	-11.79	-24.36	-7.43
	75th%	1.82	0.78	-0.93	39.24	-0.40	27.45	-2.61	35.19
	max.	120.40	98.98	818.47	214.84	790.32	368.16	377.72	647.17
	median	-8.07	-20.61	-11.17	20.75	-10.34	4.56	-10.37	11.04
	mean	-11.34	-25.27	-10.61	27.50	-12.46	12.67	-14.57	19.24
	n	419	98	399	182	1770	788	1814	1282

Table 3. Summary statistics (minimum, maximum, 25th and 75th percentiles, median, mean, and number of observations (n)) of the mean daily N_2O and CH_4 fluxes measured by the four FG towers in 2018 and 2019.

Year		2018				2019			
Tower		A	B	C	D	A	B	C	D
Day of year		180-215, 311-352	180-183, 203-215	180-215, 313-351	180-190, 194-215	9-81, 118-206, 219-256, 263-365	122-147, 230-256, 263-315, 328-365	9-81, 118-187, 194-206, 218-256, 263-365	118-173, 231-256, 263-365
Daily N_2O flux	min.	-10.76	-8.19	-9.63	-6.24	-42.68	-31.56	-40.97	-24.99
(g N_2O-N ha^{-1} d^{-1})	25th%	-3.90	4.67	-1.30	5.78	-4.47	-2.38	-2.87	0.72
	75th%	1.61	23.60	18.37	20.60	6.04	19.40	12.98	21.13
	max.	10.81	79.28	97.70	77.84	235.61	282.36	962.68	190.96
	median	-1.37	13.43	1.91	11.60	-1.24	3.77	0.01	10.29
	mean	-1.39	21.54	12.89	18.03	3.30	18.20	15.68	15.10
	n	65	15	64	27	254	120	266	176
Daily CH_4 flux	min.	-46.96	-36.72	-38.66	-7.96	-155.21	-58.14	-101.69	-42.09
(g CH_4-C ha^{-1} d^{-1})	25th%	-13.17	-22.22	-13.51	9.59	-16.81	-4.10	-14.25	-3.17
	75th%	-2.01	-3.62	-3.04	24.83	-1.69	19.86	-3.38	21.76
	max.	16.67	21.71	61.47	36.73	49.92	145.43	59.14	136.02
	median	-7.86	-8.18	-7.76	18.09	-7.55	5.52	-7.51	5.86
	mean	-8.46	-12.01	-6.51	17.60	-8.38	11.36	-9.46	13.16
	n	65	15	64	27	254	120	266	176

2.3.2.2 Precipitation and Post-Fertilization N_2O Emission Events

Precipitation has been demonstrated as a major driver of large N_2O emissions along with N fertilization in other studies (Wagner-Riddle et al., 2007; Waldo et al., 2019). For the growing season (soybean in 2018) without any N fertilizer application, N_2O emission events were observed after frequent irrigation (4 times in 6 days in early July) and heavy rainfalls (14.54 cm from July 22 to July 26) (Fig. 10a and b). However, the magnitude of the fluxes in July 2018 was much smaller than that in the growing season of 2019, when corn was the crop and N fertilizer was applied twice (on April 25 and May 24) on the farm (Fig. 10c and d). The first application (indicated by the first arrow in the figure) was followed by several rainfall events (7.34 cm from April 26 to May 5), which resulted in the first peak emission event on May 7. The second peak emission event that occurred on May 14 and 15 was triggered by frequent rainfall (3.61 cm) from May 10 to 13. Soon afterwards, the second fertilizer application to corn (indicated by the second arrow in the figure) on May 24 was followed by a 2.82 cm rainfall in less than 3 days, leading to the third emission event on May 28 in that year. Then a relatively dry period occurred from June 3 to June 12 (only 0.71 cm rain in 10 days), potentially explaining the absence of significant emission pulses during that period. Following that, the flux event on June 14 coincided with a 3.20 cm heavy rainfall event that took place the day before. The maximum N_2O fluxes were observed on June 30 after another heavier rainfall (3.78 cm) one day earlier, which followed a two-week dry period with little precipitation. On average, the response time of N_2O emissions to precipitation events was 1-2 days, given that enough nitrogen was presented in the soil. In contrast, heavy rainfall events beyond one month after N fertilizer application did not result in any increased N_2O fluxes, presumably due to lack of sufficient available nitrogen. Overall, the comparisons between the years with and without N fertilizer application and the fast response in

N_2O fluxes to precipitation events demonstrated that large N_2O emissions were highly dependent upon N fertilization and precipitation events.

2.3.2.3 Diurnal Patterns

From May to July in 2019 when intense N_2O emissions occurred, all of the four towers exhibited a diurnal pattern of increased N_2O fluxes in the afternoon and early evening (Fig. 11). No clear diurnal pattern was identified for the CH_4 flux data owing to the lack of large emission events, nor for the 2018 flux results because of the relatively short measurement period.

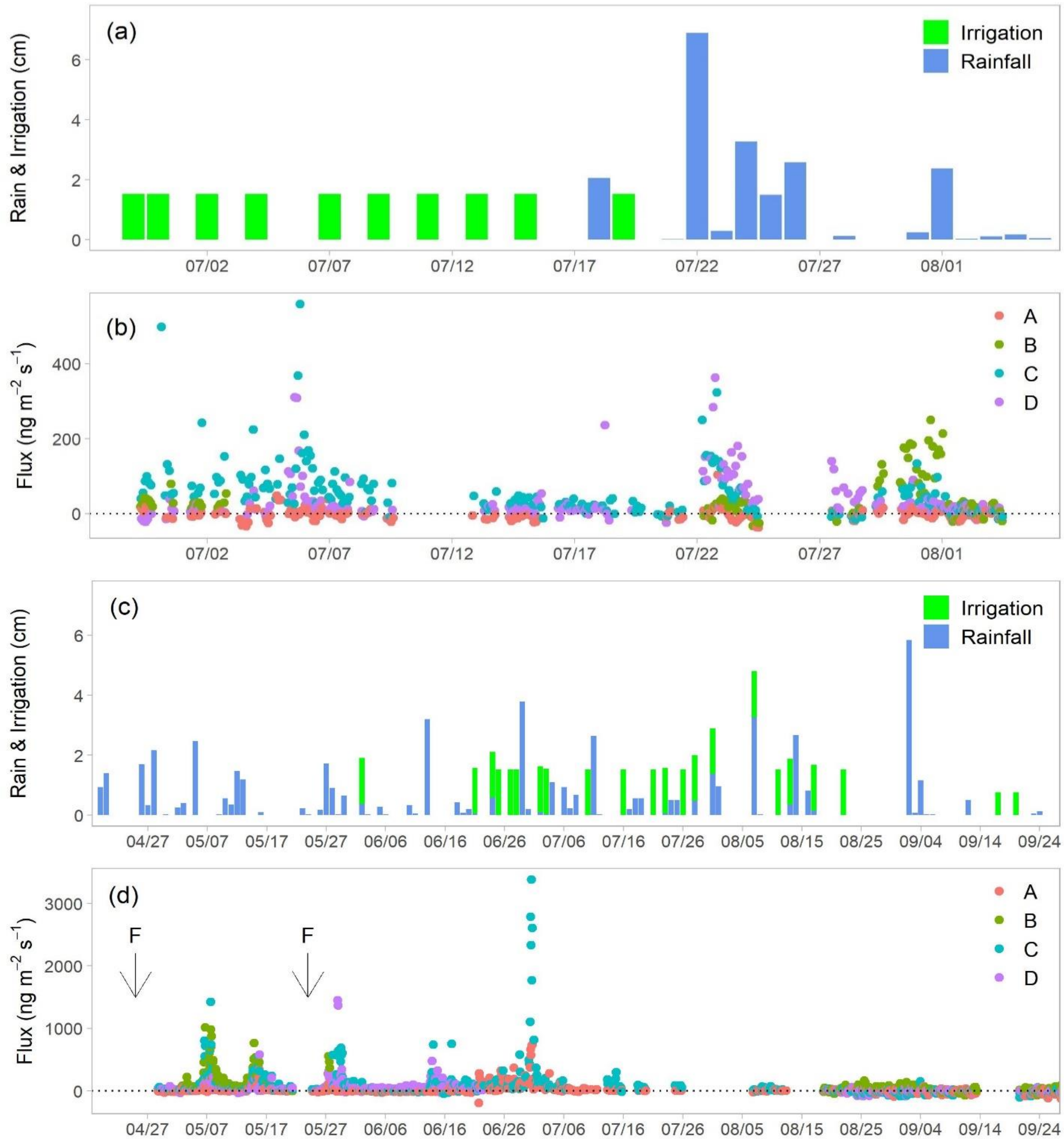

Figure 10. Daily precipitation, irrigation, and half-hourly N_2O fluxes (in units of ng m^{-2} s^{-1}) measured by the FG towers in the growing seasons of 2018 ((a) and (b)) and 2019 ((c) and (d)). Due to instrument failure, there was only approximately one-month of flux data in the summer of 2018. In the growing season of 2019, to prevent the towers from being hit by the pivot irrigation system, the top sections of the towers had to be removed when the irrigation system was on and then put back afterwards. In order to restore the towers' sampling as quickly as possible after irrigation and avoid excessive labor work, only tower A and C were used for sampling in late June and July, which explained why only these two towers' flux data were available for that period in the figure above. Note the difference in scale on the y-axis in panels b and d. The arrows indicate the dates of fertilization (F) of corn in 2019.

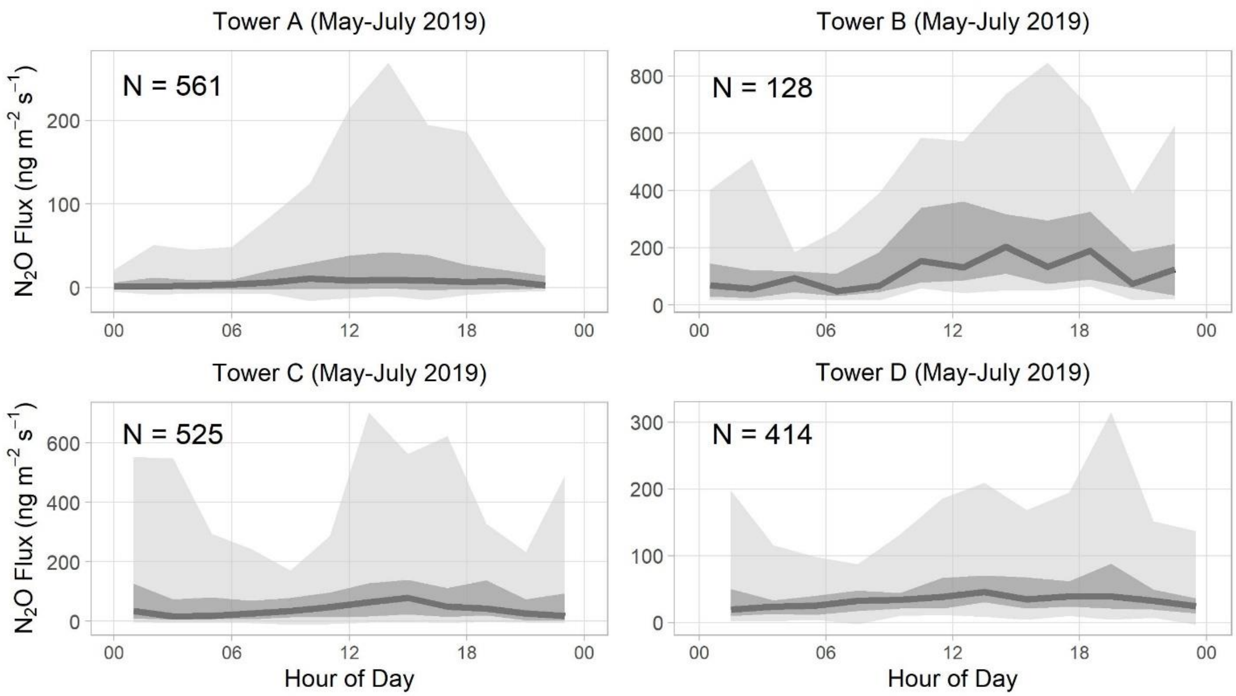

Figure 11. Diurnal patterns in N_2O fluxes (ng m^{-2} s^{-1}) measured by the FG towers from May to July in 2019 when large N_2O emissions were observed. Black lines represent median fluxes, the dark grey areas represent the ranges between 25% and 75% quantiles, and the light grey areas represent the ranges between 5% and 95% quantiles. The 'N' values denote the amount of the 30-min flux measurements made at each tower. Note differences in y-axis scales for different towers.

2.3.3 Effects of DWM on Soil N_2O and CH_4 Fluxes

2.3.3.1 Effects of DWM on Soil Moisture

From the perspective of management of the DCS (drainage control structures), the two-year experimental period consisted of four active periods when the DCS boards were installed to retain more water in the DWM plots and three inactive periods when the DCS boards were removed for the farm's management practices. In other words, I expected to see fewer differences in soil moisture and soil greenhouse gas emissions during the inactive board periods than during the active board periods. The four active board periods were Jan. 1 to Mar. 15 in 2018, Jun. 18 to Sep. 12 in 2018, Oct. 17, 2018 to Mar. 6, 2019, and May 24 to Dec. 31 in 2019.

Further details about the active and inactive board periods can be found in Hagedorn et al. (2022).

The boxplots of the differences in soil VWC (m^3 m^{-3}) between the DWM and non-DWM sites for the active and inactive board periods (Fig. 12) showed that both the mean and the median of the differences in soil VWC between DWM and non-DWM were greater during the active board periods than during the inactive board periods. The difference in soil VWC between the two treatments was analyzed because, as shown in Fig. 5d, the DWM site was consistently wetter than the non-DWM site, indicating pre-treatment natural variation. A non-parametric one-sided Wilcoxon rank sum test indicated that the differences in soil VWC between the two sites during the active board periods were larger than during the inactive periods at a significance level of $p < 0.001$. The third quartile and the maximum during the active board periods were also apparently higher than that during the inactive periods, suggesting that larger differences between the two site's soil moisture were more common during the active board periods.

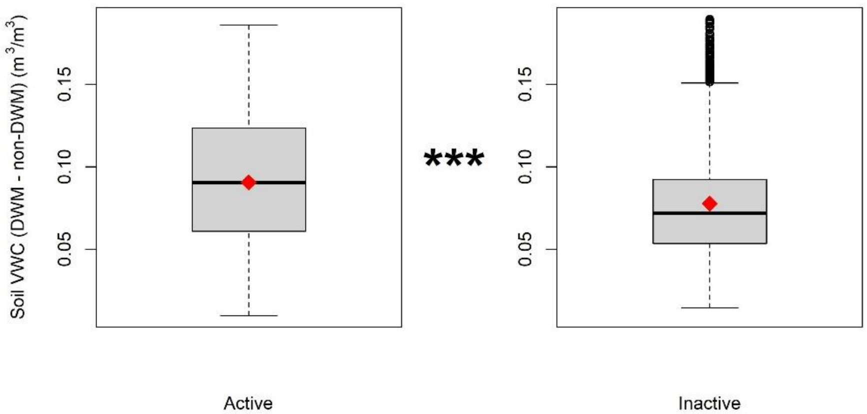

Figure 12. Box plots of the differences in soil VWC (m^3 m^{-3}) between the DWM and non-DWM sites (using DWM – non-DWM) for the active (DCS boards installed for retaining water in the DWM plots) and inactive board periods (DCS boards removed for agricultural management practices) during 2018 and 2019. The red diamond represents the mean and the black horizontal bar inside the box represents the median of the group. The lower and upper edges of the box represent the first (25%) and the third quartiles (75%) of the data, respectively. The ends of the whiskers show the minimum and the maximum without counting outliers (open circles above the whisker). Asterisks indicate that significant differences were found between the two groups using the non-parametric one-sided Wilcoxon rank sum test ($p < 0.001$).

2.3.3.2 Effects of DWM on Greenhouse Gas (GHG) Emissions

For the FG measurements made on either the DWM site or the non-DWM site, most of the significant N_2O emission pulses were seen in the late spring and early summer periods during 2018-2019. Few emission events above baseline fluxes occurred at other periods (Fig. 7 and Fig. 9). I defined June 29-August 3 as the emission pulse period in 2018 and April 28-July 25 as the emission pulse period in 2019. The mean daily fluxes during those emission pulse periods were used to perform a one-way repeated measures ANOVA as introduced in section 2.2.7 to evaluate the impact of DWM on N_2O and CH_4 fluxes. Only the days in the emission pulse periods when all of the four towers were functioning were selected to ensure impartial comparisons between the towers, leading to 14 flux daily values left for each tower (total n = 56) in July 2018 and the same number of daily flux values in May 2019 as the input of the ANOVA test. Since the emission pulse periods were within the ranges of the active board periods, there was no sense to perform a flux comparison between active DCS versus inactive DCS periods.

For N_2O, the boxplots of the mean daily N_2O fluxes measured by each tower in July 2018 reveals that the N_2O fluxes measured by tower A are significantly lower than that observed by other three towers (Fig. 13). No statistically significant differences were detected between towers B, C, and D. In May 2019, significantly larger N_2O emissions were measured at tower B compared to the measurements at tower A and tower D, and tower C had higher N_2O emissions than tower A (Fig. 15). No statistically significant differences were found in the N_2O flux measurements between tower B and tower C. The boxplots of the mean daily CH_4 fluxes measured in July 2018 shows that tower D observed significantly different CH_4 fluxes than towers A and B (Fig. 14). For CH_4 fluxes in May 2019, tower B showed distinct differences relative to towers A and C (Fig. 16). Overall, the statistical tests showed that, although there were some differences between towers, there were no consistent treatment effects of DWM (sites C and D) compared to non-DWM (sites A and B) for either gas (N_2O or CH_4) or in either crop-year (soybean in 2018 or corn in 2019). For example, in the non-DWM site in May 2019 tower B had the highest and tower A the lowest N_2O emissions, with towers C and D intermediate, suggesting that spatial heterogeneity within the study area had a greater impact on production and emission of soil greenhouse gases than the DWM treatment.

It should be noted that in the statistical comparisons, most of the CH_4 flux values at towers A, B, and C in 2018 and most of the CH_4 flux values at towers A and C in 2019 were negative, indicating net consumption of atmospheric CH_4. However, Table 4 shows that a very large proportion of the negative CH_4 concentration gradients corresponding to the negative CH_4 fluxes are within the FG system's observed minimum detection limit (MDL) defined by the zero-gradient test (see Chapter 4 for more details regarding the determination of the MDL). Therefore, I conclude that there is at most a weak soil sink for CH_4 that may not be different from zero, given detection limits of the system. As with N_2O, no consistent significant effect of the DWM treatment was found for CH_4.

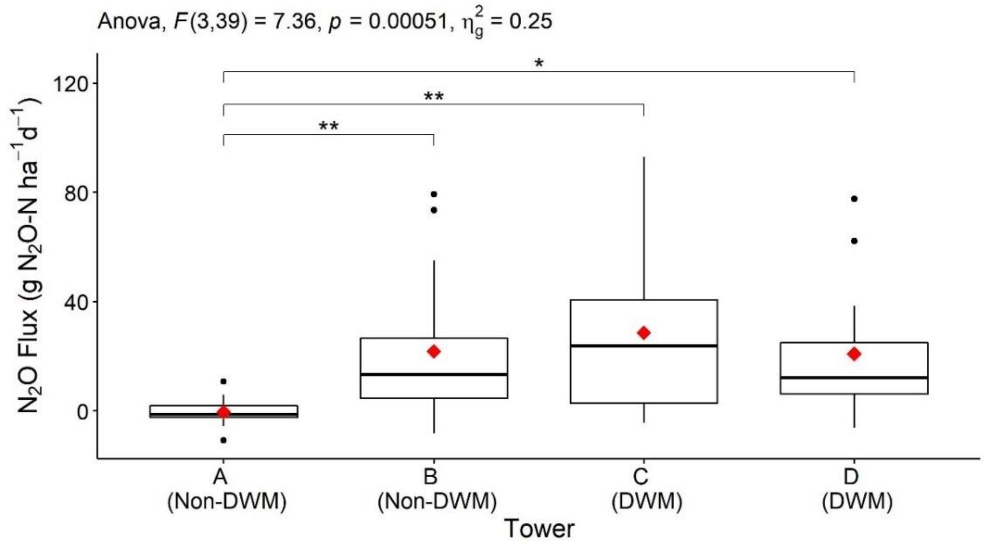

Figure 13. Box plots of the mean daily N_2O fluxes (14 daily values for each tower) measured in July 2018. Red diamonds represent means and black horizontal bars in the boxes represent medians. Asterisks indicate that significant differences were found between the two towers connected by a bracket using the one-way repeated measures ANOVA and the pairwise t-tests with the Bonferroni multiple testing correction for p-value adjustment ("*" and "**" represent significance levels $p < 0.05$ and $p < 0.01$, respectively). η_g^2 is a measure of effect size in ANOVA and indicates that 25% of the variation in N_2O flux can be explained by the variation between the towers.

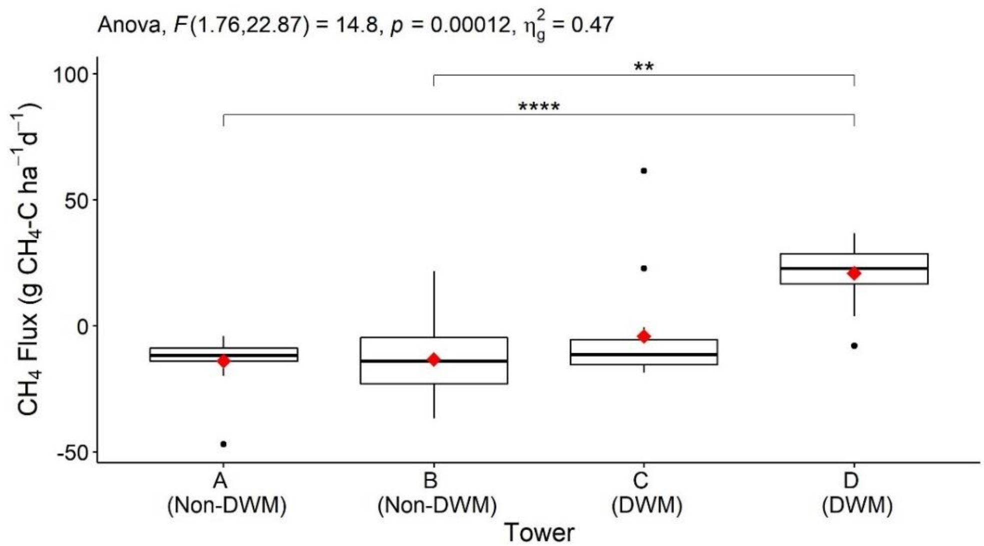

Figure 14. Box plots of the mean daily CH_4 fluxes (14 daily values for each tower) measured in July 2018. Red diamonds represent means and black horizontal bars in the boxes represent medians. Asterisks indicate that significant differences were found between the two towers connected by a bracket using the one-way repeated measures ANOVA and the pairwise t-tests with the Bonferroni multiple testing correction for p-value adjustment ("**" and "****" represent significance levels $p < 0.01$ and $p < 0.0001$, respectively). η_g^2 is a measure of effect size in ANOVA and indicates that 47% of the variation in CH_4 flux can be explained by the variation between the towers.

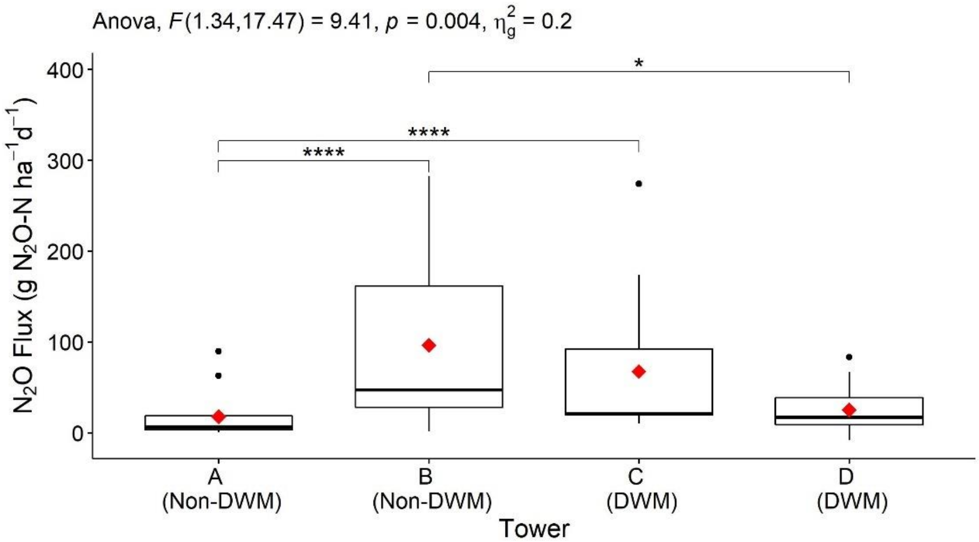

Figure 15. Box plots of the mean daily N_2O fluxes (14 daily values for each tower) measured in May 2019. Red diamonds represent means and black horizontal bars in the boxes represent medians. Asterisks indicate that significant differences were found between the two towers connected by a bracket using the one-way repeated measures ANOVA and the pairwise t-tests with the Bonferroni multiple testing correction for p-value adjustment ("*" and "****" represent significance levels $p < 0.05$ and $p < 0.0001$, respectively). η_g^2 is a measure of effect size in ANOVA and indicates that 20% of the variation in N_2O flux can be explained by the variation between the towers.

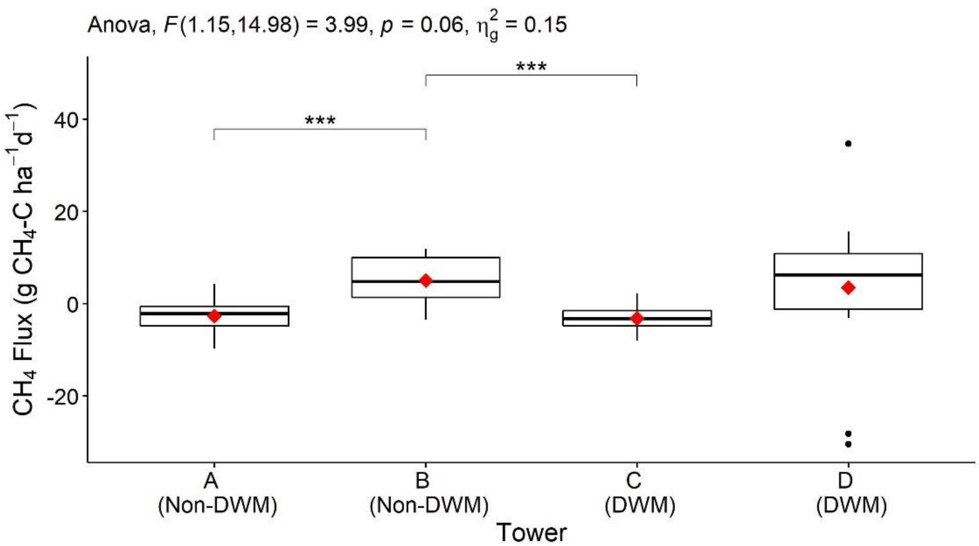

Figure 16. Box plots of the mean daily CH_4 fluxes (14 daily values for each tower) measured in May 2019. Red diamonds represent means and black horizontal bars in the boxes represent medians. No significant pairwise differences were found between towers using the one-way repeated measures ANOVA and the pairwise t-tests with the Bonferroni multiple testing correction for p-value adjustment ($p < 0.001$). η_g^2 is a measure of effect size in ANOVA and indicates that 15% of the variation in CH_4 flux can be explained by the variation between the towers.

Table 4. The mean and median values of the CH_4 concentration gradients corresponding to the CH_4 fluxes used in the statistical tests and the proportion of the measured CH_4 gradients that are within the observed minimum detection limit (MDL) of the instrument. For CH_4, the minimum detectable gradient observed during the zero-gradient test was 0.213 ± 0.141 ppb. See Chapter 4 for more details regarding the determination of the MDL.

	Tower A	Tower B	Tower C	Tower D
July 2018				
Mean (ppb)	-0.183	-0.174	0.10	0.314
Median (ppb)	-0.147	-0.220	-0.144	0.351
Within MDL	11/14	6/14	9/14	2/14
May 2019				
Mean (ppb)	-0.031	0.088	-0.035	0.055
Median (ppb)	-0.028	0.080	-0.040	0.101
Within MDL	14/14	13/14	14/14	10/14

2.3.4 Comparisons between the FG and Soil Chamber Measurements

Since no clear temporal patterns were identified for the CH_4 flux data, comparisons were only focused on the N_2O flux measurements between the FG and chamber methods.

2.3.4.1 Comparison of Flux Gradient Tower with Automated Chambers

As shown in Fig. 1, the four automated chambers were carefully installed next to tower B to ensure they were within the micrometeorological flux footprint of that tower, so only the flux measurements of tower B were used for comparisons with the automated chamber data. After the first fertilization in 2019, both the automated chamber and the FG methods captured strong pulses of N_2O emissions after rainfall events (Fig. 17). However, during the emission pulse periods, chamber 1 showed distinctly higher N_2O fluxes compared to other three automated chambers and the FG measurements, which may be ascribed to the placement of this chamber on a hot spot of soil N_2O emissions.

The measurement interval between the automated chamber measurements (in an order of chamber 1 to 4) was approximately 8 minutes. Before the linear regression was performed between the automated chamber and FG measurements, the automated chamber flux data were averaged every 2 hours regardless of the chamber number to match the measurement frequency of the FG tower. To assess the influence of the chamber with the substantially higher measured fluxes, Figures 18 and 19 show the time series comparisons and linear regressions between the two methods when the N_2O flux data of chamber 1 were included in the calculation of the 2-hour chamber means (a) and excluded in the calculation of the 2-hour means (b), respectively. For both cases, N_2O fluxes from the two methods were linearly correlated (R^2 = 0.599 and 0.544, respectively), but the differences in the slope (1.51 ± 0.11 vs. 0.95 ± 0.08) indicated that using the means of all four of the automated chambers' flux data would lead to higher estimates of soil N_2O emissions compared to the FG method.

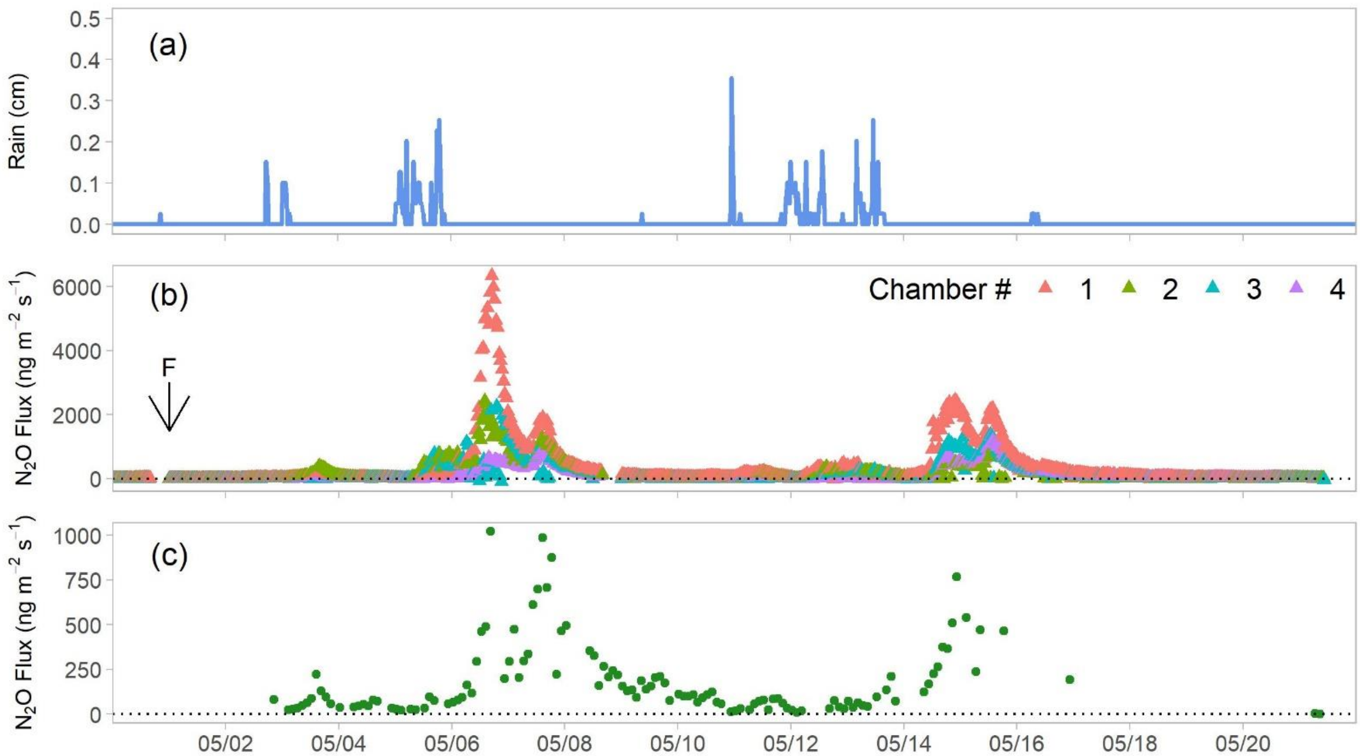

Figure 17. Rainfall (a), N_2O fluxes (in units of ng m^{-2} s^{-1}) measured by the automated chambers (8-min measurement interval) (b), and half-hourly N_2O fluxes (in units of ng m^{-2} s^{-1}) measured by tower B (c) in May 2019. The arrow indicates the first fertilization event (F) on April 25 (not corresponding to the date on the x axis). Note the difference in scale on the y axis between panel b and c, due to the large fluxes from chamber 1 in panel b.

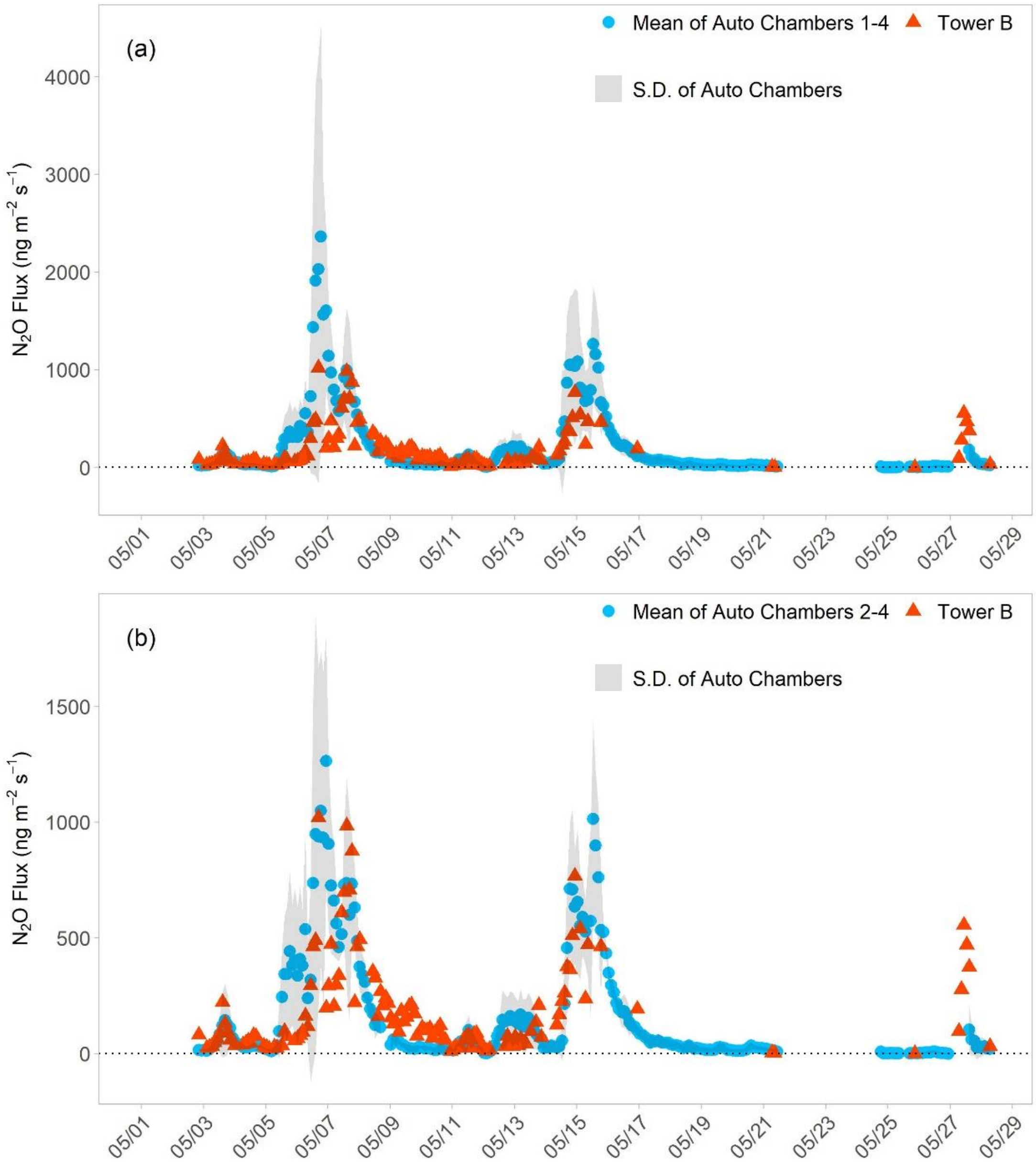

Figure 18. Comparisons of N_2O fluxes (in units of ng m^{-2} s^{-1}) measured by the automated chambers (blue triangles) and by the flux gradient method at tower B (red dots) in May 2019. The auto chamber measurements were averaged every 2 hours to match the measurement frequency of tower B. The grey shaded areas indicate standard deviations of the 2-hour means for chambers. The flux measurements of chamber #1 were included (a) and excluded (b) in the calculation of the 2-hour means. Note the difference in y axis scales.

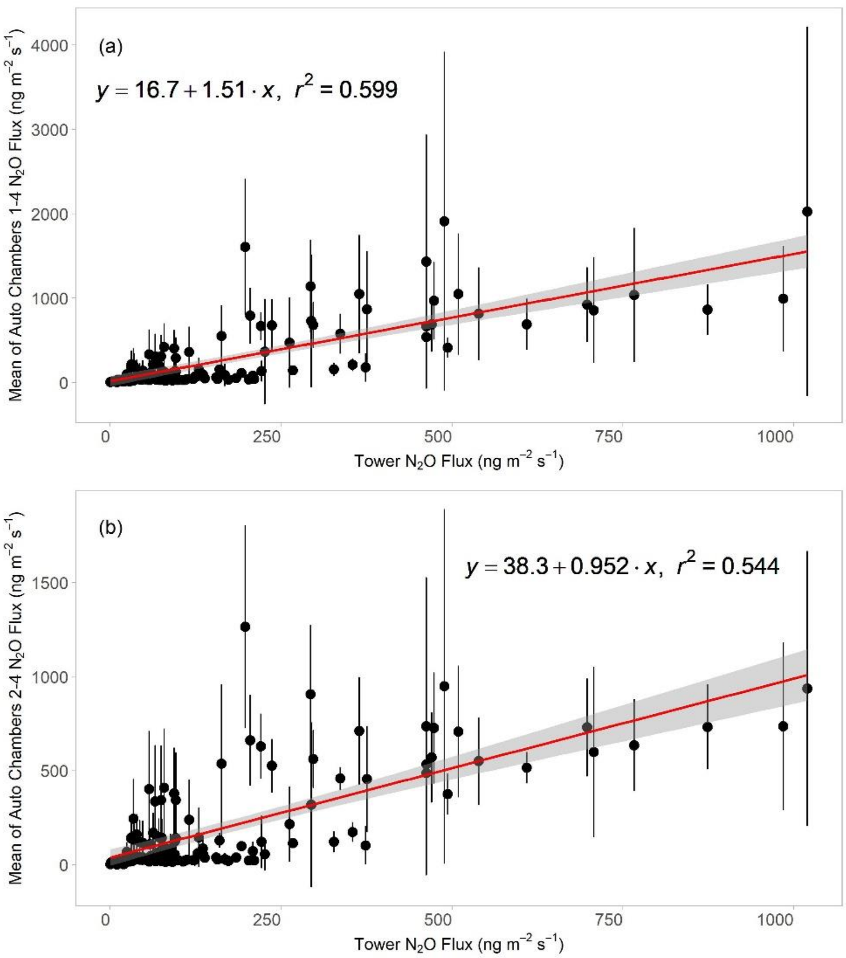

Figure 19. Linear regressions between the automated chamber measurements and the flux gradient tower (tower B) measurements in May 2019 (n = 121 flux data points). The auto chamber measurements were averaged every 2 hours to match the measurement frequency of tower B. The vertical error bars represent standard deviations of the 2-hour means for the chamber data. The grey shaded areas are the confidence interval around the linear regression line (red). The flux measurements of chamber #1 were included (a) and excluded (b) in the calculation of the 2-hour means.

2.3.4.2 Comparison of Flux Gradient Tower with Static Chambers

Soon after the first fertilization event in 2019, the manual static chambers captured similar magnitudes of vigorous N_2O production as the towers did in the growing season of the same year. Because of the relatively long interval between monthly field sampling activities and the unpredictable characteristic of N_2O emissions, the static chambers did not detect another peak emission event following the second fertilization. At other times, most N_2O fluxes were small, which agreed with the FG measurements. Further analyses about the results of the manual static chambers can be found in Hagedorn et al. (2022).

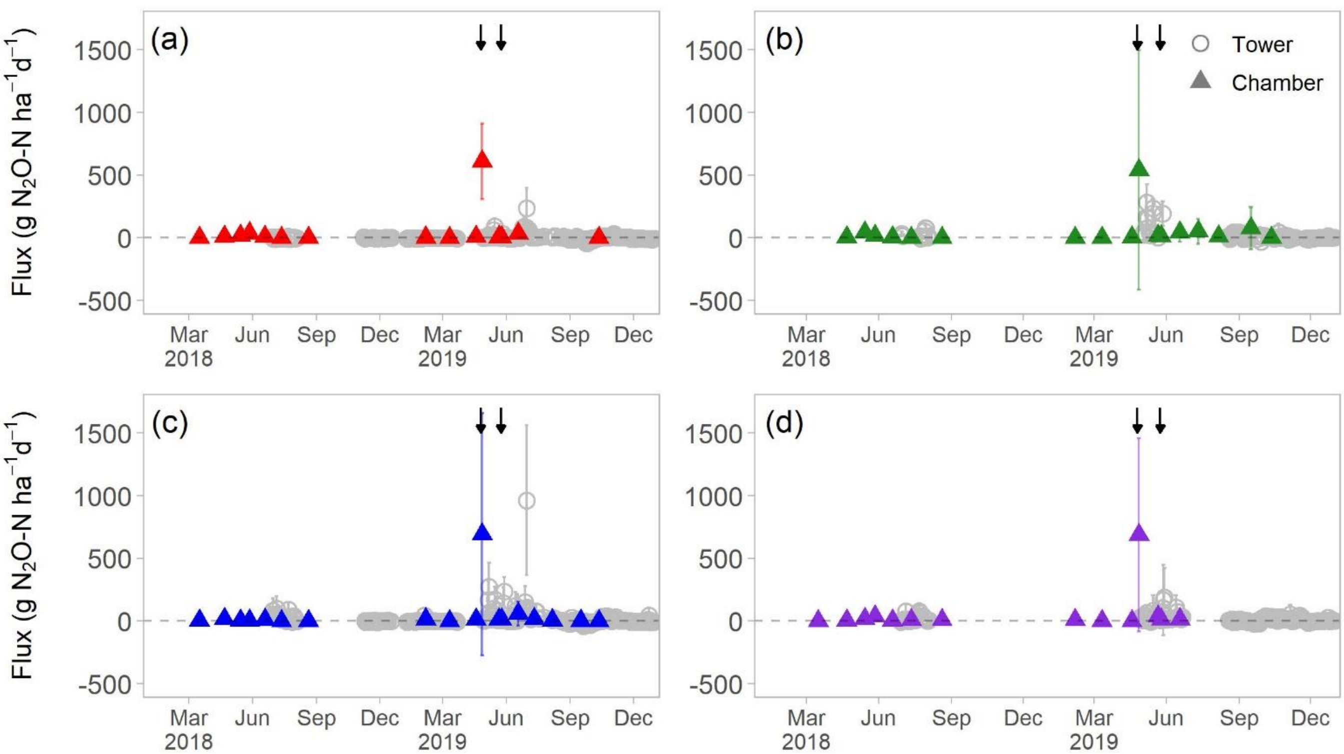

Figure 20. Comparisons of N_2O fluxes (in units of g N_2O-N ha^{-1} d^{-1}) between the static chamber (triangles) and the FG methods (open circles) on plots A (a), B (b), C (c), and D (d). For the chamber data, each triangle represents the average of the eight chamber N_2O flux measurements on the same day. For the tower data, each open circle represents a daily mean of the 30-min flux measurements. Error bars indicate standard deviations. The black arrows mark two fertilization events on April 25 and May 24, 2019.

2.4 Discussion

2.4.1 Impacts of DWM on Soil Moisture

The continuous monitored soil moisture data by the Decagon 5TE sensors showed that the DWM site was consistently wetter than the non-DWM site at the 5 cm depth. It is possible that the difference may be due to spatial variation of soil properties that is unrelated to the DWM treatment. By analyzing the difference in soil moisture between the non-DWM and DWM sites, I found that the difference was statistically significantly larger during the active board periods than during the inactive board periods. However, the manually measured soil moisture data for the same period at the same location (Hagedorn et al., 2022) showed no significant differences by treatment or board period, indicating the DWM did not affect near surface soil water content. The different conclusions of the impact of DWM on soil moisture can be ascribed to the limitations of the continuous method and the manual method for soil moisture measurements. The continuous method is restricted to natural variations of the location of the installation and does not reflect field-scale spatial variability in soil moisture, but it provides consistency for assessing high frequency and long-term temporal variation. In this study, the measurements from each high-frequency, continuously recording system were not replicated, so it was challenging to design a statistical test on the treatment effect beyond pairwise comparisons of the DWM and non-DWM probe installations. In contrast, the manual measurements can represent spatial variability within the field, but depending on the number and the choices of the measurement times and locations, may be skewed by unrepresentative sampling, both temporally and spatially. The manual methods are prone to measurement errors of inconsistent depths and limited by low-frequency measurements. For future similar studies, I recommend: 1) install replicates for each continuously recording system; 2) design the continuous and the manual measurements of soil moisture to complement each other. Using this study as an example, weekly/biweekly manual measurements of soil moisture next to the automated recording systems could be useful to evaluate the difference between these two methods. Spatial surveys of soil moisture and more frequent manual measurements outside the active periods of drainage water management could contribute to better understanding of spatial and natural variation of soil moisture in the fields, respectively.

2.4.2 Implications of Spatial Heterogeneity in GHG Emissions on Tower and Chamber Comparisons

Soil greenhouse gas emissions such as N_2O and CH_4 are highly variable spatially due to spatial heterogeneity of soil characteristics such as soil moisture and temperature, inorganic nitrogen content, carbon availability, and microbial community abundances (Firestone & Davidson, 1989; Groffman et al., 2009; Parkin, 1987). Thus, it is important to estimate the spatial coverage of the flux gradient towers and the static/automated chambers when comparing measurement results from these two methods. It is equally important to understand that hot spot chambers could contribute to the disagreement between the micrometeorological method and the chamber method (Jones et al., 2011; Waldo et al., 2019). In this study, the four automated chambers were installed within the micrometeorological flux footprint of the flux gradient tower but owing to a small number of automated chambers (n = 4) implemented, a single hot spot chamber had disproportionate impacts on the mean N_2O fluxes. The spatial coverage of the flux tower was approximately 2800 m^2 (integrating up to the 80% flux contribution area; see footprint analysis in Chapter 4), whereas the four automated chambers were clustered in a relatively small part of the tower's footprint (the soil surface area enclosed by each chamber was about 0.05 m^2) because they had to be connected to a single analytic instrument. A relatively large quantity of soil chambers is needed to better characterize spatial heterogeneity of soil N_2O emissions within the field, which also reflects the challenge in using static/automated chambers to quantify field-scale emissions. At the time when our flux measurements were taking place, this comparison between the auto-chamber and flux gradient measurements was one of the first few methodological comparisons of N_2O fluxes since these sensitive, fast response instruments had become available. In the case of the manual chambers, although general agreement was reached in the flux results between the micrometeorological method and the chamber method, differences still existed in the intensities of the captured emission pulses, which also could be attributed to some chambers' being placed on hot spots of soil N_2O emissions or not being distributed sufficiently to represent the full tower footprint area. Therefore, approximate agreement in spatial coverage is desired when comparing the micrometeorological and chamber methods, as also recommended by other studies (Laville et al., 1999; Pihlatie et al., 2005). Another recommendation based on past research findings is using the largest number of chambers as is feasible to help avoid outlier effects and approach the best feasible estimate of the site mean. A study in an Amazonian forest found that an estimate of the mean flux derived from a sample of eight randomly chosen chambers had a ≥ 90% probability of being within ±50% of the mean of a more intensive sampling of 36 chambers (Verchot et al., 1999).

2.4.3 Implications of Inter-Tower Comparisons on Adoption of DWM Practices

The statistical tests showed that no significant treatment effects of DWM were found in soil GHG emissions. However, there were two major limitations associated with the statistical tests. First, there was no way to perform a before-and-after DWM comparison for the flux measurements at the same field because the emission pulse periods fell within the ranges of the active board periods. A before-and-after comparison for the same field would eliminate the bias resulting from the differences in natural variations of soil characteristics between DWM and non-DWM fields. Second, using only data from the days when the four towers were functioning led to relatively few (n = 14) daily flux values for each tower as the input of the ANOVA test. The length of the defined emission pulse period is over 30 days in either 2018 or 2019, too few daily values may not be representative of the temporal variability of soil GHG emissions on the research site. On the other hand, these 14 measurement days included most of the periods with large post-fertilization fluxes, which is the most important period with respect to annual fluxes. The companion study by Hagedorn et al. (2022) also found null impact of DWM on soil GHG emissions by running the Wilcoxon rank sum test using the chamber-measured flux data aggregated by board period and treatment. Although the ANOVA tests in this study have limited statistical power, the results of the pairwise tower comparisons are in line with the findings of the companion study and other literature (Crézé & Madramootoo, 2019; Datta et al., 2013; Elmi et al., 2005; Nangia et al., 2013; Nash et al., 2015; Van Zandvoort et al., 2017).

While all of these studies above used the static closed chamber technique, to our knowledge, this is the first study employing a micrometeorological method to evaluate the effects of DWM on soil GHG emissions in agricultural fields. Compared to the static chamber method, the micrometeorological flux gradient method allows near continuous measurements of soil GHG emissions at a finer temporal resolution and a larger scale without disturbing the microclimate between soils and the atmosphere. These advantages confer additional confidence in the conclusion that there were not statistically significant differences between DWM and non-DWM. This study provides evidence that, although wetter soils resulting from DWM may create soil conditions favorable to increased denitrification rates, the deployment of DWM for the purpose of reducing nitrate leaching did not result in a statistically significant and consistent increase in N_2O and CH_4 fluxes from the soil surface. Hagedorn et al. (2022) showed that DWM on this farm did, indeed, reduce hydrologic export of nitrate and speculated that most of the denitrification probably occurred near the zone where groundwater enters the drainage ditches. The present study corroborates the findings that this intended effect of DWM did not create an unintended consequence of increased N_2O and CH_4 fluxes from the cropland soil surfaces within the tower footprints. Hence, for the conditions of this farm, DWM can be recommended as an effective best management practice to reduce nitrate leaching from agricultural lands, whilst avoiding undesired pollution swapping of elevated soil GHG emissions.

2.5 Conclusion

A major concern of implementation of DWM is potential production and emission of N_2O and CH_4, both of which are potent greenhouse gases. It is challenging to quantify the emissions of these trace gases from agricultural fields because they usually occur intermittently in bursts following fertilization or precipitation events. This chapter demonstrates that the micrometeorological flux gradient technique is capable of capturing the sporadic bursts of soil GHG emissions at a finer temporal resolution compared to the traditional static chamber method. The FG measurement results suggest that strong N_2O emission pulses are highly dependent on the coupled fertilizer-precipitation events and the average response time of N_2O emissions to precipitation events can be as short as 1-2 days. The magnitudes of the observed N_2O fluxes between the FG and static chamber methods are in general agreement but it is noteworthy that spatial variability of the chamber data (such as “hot spot” chambers) or differences in spatial coverage between the FG system and the chamber system could contribute to the disagreement between the micrometeorological and the chamber methods. Furthermore, the FG measurements in this chapter indicate that during the active periods of drainage water management, there were some differences in the observed N_2O and CH_4 fluxes between towers, but no consistent treatment effects of DWM were detected in comparison with the non-DWM condition for either gas or crop type (soybean in 2018 or corn in 2019). In conclusion, DWM is a promising best management practice to reduce nitrate concentrations in drainage water without imposing an environmental liability concerning intensified soil GHG emissions.

Chapter 3: Evaluation of Impacts of Biosolids Application and Drainage Water Management on Soil Greenhouse Gas Emissions Using the Flux Gradient Technique

Abstract

Existing studies have shown limited and contradictory findings with respect to whether biosolid applications on agricultural lands would lead to intensification of soil greenhouse gas (GHG) emissions. Here, I describe the results of deployment of a micrometeorological flux gradient method to quantify post-biosolid soil emissions of N_2O and CH_4 on a drainage water managed farm on the Eastern Shore of Maryland in 2020 and a comparison with the flux results of 2018 and 2019 when no fertilizer and conventional synthetic fertilizer UAN was applied, respectively. The analysis of soil extractable nitrogen shows that the post-biosolid soil has the highest nitrate concentration, contributing to the highest N_2O emissions in the growing season of 2020 compared to 2018 and 2019. Other contributors include the low C:N ratio of the biosolids and the above average precipitation in 2020. In contrast, different fertilization regimes did not generate distinct differences between the three years for CH_4 fluxes. In addition, the statistical tests showed that although differences existed between towers, no significant treatment effect of drainage water management (DWM) was found for either N_2O or CH_4, which aligns with the result of the statistical comparison in Chapter 2. The estimated N_2O EF for biosolid addition in 2020 is similar for the DWM (4.8-5.2%) and non-DWM sites (4.5-4.8%) and about 2-4 times the N_2O EF in 2019 (1-2.5%) and 3 times the IPCC Tier 1 EF (1.6%) for synthetic fertilizer, demonstrating the intensification effect of biosolid addition on soil N_2O emissions for the cropland studied here.

3.1 Introduction

Biosolids (also known as treated sewage sludge) are a semisolid product of the wastewater treatment process and rich in nutrients (such as nitrogen and phosphorus) that are essential to plant growth and organic matter that can improve soil structure. Famers began to use sewage sludge from municipal wastewater treatment plants to improve soil fertility in 1920s. Nowadays, biosolids are applied as a common amendment to croplands. Based on the annual biosolids reports collected from 41 states where the Biosolids Program is implemented, the U.S. Environmental Protection Agency (USEPA) estimated 1.15 million dry metric tons of biosolids were applied to agricultural lands in 2021 (Environmental Protection Agency, 2022). Previous studies examining the impact of biosolids application on soil greenhouse gas (GHG) emissions on agricultural lands have showed contrasting results. A study in Denmark found that sludge applications had minor influence on cumulated fluxes of N_2O and CH_4 in a barley field, and that land use (agriculture versus forest) was a much stronger controller (Ambus et al., 2001). While in Canada, researchers reported higher N_2O emissions from sandy loam soil treated with organic amendments (i.e., raw pig slurry and biosolids) than treated with mineral N fertilizer (Pelster et al., 2012). They also concluded that in the plots treated with organic amendments, mean soil nitrate availability was negatively correlated to the C:N ratio of the amendment (Chantigny et al., 2013). A meta-analysis conducted by Charles et al (2017) on the global scale reviewing N_2O emission factors (EFs) from agricultural soils receiving organic amendments yielded a global average EF of 0.57 for all organic sources, lower than the IPCC default EF of 1.6 for synthetic fertilizers. The authors also highlighted the importance of the C:N ratio of the organic amendment to the EF. These inconsistent findings mean that further research is needed to understand the different effects between biosolids and synthetic fertilizer applications on soil GHG emissions.

On this farm site, biosolids application occurred every 4-5 years with the main objective to increase soil phosphorus content as well as other nutrients and organic matter. At the microsite scale, N_2O production is controlled by soil N, soil C content, soil pH and temperature, oxygen availability and soil water content (Grossel et al., 2016; Saggar et al., 2013; Stehfest & Bouwman, 2006). The presence of both available carbon and nitrogen in biosolids suggests that its application is likely to alter the dynamics of soil N_2O emissions compared to the years when synthetic fertilizer such as UAN (urea ammonium nitrate) was used. In this chapter, I quantified soil emissions of N_2O and CH_4 using the near-continuous flux gradient (FG) measurements for the year 2020 when biosolids were added into the fields and compared them to the previous year's fluxes when mineral N fertilizer UAN was applied.

In addition to the biosolids application, drainage water management (DWM) was also implemented on this farm in 2020 to control the underground water table level to accommodate field management and meet crop water requirements in the growing season. As discussed in Chapter 2, a major concern of the implementation of the DWM practice is the potential production of soil N_2O and CH_4 emissions. Whether this unintended consequence of DWM existed for soil GHG emissions in 2020 was investigated in this chapter as well.

3.2 Materials and Methods

3.2.1 Site Description

The research site was a private farm in eastern Maryland on the Delmarva Peninsula. The owner of this farm already had drainage water management (DWM) structures installed and was willing to accommodate our research needs without disturbing standard agricultural activities. This region has a humid subtropical climate. Average annual precipitation is 114 cm and monthly average temperatures are 2 ºC in January and 24 ºC in July. Soil on this farm is classified as Fallsington fine-loamy, mixed, active, mesic Typic Endoaquults.

3.2.2 Farm Management

The typical crop rotation schedule is corn-soybean rotation with daikon radish used as the winter cover crop. However, to take full advantage of the nutrients in the addition of biosolids, the farmer planted corn again in 2020 following the previous corn year. Biosolids containing 20-25% dry content was applied at a rate of 18-20 tons per acre, which, according to the vendor's estimate, would provide 160 lbs. N/acre (179 kg N/ha) mineralizable-N for the first year and smaller amounts mineralized in subsequent years. Biosolids application occurred along with tillage to incorporate the biosolids into the soil from May 19 to June 2 and corn planting was finished at night on June 2. Herbicide was sprayed on June 24 to remove undesired vegetation. Pivot irrigation was used to supplement precipitation events in the summer. The DWM and non-DWM sites were subject to the same sludge fertilization rate, herbicide application, and irrigation rate in 2020.

3.2.3 Experimental Design

The experiment design for the flux measurements in 2020 was the same as that in the previous years, as described in Chapter 2. The aerial image of the research site showing the positions of the drainage ditches, the FG towers, and the instrument trailer can be found in Fig. 21.

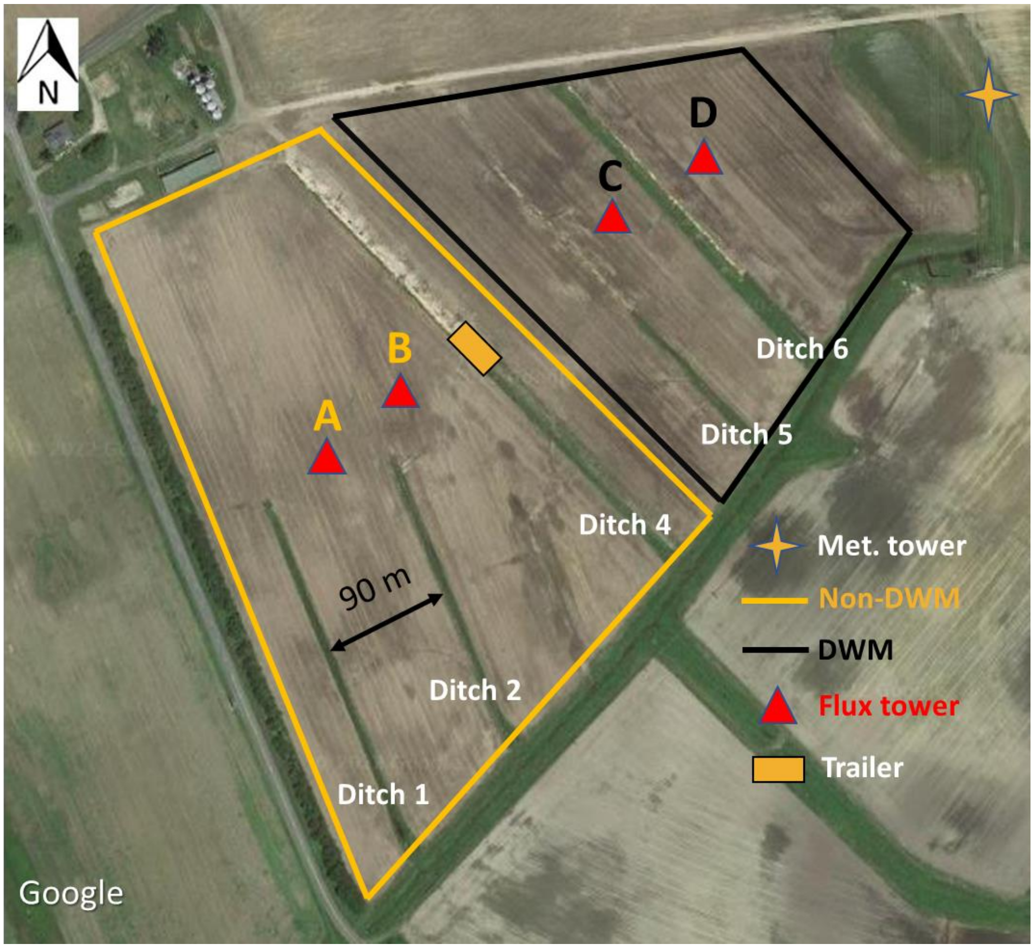

Figure 21. Google Map satellite image of the research farm with proposed siting of the DWM structures, the flux gradient measurement towers, the meteorology tower, and the instrument trailer. Towers A and B were in the free drainage (non-DWM) fields; towers C and D were in the controlled drainage (DWM) fields.

3.2.4 Flux Calculation

The flux calculation and filtering processes were the same as that in the previous chapter. Flux measurements were made from January until March 23, when the site was shut down due to the COVID-19 pandemic. Flux measurements were reinitiated on June 5, as soon after it was safe to re-enter the site after biosolids application, and continued to the end of the year, with the exception of a gap in September and October for the harvest.

3.2.5 Supplementary Environmental Data

In 2020, the meteorological tower continued to provide 30-min air temperature, relative humidity, barometric pressure, wind speed and direction, and precipitation data. The vertical profile of soil temperature and volumetric water content (VWC) were measured using the same recording systems and at the same locations in the DWM and non-DWM fields. But the measurement depths were changed to three depths only, which were approximately 5 cm, 30 cm, and 50 cm below soil surface, owing to the failure of the soil moisture and temperature sensors at other depths.

Soil samples used for nitrate and ammonium concentration analyses were taken approximately monthly in 2020 from June to December after the application of biosolids using a 2.2 cm diameter soil sampler probe. The soil samples were stored in a refrigerated cooler before transporting to the laboratory for further analysis. At the lab, each field moist sample was sifted using a 2 mm opening sieve to remove rocks, fine roots, etc. Ten grams of the sieved soil were extracted in 100 mL of 2M potassium chloride (KCl) in an Ehrlenmeyer flask and placed on a shaker table on low speed for 1 hour. The solution was allowed to settle and then extracts were vacuum filtered through a Whatman No.42 filter paper. The filtered extracts were analyzed for nitrate and ammonium concentrations by a Lachat autoanalyzer (Maynard et al., 1993). Samples that were not processed in the analyzer within 12 hours were stored at 4ºC until analysis was done within 1 month of soil sample collection.

Biosolids samples were taken from four different piles of fresh sludge at the farm before application and transported to the laboratory in a refrigerated cooler. At the lab, the samples were dried, ground to a fineness of less than 0.5 mm, and analyzed for total carbon and total nitrogen using a mass spectrometer.

3.2.6 Statistical Analyses

To test the effects of DWM on trace gas fluxes, a one-way repeated measures ANOVA test was used to detect whether there were significant differences in the flux measurements between the four towers when all of them were functioning. A logarithm transformation (log10) was applied when the data were non-normal or skewed to meet the required assumptions of normality and homogeneity of variances for all groups. A small positive offset was added to make all values positive before log transformation if needed. After the logarithm transformation, the assumptions of normality for each group and homogeneity of variances across groups were both satisfied (Fig. 22, 23 and Table 5). The one-way repeated measures ANOVA was followed up by multiple pairwise t-tests using a Bonferroni multiple testing correction method for p-value adjustment to test differences between towers. Gap-filled flux values were not used in the statistical tests to avoid bias in the comparisons. Statistical analyses were performed in R (R Core Team, 2022).

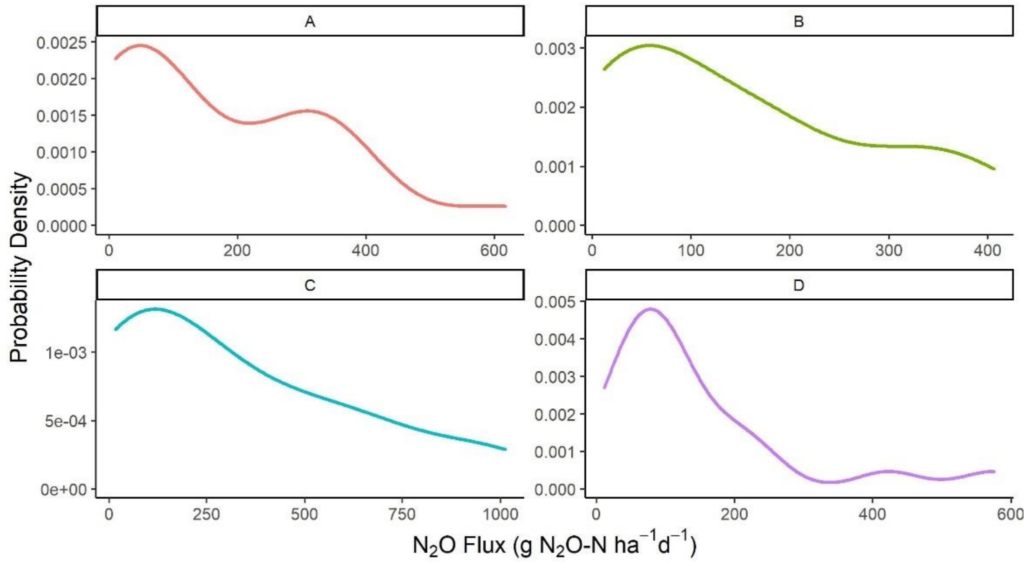

Figure 22. The density distributions of the daily N_2O fluxes measured in the period of June 8-July 9, 2020 when all of the four towers were functioning. Each tower contains 18 daily values. Notice the differences in scale on the x- and y-axes.

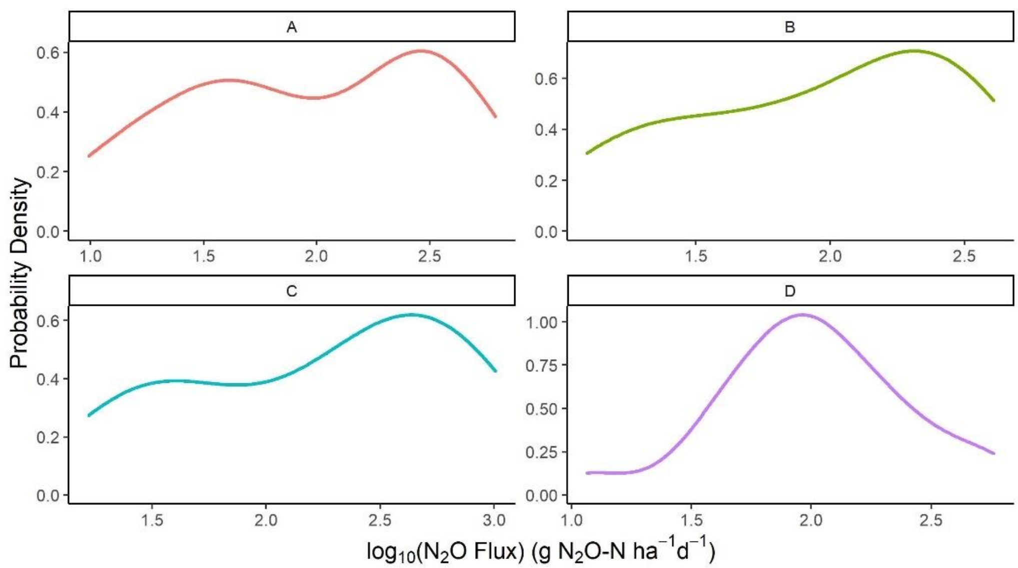

Figure 23. The density distributions of the log-transformed daily N_2O fluxes measured in the period of June 8-July 9, 2020 when all of the four towers were functioning. Each tower contains 18 daily values. Notice the differences in scale on the x- and y-axes.

Table 5. The p-values of the Shapiro-Wilk test on checking the normality of each group (tower) and the Levene's test and the Fligner-Killeen's test on checking the homogeneity of variances across groups (towers) for the daily N_2O fluxes measured in the period of June 8-July 9, 2020. The Levene's test is not sensitive to departures from normality and the Fligner-Killeen's test is very robust against departures from normality. For the Shapiro-Wilk test, a p-value less than 0.05 suggests non-normal distribution of the data. For the Levene's test and the Fligner-Killeen's test, a p-value less than 0.05 indicates significant differences between variances across groups (towers).

Test	Before log-transformation	After log-transformation
Shapiro-Wilk test		
Tower A	0.006	0.120
Tower B	0.026	0.140
Tower C	0.021	0.142
Tower D	0.0004	0.916
Levene's test	0.004	0.104
Fligner-Killeen's test	0.005	0.134

3.3 Results

3.3.1 Environmental Data

3.3.1.1 Precipitation and Air Temperature

Daily precipitation and irrigation records in this year are shown in Fig. 24a. The highest daily rainfall amount was 13.74 cm on August 4. The total annual precipitation was 167 cm, 10 cm higher than that in 2018 (157 cm) and 1.5 times higher than that in 2019 (109 cm), which made the year of 2020 the wettest year among the three years. The driest month was January with 2.73 cm precipitation and the wettest month was August with 9.77 cm precipitation. The daily average air temperature was 14.3 ºC and varied from -4.1 ºC to 29.2 ºC (Fig. 24b). Mean monthly air temperature ranged from 3.8 ºC in January to 26.0 ºC in July.

3.3.1.2 Soil Temperature and Moisture

Daily averaged soil temperature measured at 5 cm depth followed the seasonal trends observed in the air temperature data (Fig. 24c), ranging from 1.3 ºC to 31.5 ºC. In the DWM field, the daily mean of the soil volumetric water content (VWC) in the surface soil ranged from 0.147 to 0.486 m m^{-3} over the course of the one-year measurement; in the non-DWM field, the daily mean of the soil VWC varied from 0.201 to 0.429 m m^{-3} (Fig. 24d). The daily averaged surface soil VWC in both the DWM and non-DWM fields exhibited the same response to precipitation events, but the increase in soil VWC was greater in the DWM field than that in the non-DWM field, indicating a wetter soil condition for the DWM field after each precipitation event. Data gaps existed for the non-DWM site from early June to mid-August because of the malfunction of the data collecting system.

3.3.1.3 Soil Nitrogen Concentration

The soil extractable nitrate in the surface soil (5 cm) ranged from 4.72 to 66.31 mg N kg^{-1} (Fig. 24e and Fig. 25a). The application of biosolids was completed on June 2, denoted by the arrow in the figure. Soil nitrate concentration reached its highest level at the first sampling date after biosolids addition and decreased over time in both the DWM and non-DWM fields. Soil ammonium concentration rose gradually to its maximum in the first two months after biosolids application and returned to its normal values afterwards (Fig. 24f and Fig. 25b).

The comparisons of soil extractable nitrogen concentration among the three consecutive years (2018, 2019, and 2020) clearly show that the soil in both the DWM and non-DWM fields had the highest nitrate concentrations after biosolids application in 2020 and the lowest nitrate concentrations in 2018 when soybean was planted and no N fertilizer was added to the fields (Fig. 25a). For soil extractable ammonium concentration, the three-year data show relatively small ranges of variations in both fields compared to the nitrate concentrations, except for one measurement in the growing season of 2018 (Fig. 25b). Overall, the addition of biosolids in 2020 resulted in much more nitrate measured in the fields than the synthetic fertilizer did in the previous year.

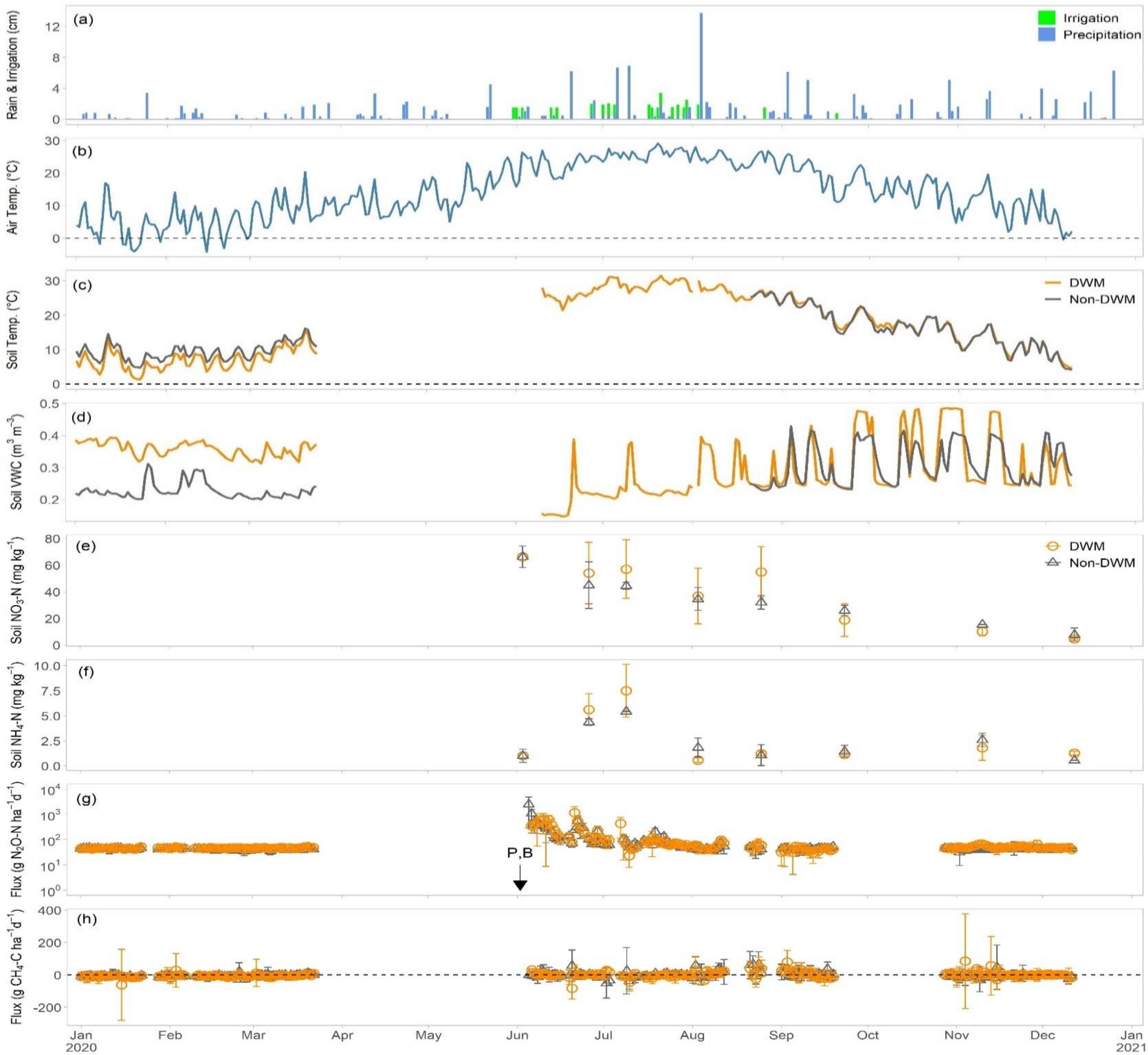

Figure 24. Timeseries of environmental, soil, and flux variables measured in 2020. (a) Precipitation and irrigation, (b) daily averaged air temperature, (c) daily averaged soil temperature of surface soil (5 cm), (d) daily averaged soil volumetric water content (VWC) in surface soil, (e) soil extractable nitrate, (f) soil extractable ammonium, (g) daily averaged N_2O fluxes (in log scale, a small positive offset (50 g N_2O-N ha^{-1} d^{-1}) was added to make all values positive before log transformation), and (h) daily averaged CH_4 fluxes. Black arrows denote planting (P) and biosolids application (B) events. Whiskers in panels (e) and (f) represent the standard deviation of the replicated samplings of the field soil (spatial heterogeneity) and whiskers in panels (g) and (h) represent the standard deviation of the daily mean calculated from half-hourly flux values (temporal heterogeneity).

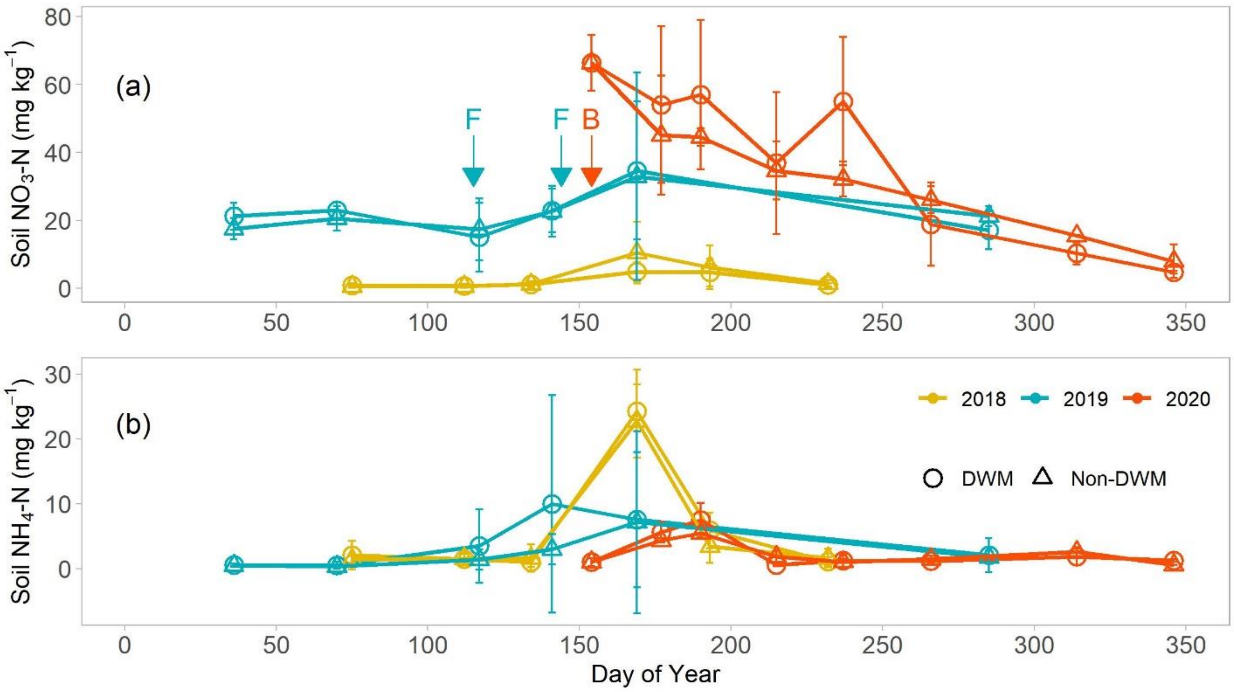

Figure 25. Comparisons of soil NO_3^--N (a) and NH_4^+-N (b) concentrations (mg kg^{-1}) between 2018 (soybean), 2019 (corn), and 2020 (corn) for the DWM (open circles) and non-DWM (triangles) sites. The error bar represents the standard deviation of multiple samplings at one site. The color-coded arrows indicate synthetic fertilizer (F) and biosolid (B) applications in 2019 and 2020.

3.3.2 The FG Measurements

In 2020, 4624 individual half-hourly flux measurements were made with the four FG towers, which had been converted into 202 daily mean flux values for the DWM site and 203 daily mean flux values for the non-DWM site (Fig. 24g and Fig. 24h). The first data gap from late March to early June was due to the shutdown of the research site due to COVID-19 and the second data gap between late September and late October was due to the farmer's harvest.

Large N_2O emissions were observed at both sites following the application of biosolids in the growing season of 2020, coinciding with precipitation events. The maximum daily N_2O flux values measured from the DWM site and the non-DWM site were 1116 and 2460 g N_2O-N ha^{-1} day^{-1} on June 21 and June 5, respectively. N_2O emissions then decreased to near-zero throughout the remainder of the year in both fields. The general trend over time observed in the 2020 N_2O emission data was the same as the temporal pattern that was found in the 2019 data. No such distinct patterns were identified in the CH_4 flux results following fertilization, with the daily flux values ranging from -82 to 85 g CH_4-C ha^{-1} day^{-1} in the DWM field and -51 to 67 g CH_4-C ha^{-1} day^{-1} in the non-DWM field.

3.3.2.1 Comparisons between the FG Towers

None of the four FG towers detected any elevated N_2O fluxes that were beyond the detection limit in the first few months of 2020 (Fig. 26). Following biosolids additions on June 2, strong pulses of N_2O fluxes were continuously observed at all four towers for approximately one month. Although the largest daily mean N_2O flux was measured at tower B, tower C had the most intensive N_2O emissions in general (Fig. 27a), consistent with the findings in 2019 when synthetic fertilizer was applied. The N_2O emissions decreased quickly over time. Beyond one month after biosolid application, significant emission pulses after precipitation events were no longer observed at any of the towers throughout the remaining months of the year, which was likely due to lack of available N. For CH_4, there were no distinct differences among the four FG towers. The measured CH_4 fluxes were within the minimum detection limit (MDL) of the system at most times. A positive flux (emission) or negative flux (uptake) beyond the MDL was rarely seen in each tower's measurements. The finding on CH_4 flux also agrees with what I learned from the 2018 and 2019 data.

3.3.2.2 Diurnal Patterns

During the emission pulse period from June to July in 2020, the highest N_2O emissions at the four towers all occurred in the late afternoon and early evening, as indicated by the diurnal patterns of the shaded areas (Fig. 28), which is likely due to temperature effects. There was no such pattern for the solid lines (median fluxes), suggesting this late-afternoon pattern of elevated N_2O emissions did not happen most days. This is reasonable because large N_2O emissions are highly dependent on a combination of precipitation events when sufficient reactive nitrogen is present, and can then further respond to diel temperature variation. No clear diurnal pattern was identified for the CH_4 flux data because of the lack of large emission pulses.

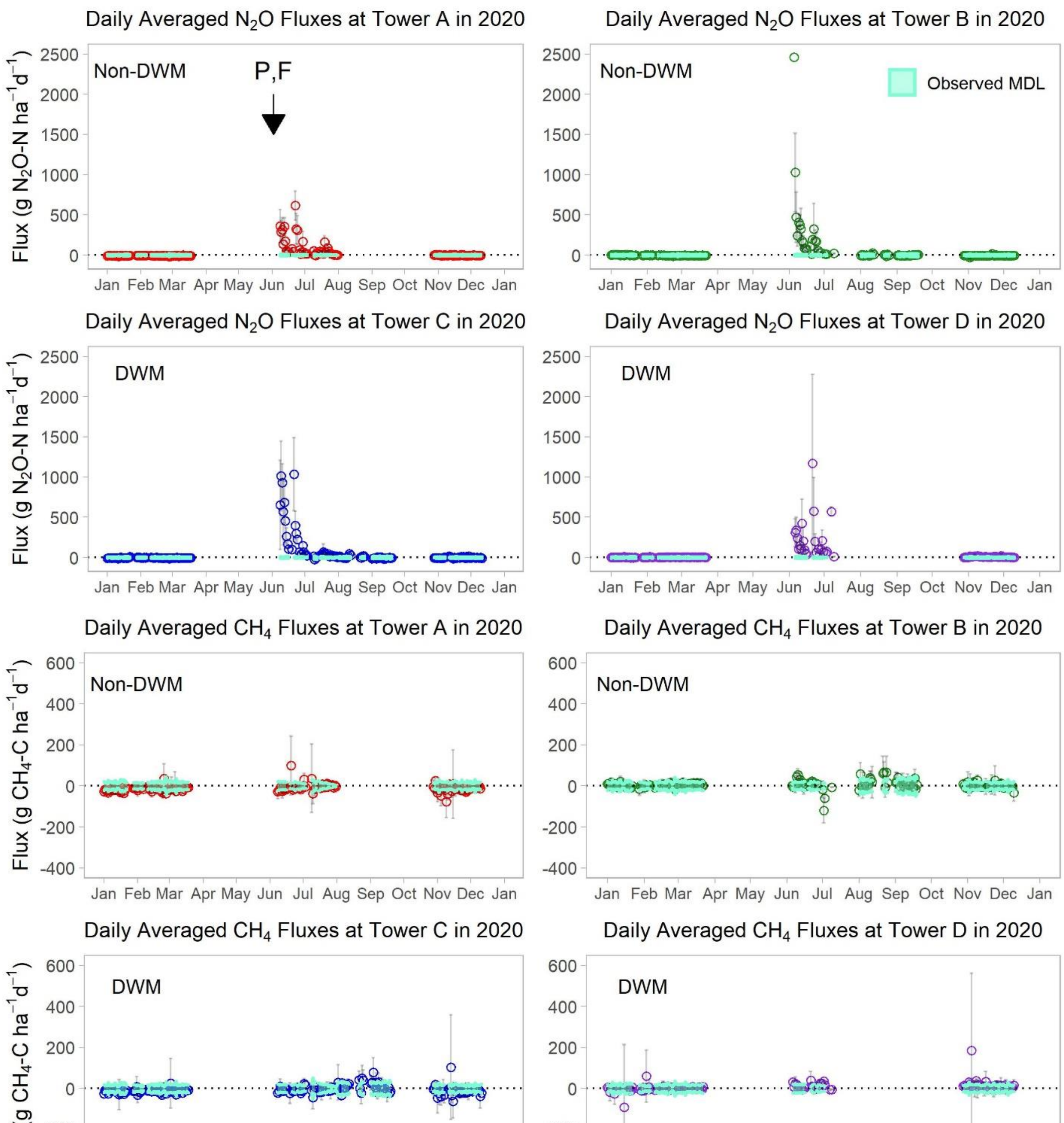

Figure 26. Mean daily N_2O and CH_4 fluxes (g N_2O-N ha^{-1} day^{-1} and g CH_4-C ha^{-1} day^{-1}, respectively) at each of the four FG towers in 2020. The shaded aquamarine areas represent the observed minimum detection limit (MDL) using the zero-gradient test for the flux data (see Chapter 4 for more details regarding the determination of the MDL). For tower B, the error bar of the highest mean daily N_2O flux was not included in order to have a consistent y-axis scale with other figures. The black arrow denotes corn planting (P) and fertilization with biosolids (F).

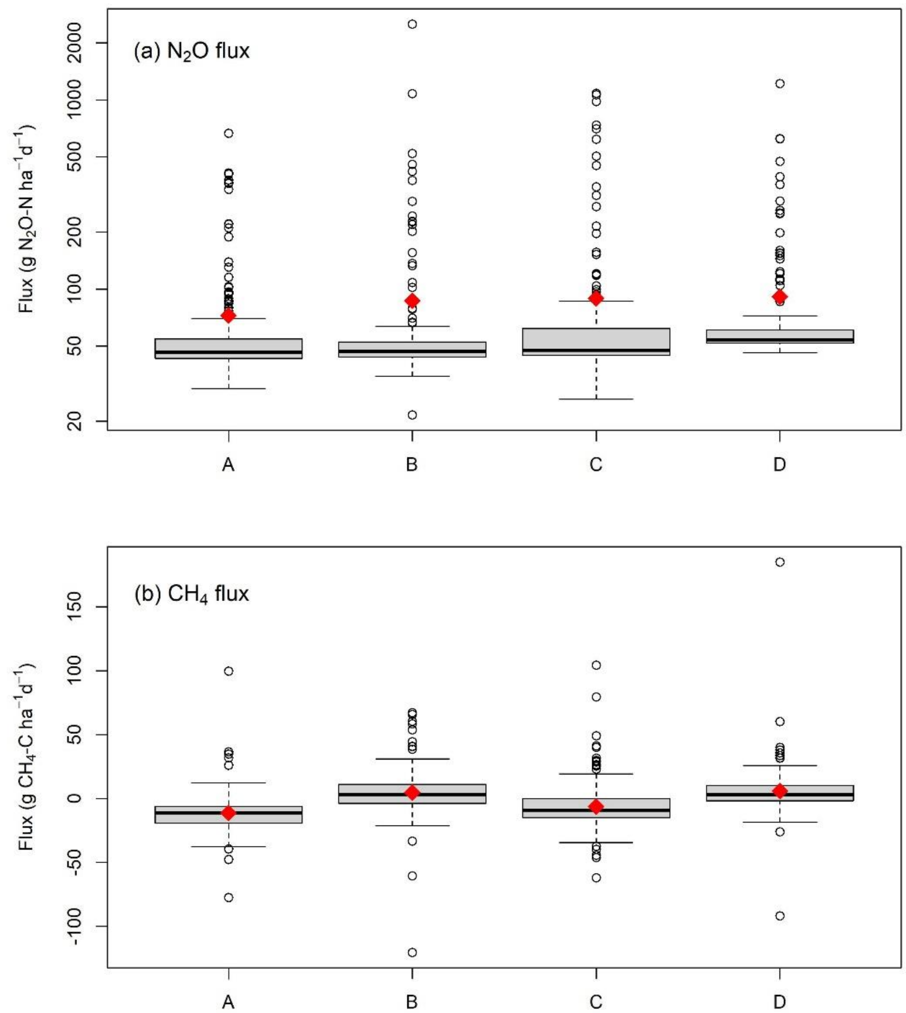

Figure 27**.** Box plots of mean daily N_2O (a) and CH_4 (b) fluxes measured by the four FG towers in 2020. Because the N_2O flux data had right-skewed distribution, a natural log transformation was applied to the data. A small positive offset (50 g N_2O-N ha^{-1} d^{-1}) was added to ensure all values were positive before log transformation. Red diamonds represent means and black horizontal bars in the boxes indicate medians. The lower and upper edges of the boxes represent the first (25%) and the third (75%) quartiles of the data, respectively.

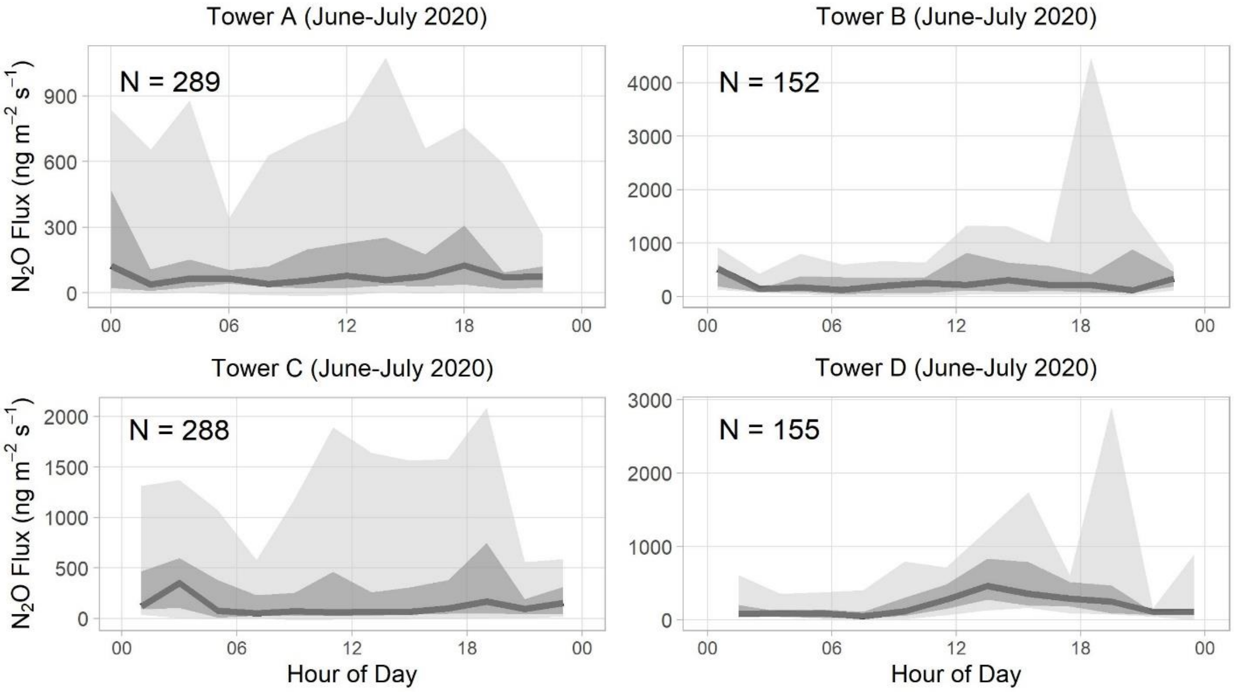

Figure 28. Diurnal patterns in N_2O fluxes (ng m^{-2} s^{-1}) measured by the FG towers in June and July of 2020 when strong emissions pulses were observed. Black lines represent median fluxes, the dark grey areas represent the ranges between 25% and 75% quantiles, and the light grey areas represent the ranges between 5% and 95% quantiles. The 'N' values denote the amount of the 30-min flux measurements made at each tower. Note the differences in scale on the y-axes in different panels.

3.3.2.3 Effects of Biosolids Application on Fluxes

The comparisons of soil N_2O emissions among the three consecutive years (2018, 2019, and 2020) demonstrate the effects of different types of fertilizers on N_2O fluxes clearly (Fig. 29): the fields had the highest N_2O emissions after the addition of biosolids in 2020 corn year and the lowest N_2O emissions in 2018 soybean year when no N fertilizer was added. After the application of synthetic fertilizer in 2019 corn year, the observed N_2O emissions were higher than that in 2018 but significantly lower than that in 2020. In the case of soil CH_4 emissions, the applications of different fertilizers/no fertilizer did not yield evident differences between the three years (Fig. 30).

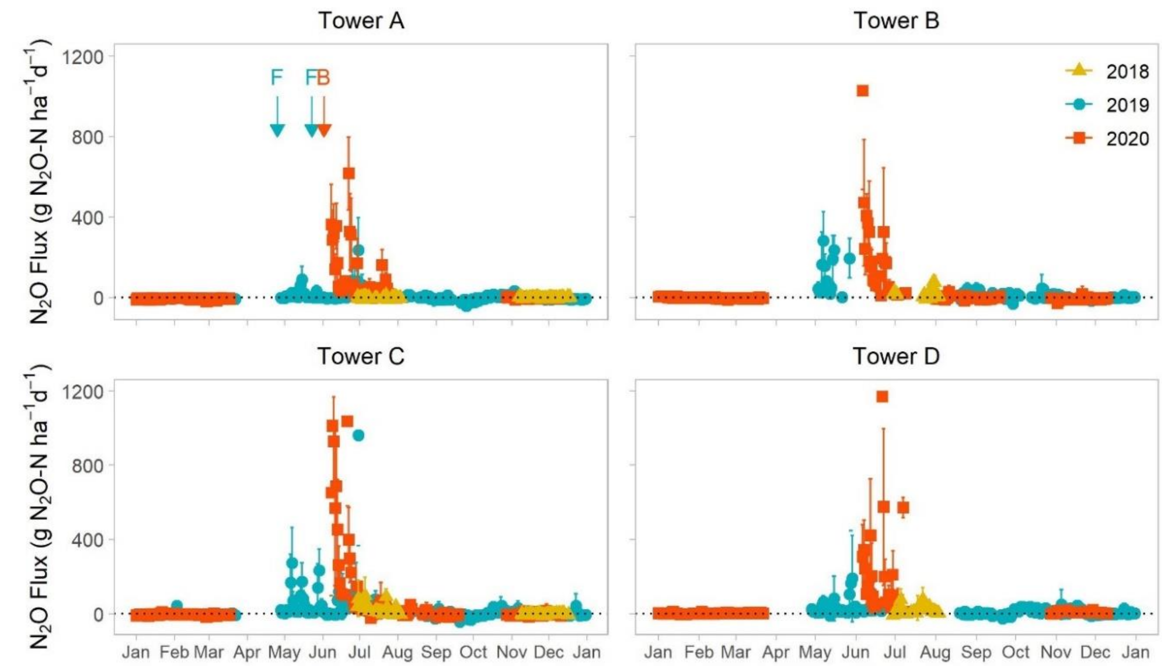

Figure 29. Comparisons of soil N_2O emissions between 2018 (soybean, no fertilizer), 2019 (corn, synthetic fertilizer), and 2020 (corn, biosolids) at each tower. The color-coded arrows indicate UAN (F) and biosolid (B) applications for 2019 and 2020, respectively. The standard deviations of some data points were not shown to make the y-axis scales consistent among the figures. For the same reason, the highest daily mean flux (2460 g N_2O-N ha^{-1} day^{-1}) measured at tower B on June 5, 2020 was not shown in the figure either.

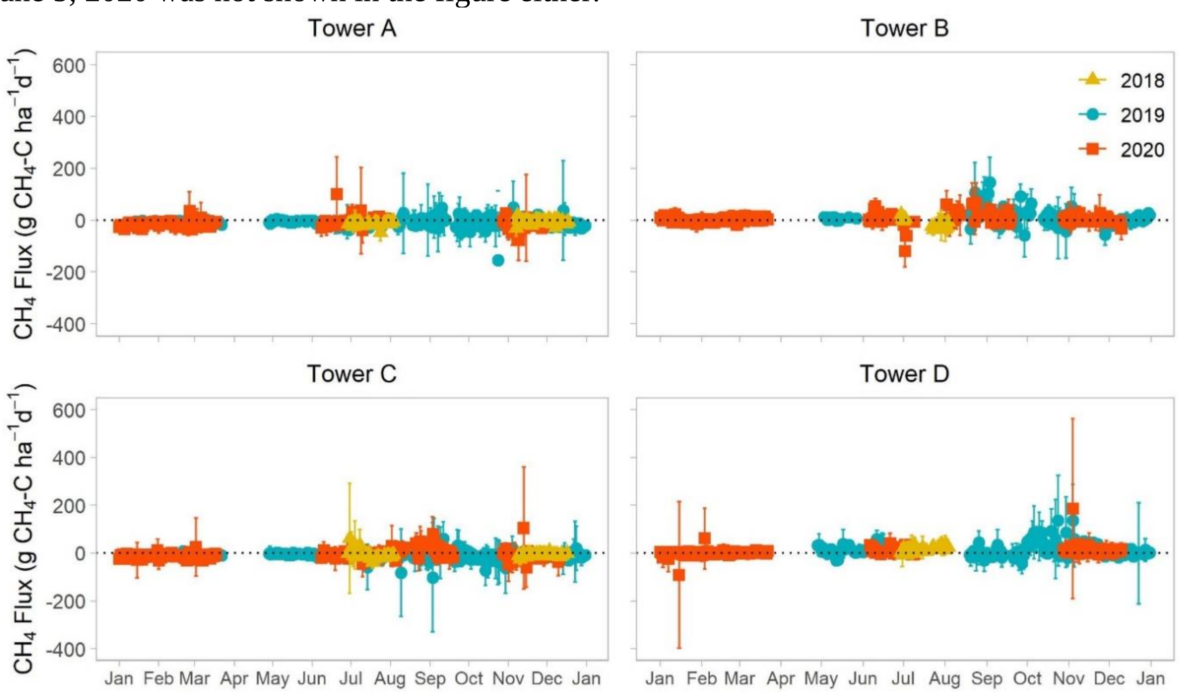

Figure 30. Comparisons of soil CH_4 emissions between 2018 (soybean, no fertilizer), 2019 (corn, synthetic fertilizer), and 2020 (corn, biosolids) at each tower. The standard deviations of some data points were not shown to make the y-axis scales consistent among the figures.

3.3.3 Effects of DWM on Soil N_2O and CH_4 Fluxes

Similar to the previous years, strong pulses of N_2O emissions were only observed in the first two months (June and July) after planting on both the DWM and non-DWM sites in 2020 (Fig. 26). The N_2O emissions decreased to background levels for the remainder of the year. I defined June 5-July 31 as the post-biosolid emission pulse period (the DWM board management records showed that the emission pulse period was within the active board period). To evaluate the effects of DWM on soil GHG emissions, a one-way repeated measures ANOVA was performed (as described in section 3.2.6) using the mean daily fluxes during this emission pulse period. Only the days when all of the four towers were functioning were selected to avoid biased comparisons, leading to 18 daily values remained for each tower from June 8 to July 9 as the input of the ANOVA test.

The boxplot of the mean daily N_2O fluxes measured by each tower in the period of the statistical comparisons suggests that tower C has the strongest emissions of N_2O (332 and 243 g N_2O-N ha^{-1} d^{-1} as the mean and median, respectively) among all of the four towers and the differences are statistically significant only between towers A and C and towers B and C (Fig. 31). For the mean daily CH_4 fluxes during the same period, tower D has significantly higher CH_4 fluxes compared to towers A and C (Fig. 32). Overall, the statistical comparisons showed that, although differences in N_2O and CH_4 emissions existed between the towers, no consistent treatment effects were found under the DWM condition (sites C and D) compared to the non-DWM condition (sites A and B). For example, in the DWM site tower C had the highest and tower D had the lowest N_2O emissions, with towers A and B intermediate, suggesting that the effects of spatial heterogeneity within the study area on soil GHG emissions surpassed that of the DWM treatment.

It is worth noting that during the statistical comparisons, some sites are on average a sink whereas the other sites are predominantly a source for CH_4. Further analysis (Table 6) shows that a very large proportion of the CH_4 concentration gradients corresponding to the observed CH_4 fluxes are within the FG system's minimum detection limit (MDL). Hence, more observations on CH_4 fluxes that are beyond the system's MDL are needed to demonstrate whether a site is a sink or source for CH_4. As with N_2O, no consistent significant impact of DWM was detected for CH_4.

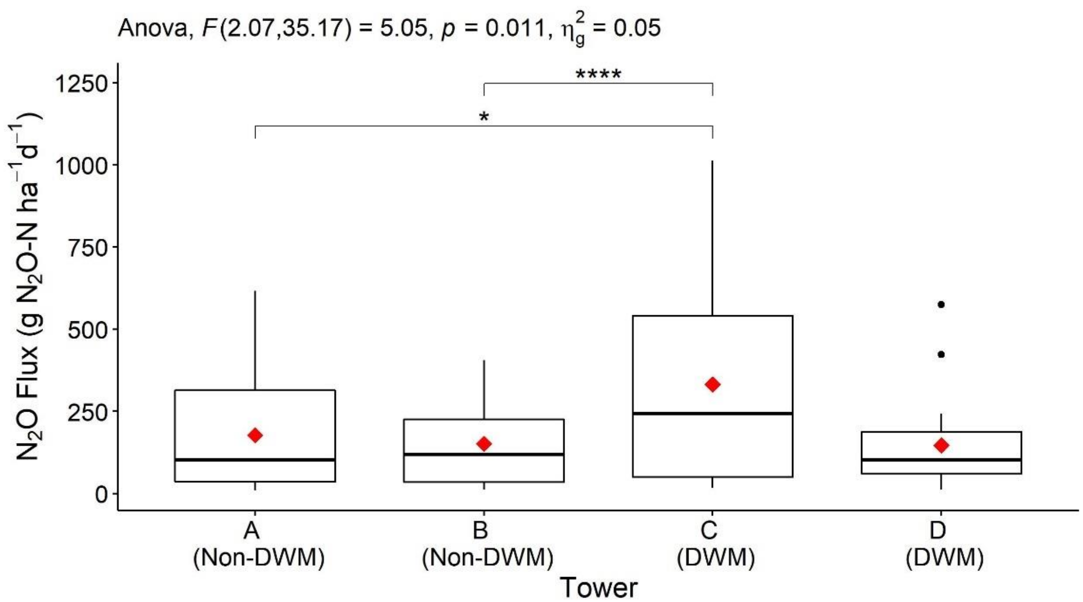

Figure 31. Box plots of the mean daily N_2O fluxes (18 daily values for each tower) measured in the period of June 8-July 9, 2020. Red diamonds represent means and black horizontal bars in the boxes represent medians. Asterisks indicate that significant differences were found between the two towers connected by a bracket using the one-way repeated measures ANOVA and the pairwise t-tests with the Bonferroni multiple testing correction for p-value adjustment ("*" and "****" represent significance levels $p < 0.05$ and $p < 0.0001$, respectively). η_g^2 is a measure of effect size in ANOVA and indicates that only 5% of the variation in N_2O flux can be explained by the variation between the towers.

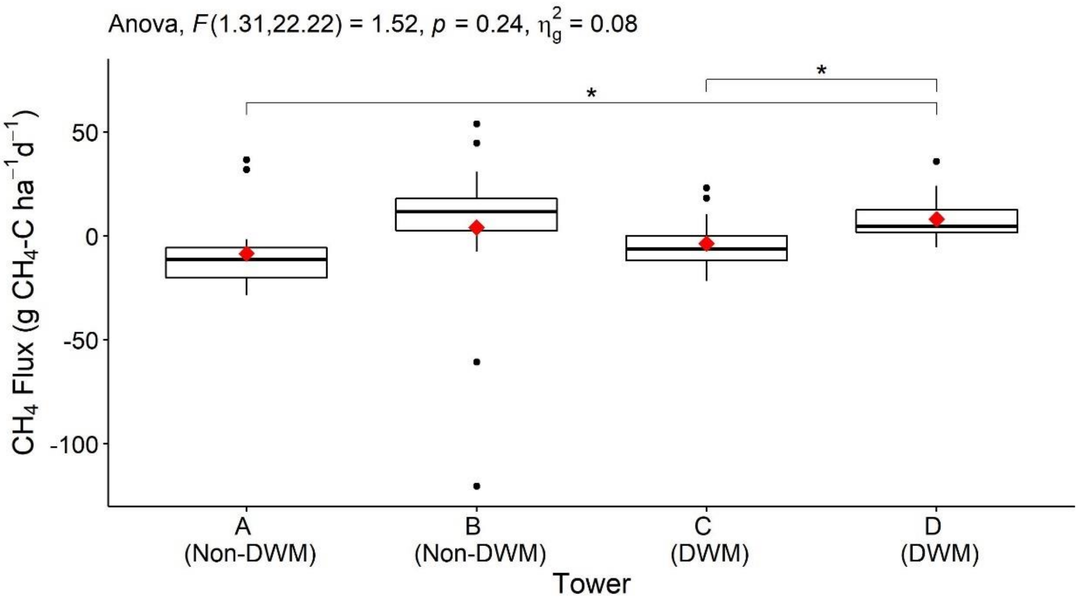

Figure 32. Box plots of the mean daily CH_4 fluxes (18 daily values for each tower) measured in the period of June 8-July 9, 2020. Red diamonds represent means and black horizontal bars in the boxes represent medians. Asterisks indicate that significant differences were found between the two towers connected by a bracket using the one-way repeated measures ANOVA and the pairwise t-tests with the Bonferroni multiple testing correction for p-value adjustment ($p < 0.05$). η_g^2 is a measure of effect size in ANOVA and indicates that only 8% of the variation in CH_4 flux can be explained by the variation between the towers.

Table 6. The mean and median values of the CH_4 concentration gradients corresponding to the CH_4 fluxes used in the statistical tests and the proportion of the measured CH_4 gradients that are within the minimum detection limit (MDL) of the instrument. For CH_4, the observed minimum detectable gradient during the zero-gradient test was 0.213 ± 0.141 ppb. See Chapter 4 for more details regarding the determination of the MDL.

	Tower A	Tower B	Tower C	Tower D
Mean (ppb)	-0.070	0.059	0.002	0.105
Median (ppb)	-0.105	0.201	-0.046	0.055
Within MDL	11/18	9/18	15/18	13/18

3.3.4 Comparisons of N_2O Emission Factor between Treatments and Years

3.3.4.1 Annual Soil N_2O Emission Estimates

Gaps of the daily N_2O emissions were filled using linear interpolation for the purpose of simplicity. For long data gaps (> 1 month), an average of the fluxes in adjacent months was used to fill the missing data. Uncertainties in the daily fluxes were summed in quadrature (by taking the square root of the sum of the squares of the uncertainties associated with daily fluxes) and propagated to the cumulative annual emission estimate. A detailed comparison of different gap-filling techniques is discussed in the subsequent chapter. Only the annual N_2O emission estimates for 2019 and 2020 were calculated in this section (there were too few measurements in 2018).

The cumulative N_2O fluxes indicate that the N_2O-N emissions in the year (2020) of biosolids amendments were elevated in both the DWM and non-DWM fields compared to the year (2019) of synthetic fertilizer use (Table 7 and Fig. 33). However, the increase of annual flux estimate from 2019 to 2020 in the non-DWM field was approximately 1.8 times the increase in the DWM annual estimate. In other words, the difference between treatments was reduced in 2020. This could be ascribed to: 1) our interpolation method could lead to underestimation of the cumulative fluxes because there was a long period with missing data (about 2.5 months, Fig. 34) starting from late March to early June in 2020 due to the COVID-related shutdown of the research site for this period, and the underestimation might be greater for the DWM fields considering their wetter soil conditions; 2) the total annual precipitation in 2020 (167 cm) was 1.5 times higher than that in 2019 (109 cm), and this higher precipitation could contribute to higher fluxes and counteract the treatment effect (different underground water table depths) between DWM and non-DWM during the active board periods; 3) the error terms were larger for the 2020 data and the non-DWM site in 2020 had the largest uncertainty.

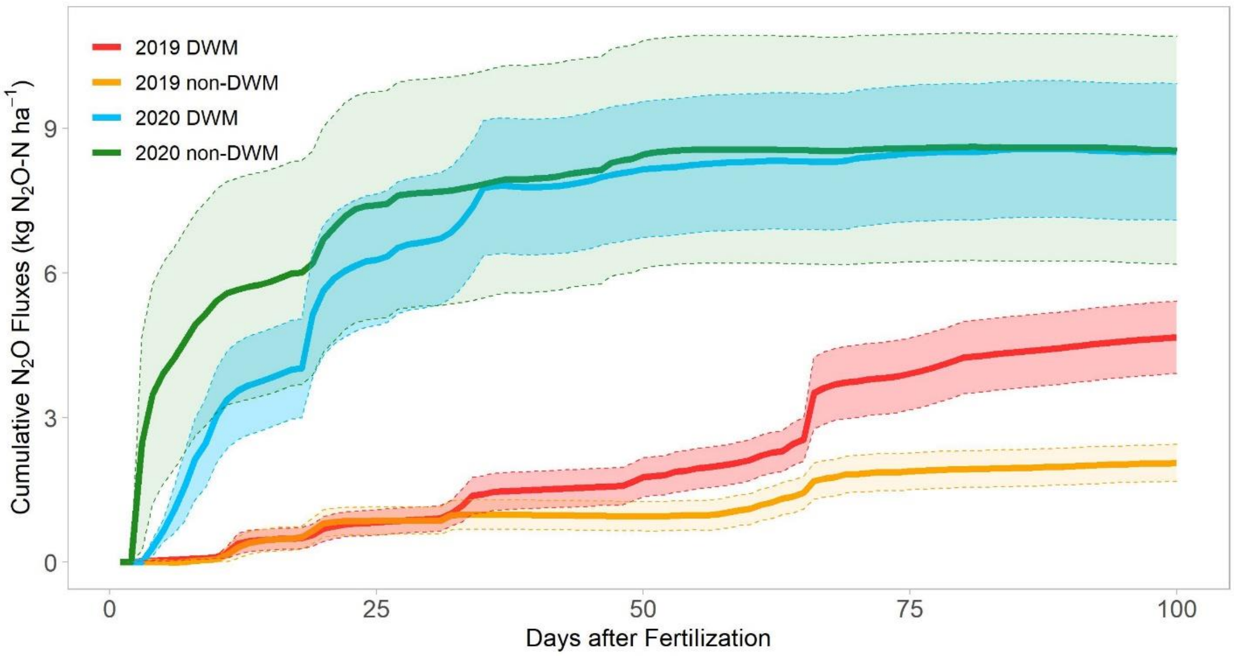

Figure 33. Cumulative N_2O emissions (kg N_2O-N ha^{-1}) at the DWM and non-DWM sites in 2019 and 2020. The numbers on the x-axis stand for the numbers of days after the N fertilization event(s). For 2019, the second fertilization event occurred on day 29. The shaded areas indicate uncertainties propagated from the daily fluxes to the cumulative emissions.

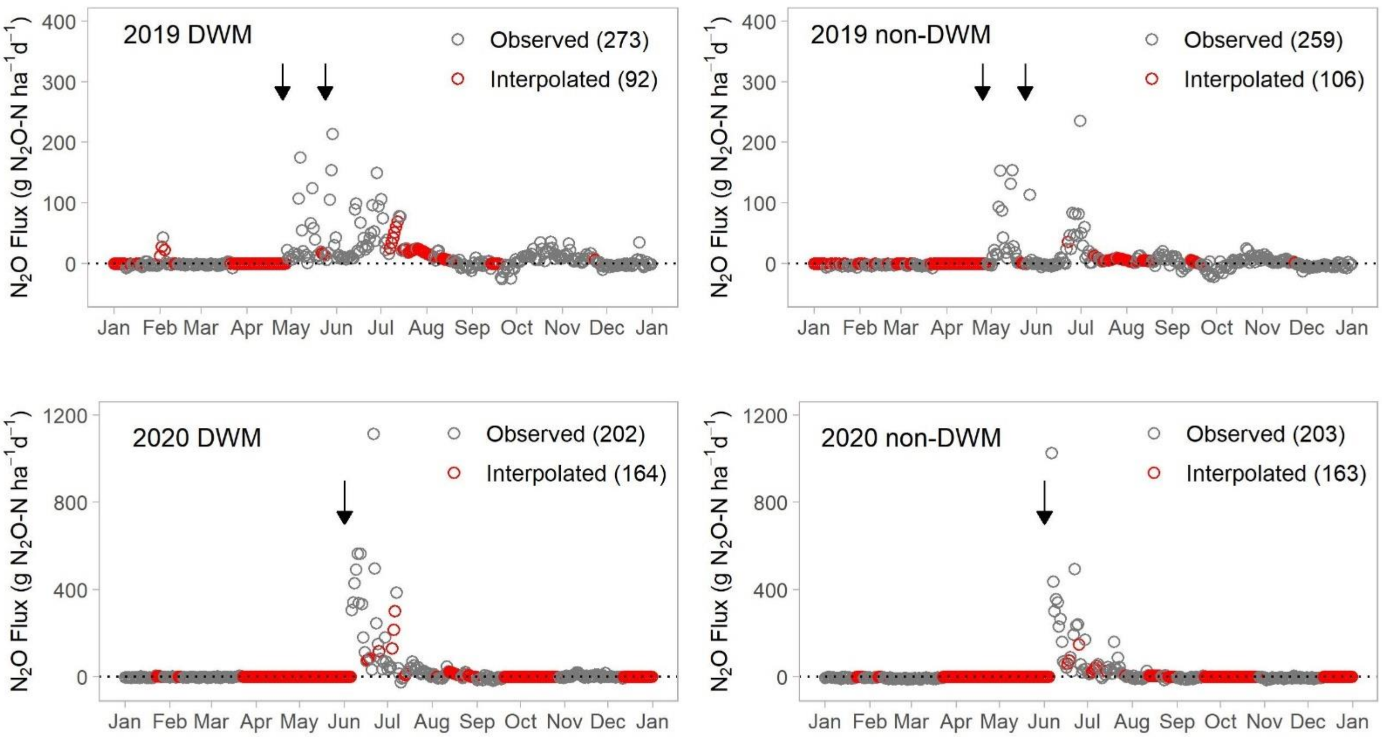

Figure 34. Daily N_2O fluxes (g N_2O-N ha^{-1} day^{-1}) after gap-filling at the DWM and non-DWM sites in 2019 and 2020. Gaps of the daily N_2O emissions were filled using linear interpolation for simplicity. For long data gaps (> 1 month), an average of the fluxes in adjacent months was used to fill the gaps. The maximum daily flux (963 g N_2O-N ha^{-1} day^{-1}) at the DWM site in 2019 and the maximum daily flux (2460 g N_2O-N ha^{-1} day^{-1}) at the non-DWM site in 2020 are not shown in the figures so that the y-axis scales are consistent between DWM and non-DWW for the same year. The numbers in the brackets next to the figure legend indicate the number of the observed fluxes and the number of the interpolated fluxes in the year. Black arrows denote synthetic fertilizer applications in 2019 and biosolids application in 2020. Notice the difference in scale on the y-axis between 2019 and 2020.

3.3.4.2 N_2O Emission Factor

The nitrous oxide emission factor (EF) was calculated by dividing annual N_2O emissions, aggregated by treatment, by the N fertilization rate for the corn years 2019 and 2020. For 2019 when synthetic fertilizer was used, the N fertilization rate was 213 kg N ha^{-1} (22 kg N ha^{-1} was knifed-in on April 25 and 191 kg N ha^{-1} was broadcast-applied on May 24). In the case of 2020, the vendor reported to the farmer applying 20-22 tons of biosolids per acre at 20-25% dry content, which they calculated would provide 160 lbs. N $acre^{-1}$ (179 kg N ha^{-1}) mineralizable N for the first year and smaller amounts mineralized in subsequent years. I generated independent estimates by analyzing the biosolids samples that were collected at the farm before application. I measured 14.9 ± 3.14% dry content and 0.059 ± 0.0067 g total N per gram dry weight in 12 biosolid samples. Different assumptions on the N mineralization rates affect the calculated emission factors for the three scenarios (S1-S3) discussed below:

S1: Use the number (179 kg mineralizable N ha^{-1}) provided by the vendor directly as the N fertilization rate.

S2: Using the average value of the measured dry content (15%) and the N concentration (5.9%) and assuming that the vendor was reporting US short tons, I calculated that the total N in the biosolid addition was 397-436 kg N ha^{-1} (corresponding to 20-22 tons/acre biosolids as reported). If a 100% N mineralization rate is assumed, the mean N application rate would be 417 kg N ha^{-1}.

S3: The farmer explained to us that he expected 35-40% mineralization rate for the first year. If we assume the rate to be 40% of 417 kg N ha^{-1}, then the N fertilization rate is 167 kg N ha^{-1}, which is close to the vendor's expectation of around 179 kg N ha^{-1} as the amount of the first-year mineralized N.

Although a 100% N mineralization rate is not realistic, using the total amount of N in the biosolids addition as the N fertilization rate provides a lower bracket estimate for the EF in each situation. Besides, the water content at the time of sampling was likely affected by rain in the previous few days, which could contribute to difference in dry content percentage between the vendor's estimate and our own measurements. The scenario analyses using different N application rates yield an uncertainty range for the EF on this farm.

In 2019, the N_2O EFs of the DWM and non-DWM sites were 2.5% and 1.0%, respectively (Table 7). The EF calculations used the flux data aggregated by treatment, so the unusually low EF of the non-DWM site can be ascribed to the unusually low N_2O emissions at tower A. The default value of the updated Tier 1 EF in the current IPCC guidelines is 1.6% (uncertainty range 1.3-1.9%) for synthetic fertilizer inputs in wet climates with greater than 1000 mm annual precipitation (Hergoualc'h et al., 2021; IPCC, 2019). Our N_2O EF estimates are a little lower than the lower bound of the IPCC Tier 1 EF at non-DWM and slightly higher than the upper bound at DWM. However, background N_2O emissions from an unfertilized agricultural site were not taken into account in our calculation. Subtracting an annual estimate of background emissions from the annual emissions of 2019 would result in smaller N_2O EFs for both the DWM and non-DWM sites.

Based on the aforementioned scenario analyses, the uncertainty ranges of the N_2O EF at the DWM and non-DWM sites in 2020 were 2.1-5.2% and 1.9-4.8%, respectively (Table 7). The most likely N_2O EFs according to the amounts of the first-year mineralized N provided by the vendor (scenario 1) and estimated by our biosolid analyses (scenario 3) are 4.8-5.2% and 4.5-4.8% for the DWM and non-DWM sites, respectively, without corrections for background N_2O emissions from an unfertilized site. The estimated N_2O EFs could be lower if more than 40% of the N in the biosolids was mineralized in the first year after the application, given a lower bound of approximately 2% estimated in scenario 2. The 2020 N_2O EF is only slightly higher at the DWM site than at the non-DWM site. An N_2O EF in an agricultural setting is impacted by both environmental factors (such as soil type and climate) and management-related factors (such as N application rate and fertilizer type). The ranges of the N_2O EF obtained for 2020 suggest that the biosolids application intensified soil N_2O emissions on this farm, when being compared to the N_2O EF of 2019 and the IPCC Tier 1 EF for synthetic fertilizer applications.

Table 7. Summary of cumulative annual N_2O emissions and emission factor (EF) at the controlled drainage (DWM) and free drainage (non-DWM) sites in 2019 and 2020. The error terms in annual emission estimates were uncertainties in the daily fluxes summed in quadrature and propagated to the cumulative emissions. Scenarios (S1-S3) correspond to the scenario analyses in section 3.3.4.2 for the N fertilization rate in 2020.

	Annual N_2O Emissions ($kg\ N\ ha^{-1}\ yr^{-1}$)		N input ($kg\ N\ ha^{-1}$)	Emission Factor (%)	
Year	DWM	Non-DWM		DWM	Non-DWM
2019	5.32 ± 0.77	2.09 ± 0.42	213	2.50 ± 0.36	0.98 ± 0.20
2020	8.62 ± 1.42	7.99 ± 2.36			
S1: vendor's estimate			179	4.82 ± 0.79	4.46 ± 1.32
S2: 15% dry matter and 100% mineralization rate			417	2.07 ± 0.34	1.92 ± 0.57
S3: 15% dry matter and 40% mineralization rate			167	5.16 ± 0.85	4.78 ± 1.41

3.4 Discussion

3.4.1 Factors Controlling Soil N_2O Emissions

The interannual comparisons for soil GHG flux measurements and N_2O emission factors indicated that the biosolids addition intensified the soil emissions of N_2O compared to synthetic fertilizer. The relationship between high soil N_2O emissions and high soil nitrate concentrations due to the application of biosolids measured in the same year (2020) also demonstrated that soil nitrate concentration was one of the major controlling factors for soil production and emission of N_2O. Moreover, the analysis of the 12 dry biosolid samples collected before application in 2020 showed a C:N ratio of 6.54 ± 0.44%, which is considerably lower than the C:N ratio of 11.8 ± 0.5% in the top 5 cm of soil at this farm (Hagedorn et al., 2022). The low C:N ratio in the biosolids meant that there was little C to promote N immobilization, so the mineralized N was quickly nitrified to nitrate and supported N_2O production (Jones et al., 2007). Other studies also showed that N_2O emission was negatively correlated to the C:N ratio of organic amendments. De Rosa et al. (2016) found that the treatment plots receiving raw chicken manure with a C:N ratio of 3.3 showed significantly higher N_2O emissions than the plots receiving composted manure with a C:N ratio of 12. Both Roman-Perez et al. (2021) and Obi-Njoku et al. (2022) reported that soil amended by mesophilic anaerobically digested biosolids emitted more N_2O than soil amended by composted and alkaline-stabilized biosolids. The C:N ratios of these three types of biosolids were 6.7, 12.4, and 15.7 in Roman-Perez et al. (2021) and 4.7, 19.8, and 20.9 in Obi-Njoku et al. (2022), respectively. With such wide ranges of C:N ratios in organic soil amendment it is not surprising that emissions and EFs also vary widely.

The wetter weather and soil conditions in 2020 may have contributed to the higher N_2O emissions as well. The total annual precipitation in 2020 (167 cm) was 1.5 times higher than that in 2019 (109 cm). The soil moisture at 5 cm depth ranged from 0.14 to 0.35 m^3 m^{-3} with a median of 0.22 m^3 m^{-3} and from 0.15 to 0.39 m^3 m^{-3} with a median of 0.23 m^3 m^{-3} during the post-fertilization emission pulse periods in 2019 and 2020, respectively. The higher upper limit and median of soil moisture in 2020 reflected generally wetter soil conditions as a result of heavier precipitation.

In addition, higher N_2O emissions in 2020 could also partially be attributed to field tillage that occurred along with biosolids application, which is necessary to incorporate the biosolids into the soil. Past studies show elevated N_2O emissions in tilled fields compared to untilled fields (Cowan et al., 2016; Kumar et al., 2014; Wagner-riddle et al., 2007; Waldo et al., 2019). One possible explanation is that large quantities of crop residues ploughed into the soils provide an additional source of organic nitrogen for mineralization and release more readily available carbon, which would provide more substrates for the subsequent denitrification process (Cowan et al., 2016). Another explanation is that tillage creates more pathways for quick diffusion of N_2O from the soil to the atmosphere. Separating the N addition and tillage effect is somewhat academic given that they always go together as a biosolids treatment protocol.

Overall, the post-biosolid intensification of soil N_2O emissions could be the coupled effect of field tillage, increased nitrogen input, and wetter weather/soil conditions, which is generally in line with the major findings in the previous chapter. However, the large difference in soil extractable nitrate between years (Fig. 25a) may be the dominant driver considering the difference in soil moisture is relatively small.

3.4.2 Impacts of DWM and Biosolid Application on CH_4 Fluxes

When DWM is in effect and the water table is maintained closer to the surface, CH_4 fluxes could be produced by methanogenesis due to increased anoxic conditions. Studies have shown peaked

CH_4 emissions in flooded rice paddies and depressed CH_4 emissions when the fields were aerated or drained (Z. Cai et al., 1997; Tyagi et al., 2010). Methane emissions have also been reported for other agricultural systems with a variety of tillage and fertility regimes (Chan & Parkin, 2001; Mosier et al., 2006). However, the flux gradient measurements in this study showed no consistent significant impact of DWM on promoting production and emission of CH_4 under three fertilization regimes (no fertilizer vs. UAN vs. biosolid) (Fig. 30). Even when carbon was readily available from the biosolids application in 2020, the DWM did not appear to make a large enough difference in soil moisture to provoke methanogenesis. The difference in this conclusion compared to Chapter 2 is that in this case there was a lot of carbon in available form to boost microbial respiration that could exhaust oxygen and promote methanogenesis. However, the biosolids application is broadcast on the soil surface and, in this case, apparently the surface soils did not become sufficiently anaerobic to promote methanogenesis.

3.4.3 Comparison with N_2O Emission Factors in Similar Studies

The estimated annual N_2O EF for biosolids addition is 4.5-5.2%, given a first-year mineralization rate of 40%, which is about 8 times the default value of the updated Tier 1 EF (0.6% with an uncertainty range 0.1-1.1%) in the current IPCC guidelines for organic amendments, animal manures, and other N input in wet climates (IPCC, 2019). However, this high EF estimate is not unusual. Jones et al. (2007) reported an annual N_2O EF of 4.3 ± 0.5% when sewage sludge pellets were applied to a temperate grassland in Scotland. The highest N_2O flux that they measured (3.49 kg N_2O-N ha^{-1} day^{-1}) is also associated with the sewage sludge treatment and comparable to the peak value that I observed (2.46 kg N_2O-N ha^{-1} day^{-1}). The authors attributed the high N_2O losses to several factors including a high total N input, a cumulative residual effect, stimulated denitrification due to the addition of organic C, and a priming effect, all of which are relevant to the present study. A recent study (Obi-Njoku et al., 2022) in Quebec, Canada found that treatment plots receiving digested biosolids and/or urea emitted more N_2O during the corn growing season than treatments receiving composted biosolids, alkaline-stabilized biosolids, urea, and combinations of these. The N_2O EFs for treatments receiving digested biosolids only were 4.9 ± 3.7% in the first year of the study and 9.7 ± 4.3% in the second year and for treatments receiving digested biosolids and urea were 4.5 ± 2.5% in the first year and 4.6 ± 2.9% in the second year, which are similar to our EF estimate for the biosolids application. The authors emphasized the contributions of lower C:N ratio and lower dry matter in the digested biosolids, in comparison with the alkaline-stabilized and composted biosolids, to the higher N_2O emissions. In contrast to the large N_2O EFs discussed above, some studies reported small N_2O EFs from organically amended soils that were comparable to the Tier 1 EF in the IPCC guidelines. Roman-Perez et al. (2021) found that annual N_2O EFs from soils amended with three different types of biosolids and granular urea ranged from 0.12-1.33% in Central Alberta, Canada. Similarly, a meta-analysis performed by (Charles et al., 2017) on the global scale reviewing N_2O EF of soils receiving organic amendments yielded a global average of 0.57 ± 0.30% for all organic sources. In addition, the authors classified the organic amendments into low-, medium-, and high-risk groups based on their characteristics (i.e., water content, C:N ratio, and mineral N content). Biosolid belongs to the high-risk group (higher water content, lower C:N ratio, and higher mineral N content), which had a N_2O EF of 1.21 ± 0.14%. The low- and medium-risk groups contained more stabilized products with higher C:N ratio and higher dry matter content and had N_2O EFs of 0.02 ± 0.13% and 0.35 ± 0.13%, respectively. The N_2O EF of an organic amendment is influenced by many factors such as the organic amendment's composition, soil characteristics and climate conditions. As a result, it may vary over a wide range. However, the inconsistency in

N_2O EF of organic amendments indicates that the use of a universal EF (such as the IPCC Tier 1 N_2O EF for organic amendments) might underestimate or overestimate soil N_2O emissions depending on the type of organic amendment used and the soil and weather conditions of the area and highlights the need for an algorithm that calculates N_2O EF based on C:N ratio of organic amendments, soil properties, and climate conditions, and other factors.

3.5 Conclusion

Our flux gradient measurements of N_2O and CH_4 emissions after biosolids addition is, to our knowledge, the first study that employs a micrometeorological method to evaluate the impacts of DWM and biosolids application on soil GHG emissions concurrently. Following the addition of biosolids, N_2O emissions were intensified compared to the previous years because of high nitrate concentrations in the post-biosolid soil and large amounts of rain but CH_4 emissions did not show distinct differences. Statistical tests showed that although differences existed between towers, no significant treatment effect of DWM was found for N_2O or CH_4. The test results align with the findings of Chapter 2 and reinforce that DWM can be used as an effective best management practice to reduce hydrologic nitrate export from croplands without major concerns of significant pollution swapping of elevated soil GHG emissions. Our estimate of N_2O EF of the biosolid-amended soil is considerably higher than the IPCC Tier 1 N_2O EF for organic amendments, indicating that variation in properties of organic amendments, such as C:N ratio, may need to be considered to derive improved estimates of EFs. Our research provides a more accurate quantification of soil GHG emissions under the conditions of this farm in Eastern Maryland compared to the estimates using the IPCC Tier 1 N_2O EF and emphasizes that more similar efforts are needed to provide a better basis for estimating EFs for organic amendments.

Chapter 4: Addressing Concerns about the Flux Gradient Technique and Comparing Two Common Gap Filling Methods for N_2O Fluxes from Agricultural Soils

Abstract

The advantage of the flux gradient (FG) method is that it allows near-continuous measurements of soil trace gas fluxes at multiple plots with a single laser instrument at a fine temporal resolution without disturbing the microclimate between soils and the atmosphere. However, whether this advantage could possibly be outweighed by any concerns associated with the micrometeorological method requires further consideration. In this chapter, four potential concerns related to the FG method were considered: (1) the minimum resolvable N_2O/CH_4 concentration gradient; (2) towers' flux footprint overlap/contamination; (3) the validity of the aerodynamic method to calculate the eddy diffusivity coefficient; and (4) the choice of the gap-filling techniques for N_2O flux data. To summarize the conclusions: (1) the minimum detectable half-hourly N_2O and CH_4 gradients were quantified theoretically and experimentally; (2) the footprint climatology analysis showed that at least 90% of the observed N_2O and CH_4 fluxes were generated in the experimental plots and there was no footprint overlap between the 80% flux contribution area of the FG towers; (3) the broad agreement for CO_2 fluxes between the FG and eddy covariance (EC) methods suggests that the FG method is generally reliable; (4) in this case the artificial neural networks (ANN) did not exhibit improved performance in estimation for the missing N_2O flux values compared to the linear interpolation method and thus using the latter for N_2O data gap-filling was adequate. These conclusions confer confidence that the FG method can be applied simultaneously to multiple plots for N_2O and CH_4 flux measurements.

4.1 The Minimum Detectable Concentration Gradient for N_2O/CH_4

4.1.1 Introduction

The flux gradient (FG) method enables the integration of high temporal and spatial resolution measurements of soil-atmosphere N_2O and CH_4 exchanges by continuously measuring the difference in concentration of N_2O and CH_4 at two heights on multiple towers (which is also known as trace gas gradient measurements) at a frequency of 1Hz using a sensitive and fast-response quantum cascade laser (QCL) trace gas monitor (Aerodyne Research Inc., MA, U.S.A.). The concentration gradients between the two heights are averaged over an interval of 30 minutes, which is the designed sampling period for each tower in the four-tower rotation scheme, and then combined with the micrometeorological data collected every half hour at each tower with a sonic anemometer to calculate the half-hourly N_2O and CH_4 fluxes. Rapid development of laser spectroscopic techniques in the modern age has greatly improved the sensitivity to reliably measure small concentration gradients, but every instrument has its detection limit. To find out what the minimum detectable flux of the FG method is, a key question is: what is the minimum resolvable half-hourly averaged N_2O/CH_4 concentration gradient using the QCL? This concern needs to be addressed before flux measurement results can be delivered with confidence.

4.1.2 Methods

A zero-gradient test was performed from July 7 to July 10 in 2020 to investigate the minimum detectable N_2O/CH_4 concentration gradient by co-locating the upper and lower sampling inlets at the same height on a single tower. Zero-gradient tests have been commonly used in other studies to quantify any bias in the flux gradient measurement (Waldo et al., 2019; Zhang et al., 2015). The zero-gradient test eliminated the possibility that the difference in concentration resulted from the actual height difference between the upper and lower inlets, and as a result, the only cause of the concentration difference was the noise of the whole measurement system. Therefore, the absolute values of the half-hourly concentration differences between the two inlets during this test period were averaged to calculate the minimum detectable N_2O/CH_4 concentration gradient. Any gradient that was smaller than this threshold was considered as the gradient measurement noise of the laser instrument as implemented in the measurement system.

In addition, the mean of the gradients calculated for the zero-gradient test was compared to the theoretical minimum detection limit (MDL) defined by Pattey et al. (2006):

$$\Delta S_{min} = \sqrt{\frac{H}{n}\sigma_S} \qquad [1]$$

where ΔS_{min} is the resolution of the sampled gradient, H is the number of sampling heights (H = 2 in a two-level gradient sampling system), σ_S is the random instrument noise over a specified integration period[2] (for the Aerodyne QCL, σ_S is 0.06 ppb on a 1-s basis for N_2O and 0.30 ppb on a 1-s basis for CH_4 according to the manufacturer's specifications), and n is the number of samples taken at each level over the sampling period (on average, n = 622 independent measurements per height over the half-hour sampling period after data filtering and removal).

4.1.3 Results and Discussion

Figure 35 shows a time series of half-hourly gradient measurements of N_2O/CH_4 in the growing season, encompassing the zero-gradient test from July 7 18:00 to July 10 16:00. During the test, the observed 30-min gradients were several orders of magnitudes smaller than that in the post-test measurements when the upper and lower inlets were restored to the original heights. The

[2] Here I used the manufacturer specified instrument precision @ 1270 cm^{-1} to represent the random instrument noise of the QCL.

elimination of larger gradients introduced by the actual height difference between the inlets demonstrates that the zero-gradient test succeeded.

By taking the mean of the absolute values of the 140 independent half-hourly concentration gradient measurements, the minimum detectable gradients between the inlets for the 30-min average were 0.042 ± 0.033 ppb for N_2O and 0.213 ± 0.141 ppb for CH_4 (Fig. 36 and Table 8). This five-fold higher minimum detection limit for CH_4 is consistent with the manufacturer's specifications of the Aerodyne QCL, which indicate that the precisions of N_2O and CH_4 mixing ratio measurements are 60 and 300 ppt, respectively on a 1-s basis and 20 and 100 ppt, respectively on a 100-s basis; namely, the instrument noise of CH_4 measurements is 5 times that of N_2O measurements for the QCL.

Using Pattey's equation, the theoretical MDL for the 30-min averaged gradient were 0.014 ppb for N_2O and 0.031 ppb for CH_4, which are 3 and 7 times lower, respectively, than the measured zero gradient estimates. This difference probably reflects the fact that the half-hourly zero gradient measurements may include several sources of variation in the whole measurement system in addition to the QCL instrument noise, such as possible variation in pump speed, air pressure, and other unknown measurement system noise. In addition, the theoretical MDL for CH_4 by Pattey's equation is only 2.2 times higher than for N_2O compared to a five-fold difference from the zero gradient measurement tests. This difference is due to the square-root transformation in the calculation process of the theoretical MDL, as the square root of 5 is approximately 2.2 (see Eq. 1).

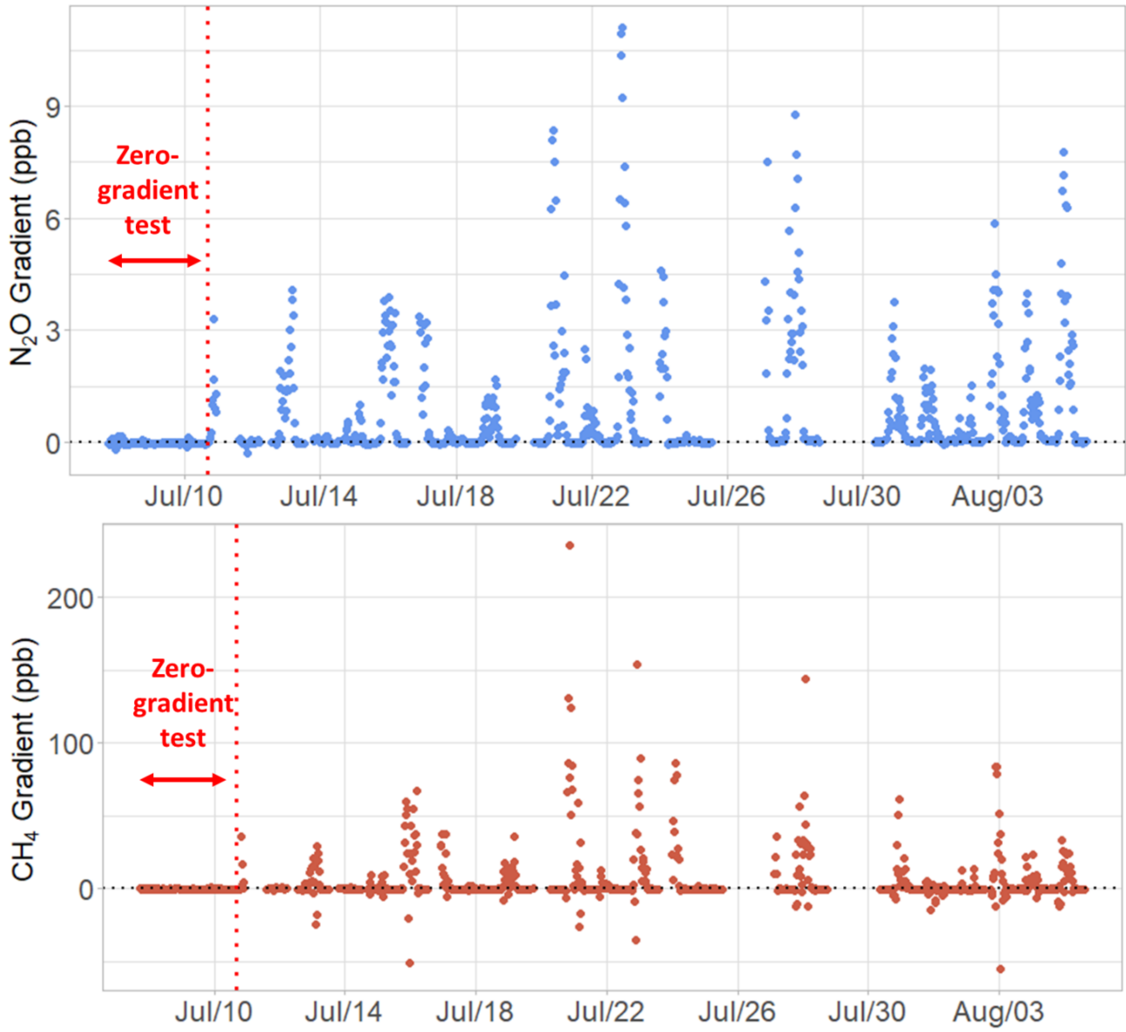

Figure 35. The zero-gradient test was performed from July 7 18:00 to July 10 16:00 (local time), when the upper and lower sampling inlets were mounted at the same height. The concentration gradients here were calculated as the concentration at the lower inlet minus the concentration at the upper inlet.

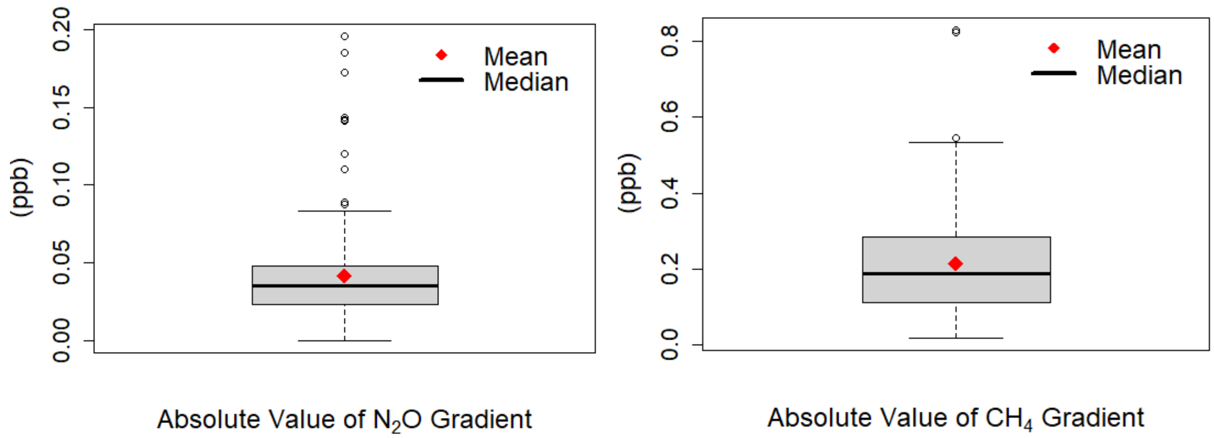

Figure 36. Box plots of the absolute values of the 30-min concentration gradients during the zero-gradient test. The red diamond in each figure represents the mean and the black horizontal bar inside the box represents the median of the data. The lower edge of the box represents the first quartile (25%) and the upper edge represents the third quartile (75%) of the data. The ends of the whiskers show the minimum and the maximum without counting outliers (open circles).

Table 8. Summary of the minimum detectable concentration gradients determined by the zero-gradient test and the theoretical minimum detection limit (MDL) equation (S.D.: standard deviation; N: the number of half-hourly measurements during the test).

	N_2O gradient (ppb)		**CH_4 gradient (ppb)**	
Zero-gradient test	Median	Mean ± S.D.	Median	Mean ± S.D.
(N = 140)	0.035	0.042 ± 0.033	0.188	0.213 ± 0.141
Theoretical MDL	0.014		0.031	

4.1.4 Conclusion

In this section, the zero-gradient test has been demonstrated as an effective method to quantify the instrument noise in the concentration gradient measurements. The Pattey et al. (2006) equation enables us to calculate the theoretical MDLs for the concentration gradients of N_2O and CH_4 with the QCL under ideal conditions, while the zero-gradient test provides the best estimates of the MDLs for field measurement of the trace gas gradients because in addition to the QCL instrument noise, other parts of the sampling system may introduce some unknown measurement noise. In short, the question concerning the minimum detectable half-hourly N_2O and CH_4 gradients has been addressed theoretically and experimentally. The observed minimum detectable gradient using the zero-gradient test combined with the micrometeorological data collected every 30-min were used to calculate the minimum resolvable half-hourly N_2O and CH_4 fluxes under varying micrometeorological conditions[3] in Chapter 2 and 3.

[3] Because the flux resolution of the flux gradient system depends not only on the instrument noise but also on the atmospheric conditions and the inlet separation (Pattey et al. 2006), it varies over time in a time series of flux measurements. To calculate the minimum resolvable 30-min flux of N_2O/CH_4, replace the concentration gradient term (ΔC) in Eq. [1] of Chapter 2 with the MDL for N_2O/CH_4 gradients.

4.2 Flux Footprint Analysis

4.2.1 Introduction

The flux gradient (FG) method allows near-continuous, year-round integrated measurements of N_2O and CH_4 emissions from soils across spatial heterogeneity within a field and across temporal variation such as diel cycles, rainfall, and fertilization events, and seasonal and inter-annual variation. However, as a tower-based micrometeorological method, some concerns need to be resolved before field measurements can be conducted with confidence, and flux footprint is one of them. The Flux footprint is defined as the upwind area that is sampled by the flux sensor when measuring turbulent flux. It describes the relative contribution of surface sources to the measured vertical flux (Horst & Weil, 1994; Schmid, 2002; Schuepp et al., 1990) and varies greatly with wind direction, atmospheric stability, surface roughness, and sensor observation height (Lee, 2018). In this study, the FG method was chosen for multi-plot sampling and flux towers that were erected in the two control and two treatment plots. To avoid footprint contamination between two adjacent flux towers or between the towers and other external structures, two important criteria must be met. First, each tower should have enough upwind fetch area to ensure that a large proportion of the observed N_2O and CH_4 fluxes originate from within each experiment plot. If the footprint extends far beyond the corn/soybean field, for example, to the unpaved/paved roads, the observed flux will no longer represent the true surface-air exchange of the corn/soybean ecosystem (Lee, 2018). Second, the flux towers should be properly placed in the experimental plots to guarantee that a tower's footprint is dominated by only one plot and only one drainage control structure treatment. In other words, for each of the four flux towers to be independent measurements, the footprints should not have much overlap, especially between the treatment plots and the control plots. Thus, footprint calculation is an indispensable part of post-field data analysis to ensure observations satisfy the preset footprint criteria.

4.2.2 Methods

The model used to investigate the flux tower footprint for each 30-min FG measurement was developed by Kljun et al. (2015) and has been widely used by other researchers (Waldo et al., 2019; Zhao et al., 2019). The model provides a two-dimensional flux footprint prediction including not only the extent but also the width and shape of footprint estimates and is valid for a wide range of atmospheric boundary layer conditions and measurement heights (Kljun et al., 2015). For each 30-min FG measurement, a footprint was calculated. All footprints for the half-hourly time series data were aggregated to a footprint climatology characteristic of a one-month period. Input data needed for this model include measurement/receptor height, the Obukhov length, the standard deviation of lateral velocity fluctuations, friction velocity, planetary boundary layer height, roughness length, displacement height, and wind direction. The Obukhov length, the standard deviation of the crosswind component, and friction velocity were measured by the sonic anemometer on each tower. The displacement height and roughness length were assumed as 2/3 and 1/10 of the canopy height, respectively. Wind direction data were collected by a wind monitor (R. M. Young Company, Michigan, USA) on a 3.5 m meteorological tower located next to the experimental field. Planetary boundary layer height data were downloaded from the fifth-generation reanalyzed ERA5 hourly data on single levels by the European Center for Medium-Range Weather Forecasts (https://cds.climate.copernicus.eu/). The extracted sub-region was 39.12° N, 75.81° W, 39.11° N, and 75.80° W. Unlike the eddy covariance method, the gas concentration measurements using the FG method were made at two heights rather than a single height. Horst (1999) found that the footprint associated with vertical concentration gradient flux estimates was similar to the footprint for eddy covariance flux measurements, only when the eddy covariance measurements were made at a height equal to the geometric mean of the highest and lowest profile measurement heights for unstable atmospheric condition or the arithmetic mean for stable atmospheric condition. Therefore, in this study, the geometric mean of the heights of the upper and lower intakes was used as the measurement height under unstable stratification and the arithmetic mean was used as the measurement height under stable/neutral stratification, although these two numbers were very close.

4.2.3 Results and Discussion

The flux footprint climatology was established only for the period when significant emissions were observed. Following planting of soybean in June 2018, noticeable N_2O fluxes were measured during the month of July, until the malfunction of the main instrument. In 2019, significant N_2O emissions were observed in May and June following the planting of corn and the application of fertilizer. In 2020, strong N_2O emissions were also observed in June and July after the planting of corn and the application of biosolids.

4.2.3.1 Footprint Climatology[4]

The wind rose located in the top left corner of each satellite map shows the general wind speed, wind direction, and how often the wind blew from that direction for each one-month FG measurement period. For example, the wind rose inset in Fig.37b shows that the prevailing wind was from the east and the southwest for the month of May in 2019, which explains why the tower's aggregated footprint for the month, shown with contour lines, extended further in those two directions. The boundary of the 90% contour of the flux footprint was still far away from the

[4] The footprint climatology of tower A is used here as an example. Figures related to other three towers can be found in the appendices at the end of this dissertation.

paved road, which addresses the concern about the upwind fetch area and ensures at least 90% of the observed fluxes originated from the experimental plots. Sometimes, tower A's footprint possibly overlapped with tower B's footprint (Fig.37b), but considering that these replicate plots were under the same water table management practices and the 80% of the footprint boundary encompassed a much smaller amount of area, this minor footprint overlap appears acceptable. In addition, the comparison of the flux footprint between May and June in 2019 (or June and July in 2020) shows that the footprint shrank when the crop grew taller. The smaller footprints were due to the fact that, although the lower and upper inlet tubes for concentration gradient measurements were raised as the canopy height increased, they were not raised in proportion to the increased height of the corn canopy. A smaller distance between the lower inlet and the top of the canopy results in a smaller calculated footprint. Unfortunately, the height of the pivot irrigation system on the farm prevented raising the inlets as high as would have been needed for maintaining a constant ratio between the measurement height and the height of the canopy.

All of the FG towers' footprint climatologies by month are overlain onto the same satellite image of the research site to better elucidate the question of whether a flux tower had footprint overlap with its neighbor (Fig. 38). The outermost contour and the second outermost contour depict the extent of 90% and 80% of the source area of the measured flux for each tower, respectively. The towers' footprints differed slightly in shape because data gaps existed at different times throughout the month for different towers. With the exception of a small amount of footprint overlap between plots C and D, which were also under the same DWM practices, these integrated footprint maps demonstrate that the placement of the flux towers satisfied the aforementioned criteria.

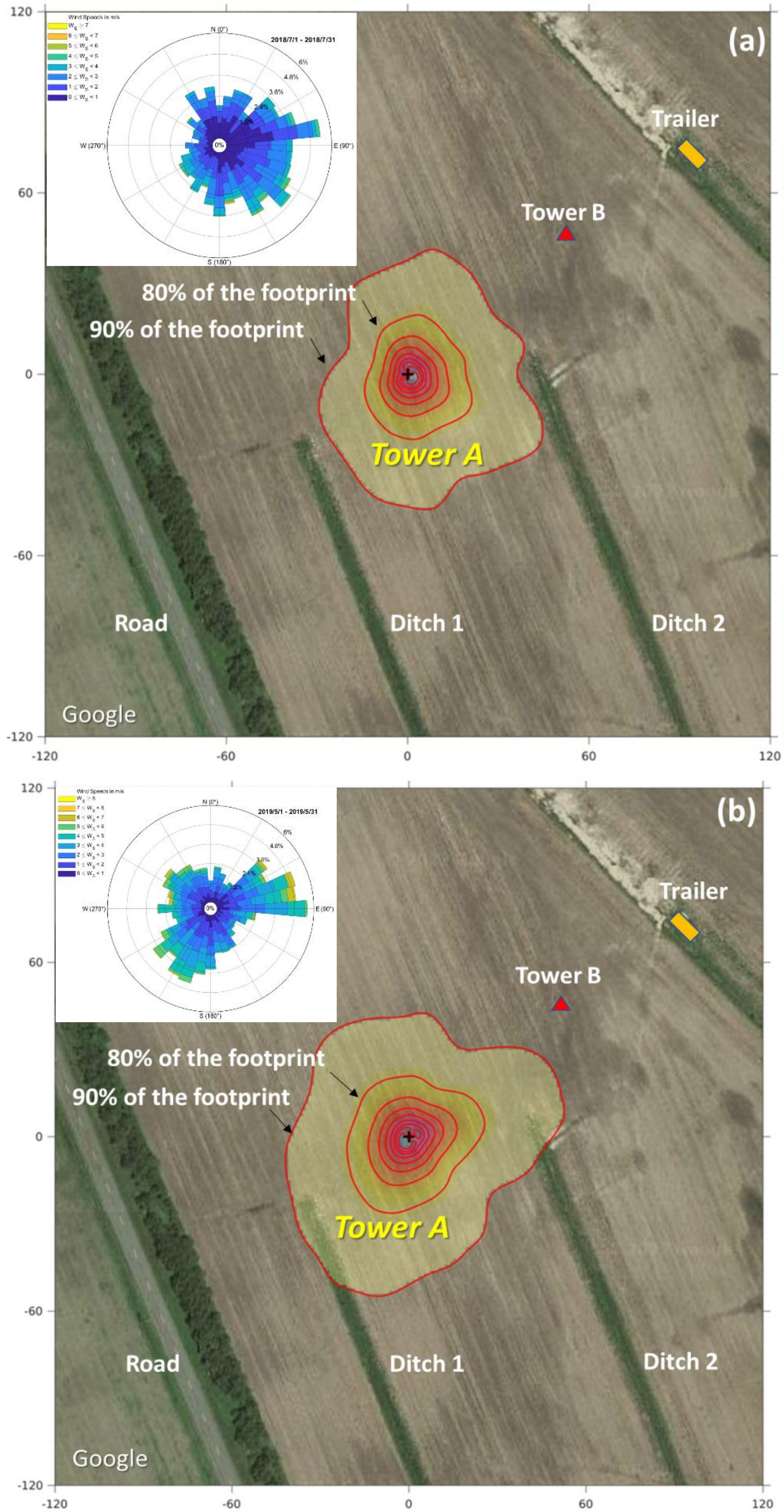
(a)
2018/7/1 - 2018/7/31
Trailer
Tower B
80% of the footprint
90% of the footprint
Tower A
Road
Ditch 1
Ditch 2
Google
(b)
2019/5/1 - 2019/5/31
Trailer
Tower B
80% of the footprint
90% of the footprint
Tower A
Road
Ditch 1
Ditch 2
Google

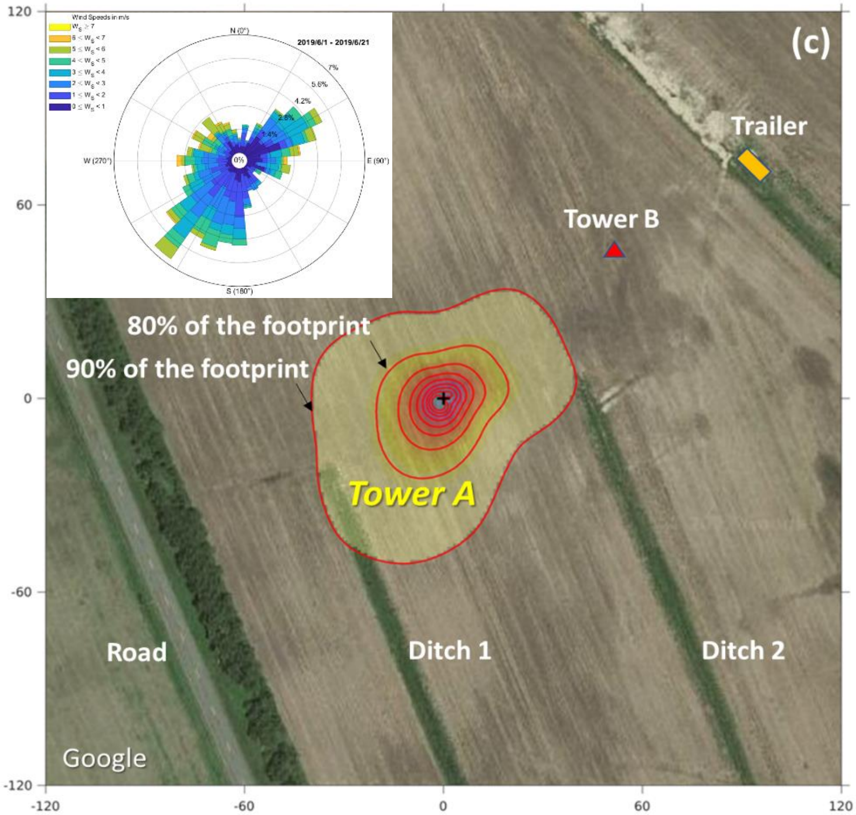
(c)
2019/6/1 - 2019/6/21
Trailer
Tower B
80% of the footprint
90% of the footprint
Tower A
Road
Ditch 1
Ditch 2
Google

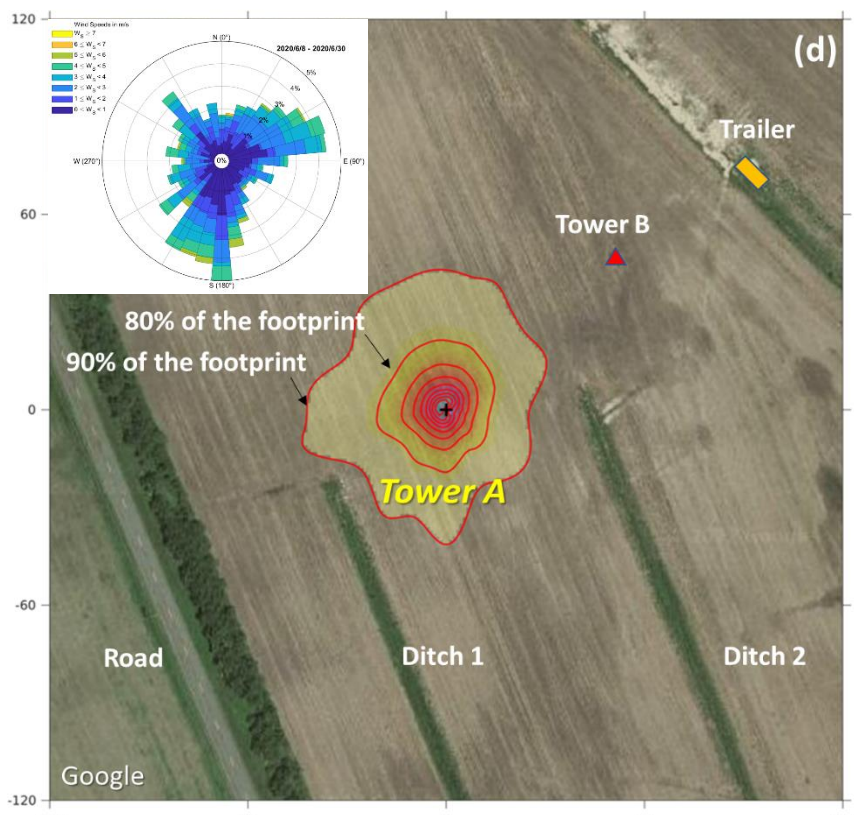
(d)
2020/6/8 - 2020/6/30
Trailer
Tower B
80% of the footprint
90% of the footprint
Tower A
Road
Ditch 1
Ditch 2
Google

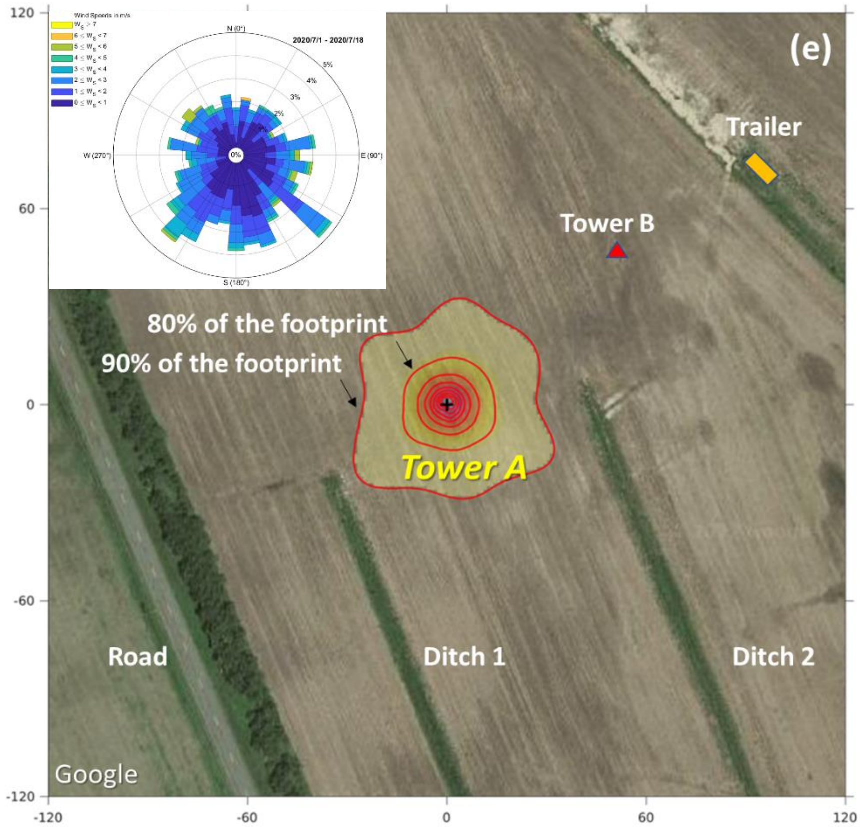

Figure 37. The footprint climatology of tower A for July 1-31, 2018 (a), May 1-31, 2019 (b), June 1-21, 2019 (c), June 8-30, 2020 (d), and July 1-18, 2020 (e). The background Google Map satellite images were extracted from the non-growing season for demonstration purposes so there is no crop in the field. The top left wind rose shows wind directions over the same FG measurement period. The contour lines indicate the source area of the measured flux in percentage from 10% to 90%, in a step of 10%. The background color shading between the contour lines represents the normalized footprint function value of the footprint climatology in a unit of m^{-2}. The darker the color is, the greater the value is. The center of the contour lines indicates the position of the FG tower. The unit of the distance on the x-axis (or y-axis) is meters.

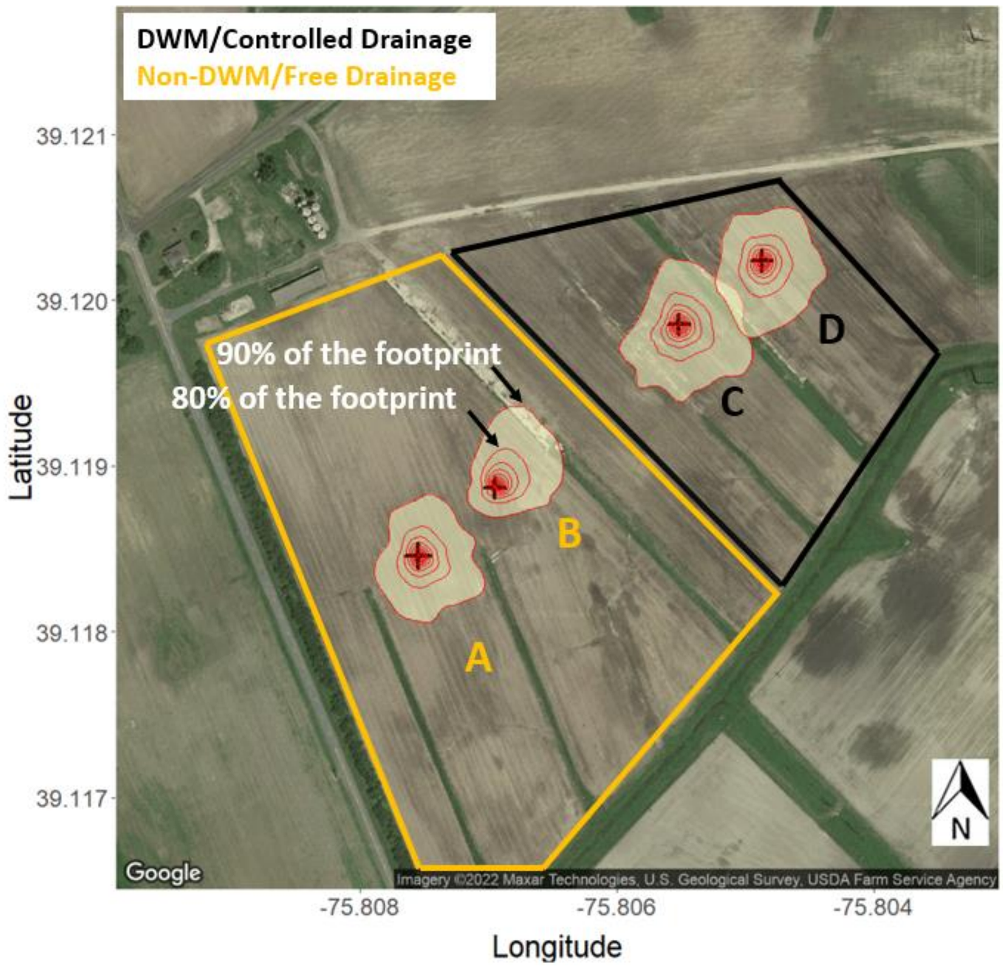

Figure 38. The integration of four towers' footprint climatology on an aerial image of the research site for July 2018 (the month of July in 2018 was chosen because it was the only month during the growing season when all four towers were functioning). The outermost contour lines and the second outermost contour lines in the figure indicate 90% and 80% of the source area of the observed flux, respectively. The center of the contour lines shows the location of each FG tower.

4.2.3.2 Flux Rose (Polar Plot)[5]

Following Waldo et al. (2019), the flux rose (or flux polar plot, similar to the wind rose) of half-hourly N_2O flux measurements for each tower over maximum emission periods in three consecutive years 2018, 2019, and 2020 was made (Fig. 39), using the 1-D Flux Footprint Prediction (FFP) model in Kljun et al. (2015). The figures on the left side show that the 50% flux contribution extent only has a 10-m radius, while the figures on the right panel indicate that the 80% flux contribution extent has a radius over 20 m. Moreover, these figures reflect the direction where peak emissions were generated relative to the FG tower for each half-hourly measurement. For instance, the distribution of the dots in Fig.39d reveals that at most times peak emissions were generated on the western side of the flux tower in May and June of 2019. The flux rose analysis is especially helpful for comparing the spatial coverage of the FG measurements and static chamber measurements.

[5] The flux rose of tower C is used here as an example. Figures related to other towers can be found in the appendices at the end of this dissertation.

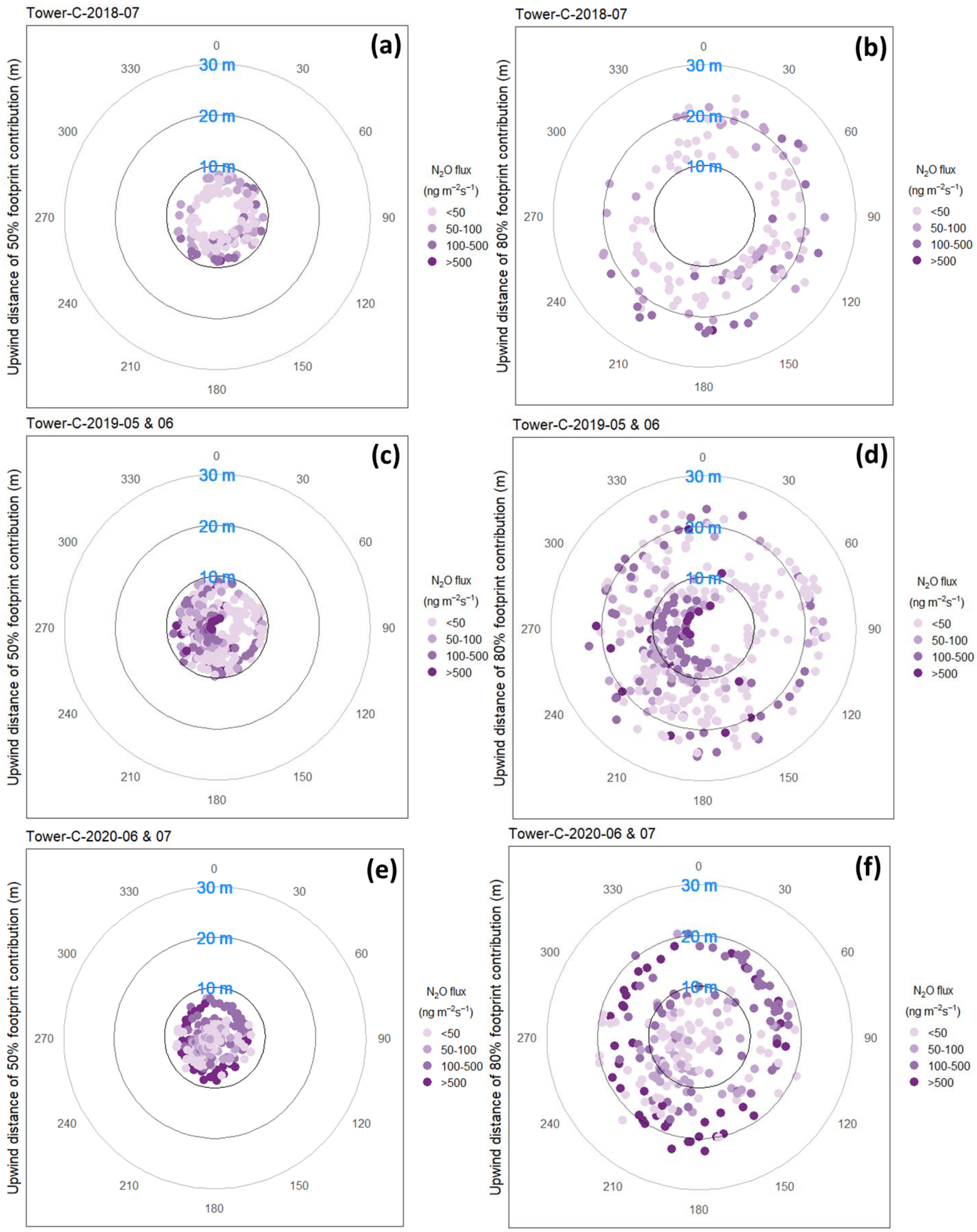

Figure 39. Flux roses of tower C's half-hourly N_2O flux data during the peak emission periods (July 1-31, 2018 (a and b), May 1-June 30, 2019 (c and d), and June 8-July 31, 2020 (e and f)). The radii of the rings are 10 m, 20 m, and 30 m, and the tower is located at the center of the rings. In the figures on the left side (a, c, and e), the distance of the dot from the center represents the 50% flux contribution extent. In the figures on the right (b, d, and f), the distance of the dot from the center represents the 80% flux contribution extent. The darker the dot is, the stronger N_2O emission it indicates.

4.2.4 Conclusion

In this section, I evaluated whether the placement of the FG towers satisfied the preset criteria for ensuring that valid flux comparisons can be made between the DWM plots and the non-DWM plots, using the FFP model in Kljun et al. (2015). The footprint climatology analysis showed that each tower had adequate upwind fetch area and indicated that at least 90% of the observed N_2O and CH_4 fluxes were generated in the experimental plots and that the observations can be used to represent the surface-atmosphere air exchange of the local crop ecosystem. The integrated footprint climatology also illustrated that there was no footprint overlap between the 80% flux contribution area of the FG towers. There was some footprint overlap between the 90% flux footprint extent of tower C and tower D, or possibly between tower A and tower B. Because each of these pairs of plots was under the same water table management practices, this minor overlap of replicate plots within a treatment is not a major concern for detection of the treatment effect. The flux rose showed the spatial coverage of the FG measurement system along with the distribution of peak emissions relative to the position of the flux tower and is considered as a useful tool for further tower and chamber comparison. Overall, the potential concerns related to the FG towers' footprints have been resolved here.

4.3 A Comparison between Eddy Diffusivities Calculated from the Aerodynamic Method and a Combined Method

4.3.1 Introduction

The flux gradient (FG) method was selected as the primary method to study the patterns of N_2O and CH_4 emissions at this field site because it allows continuous measurements of N_2O and CH4 emissions from multiple plots within a field using a single trace gas analyzer. The FG method requires a measurement of a concentration gradient ($\Delta[N_2O]/\Delta z$) multiplied by the eddy diffusivity (K) based on aerodynamic measurements from a sonic anemometer:

$$F = K \times \Delta[N_2O]/\Delta z \tag{1}$$

Laubach et al. (2016) proposed an alternate method that combines FG measurements of N_2O and CH_4 concentration gradients with Eddy Covariance (EC) measurements of CO_2 flux. They assumed that the turbulent diffusivities (K) for CO_2, CH_4, and N_2O are the same. This allows the flux of N_2O (or CH_4) to be calculated based on the ratio of their concentration gradient over the CO_2 concentration gradient multiplied by the CO_2 flux measured by EC:

$$F_{N_2O} = F_{EC-CO_2} \times \Delta[N_2O]/\Delta[CO_2] \tag{2}$$

In essence, a value for the diffusivity (K) is substituted by $F_{EC-CO_2} \times \Delta z/\Delta[CO_2]$ from the EC measurements.

Since the introduction of fast-response gas analyzers, the EC method has become the most widely used approach to measure trace gas exchanges between the surface and the atmosphere and has been seen as the gold standard for other approaches to compare with. Here I explored the method of Laubach et al. (2016) by combining simultaneous measurements of trace gas fluxes using both methods. In the summer of 2021, CO_2 fluxes were measured for approximately 3 weeks using the EC and FG techniques at the Marydel farm while N_2O and CH_4 fluxes were measured by the FG technique. I compared the estimated K values from the aerodynamic method with K estimated from the combined method.

4.3.2 Methods

In 2021, the study site was planted in soybean on May 1 and harvested on October 20. Because there was only one EC system, only one of the four towers was reinstalled in the field in 2021. Tower C was chosen because its distance to the instrument trailer provided an appropriate flow rate for the FG method. An LI-7200RS enclosed CO_2/H_2O analyzer (LI-COR, Lincoln, Nebraska, U.S.A.) was mounted on tower C along with the LI-7550 analyzer interface unit and the flow module to measure CO_2 fluxes using the EC method. The inlet of the LI-7200RS was placed next to the sonic anemometer (CSAT3B, Campbell Scientific, Logan, Utah, U.S.A.), which was the same sonic anemometer shared with the FG method (Fig. 40). CO_2 flux is equal to the product of the mean air density and the mean covariance between instantaneous deviations in vertical wind and CO_2 mixing ratio (Burba, 2013).

$$F_{EC} = \overline{\rho_d}\,\overline{w's'} \tag{3}$$

where ρ_d is air density, w is vertical wind speed, and s is CO_2 mixing ratio. The overbar symbol denotes 30-min average, and the prime symbol indicates instantaneous deviations from the mean. F_{EC} represents CO_2 flux measured using the EC method. The LI-7200RS and the sonic anemometer were responsible for measuring CO_2 mixing ratio and vertical wind speed at a very high frequency 10Hz, respectively. Because the on-site data processing module SmartFlux 1 was not compatible with the CSAT3B sonic anemometer, both the LI-7200RS and the sonic anemometer raw data were stored on a CR6 datalogger (Campbell Scientific, Logan, Utah, U.S.A.). The measurements were conducted from July 14 to August 5. During this period canopy height changed from 0.70 to 0.95 m.

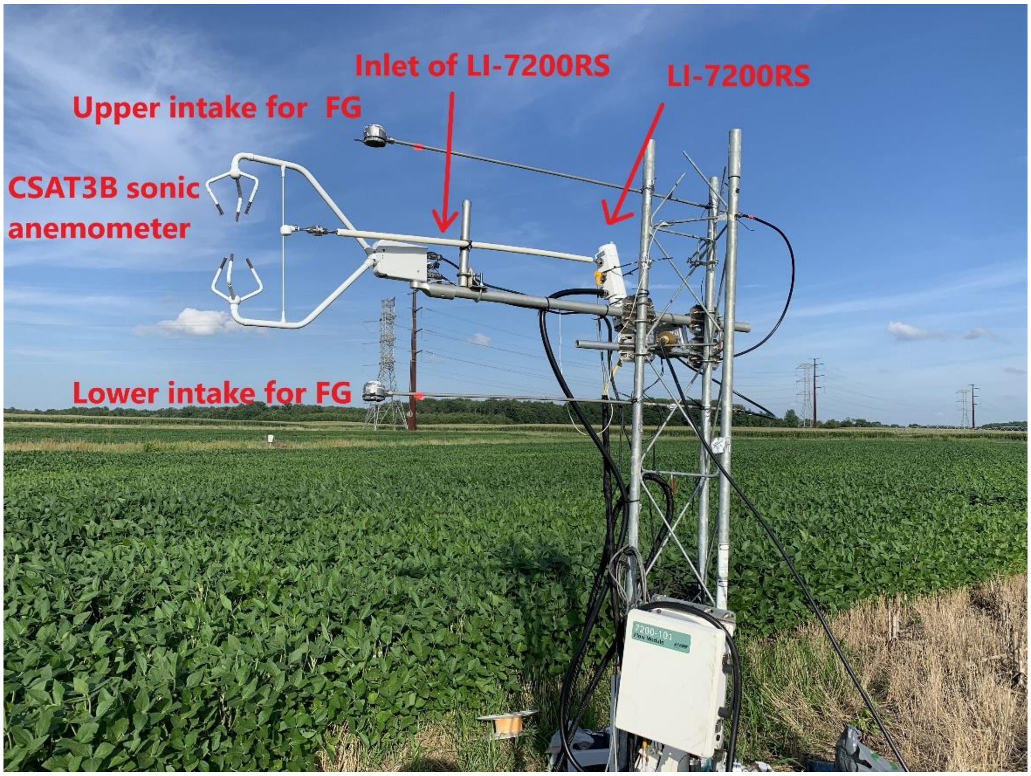

Figure 40. Setup of the EC system and the FG system on tower C.

Raw data from the LI-7200RS and the sonic anemometer were processed using the EddyPro® Software v7.0.7 (LI-COR Inc., Lincoln, Nebraska, U.S.A.) to calculate CO_2 fluxes measured by the EC method. Corrections were applied in the Advanced Mode, including axis rotations for the anemometer tilt correction (double rotation), quality check (Mauder and Foken, 2004), statistical analysis for raw data screening (i.e., spike count/removal (Vickers and Mahrt, 1997), amplitude resolution, drop-outs, absolute limits, and skewness and kurtosis), and corrections of high-pass filtering effects (Moncrieff et al., 2004) and low-pass filtering effects (Moncrieff et al., 1997). The WPL correction aiming to compensate for density fluctuations was not included because CO_2 and H_2O concentrations were expressed as mixing ratios (moles of gas per mole of dry air), which can be used for computing eddy covariance fluxes without the need for density corrections (Webb et al., 1980).

Simultaneously, CO_2 fluxes were also measured at tower C using the FG method using an LI-6252 CO_2 analyzer (LI-COR, Lincoln, Nebraska, U.S.A.) located in the upstream of the Quantum Cascade Laser (QCL) trace gas (N_2O and CH_4) analyzer (Aerodyne, Billerica, MA, U.S.A.). FG-CO_2 fluxes were calculated using the equation below:

$$F_{FG} = -K \frac{\partial C}{\partial z} \tag{4}$$

where K is the eddy diffusivity ($m^2 s^{-1}$) of CO_2 at height z and $\partial C/\partial z$ is the CO_2 concentration gradient. F_{FG} represents CO_2 flux measured using the FG method. The eddy diffusivity for sensible heat was given by:

$$K_{heat} = \frac{u_* \kappa (z_2 - z_1)}{\left[ln\left(\frac{z_2 - d}{z_1 - d}\right) - \psi_{h2} + \psi_{h1}\right]} \tag{5}$$

Assuming similarity between sensible heat and CO_2 turbulent transport, integration of Eq. (4) between two heights (z_1 and z_2) leads to:

$$F_{FG} = \frac{u^* \kappa \Delta C}{\left[ln\left(\frac{z_2 - d}{z_1 - d}\right) - \psi_{h2} + \psi_{h1}\right]} \tag{6}$$

where u_* is the friction velocity, κ is the von Karman constant (= 0.41), d is the displacement height (= 0.67 x canopy height), and ψ_{h1} and ψ_{h2} are the integrated Monin-Obukhov similarity functions for sensible heat at sampling heights z_1 and z_2. These functions were calculated using the stability parameter ζ = (z-d)/L, where L is the Obukhov length (Wagner-riddle et al., 2007). The sonic anemometer CSAT3B was installed at 2.05 m on tower C to measure sensible heat and friction velocity over soybean. The lower and upper sampling intakes were set at 1.7 m and 2.4 m, respectively, and the end of each intake was connected to a three-way air-control solenoid valve (Parker Hannifin, Cleveland, Ohio, U.S.A.). Air sampling switched between the upper and lower intakes every 20 s, which was controlled by a 16 channel AC/DC controller SDM-

CD16AC (Campbell Scientific, Logan, Utah, U.S.A.) and a datalogger CR1000 (Campbell Scientific, Logan, Utah, U.S.A.). After being transported to the trailer via 120 m of Synflex tubing, air samples were directed into the LI-6252 CO_2 analyzer and then into the QCL. Trace gas concentration gradients were averaged every half hour to be accordant with the sonic anemometer output and CO_2 fluxes measured using the EC technique.

Because the output of the embedded CR6 program and the EddyPro® software both contained processed turbulence data such as u* and L, the calculation of the diffusivity K using Eq. (5) yielded two groups of K value that were slightly different from each other. Detailed comparisons are discussed in Section 4.3.3.

A zero-gradient test was performed from July 7 to July 10 to quantify the minimum detectable CO_2 gradient between the lower and upper inlets by co-locating the two inlets at the same height (Fig. 41). By taking the mean of the absolute values of the 140 independent half-hourly data points, the minimum measurable concentration difference between the two inlets was 1.05±0.47 ppm for the 30-min average.

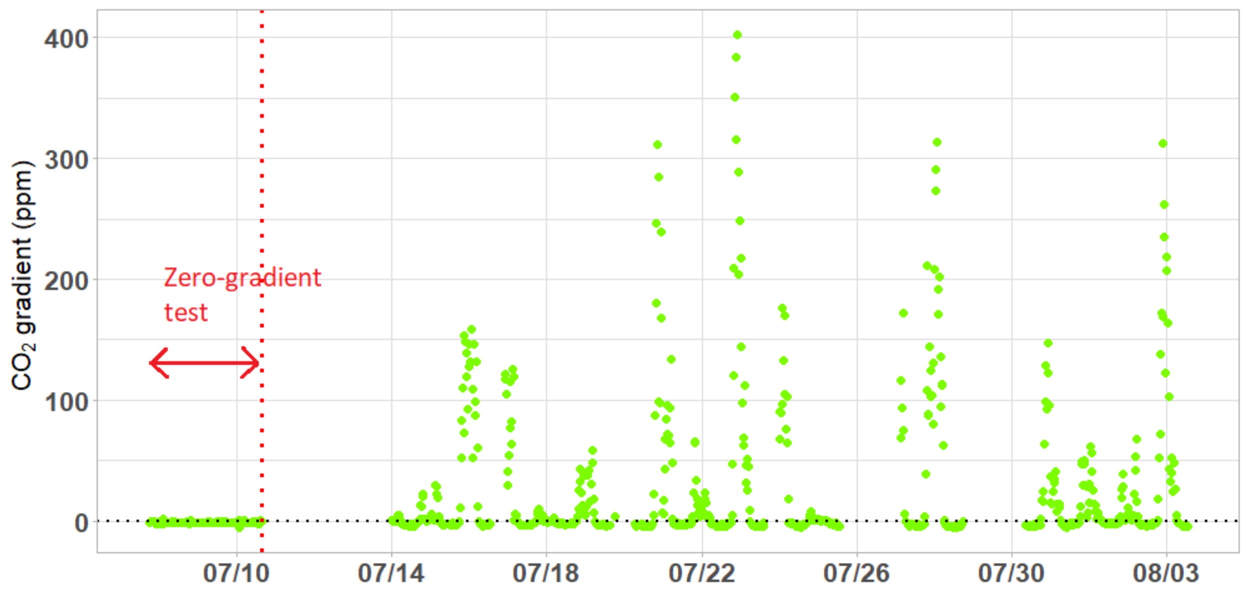

Figure 41. Differences in CO_2 mixing ratio between the lower and upper inlets (lower minus upper). The two inlets were mounted at the same height from 18:00 on July 7 to 16:00 on July 10, 2021.

Both the CO_2 fluxes calculated from the FG method and that from the EC method were subjected to two additional filters: the spike/outlier detection filter (Papale et al., 2006) and the u* filter. The spike removal method was based upon the double-differenced time series and used the median of the absolute deviations from the data's median (MAD) which is a robust measure of the variability of a univariate data set. For each half-hourly CO_2 flux, the d value is calculated as a double-differenced time series:

$$d_i = (flux_i - flux_{i-1}) - (flux_{i+1} - flux_i) \quad (7)$$

Md is the median of this time series and MAD is defined as:

$$MAD = median(|d_i - Md|) \quad (8)$$

The value is flagged as spike/outlier if:

$$d_i < Md - \left(\frac{z \cdot MAD}{0.6745}\right) \quad (9)$$

or

$$d_i > Md + \left(\frac{z \cdot MAD}{0.6745}\right) \tag{10}$$

where z is the threshold value. Following Papale et al. (2006), three z values (4, 5.5, and 7) were used to evaluate the effect on data screening and the sensibility of this method.

The purpose of the u* filtering was to filter out fluxes measured under insufficient turbulence conditions (indicated by low u* values). For the EC method, the friction velocity threshold was estimated according to the moving point method in Wutzler et al. (2018) and Papale et al. (2006). First, data were split into 19 equally sized u* bins (Fig. 42). Then, the threshold was defined as the mean of the u* bin where the average nighttime CO_2 flux was greater than 95% of the average nighttime flux at the higher u* classes. The time span of the data collected at our site was only 3 weeks long, so the nighttime data were not split into seasons or temperature subsets. The estimated u* threshold was approximately 0.09 m/s for the EC method (Fig. 42). In practice, the u* threshold is site and season specific and varies typically from 0.1 to 0.5 m/s (Aubinet et al., 2012). For the FG method, the same u* threshold was applied.

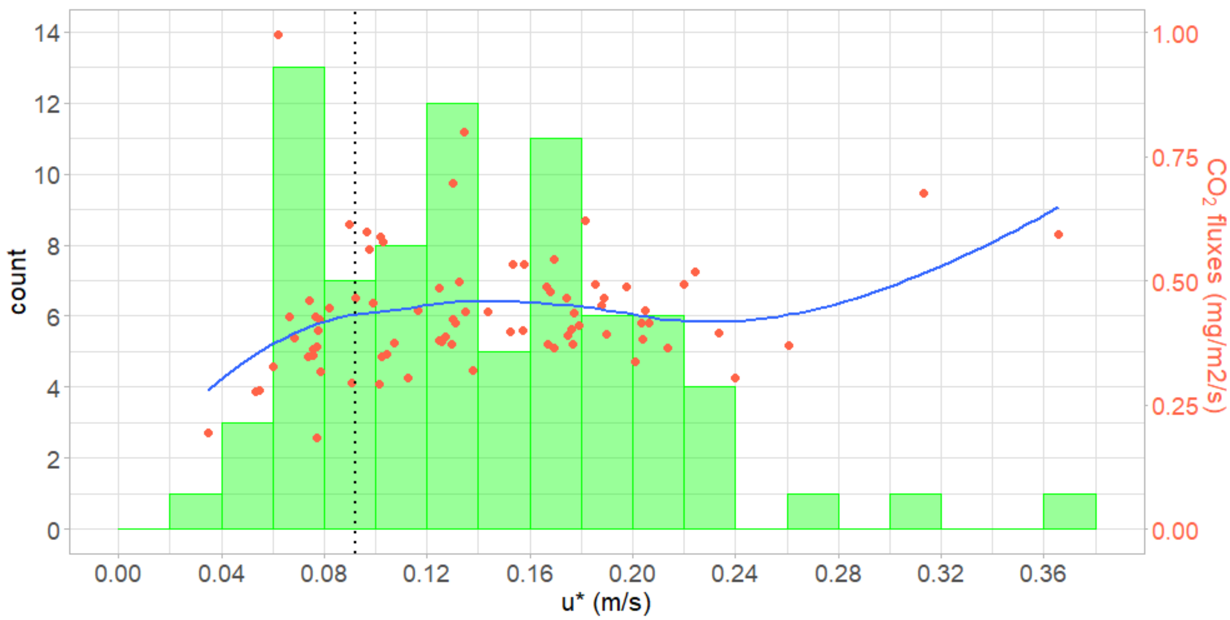

Figure 42. The bar plots represent the number of data points in each bin after the nighttime CO_2 flux data were split into 19 equally sized u* bins (the corresponding y-axis is on the left). The red dots show the evolution of nighttime CO_2 flux with friction velocity (the corresponding y-axis is on the right). The blue line is the locally weighted regression (LOESS) line for those dots. The estimated u* threshold (dashed line) is 0.09 m/s.

In EddyPro®, quality flags are calculated for all fluxes (heat, momentum, and gas fluxes) and the final flags in the output files are based upon a combination of partial flags calculated as a result of two tests, known as the steady state test and the developed turbulent conditions test (or the integral turbulence characteristics test) (Foken et al., 2004; Mauder & Foken, 2015). To make maximum use of the available data, CO_2 fluxes with the final flags “0” (best quality data) and “1” (moderate quality data) were retained under the “Mauder and Foken 2004” flagging policy, which means for the above two tests, class 6-9 (low quality) data were discarded from the results (Fig. 43). To assess the effect of retaining higher quality fluxes on the volume of the remaining data and the goodness of agreement between the EC and FG techniques, data filtering was conducted using multiple combinations of different classes for the two tests and the aforementioned threshold values for the spike removal process (Fig. 44 and Table 9).

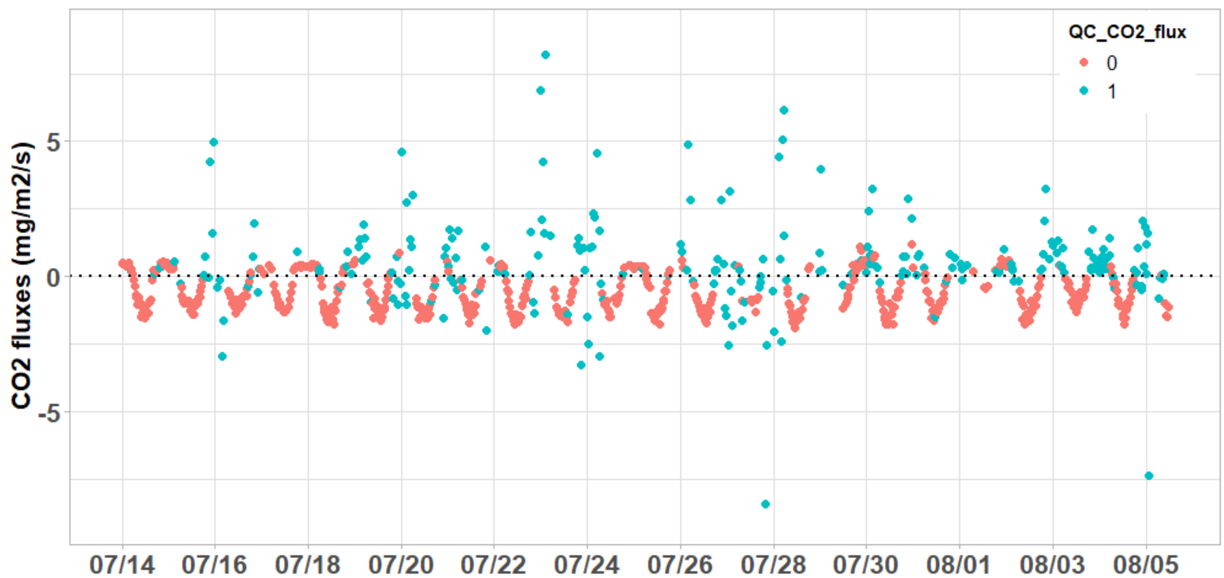

Figure 43. Half-hourly CO_2 fluxes calculated from EddyPro® (colored coded by the final flag of CO_2 flux). “0” (red) corresponds to class 1 and 2 for the steady state test and the integral turbulence characteristics (ITC) test, and “1” (blue) corresponds to class 3-5 for the steady state test and ITC test.

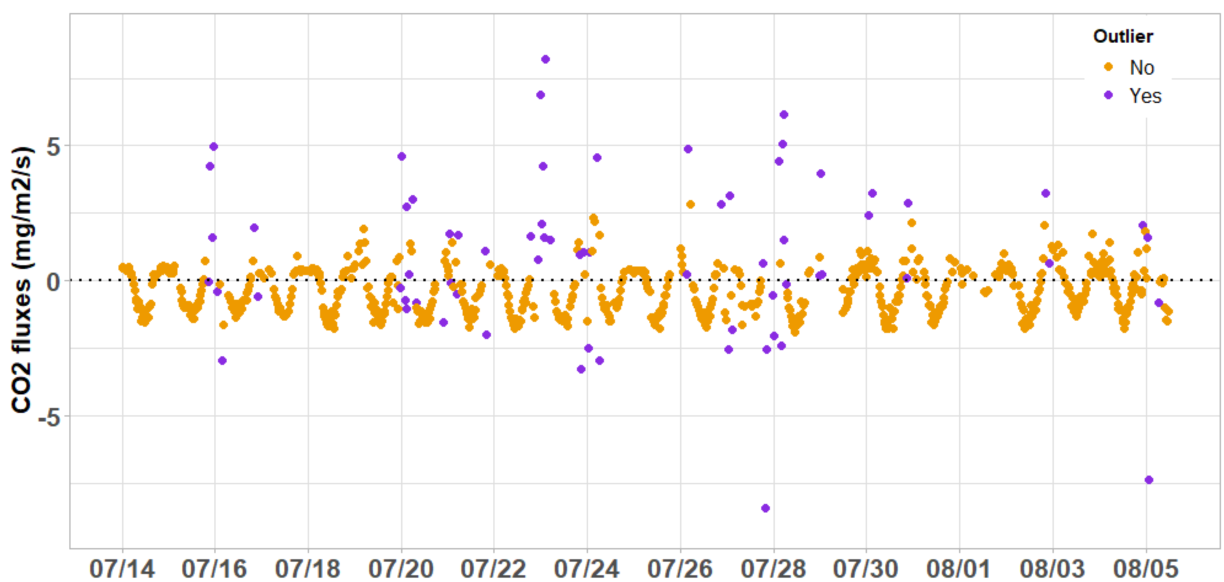

Figure 44. Half-hourly CO_2 fluxes calculated from EddyPro®. Data categorized as class 5 and below were retained using the classification schemes for the steady state test and the ITC test. Purple dots (Yes) were identified as outliers using the spike detection method with a threshold value z=7.

Table 9. Percentage of half-hourly CO_2 fluxes (the EC method) discarded in different scenarios. The numbers in brackets indicate the actual numbers of half-hourly fluxes discarded.

QC_flag	Spike detection z=7	Spike detection z=5.5	Spike detection z=4
SST <=5 & ITCT <=5	8.77 (68)	10.45 (81)	12.65 (98)
SST <=4 & ITCT <=4	12.65 (98)	14.45 (112)	17.16 (133)
SST <=3 & ITCT <=3	23.48 (182)	24.13 (187)	25.16 (195)

Considering the short measurement window, the principle was to keep as much reasonable CO_2 flux data as possible. Besides, the more radical spike removal strategy (z = 5.5 or 4) did not improve the performance of the linear fitting between the EC and FG techniques (data were not shown here). Hence, a more conservative strategy was adopted, which was for the steady state test and the ITC test flux data defined as class 5 and below were retained and the spike removal threshold z=7 was applied, resulting in 8.77% of the data points filtered out (figures of other scenarios, e.g., the second row in Table 9, were not shown here). In addition to the spike removal process, the u* filter eliminated another 22.84% (177 half-hourly fluxes) of the data.

4.3.3 Results and Discussion

Overall, CO_2 fluxes measured in 2021 using the EC and FG techniques exhibited quite good agreement (Fig. 45 and Fig. 46). The slope (0.83) and the coefficient of determination (0.83) indicated that CO_2 fluxes measured by the two techniques were highly correlated, but FG slightly overestimated the fluxes (assuming that EC is the more authoritative method). The slope (F_{EC}/F_{FG}) is also known as the enhancement factor (Simpson et al., 1998). For the entire three weeks data, a 10-day moving window was used to create a series of subsets, and for each 10-day subset a linear regression between EC and FG was calculated. Figure 47 shows that the regression slope (the enhancement factor) declined further below 1.0 as the 10-day window moved forward, indicating poorer agreement between the methods as the canopy height increased. Unfortunately, the existence of the pivot irrigation system on the farm prevented adjusting the sampling intakes at a higher position, which is a challenge for flux measurement in on-farm research.

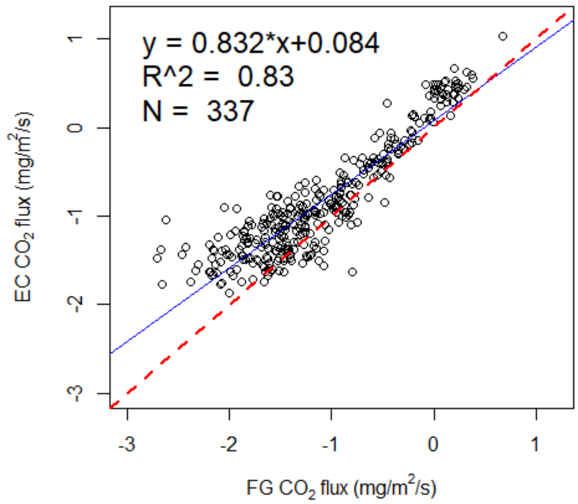

Figure 45. Linear regression of half-hourly CO_2 fluxes between the EC and FG techniques after the applications of the spike removal and u* filters. The red dashed line is the 1:1 line. There were 337 half-hourly flux data points remained for the time when both the EC and FG measurements were valid and available. The slope (F_{EC}/F_{FG}) is also known as the enhancement factor.

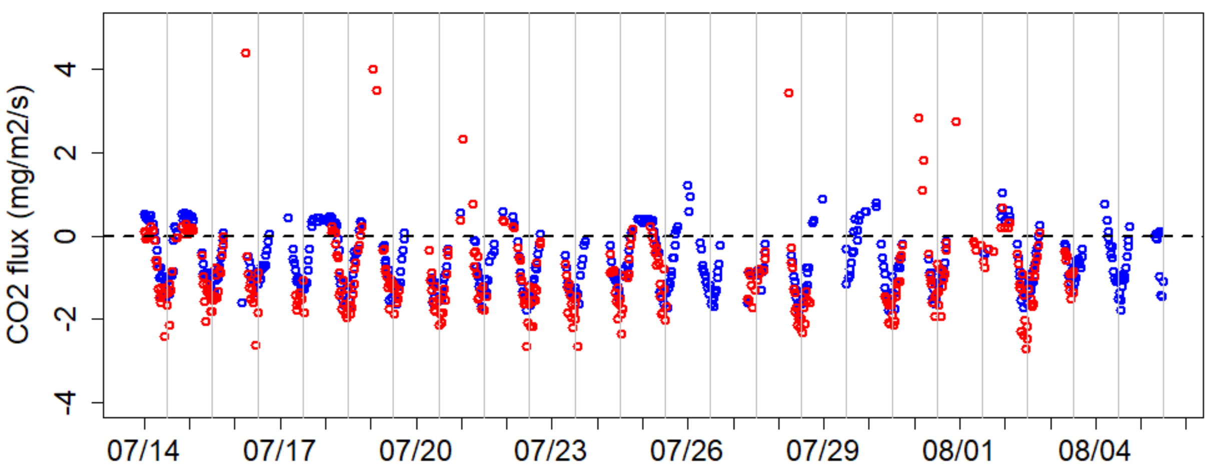

Figure 46. Timeseries plot of the CO_2 fluxes measured by the FG (red) and EC (blue) methods.

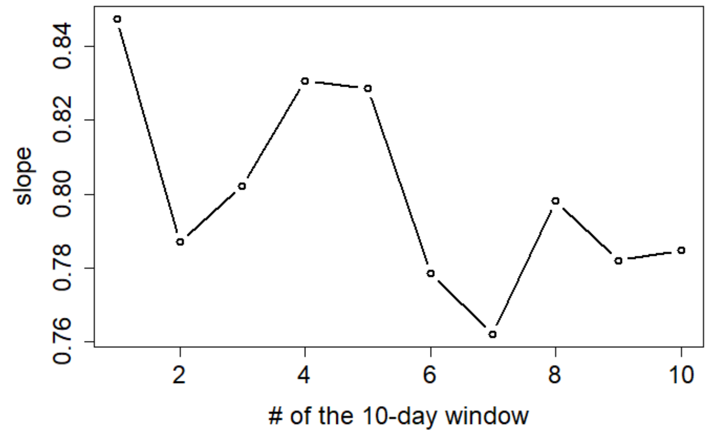

Figure 47. Changes of the slope (F_{EC}/F_{FG}, enhancement factor) using the 10-day moving linear regression method.

To assess whether the aerodynamic approach that I used to calculate the eddy diffusivity (K) for N_2O and CH_4 fluxes obtained in the previous years with FG was appropriate, another task of this section was to get an estimated eddy diffusivity (K) following Laubach et al. (2016), using the 30-min CO_2 fluxes from the EC measurements and the 30-min CO_2 concentration gradients between the upper and lower sampling intakes at the same tower from the FG measurements (here I call this the “combined” method). The eddy diffusivity from the combined method (K-estimated) was calculated based on Eq. (11) and compared to the two groups of aerodynamic diffusivities calculated from Eq. (5) using processed turbulence data provided by the embedded CR6 program (K-CR6) and the EddyPro® software (K-EddyPro). Based on the zero-gradient test, the minimum detectable CO_2 gradient was approximately 1 ppm. Thus, for the estimated K from the reverse calculation, CO_2 gradients whose absolute values were less than 1 ppm were discarded so that a small gradient in the denominator would not lead to an unreasonably large K value.

$$K_{estimated} = F_{EC} \times \frac{\Delta z}{\Delta C} \tag{11}$$

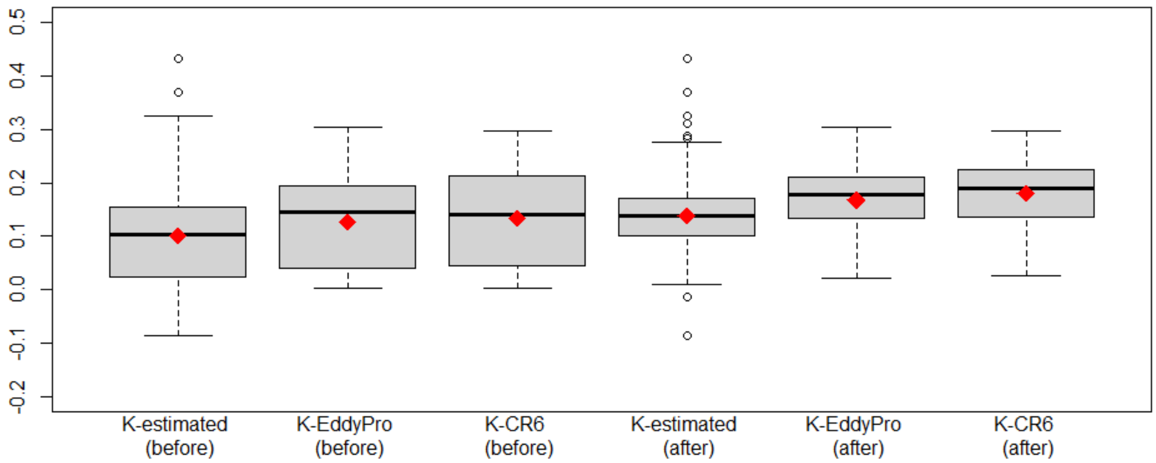

Figure 48. Boxplots of eddy diffusivity (K) from 3 different ways of calculation (K-estimated, K-EddyPro, and K-CR6) before and after the applications of the u* and spike detection filters. Black horizontal bar indicates median and red diamond indicates mean. For the first boxplot, two outliers were excluded to avoid an excessively large y-axis scale for the rest of the boxplots (outliers were not excluded from the calculation of the mean, median and variance of K in Table 10).

Data filtering with the u* and spike detection filters resulted in higher K values for all the three different types of eddy diffusivities because the u* filter eliminated data under weak turbulence conditions with low K values (Fig. 48 and Table 10). The fact that FG slightly overestimated the fluxes compared to EC is also reflected in the K comparisons: the second (K-EddyPro) and the third (K-CR6) method using the aerodynamic equation (5) tend to estimate higher K values compared to the first method (K-estimated) using the combination of CO_2 fluxes from the EC measurements and CO_2 concentration gradients from the FG measurements. This was likely due to the assumption of linear change in trace gas concentration between two levels in K-theory was violated when the intake ports of the FG system were too close to the plant canopy (i.e., non-diffusive region) (Thurtell, 1989). When the canopy was taking up CO_2 strongly during the day, CO_2 concentration near the top of the canopy was drawn down at a greater rate than that far away above the canopy, resulting in a nonlinear gradient close to the canopy. At higher elevations, the concentration gradient became closer to linear. In this instance, if the intake ports were too close to the canopy, they might be sampling a nonlinear portion of the CO_2 concentration gradient. Because the larger concentration gradient at the lower intake elevation was misinterpreted as "the linear gradient", the FG method overestimated CO_2 fluxes, resulting in the enhancement factor < 1. The EC method does not depend on an assumption of linear concentration gradients and therefore the concentration changes at a single intake port that are correlated with eddies would be less affected.

There was no large discrepancy among the last two methods (K-EddyPro vs. K-CR6) before or after the u* and spike detection filtering. The minor differences between these two methods can be attributed to different algorithms in the EddyPro® software and the embedded CR6 program to process the high-frequency raw turbulence data.

Table 10. Statistical summary of eddy diffusivity (K) from 3 different ways of calculation (K-estimated, K-EddyPro, and K-CR6) before and after the applications of the u* and spike detection filters (SD: standard deviation; N: number of valid K values for the same timestamps).

	K-estimated (before)	K-EddyPro (before)	K-CR6 (before)	K-estimated (after)	K-EddyPro (after)	K-CR6 (after)
Median	0.103	0.144	0.141	0.137	0.178	0.191
Mean	0.1	0.126	0.134	0.138	0.167	0.18
SD	0.088	0.082	0.087	0.063	0.06	0.06
N	432	427	432	287	287	287

4.3.4 Conclusion

Although the temporal coverage of our flux measurements in 2021 was relatively short compared to other studies (due to COVID-19 and other restrictions), the observed CO_2 fluxes over soybean using the EC and FG techniques exhibited good agreement for direct flux comparisons and for calculations of eddy diffusivity (K). There was some bias in the FG method, indicating that it overestimated CO_2 fluxes, especially large uptake fluxes when the intake inlets were too close to the canopy. However, the broad agreement for CO_2 fluxes suggests that the method is generally reliable, which confers confidence that the FG method can be applied simultaneously to multiple towers for N_2O and CH_4 flux measurements.

4.4 A Comparison for N_2O Flux Gap-Filling between Linear Interpolation and Artificial Neural Networks

4.4.1 Introduction

Data gaps exist because of data filtering, instrument maintenance or repair, and interruption by the COVID shutdown or by on-farm agricultural activities such as planting, fertilization, or harvest, etc. There have been a number of gap-filling approaches available for CO_2 flux, such as interpolation, mean diurnal variation, look-up tables, nonlinear regression, artificial neural networks (ANN) and so on (Falge et al., 2001; Moffat et al., 2007). Filling gaps in CO_2 data is relatively straightforward because CO_2 fluxes not only follow a diurnal pattern but also have seasonal and inter-annual similarities (Mishurov & Kiely, 2011). Due to the highly temporal and spatial variabilities of N_2O emissions and the presence of pulse events driven by fertilizer application or wetting-drying cycles, some of the approaches that work well for CO_2 flux may not be as useful for N_2O, but gap-filling of N_2O fluxes is still needed. In this section, I will compare two common techniques, linear interpolation and ANN, to decide which one is more suitable for our study of N_2O fluxes.

Data gaps can be filled using linear interpolation of fluxes in measurement periods adjacent to the missing data. Taki et al. (Taki et al., 2019) used this method to reconstruct missing N_2O flux data for their research site in Canada, assuming “a missing flux value for a day connected each day with every neighbor in a way that is similar to its neighbors (the adjacent days)”. Scanlon and Kiely (Scanlon & Kiely, 2003) also used linear interpolation to rebuild their daily average N_2O flux for an intensely grazed, fertilized grassland. The bias of this method stems from the fact that the variations in N_2O fluxes might not be linear, as N_2O emissions usually occur intermittently in the format of bursts. Moreover, if the gap needed to be filled is long (> 2 weeks), this method becomes less reliable.

ANN is a multi-layer, feed-forward neural network consisting of neurons connected based on various weights that are the regression parameters. It has been used as a computational tool to predict relationships between various nonlinear variables (Dengel et al., 2013; Järvi et al., 2012; Moffat et al., 2007; Taki et al., 2019). The multi-layer structure includes three layers: (i) an input layer, (ii) at least one hidden layer, and (iii) an output layer (Fig. 49). Information is fed into the input layer and signals are weighted before being transmitted through neurons organized in hidden layer(s). Then the weighted signals are summed and scaled using a transfer function in neurons before entering the next layer. At the initial step, values for the weights are randomly picked and then adjusted by a back-propagation learning algorithm in the training process (Järvi et al., 2012; Moffat et al., 2007). The common way to determine the optimal number of neurons in the hidden layer is through training the network multiple times with varying number of neurons until the uncertainty originating from the randomly initialized network has been minimized (Järvi et al., 2012; Taki et al., 2019). This method was chosen because it is capable of capturing nonlinear relationships between N_2O fluxes and environmental variables. The bias of this method is affected by the number of gaps: the more the number of gaps exist, the higher the bias is. The flux magnitude also influences the bias (Richardson et al., 2008; Taki et al., 2019).

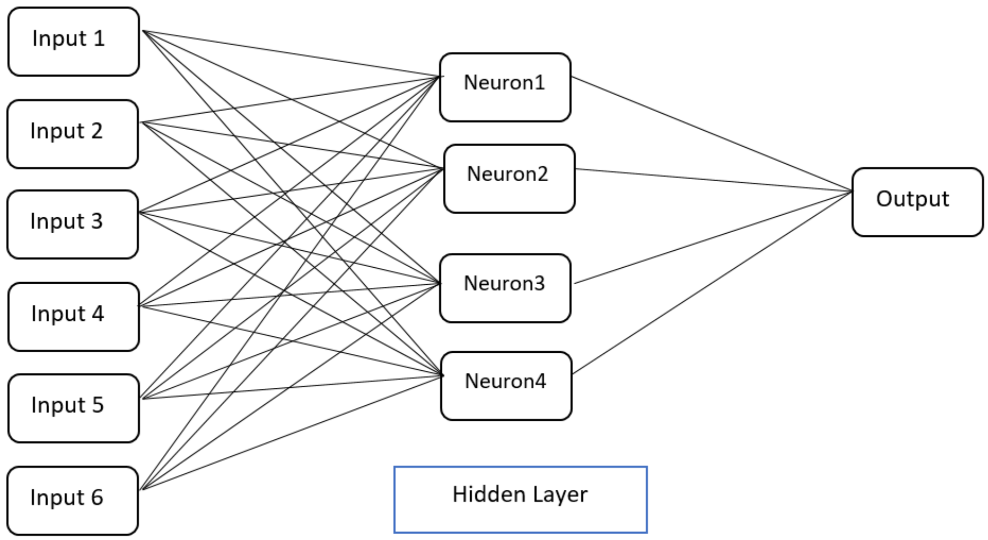

Figure 49. The architecture of the ANN with input variables on the left side, a hidden layer in the middle, and an output layer on the right side (adapted from Taki et al. (2019)).

4.4.2 Materials and Methods

4.4.2.1 Flux and Environmental Data

The mean daily N_2O fluxes of tower C in 2020 were selected as an example dataset to show the gap-filling processes and results using linear interpolation and ANN techniques. Environment variables that were used as input variable candidates for the ANN model included daily averaged total water input (precipitation and irrigation), daily averaged air temperature, daily averaged relative humidity, daily averaged soil moisture and temperature, and daily soil nitrate and ammonium concentrations. The monthly measured soil nitrate and ammonium concentrations were linearly interpolated to obtain the daily values of soil nitrate and ammonium. A lag time from 1 to 4 days was applied to daily water input (resulting in another four candidates for input parameters) to take into account a potential lag effect of precipitation and irrigation on N_2O emissions. In addition, the number of days after biosolids addition and the variation in daily soil moisture (the difference in soil moisture between each day and its previous day) were created as input variable candidates as well.

4.4.2.2 Linear Interpolation

Linear interpolation was done in R (R Core Team, 2022) using the function “approx”, assuming similarities between the missing data and the data in the adjacent days.

4.4.2.3 ANN Construction Procedures

Before selecting the final input combination of variables, candidate input variables with significant cross-correlations (correlation coefficient > 0.8) were removed (Fig. 50). A stepwise linear regression between the remaining environment variables and N_2O flux was then performed to select a combination of variables showing correlations with N_2O flux at a significance level of $p < 0.1$. The final input combination consisted of five parameters including daily water input (“Tot_H2O_Input”), air temperature (“AirTC_AVG”), soil nitrate (“Nitrate”) and ammonium concentrations (“Ammonium”), and daily variation in soil moisture (“DeltaVWC”). Following Bigaignon et al. (2020), the five input variables and the output variable were standardized/normalized to improve the performance of the neural network: each input variable was standardized by subtracting the mean value and dividing by the standard deviation; the output variable was normalized by subtracting the minimum value and dividing by the range of the variation. After standardization/normalization, the complete dataset (five input variables + one output variable) without any missing values was partitioned into a training dataset (50%) and a test dataset (50%) 40 times randomly, creating 40 different draws of training and test datasets. For each draw, an ANN was constructed using the training dataset and trained over 1000 iterations and meanwhile saved every 10 iterations. Thus, the training process resulted in total 4000 (40 draws times 100 saved neural networks for each draw) trained ANNs for a specific neuron number. These 4000 ANNs were applied to the input variables of the testing datasets and the predicted N_2O fluxes by the models were compared to the measured N_2O fluxes. The evaluation of the ANN model performance was based on the following statistical metrics including the coefficient of determination (R^2) and the root mean squared error (RMSE):

$$R^2 = \frac{(\sum(p_i - \bar{p})(o_i - \bar{o}))^2}{\sum(p_i - \bar{p})^2 \sum(o_i - \bar{o})^2} \quad [1]$$

$$RMSE = \sqrt{\frac{1}{N}\sum(p_i - o_i)^2} \quad [2]$$

where N is the number of observations, oi and pi are the observed fluxes and predicted fluxes, respectively, and $\bar{o}$ and $\bar{p}$ denote their means. For each draw, the desired iteration step to construct the best ANN model was determined by the principle of the lowest RMSE to prevent under or overfitting. Then the 40 draws with each's best iteration step were ranked based upon the R^2 value from high to low. The iteration step and draw number that led to the lowest RMSE and highest R^2 values were considered as the optimal choice of combination to construct the best ANN model. In addition to these general rules, visual checking was also done for the fitting results of the test dataset when these two criteria did not align to produce a single best option (e.g., visual checking on whether the RMSE converges as the iteration step increases).

To determine the optimal number of hidden neurons for the best ANN configuration, the neuron number was increased from 1 to 10 and the ANN was trained 4000 times (40 draws and 100 saved networks for each draw) for each number. The process of choosing the optimal neuron number also conformed to the previously described principle (the lowest RMSE and highest R^2 values).

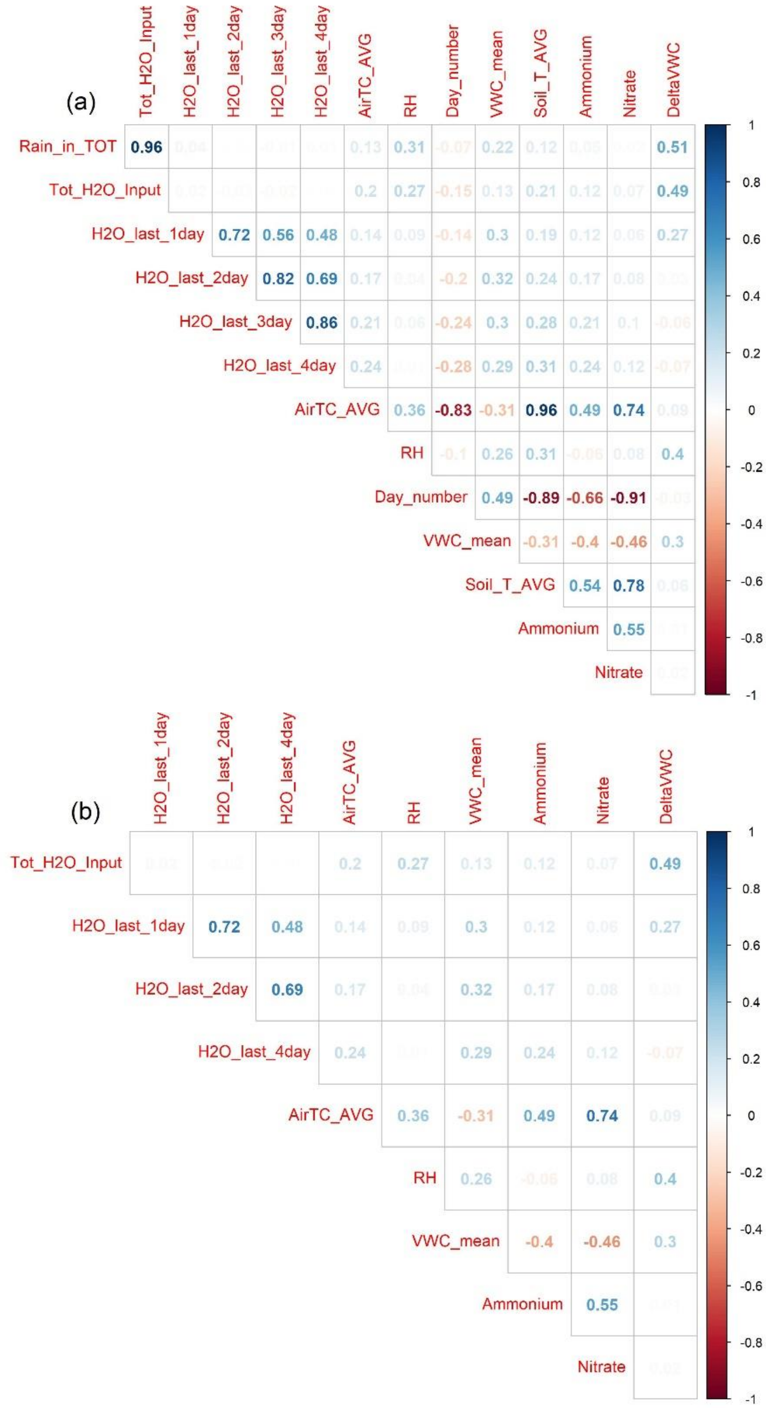

Figure 50. Correlation matrices for all input variable candidates before (a) and after (b) significant cross-correlations (correlation coefficient > 0.8) were removed. The variables in panel (a) are (from top to bottom): precipitation, daily water input (rain + irrigation), 1-day lagged daily water input, 2-day lagged daily water input, 3-day lagged daily water input, 4-day lagged daily water input, air temperature, relative humidity, the number of days after fertilization, soil moisture, soil temperature, soil NH_4^+-N, and soil NO_3^--N.

4.4.3 Results

The highest R^2 calculated on the test dataset from 4000 ANNs for each number of hidden neurons varying from 1 to 10 was achieved when the neuron number was three (Table 11). However, the best ANN with four neurons showed a slightly lower R^2 value (0.936 vs. 0.939) but a significantly improved RMSE (90.29 vs. 107.85 ng m^{-2} s^{-1}). Therefore, four neurons were chosen to build the model. The configuration of the final ANN model was a structure consisting of five input variables, four hidden neurons, and one output (Fig. 51).

The best ANN model with four neurons was obtained when the draw number was 31 and the iteration stopped at 30 steps (Table 11). Figure 52 shows the development of RMSE for the training and test datasets in function of iteration steps for draw numbers 18 and 31. For draw number 31, the lowest RMSE calculated on the test dataset was reached after 30 iteration steps and thus 30 was used as the iteration number to build the best ANN for that draw. For draw number 18, the best ANN was created at iteration step 360 for the same reason. Below or above that iteration step led to under- or over-fitting of the ANN model. Figure 53 shows comparisons between the observed and model predicted daily N2O fluxes using the test datasets of draws 31 and 18. Although the ANN model built upon draw number 31 had slightly higher R^2 and lower RMSE values, the model built on draw number 18 predicted fewer negative N_2O fluxes over the entire period from June to December. This was also demonstrated in the final gap-filled results (Fig. 54). Negative N_2O fluxes from the atmosphere to the soil (or N_2O uptakes) are possible, but mainly occur at high water-filled pore space (WFPS) and at low NO_3^- availability (Chapuis-lardy et al., 2007). The comparison of soil extractable nitrate concentration among 2018, 2019, and 2020 clearly show that the soil at this study site had the highest nitrate concentrations after biosolids application in 2020 (see Section 3.3.1.3 in Chapter 3). Therefore, net consumption of

N_2O is unlikely to take place during the period of June-December in 2020. After carefully examining the evolution of the RMSE value as a function of iteration step, the fitting results of the test dataset and the corresponding observed data, and the final gap-filled data, I considered the ANN model built upon draw number 18 and iteration step 360 with 4 neurons as a better alternative.

Table 11. Summary of the best ANN's configuration and statistics calculated on the test dataset for each number of neurons (N) varying from 1 to 10. The selected model is indicated by bold font. The mean daily N_2O fluxes of tower C in 2020 provided the full dataset.

N	RMSE (ng m^{-2} s^{-1})	R^2	Draw	Iteration
1	109.50	0.925	31	90
2	97.57	0.862	30	80
3	107.85	0.939	3	30
4	**90.29**	**0.936**	**31**	**30**
5	101.11	0.880	15	40
6	87.56	0.898	15	60
7	88.82	0.857	30	60
8	128.83	0.896	18	60
9	69.94	0.909	30	60
10	122.34	0.908	34	150

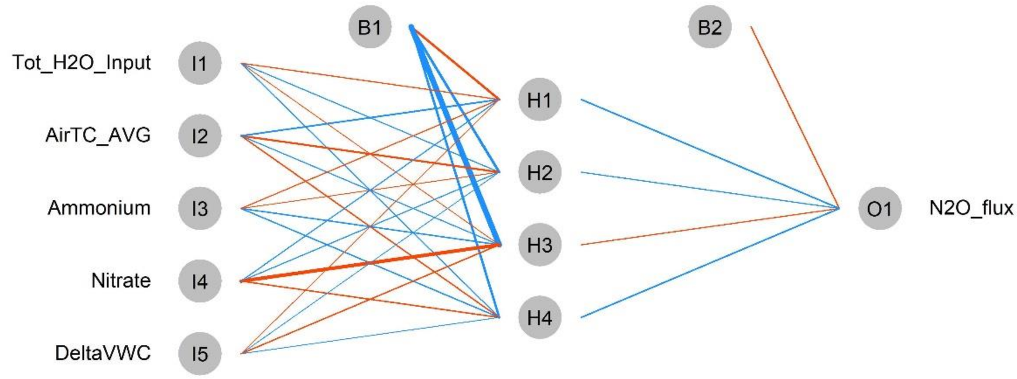

Figure 51. The configuration of the final ANN model (for tower C's daily N_2O fluxes in 2020), showing the input layer (I), hidden layer (H), bias terms (B), and output layer (O). The input layer consists of five input variables: daily total water input (precipitation + irrigation), air temperature, soil ammonium concentration, soil nitrate concentration, and daily variation of soil moisture. The input variables are connected with each of the neurons in the hidden layer by either blue lines (indicating positive weights) or red lines (indicating negative weights). The thickness of the line represents the absolute magnitude of the weight. Bias terms are analogous to intercept terms in a standard regression model (Beck, 2018) and the color and thickness of each line connecting the bias layer to the hidden/output layer have the same meaning as the lines connecting the input layer to the hidden layer. The hidden layer consists of four hidden neurons and is connected with the output layer/variable (daily N_2O flux) via the blue and red lines.

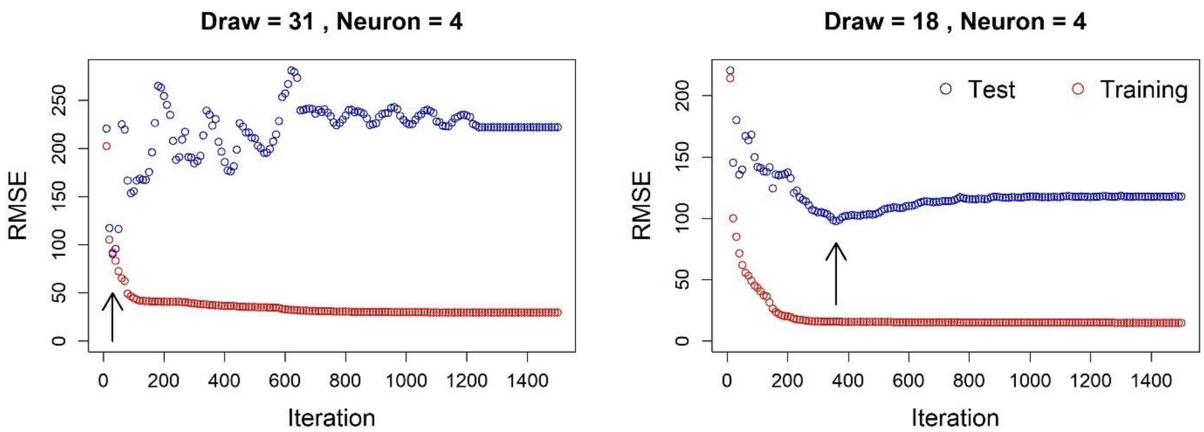

Figure 52. Evolution of RMSE (ng m^{-2} s^{-1}) for the training (red) and test (blue) datasets of draws 31 (left panel) and 18 (right panel) when the neuron number is four. The arrows indicate that the lowest RMSE values calculated on the test dataset are reached at iterations step 30 (left panel) and step 360 (right panel). The RMSE value of the test dataset stabilized after fewer iterations in the right panel. The mean daily N_2O fluxes of tower C in 2020 provided the full dataset.

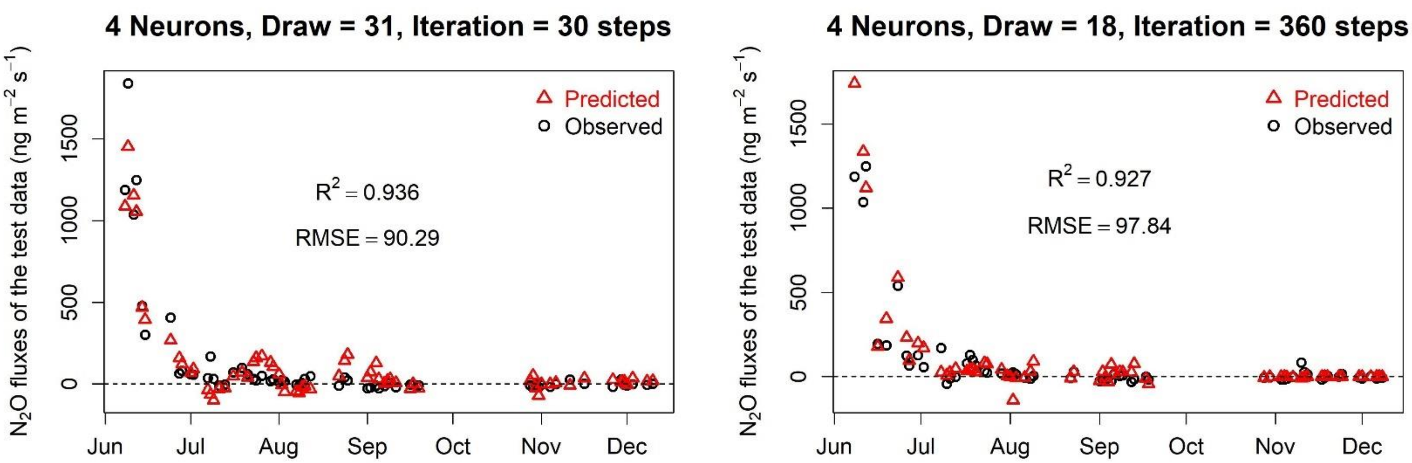

Figure 53. Comparison between the observed (black open circle) and model predicted (red triangle) N_2O daily fluxes for tower C in 2020 using the test datasets of draws 31 (left panel) and 18 (right panel) with 4 neurons. For each model, the coefficient of determination (R^2) and the root mean squared error (RMSE) are listed in the figure.

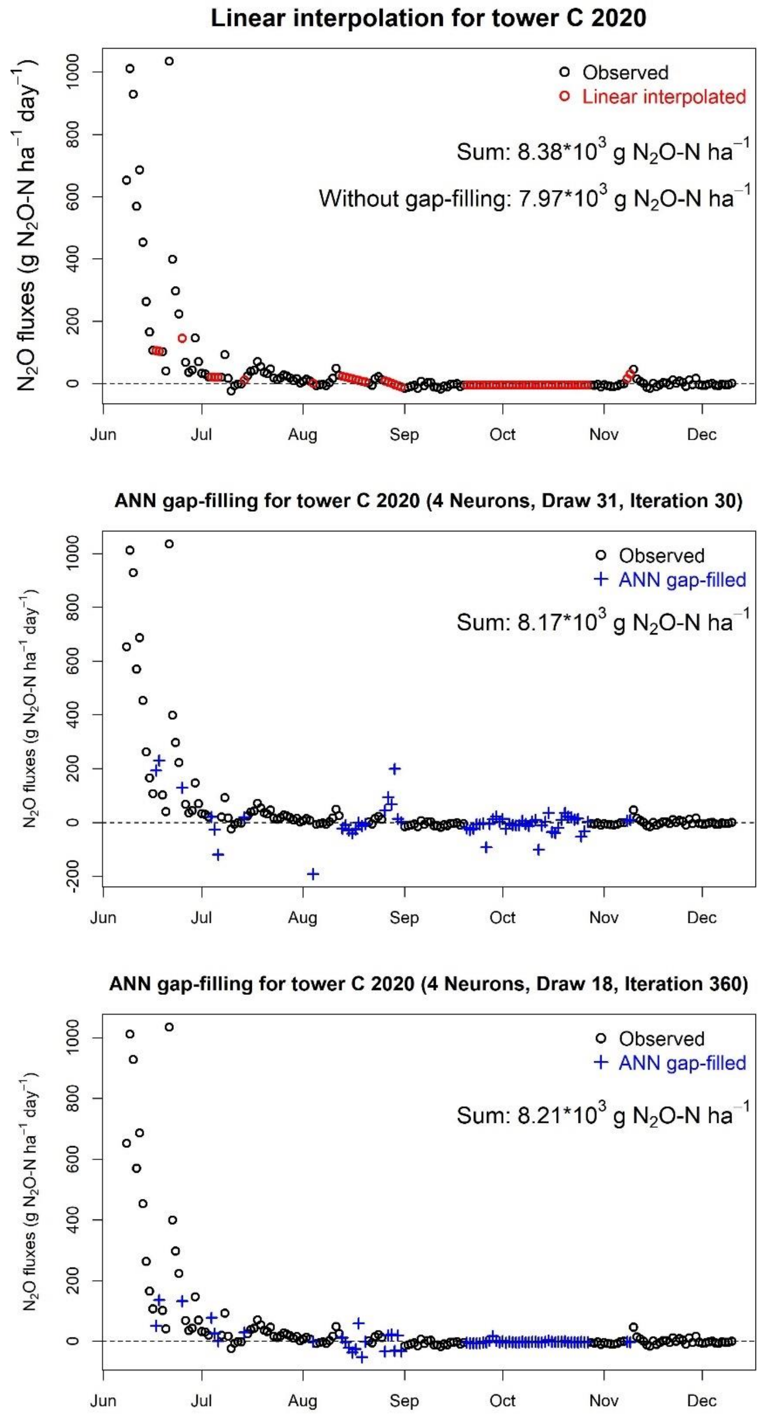

Figure 54. Comparisons between the gap-filled results using linear interpolation (top) and two ANN models (middle and bottom) for tower C's daily N_2O flux data in 2020. The cumulative fluxes were also calculated for each case.

4.4.4 Discussion

When compared to the gap-filled daily N_2O fluxes using linear interpolation, the gap-filled data using the best ANN model that I constructed in the section above did not exhibit a clear difference in the general temporal pattern or the cumulative sum of N_2O emissions. The ANN and linear interpolation methods only increased the annual estimate by 3% and 5%, respectively, and the difference between those adjustments (0.24-0.41 kg N_2O-N ha^{-1}) is well within the margin of uncertainty of the cumulative annual N_2O emissions even (8.62 ± 1.42 kg N_2O-N ha^{-1} yr^{-1} for the DWM field and 7.99 ± 2.36 kg N_2O-N ha^{-1} yr^{-1} for the non-DWM in 2020; see Table 7 in Section 3.3.4 in Chapter 3 for details). One reason why the ANN and the linear interpolation methods did not exhibit larger differences in predicted fluxes was that there was only one large pulse in June, followed by relatively unimportant variation thereafter. Any method that approximates that large June flux pulse is likely to perform well with respect to characterizing the seasonal variation and the annual sum. ANN may be a viable/preferable option for other flux datasets that have more complex trends, but it was not more useful than the linear interpolation method in this particular case.

Another reason why the ANN method did not clearly improve performance for estimation of the missing N_2O flux data compared to the linear interpolation method can be probably ascribed to the low temporal resolution of soil ammonium and nitrate concentration data, which were among the most important driving variables of the ANN model. Using Garson's algorithm (Beck, 2018; Garson, 1991; Goh, 1995), the relative importance of each input variable affecting the performance of the best ANN model was computed (Fig. 55). Soil nitrate concentration was found to be one of the dominant driving variables, as important as air temperature. However, there were only eight times of soil sampling events from June to December in 2020 after the biosolids addition, leading to a monthly sampling interval approximately. The linearly interpolated data were unable to reflect the actual variations in soil nitrate concentration for the remaining days. Although the selected ANN model was the best in thousands of candidate models, its performance cannot be improved further if the dominant explanatory variable is not accurately measured or estimated with sufficient frequency. Considering the ANN method did not provide a better estimation of the missing N_2O data due to low temporal resolution of soil mineral nitrogen content, I only applied linear interpolation to fill data gaps for N_2O flux and estimate annual cumulative N_2O emissions in other parts of this dissertation for the sake of simplicity. ANN was also applied to gap-filling for other towers' daily N_2O flux data in 2019 and 2020 but in all cases it did not outperform the linear interpolations.

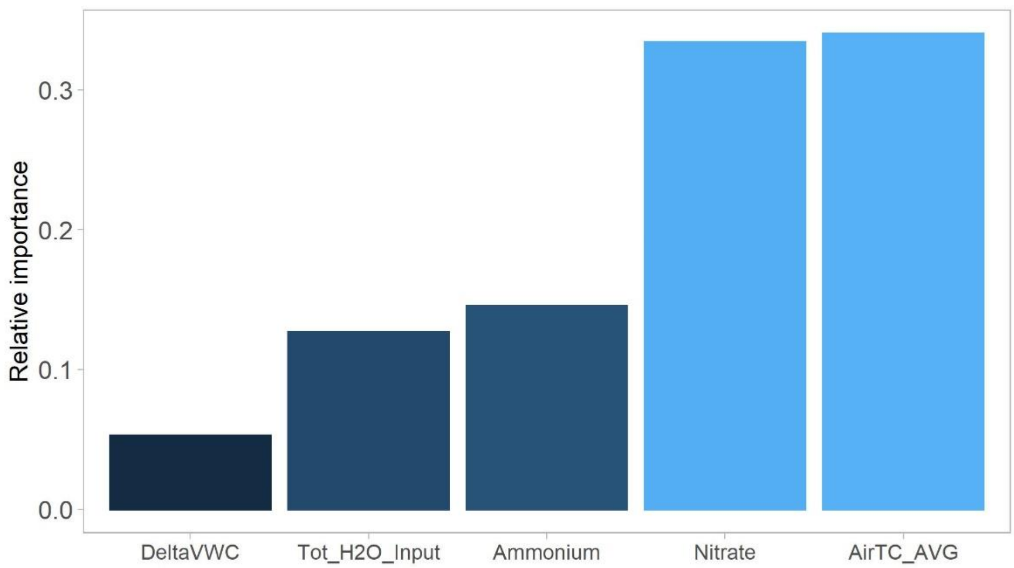

Figure 55. Relative importance of each input variable in the best ANN model (for tower C's daily N_2O flux data in 2020) based on Garson's algorithm. Input variables are (from left to right): variation in daily soil moisture, daily water input (precipitation + irrigation), daily soil ammonium concentration, daily soil nitrate concentration, and daily air temperature.

4.4.5 Conclusion

Using the N_2O fluxes measured by tower C in 2020 as an example, multiple ANNs were built between the input environmental variables and the output variable (N_2O flux) via connections with a hidden layer with neurons and the best ANN was selected based upon two statistical indicators (R^2 and RMSE) and visual check. However, in our case the best ANN did not provide a better estimation for the missing N_2O flux values compared to the linear interpolation method and thus ANN could not be proved to be a superior technique for N_2O data gap-filling in this study. The underlying reasons could be the dominance of a single pulse event for the annual flux estimate and the insufficient soil samplings for soil nitrate concentration, which was one of the dominant drivers for the selected best ANN. If this monthly sampling event could have been more frequent, the ANN method may have exhibited improved performance for N_2O data gap-filling.

Chapter 5: Conclusion

A major objective of this dissertation project is to evaluate whether implementation of drainage water management would trade reduction in nitrate concentration in ditch water for increases in soil N_2O and CH_4 emissions. To answer this question, reliable quantification of soil N_2O and CH_4 fluxes is the key. Chapter 2 and 3 demonstrated the feasibility of applying the tower-based micrometeorological flux gradient method to simultaneously and continuously measure intermittent bursts of soil N_2O and CH_4 emissions at a fine temporal resolution on multiple adjacent plots. The DWM practice increased the difference in the 0-5 cm soil moisture between treatment and control plots during the active periods of DWM, indicating that it was effective in retaining water on site. The flux measurement results in these two chapters indicated large N_2O emissions were highly dependent on fertilization and precipitation events: high nitrate concentration in the post-fertilization soil and large amounts of rain contributed to strong N_2O emissions. Statistical analyses of N_2O and CH_4 fluxes measured during the active periods of DWM revealed that no consistent treatment effects of DWM on soil GHG emissions were observed between DWM and non-DWM conditions for any of the study years, which included different fertilization regimes and crops.

The magnitudes of the observed N_2O fluxes between the FG and static chamber methods were in general agreement, but it is worth noting that spatial variability of the chamber measurements (such as “hot spot” chambers) or differences in spatial coverage between the FG towers and the chamber system could contribute to the disagreement between the micrometeorological and the chamber methods. At the time when our flux measurements were taking place, the comparison between the auto-chamber and flux gradient measurements was one of the first few methodological comparisons of N_2O fluxes since these sensitive, fast response instruments had become available.

For the first time to our knowledge, the micrometeorological FG method was employed to provide an in-situ quantitative assessment of the impacts of biosolids application on soil GHG emissions. The biosolid addition in 2020 led to the largest N_2O emissions in the growing season among the three years. The estimated N_2O EF for the biosolid-amended soil on this farm ranged from 4.5-5.2% and is considerably higher than the IPCC Tier 1 N_2O EF for organic amendments, indicating that variation in properties of organic amendments, such as C:N ratio, may need to be considered to derive improved estimates of EFs. This work emphasizes the general need for a better basis for estimating EFs for organic amendments.

In addition, four potential methodological concerns that could possibly outweigh the advantage of the micrometeorological approach were addressed: (1) the minimum detectable 30-min N_2O and CH_4 concentration gradients were quantified theoretically and experimentally and determined to be adequate for the research objective of this study; (2) at least 90% of the observed N_2O and CH_4 fluxes originated within the experiment plots and there was no footprint overlap between the 80% flux contribution area of the FG towers; (3) the aerodynamic method to calculate the eddy diffusivity coefficient was generally reliable; (4) the linear interpolation method for N_2O data gap-filling was adequate in this study.

This study could be improved by installing replicates for each of the continuously soil moisture and temperature monitoring systems that would facilitate a statistical test on the treatment effect beyond pairwise comparisons of the DWM and non-DWM probe installations. Spatial surveys and more frequent manual measurements of soil moisture outside the active periods of DWM could provide more indication of spatial and natural variation of soil moisture on this farm. The manual chambers could be distributed with more care to ensure sufficient representation of the towers' footprint area. Future similar studies should pay attention to guaranteeing a sufficient number of days when all the towers are functioning, especially for the post-fertilization flux measurements, so that the ANOVA tests evaluating the treatment effect have improved statistical power. Moreover, quantification of background N_2O emissions from an unfertilized agricultural site and a measured N mineralization rate in-situ could improve estimation of N_2O EFs for biosolid amendments in this research. Lastly, increasing the frequency of soil sampling for inorganic-N extractions could improve the performance of the ANN method for N_2O data gap-filling.

To our knowledge, this is the first study employing a micrometeorological method to evaluate the effects of DWM on soil GHG emissions in agricultural fields. Taken together, these results indicated that DWM may be employed to reduce nitrate leaching without the "pollution swapping" concern of increased GHG emissions from cropland soil surfaces.

Appendices

Appendix A. Ch. 2 The Friedman test when the assumption of normality was violated for the compared fluxes in 2018 and 2019.

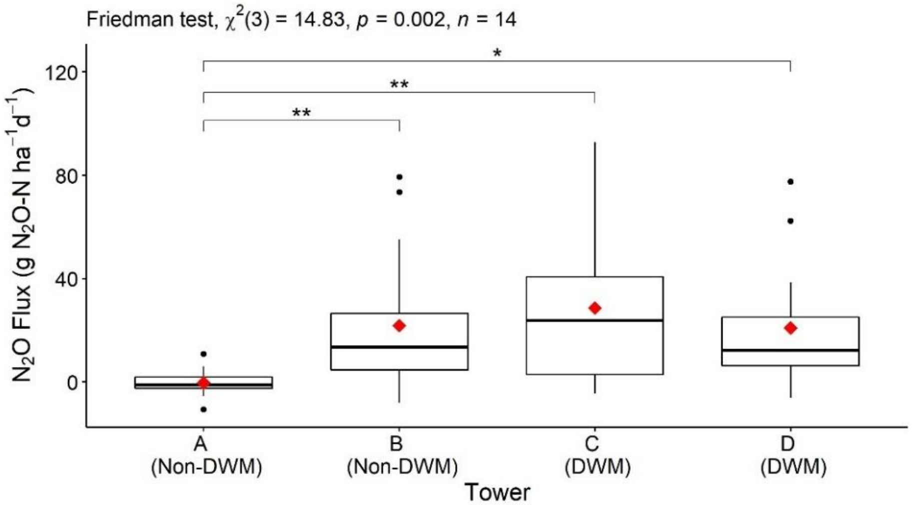

Figure A 1. Box plots of the mean daily N_2O fluxes (14 daily values for each tower) measured in July 2018. Red diamonds represent means and black horizontal bars in the boxes represent medians. Asterisks indicate that significant differences were found between the two towers connected by brackets using the Friedman test and the pairwise Wilcoxon signed-rank tests with the Bonferroni multiple testing correction for p-value adjustment ("*" and "**" represent significance levels $p < 0.05$ and $p < 0.01$, respectively). n is the number of daily flux values in each tower group.

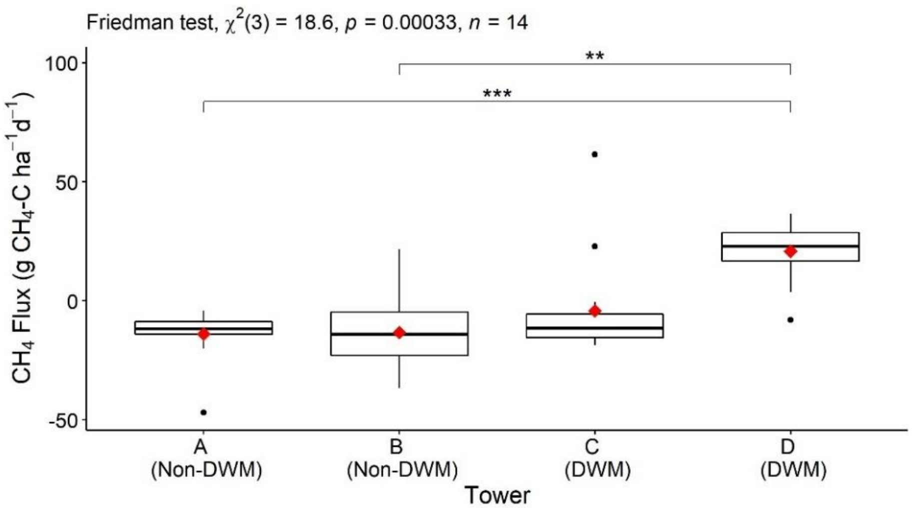

Figure A 2. Box plots of the mean daily CH_4 fluxes (14 daily values for each tower) measured in July 2018. Red diamonds represent means and black horizontal bars in the boxes represent medians. Asterisks indicate that significant differences were found between the two towers connected by brackets using the Friedman test and the pairwise Wilcoxon signed-rank tests with the Bonferroni multiple testing correction for p-value adjustment ("**" and "***" represent significance levels $p < 0.01$ and $p < 0.001$, respectively). n is the number of daily flux values in each tower group.

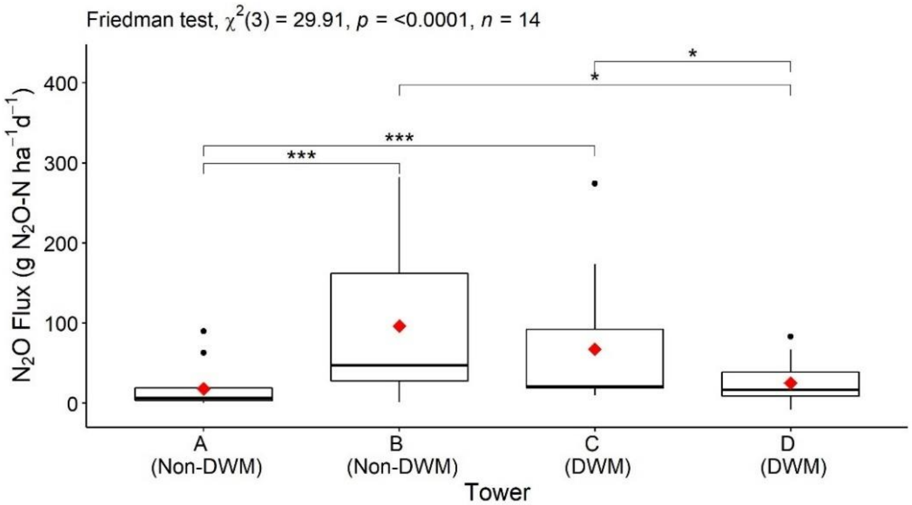

Figure A 3. Box plots of the mean daily N_2O fluxes (14 daily values for each tower) measured in May 2019. Red diamonds represent means and black horizontal bars in the boxes represent medians. Asterisks indicate that significant differences were found between the two towers connected by brackets using the Friedman test and the pairwise Wilcoxon signed-rank tests with the Bonferroni multiple testing correction for p-value adjustment ("*" and "***" represent significance levels $p < 0.05$ and $p < 0.001$, respectively). n is the number of daily flux values in each tower group.

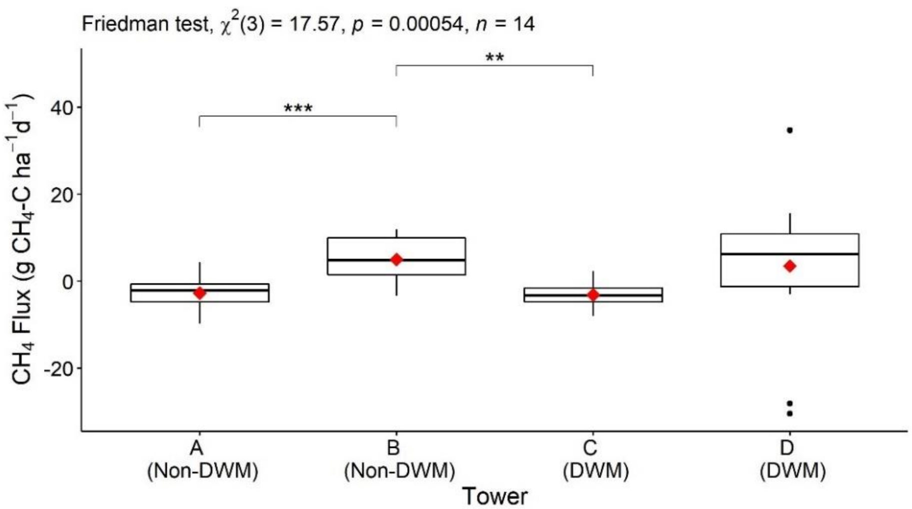

Figure A 4. Box plots of the mean daily CH_4 fluxes (14 daily values for each tower) measured in May 2019. Red diamonds represent means and black horizontal bars in the boxes represent medians. Asterisks indicate that significant differences were found between the two towers connected by brackets using the Friedman test and the pairwise Wilcoxon signed-rank tests with the Bonferroni multiple testing correction for p-value adjustment ("**" and "***" represent significance levels $p < 0.01$ and $p < 0.001$, respectively). n is the number of daily flux values in each tower group.

Appendix B. Ch. 3 The weight percentages of total carbon and total nitrogen in the dry biosolids samples.

Table B 1. The weight percentages of total carbon (%C) and total nitrogen (%N) in the dry biosolids samples.

Sample ID	%C	%N	C: N
1	39.27	6.23	6.30
2	39.66	6.19	6.41
3	36.87	5.10	7.22
4	32.83	4.82	6.81
5	41.06	6.88	5.97
6	39.71	6.55	6.06
7	36.12	4.95	7.30
8	39.42	6.12	6.44
9	39.81	6.12	6.50
10	39.08	6.19	6.32
11	37.54	5.35	7.01
12	38.62	6.27	6.16
Mean ± S.D.	38.33 ± 2.21	5.90 ± 0.67	6.54 ± 0.44

Appendix C. Ch.4 Footprint climatologies and flux roses of other towers.

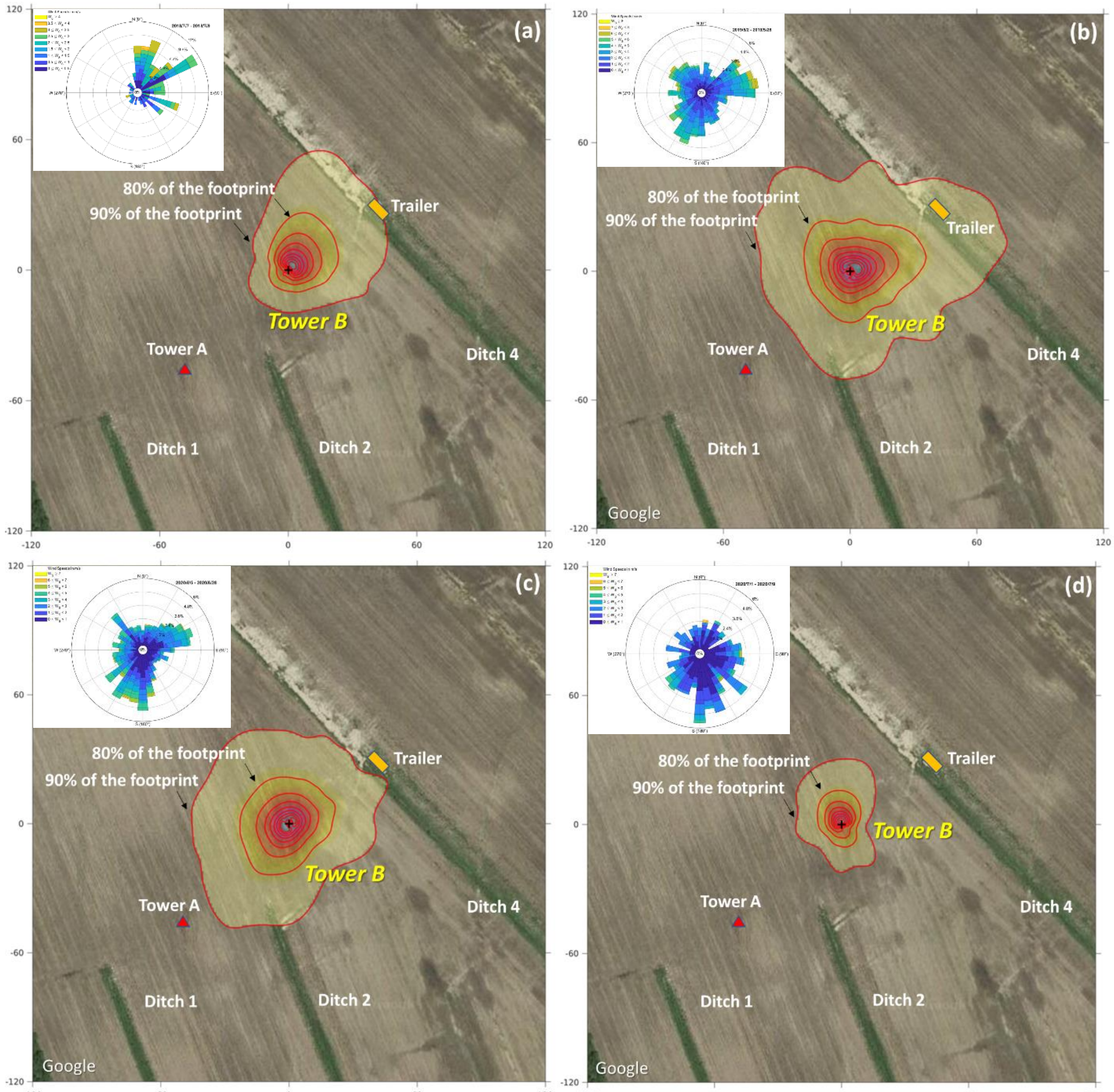

Figure C 1. The footprint climatology of tower B for July 7-9, 2018 (a), May 2-28, 2019 (b), June 5-28, 2020 (c), and July 1-9, 2020 (d). The background Google Map satellite images were extracted from the non-growing season for demonstration purposes so there is no crop in the field. The top left wind rose shows wind directions over the same FG measurement period. The contour lines indicate the source area of the measured flux in percentage from 10% to 90%, in a step of 10%. The background color shading between the contour lines represents the normalized footprint function value of the footprint climatology in a unit of m^{-2}. The darker the color is, the greater the value is. The center of the contour lines indicates the position of the FG tower. The unit of the distance on the x-axis (or y-axis) is meter.

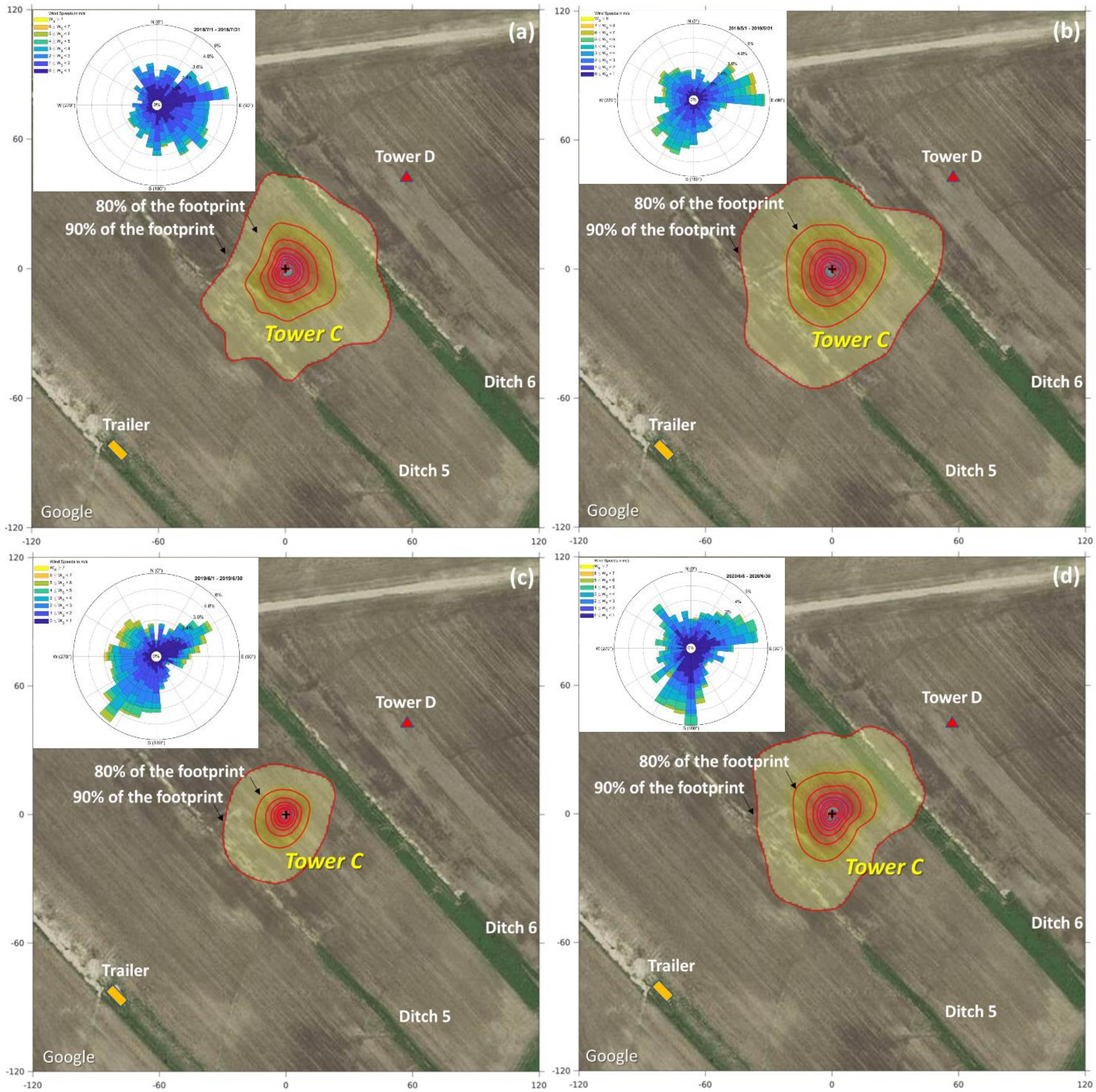

(a)
(b)
(c)
(d)
Tower D
Tower C
80% of the footprint
90% of the footprint
Ditch 6
Ditch 5
Trailer
Google

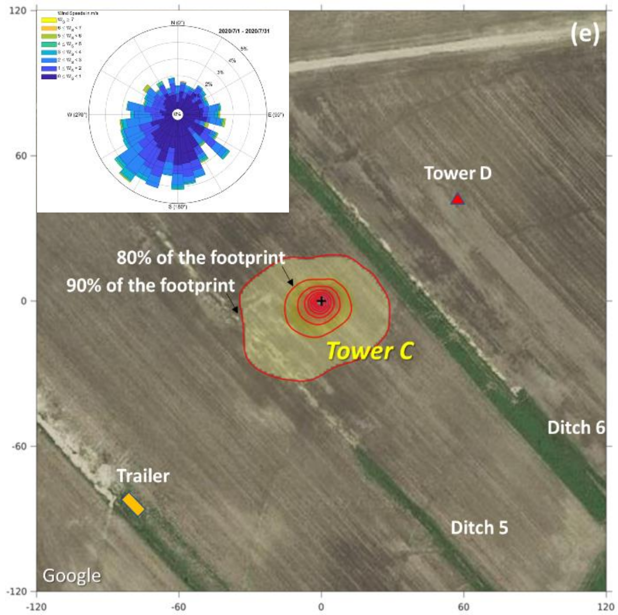

Figure C 2. The footprint climatology of tower C for July 1-31, 2018 (a), May 1-31, 2019 (b), June 1-30, 2019 (c), June 8-30, 2020 (d), and July 1-31, 2020 (e). The background Google Map satellite images were extracted from the non-growing season for demonstration purposes so there is no crop in the field. The top left wind rose shows wind directions over the same FG measurement period. The contour lines indicate the source area of the measured flux in percentage from 10% to 90%, in a step of 10%. The background color shading between the contour lines represents the normalized footprint function value of the footprint climatology in a unit of m^{-2}. The darker the color is, the greater the value is. The center of the contour lines indicates the position of the FG tower. The unit of the distance on the x-axis (or y-axis) is meter.

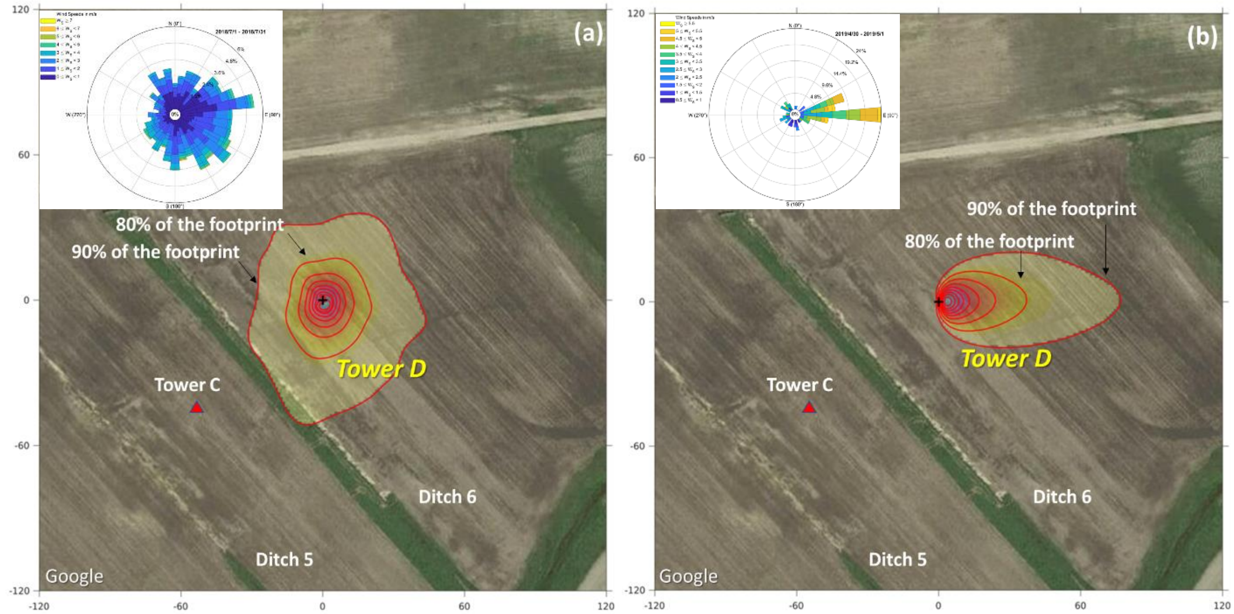

Figure C 3. The footprint climatology of tower D for July 1-31, 2018 (a) and April 30-May 1, 2019 (b) (due to the malfunction of the datalogger, the sonic anemometer on tower D did not provide enough 10Hz data for footprint analysis of the year 2019 and 2020). The background Google Map satellite images were extracted from the non-growing season for demonstration purposes so there is no crop in the field. The top left wind rose shows wind directions over the same FG measurement period. The contour lines indicate the source area of the measured flux in percentage from 10% to 90%, in a step of 10%. The background color shading between the contour lines represents the normalized footprint function value of the footprint climatology in a unit of m^{-2}. The darker the color is, the greater the value is. The center of the contour lines indicates the position of the FG tower. The unit of the distance on the x-axis (or y-axis) is meter.

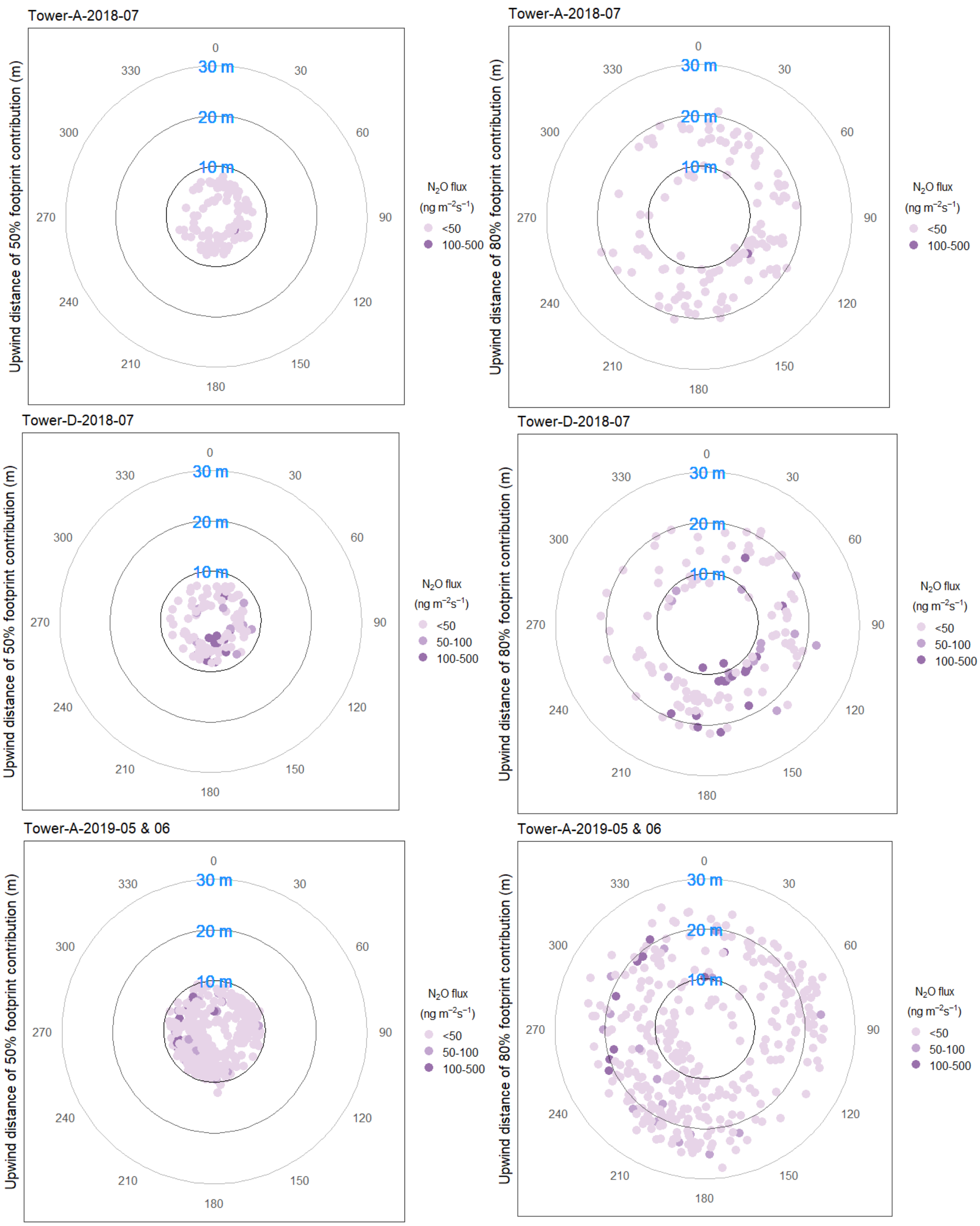

Tower-A-2018-07
Upwind distance of 50% footprint contribution (m)
Tower-A-2018-07
Upwind distance of 80% footprint contribution (m)
Tower-D-2018-07
Upwind distance of 50% footprint contribution (m)
Tower-D-2018-07
Upwind distance of 80% footprint contribution (m)
Tower-A-2019-05 & 06
Upwind distance of 50% footprint contribution (m)
Tower-A-2019-05 & 06
Upwind distance of 80% footprint contribution (m)
10 m
20 m
30 m
0
30
60
90
120
150
180
210
240
270
300
330
N2O flux
(ng m−2s−1)
<50
50-100
100-500

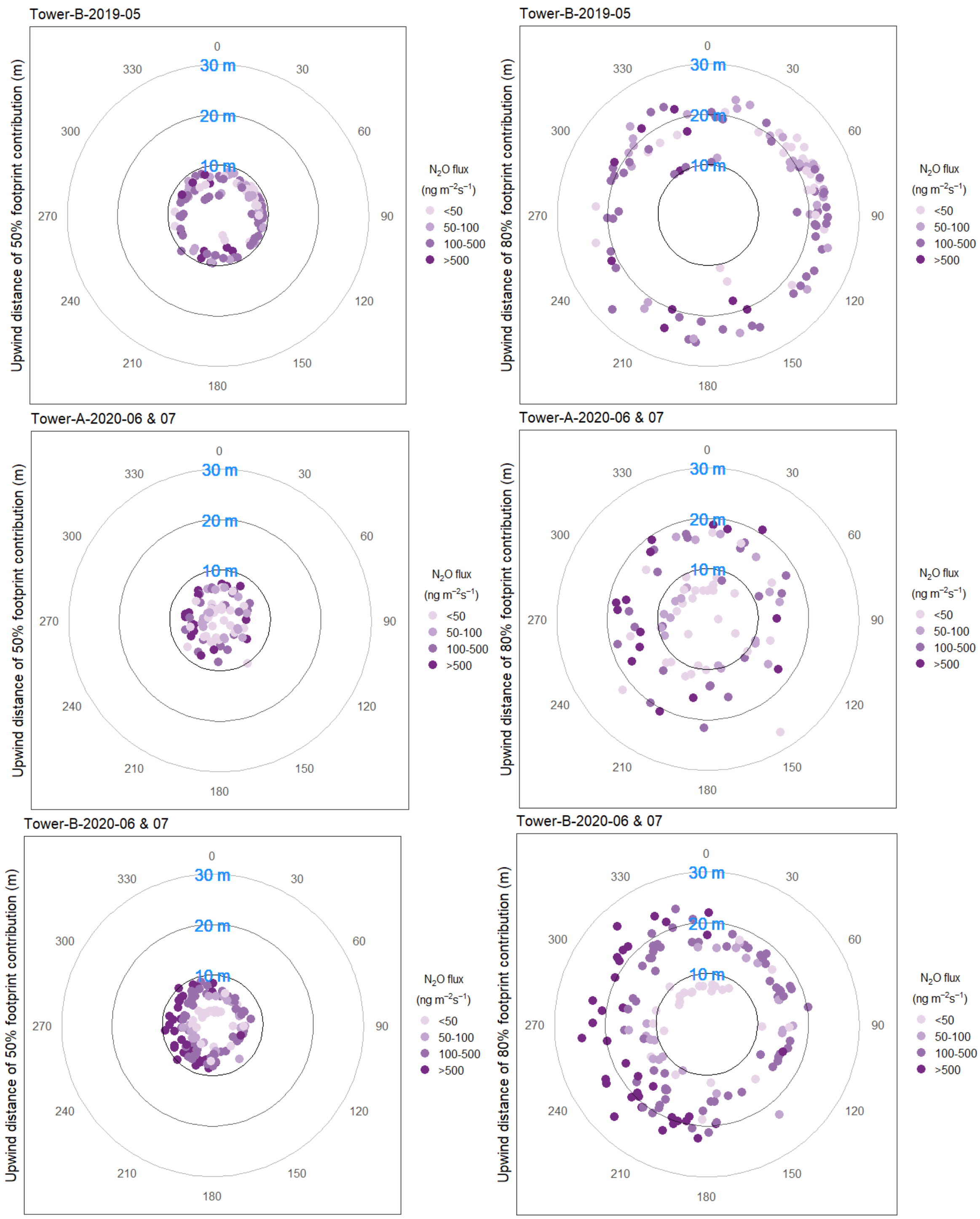

Figure C 4. Flux roses of towers A, B, and D using the observed half-hourly N_2O flux data during the peak emission periods in 2018, 2019, and 2020. The radii of the rings are 10 m, 20 m, and 30 m, and the tower is located at the center of the rings. In the figures on the left side, the distance of the dot from the center represents the 50% flux contribution extent. In the figures on the right, the distance of the dot from the center represents the 80% flux contribution extent. The color of the dots indicates N_2O flux magnitude ($ng/m^2/s$). The darker the dot is, the stronger emission it indicates.

Appendix D. Ch.4 Random errors in the flux gradient measurements.

For the flux gradient method, the relationship between the flux (F) and the concentration (C) difference is expressed as:

$$F = -K\frac{\partial C}{\partial z} \quad [1]$$

where K is the eddy diffusivity ($m^{-2}\ s^{-1}$) of the trace gas (e.g., N_2O or CH_4), and $\partial C/\partial z$ is the concentration gradient of this gas (kg m^{-4}). K was calculated as:

$$K = \frac{u_* \kappa (z_2 - z_1)}{\left[ln\left(\frac{z_2 - d}{z_1 - d}\right) - \psi_{h2} + \psi_{h1}\right]} \quad [2]$$

where u_* is the friction velocity, κ is the von Karman constant (= 0.41), d is the displacement height (= 0.67 times canopy height), and ψ_{h1} and ψ_{h2} are the integrated Monin-Obukhov similarity functions for sensible heat at sampling heights z_1 and z_2:

$$\psi = \begin{cases} -4.7\frac{z-d}{L} & Stable \\ 2\ln\left(\frac{1+x^2}{2}\right), x = \left(1 - 15\frac{z-d}{L}\right)^{\frac{1}{4}} & Unstable \\ 0 & Neutral \end{cases} \quad [3]$$

where L is the Obukhov length:

$$L = \frac{-u_*^3 T_v}{\kappa g \overline{w'T_v'}} \quad [4]$$

where T_v is the virtual temperature, g is the acceleration due to gravity, and $\overline{w'T_v'}$ is the kinematic virtual temperature flux which is related to sensible heat flux (H):

$$\overline{w'T_v'} = {}^{H}/_{\rho_a C_p} \quad [5]$$

where ρ_a is the air density and C_p is the heat capacity of air.

The random errors in the flux gradient measurements were determined by propagating the random error associated with each component of the flux gradient equation (K, ΔC, and Δz). The general equation for error propagation in a function $Q = f(x, y)$ is (Brown & Wagner-Riddle, 2017; J. Taylor, 1997):

$$\sigma_Q = \sqrt{\left(\frac{\partial f}{\partial x}\sigma_x\right)^2 + \left(\frac{\partial f}{\partial y}\sigma_y\right)^2 + 2Cov(x,y)\left(\frac{\partial f}{\partial x}\sigma_x\right)\left(\frac{\partial f}{\partial y}\sigma_y\right)} \qquad [6]$$

where the σ values stand for the random error of each term and the second term under the square root is the error of the covariances between terms, which are usually ignored (Mukherjee et al., 2014; Salesky & Chamecki, 2012).

Applying Eq. [6] to Eq. [1] and [2] resulted in:

$$\sigma_F = \sqrt{\left(\frac{\partial F}{\partial K}\sigma_K\right)^2 + \left(\frac{\partial F}{\partial \Delta C}\sigma_{\Delta C}\right)^2 + \left(\frac{\partial F}{\partial \Delta z}\sigma_{\Delta z}\right)^2} \qquad [7]$$

$$\sigma_K = \sqrt{(\frac{\partial K}{\partial u_*}\sigma_{u_*})^2 + (\frac{\partial K}{\partial \overline{w'T_v'}}\sigma_{\overline{w'T_v'}})^2 + (\frac{\partial K}{\partial T_v}\sigma_{T_v})^2} \qquad [8]$$

The parameter Δz (measurement height difference) was assumed to be constant ($\sigma_{\Delta z} = 0$) over the 30-min averaging period. Combining Eq. [7] and [8] led to:

$$\sigma_F = \sqrt{\left(\frac{\partial F}{\partial \Delta C}\sigma_{\Delta C}\right)^2 + \left(\frac{\partial F}{\partial u_*}\sigma_{u_*}\right)^2 + \left(\frac{\partial F}{\partial \overline{w'T_v'}}\sigma_{\overline{w'T_v'}}\right)^2 + \left(\frac{\partial F}{\partial T_v}\sigma_{T_v}\right)^2} \qquad [9]$$

Applying Eq. [6] to the equation of friction velocity $u_* = \left(\overline{u'w'}^2 + \overline{v'w'}^2\right)^{0.25}$ gives the random error of u_*:

$$\sigma_{u_*} = \sqrt{\left(\frac{\partial u_*}{\partial \overline{u'w'}}\sigma_{\overline{u'w'}}\right)^2 + \left(\frac{\partial u_*}{\partial \overline{v'w'}}\sigma_{\overline{v'w'}}\right)^2} \qquad [10]$$

where $\overline{u'w'}$ and $\overline{v'w'}$ are the covariance between the horizontal (u), the transverse (v), and the vertical (w) wind speeds. Random errors of the variables $\overline{w'T_v'}$, T_v, $\overline{u'w'}$ and $\overline{v'w'}$ were calculated using the filtering method mentioned in Salesky and Chamecki (2012).

The random error in the trace gas concentration gradient ($\sigma_{\Delta C}$) was calculated as (Waldo et al., 2019):

$$\sigma_{\Delta C} = \sqrt{\frac{{\sigma_{z_1}}^2}{n_1} + \frac{{\sigma_{z_2}}^2}{n_2}} \qquad [11]$$

where σ_{z1} and σ_{z2} are the standard deviations of the 30-min concentration measurements at sampling heights z_1 and z_2, and n_1 and n_2 are the numbers of measurements taken at the two heights in the 30-min period.

Statistical details about the random error (σ) and fractional error (ε, also called relative error) of each component in the 30-min N_2O flux calculation for May 2019 are presented in Table D 1 as an example. The variation in the fractional error of N_2O concentration difference (ΔC) was the major contributor to the variation in the fractional error of N_2O flux (F). Figure D1 contains boxplots of the fractional error for each term in the flux gradient equation for the same period. The random error in the 30-min averaged turbulence covariance $\overline{v'w'}$ contributed most to the random error in the flux measurements, with a median fractional error of 40%. The large fractional error in $\overline{v'w'}$ can be attributed to the fact that the variable in question had many near-zero values. The second largest contributor the random error of the 30-min N_2O fluxes was the random error in the measurement of the N_2O concentration difference ΔC.

Table D 1 Statistical summary of each component in the flux gradient equation and random error and fractional error associated with each term. S.D.: standard deviation. Fractional error ε = random error σ/ |x|, where x is the measured variable. All variables are measured/calculated in a time interval of 30 minutes.

	ΔC (ppbv)	$\overline{u'w'}$ ($m^2\ s^{-2}$)	$\overline{v'w'}$ ($m^2\ s^{-2}$)	$\overline{w'T_v'}$ ($m\ K\ s^{-1}$)	T_v (K)	u_* ($m\ s^{-1}$)	K ($m^2\ s^{-1}$)	F (ng N $m^{-2}\ s^{-1}$)
Median	0.092	0.006	0.002	0.015	293.7	0.228	0.089	16.85
Mean	0.299	-0.012	0.001	0.031	293.9	0.239	0.088	45.0
S.D.	0.574	0.079	0.023	0.044	5.88	0.091	0.036	82.55
Random Error (σ)								
Median	0.020	0.006	0.005	0.002	0.296	0.094	0.036	10.52
Mean	0.045	0.007	0.006	0.003	0.353	0.154	0.060	29.60
S.D.	0.081	0.004	0.004	0.002	0.231	0.187	0.073	58.15
Fractional Error (ε)								
Median	0.206	0.113	0.399	0.084	0.015	0.429	0.438	0.619
Mean	0.975	0.143	0.598	0.131	0.017	0.631	0.645	1.394
S.D.	3.483	0.119	0.591	0.167	0.010	0.587	0.590	3.450

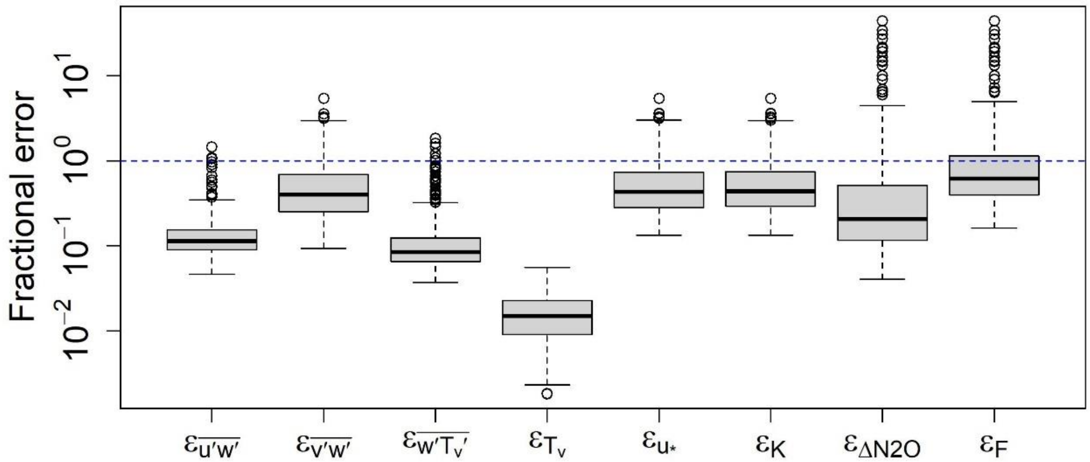

Figure D 1. Boxplots of the fractional errors of the components in the flux calculation equation for May 2019. The dashed line indicates fractional error = 1.The figure is adapted from (Brown & Wagner-Riddle, 2017).

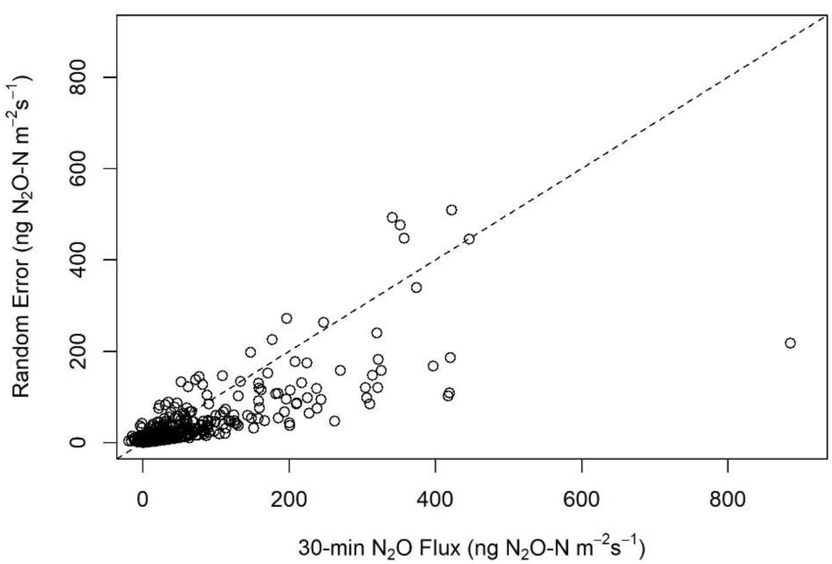

Figure D 2. The 30-min N_2O flux (ng N_2O-N m^{-2} s^{-1}) and its random error (ng N_2O-N m^{-2} s^{-1}) for the measurement period of May 2019. The dashed line is the 1:1 line.

Appendix E. Ch.2 Cross-calibration of the Decagon 5TE water content, EC, and temperature sensors.

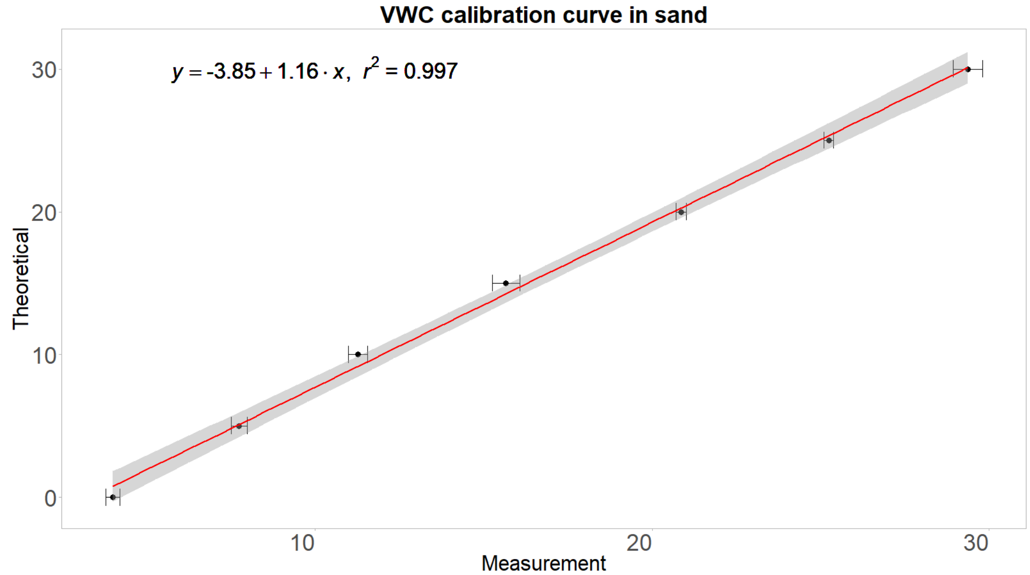

Figure E 1. Cross calibration for volumetric water content (VWC) in sand between four Decagon 5TE water content, EC, and temperature sensors. The measured VWC values (%) are on the x-axis and the theoretical VWC values (%) based on calculations are on the y-axis. The grey area represents the 95% confidence interval for predictions from the linear regression ("red line"). Error bars stand for standard deviations of the four sensors' measurements.

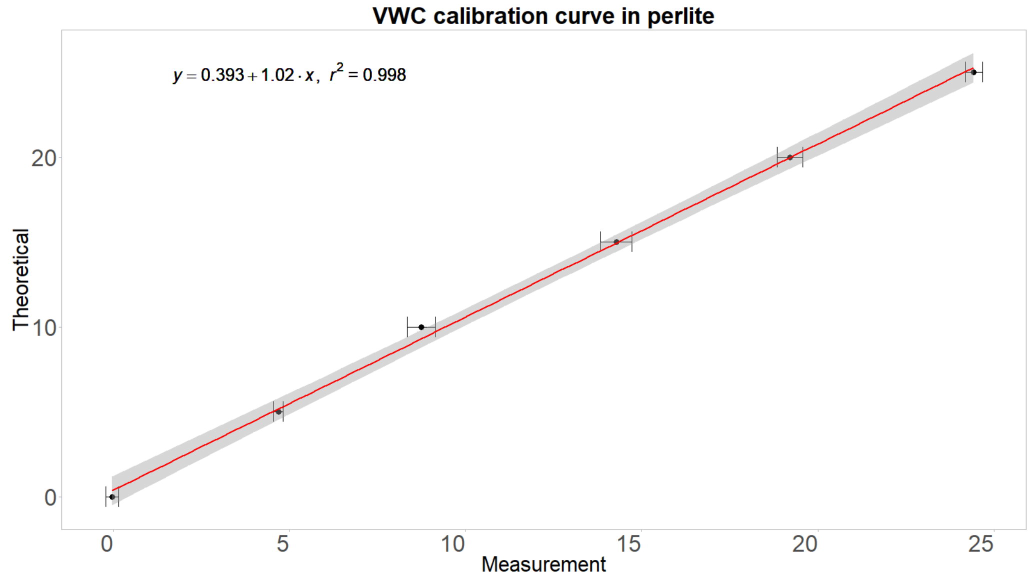

Figure E 2. Cross calibration for volumetric water content (VWC) in perlite between four Decagon 5TE water content, EC, and temperature sensors. The measured VWC values (%) are on the x-axis and the theoretical VWC values (%) based on calculations are on the y-axis. The grey area represents the 95% confidence interval for predictions from the linear regression ("red line"). Error bars stand for standard deviations of the four sensors' measurements.

Appendix F. Ch.2 & Ch.3 Vertical profiles of soil moisture and temperature using the Decagon 5TE water content, EC, and temperature sensors.

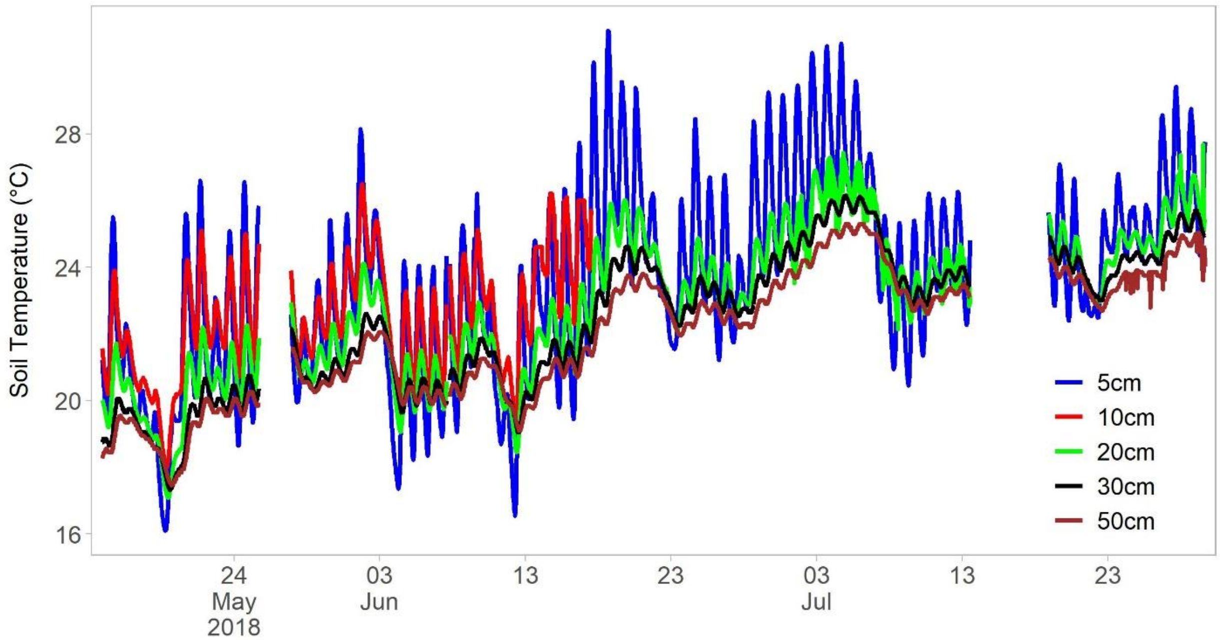

Figure F 1. Soil temperature at five depths (5 cm, 10 cm, 20 cm, 30 cm, and 50 cm) measured by the Decagon 5TE water content and temperature sensors near tower A from May 14 to July 29 in 2018.

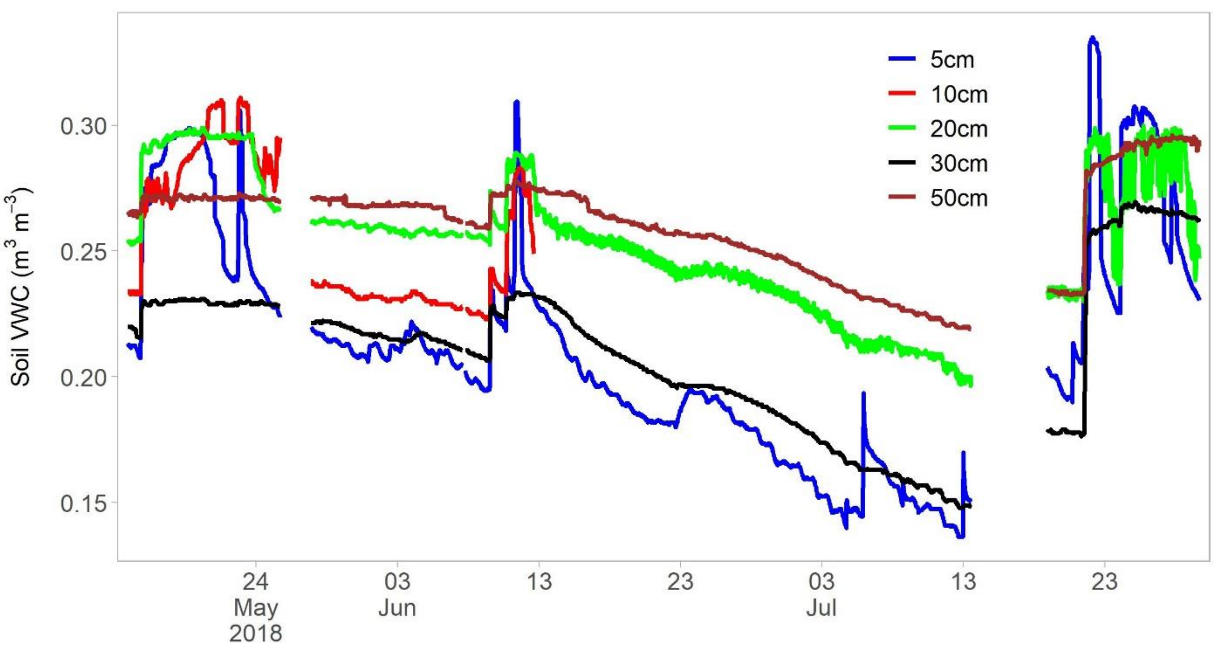

Figure F 2. Soil volumetric water content (VWC) at five depths (5 cm, 10 cm, 20 cm, 30 cm, and 50 cm) measured by the Decagon 5TE water content and temperature sensors near tower A from May 14 to July 29 in 2018.

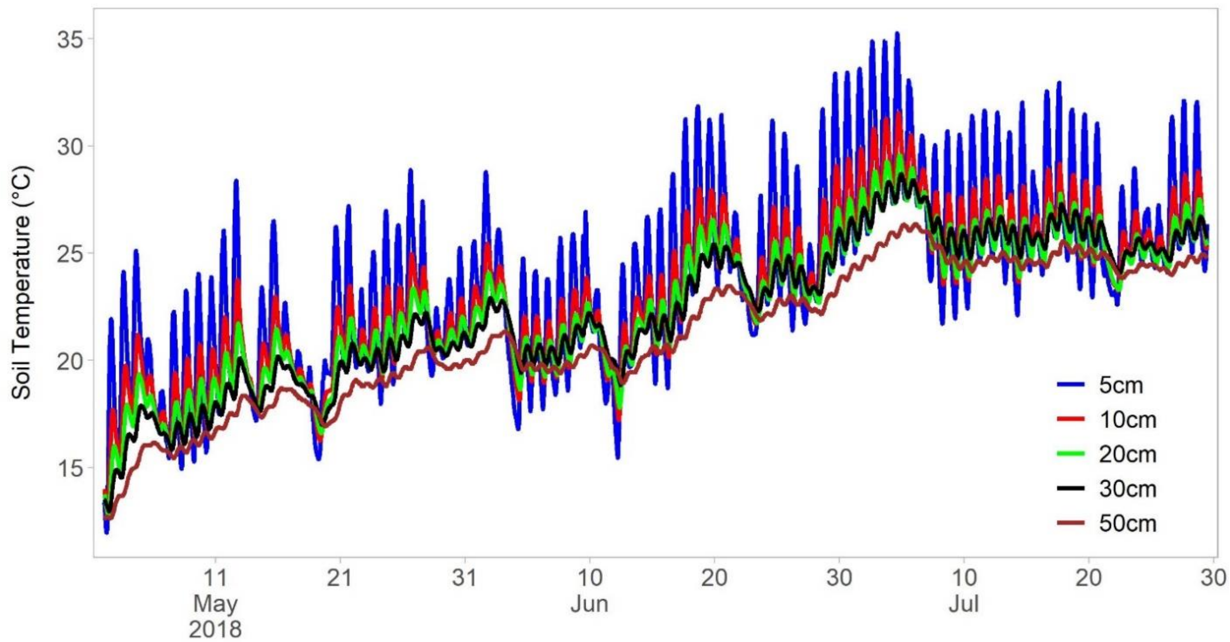

Figure F 3. Soil temperature at five depths (5 cm, 10 cm, 20 cm, 30 cm, and 50 cm) measured by the Decagon 5TE water content and temperature sensors near tower C from May 2 to July 29 in 2018.

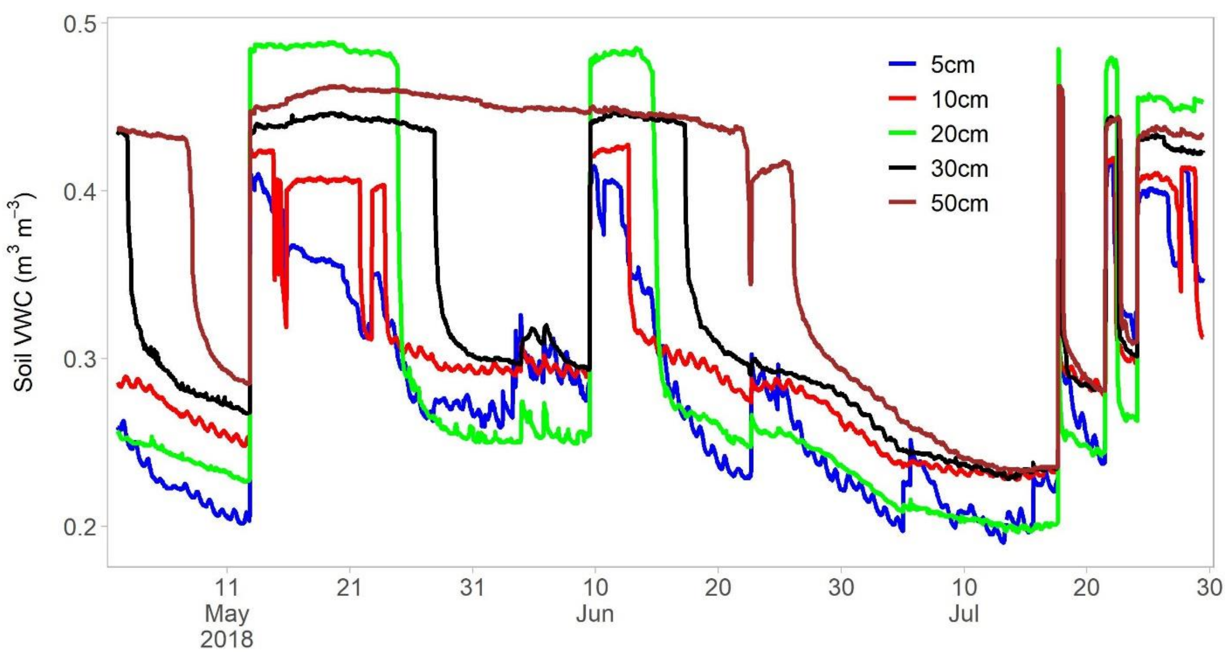

Figure F 4. Soil volumetric water content (VWC) at five depths (5 cm, 10 cm, 20 cm, 30 cm, and 50 cm) measured by the Decagon 5TE water content and temperature sensors near tower C from May 2 to July 29 in 2018.

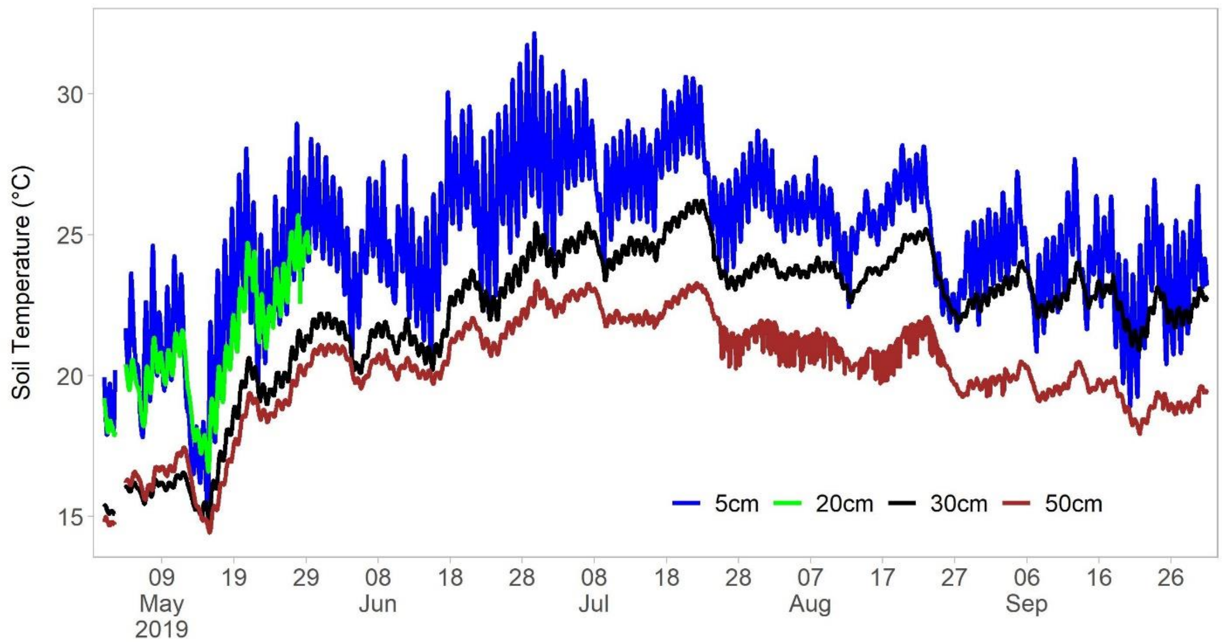

Figure F 5. Soil temperature at four depths (5 cm, 20 cm, 30 cm, and 50 cm) measured by the Decagon 5TE water content and temperature sensors near tower A from May 1 to September 30 in 2019.

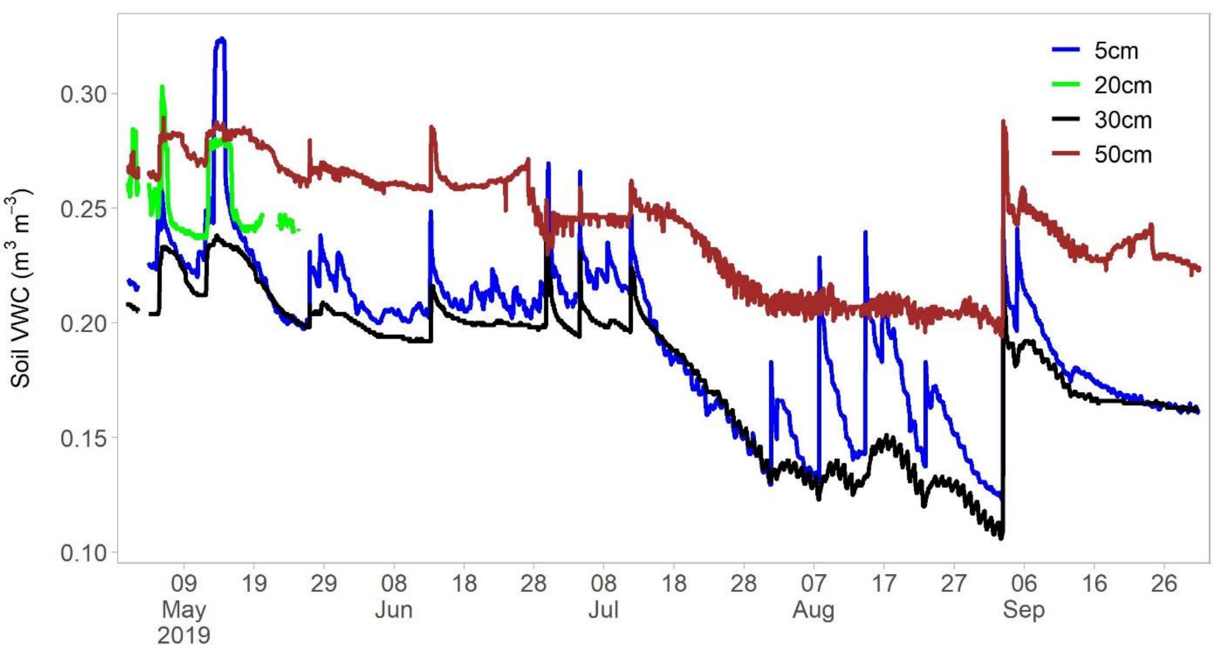

Figure F 6. Soil volumetric water content (VWC) at four depths (5 cm, 20 cm, 30 cm, and 50 cm) measured by the Decagon 5TE water content and temperature sensors near tower A from May 1 to September 30 in 2019.

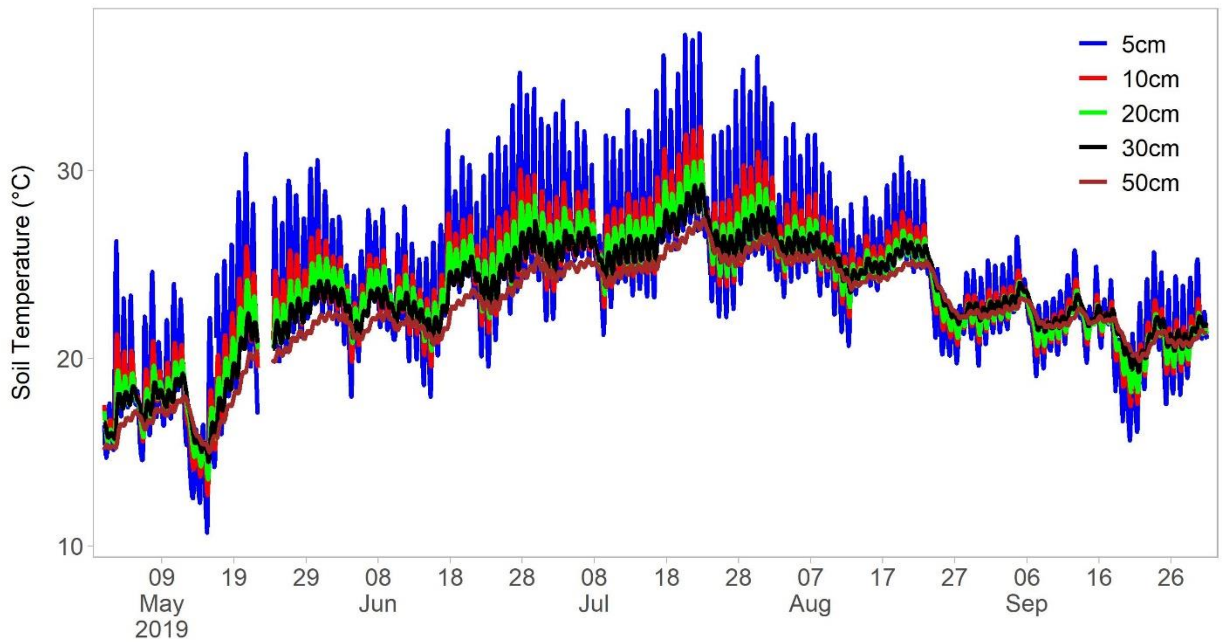

Figure F 7. Soil temperature at five depths (5 cm, 10 cm, 20 cm, 30 cm, and 50 cm) measured by the Decagon 5TE water content and temperature sensors near tower C from May 1 to September 30 in 2019.

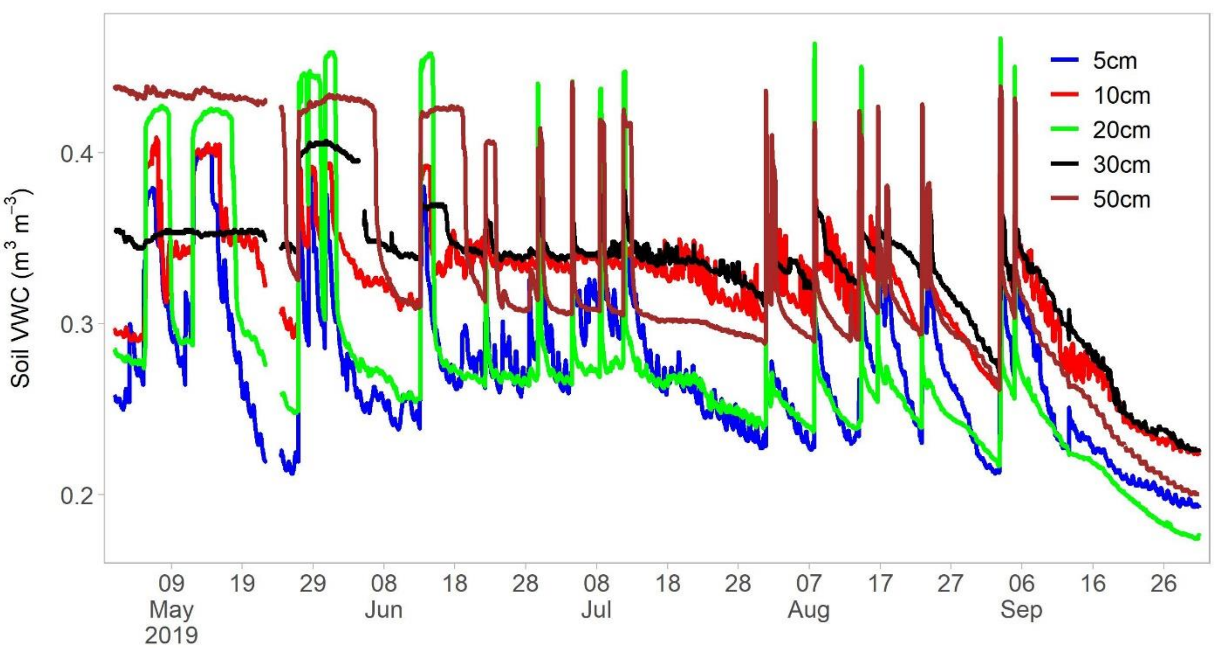

Figure F 8. Soil volumetric water content (VWC) at five depths (5 cm, 10 cm, 20 cm, 30 cm, and 50 cm) measured by the Decagon 5TE water content and temperature sensors near tower C from May 1 to September 30 in 2019.

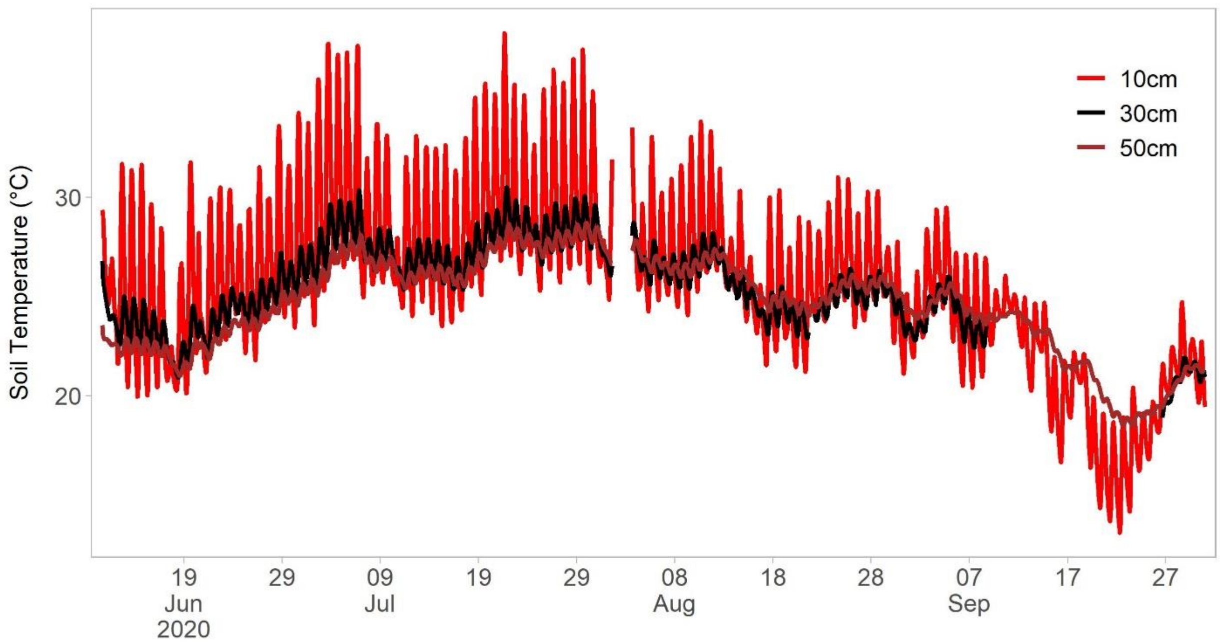

Figure F 9. Soil temperature at three depths (10 cm, 30 cm, and 50 cm) measured by the Decagon 5TE water content and temperature sensors near tower C from June 10 to September 30 in 2020.

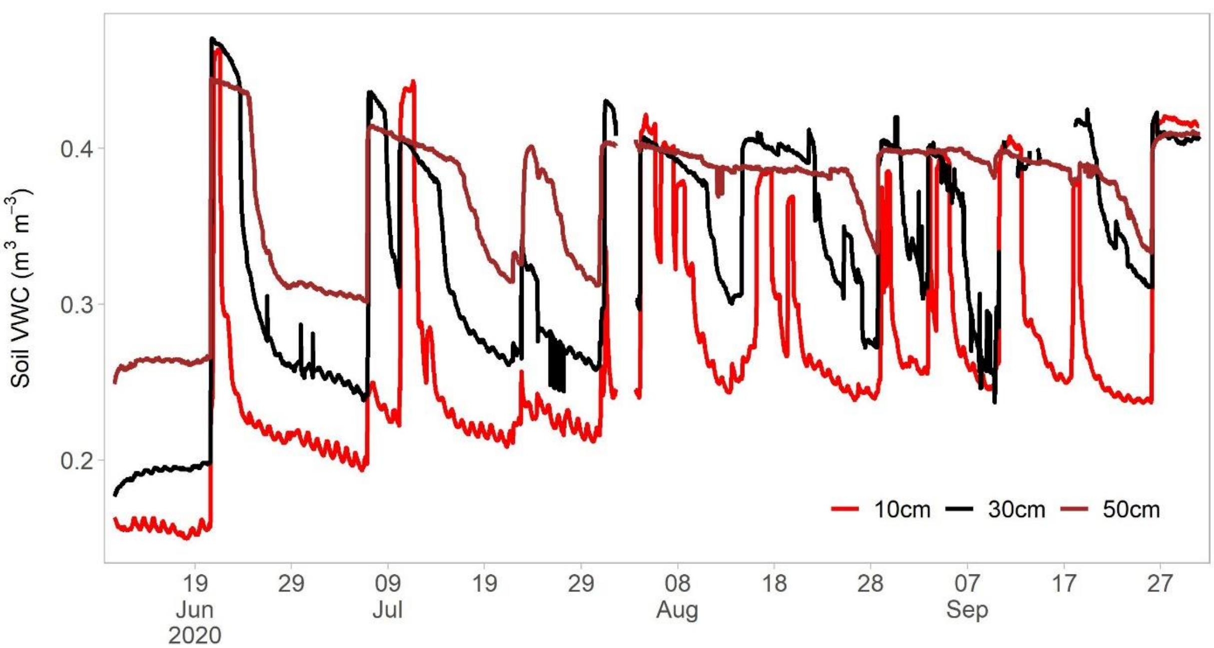

Figure F 10. Soil volumetric water content (VWC) at three depths (10 cm, 30 cm, and 50 cm) measured by the Decagon 5TE water content and temperature sensors near tower C from June 10 to September 30 in 2020.

Bibliography

Abernethy, S., O'Connor, F. M., Jones, C. D., & Jackson, R. B. (2021). Methane removal and the proportional reductions in surface temperature and ozone. *Philosophical Transactions of the Royal Society A: Mathematical, Physical and Engineering Sciences*, *379*(2210). https://doi.org/10.1098/rsta.2021.0104

Ambus, P., Jensen, J. M., Priemé, A., Pilegaard, K., & Kjøller, A. (2001). Assessment of CH4 and N2O fluxes in a Danish beech (Fagus sylvatica) forest and an adjacent N-fertilised barley (Hordeum vulgare) field: Effects of sewage sludge amendments. *Nutrient Cycling in Agroecosystems*, *60*(1–3), 15–21. https://doi.org/10.1023/A:1012612211933

Ator, S. W., & Denver, J. M. (2015). *Understanding Nutrients in the Chesapeake Bay Watershed and Implications for Management and Restoration — the Eastern Shore Circular 1406* (Issue May). https://doi.org/10.3133/cir1406

Beck, M. W. (2018). *NeuralNetTools: Visualization and Analysis Tools for Neural Networks*. *85*(11), 1–20. https://doi.org/10.18637/jss.v085.i11

Bigaignon, L., Fieuzal, R., Delon, C., & Tallec, T. (2020). Agricultural and Forest Meteorology Combination of two methodologies , artificial neural network and linear interpolation , to gap-fill daily nitrous oxide flux measurements. *Agricultural and Forest Meteorology*, *291*(January), 108037. https://doi.org/10.1016/j.agrformet.2020.108037

Brown, S. E., & Wagner-Riddle, C. (2017). Assessment of random errors in multi-plot nitrous oxide flux gradient measurements. *Agricultural and Forest Meteorology*, *242*(April), 10–20. https://doi.org/10.1016/j.agrformet.2017.04.005

Cai, Y., Ding, W., & Luo, J. (2013). Nitrous oxide emissions from Chinese maize-wheat rotation systems: A 3-year field measurement. *Atmospheric Environment*, *65*, 112–122.

https://doi.org/10.1016/j.atmosenv.2012.10.038

Cai, Z., Xing, G., Yan, X., Xu, H., Tsuruta, H., Yagi, K., & Minami, K. (1997). Methane and nitrous oxide emissions from rice paddy fields as affected by nitrogen fertilisers and water management. *Plant and Soil*, *196*(1), 7–14. https://doi.org/10.1023/A:1004263405020

Carstensen, M. V., Hashemi, F., Hoffmann, C. C., Zak, D., Audet, J., & Kronvang, B. (2020). Efficiency of mitigation measures targeting nutrient losses from agricultural drainage systems: A review. *Ambio*, *49*(11), 1820–1837. https://doi.org/10.1007/s13280-020-01345-5

Chadwick, D. R., Cardenas, L., Misselbrook, T. H., Smith, K. A., Rees, R. M., Watson, C. J., Mcgeough, K. L., Williams, J. R., Cloy, J. M., Thorman, R. E., & Dhanoa, M. S. (2014). Optimizing chamber methods for measuring nitrous oxide emissions from plot-based agricultural experiments. *European Journal of Soil Science*, *65*(2), 295–307. https://doi.org/10.1111/ejss.12117

Chan, A. S. K., & Parkin, T. B. (2001). Effect of Land Use on Methane Flux from Soil. *Journal of Environmental Quality*, *30*(3), 786–797. https://doi.org/10.2134/jeq2001.303786x

Chantigny, M. H., Pelster, D. E., Perron, M. H., Rochette, P., Angers, D. A., Parent, L. É., Massé, D., & Ziadi, N. (2013). Nitrous oxide emissions from clayey soils amended with paper sludges and biosolids of separated pig slurry. *Journal of Environmental Quality*, *42*(1), 30–39. https://doi.org/10.2134/jeq2012.0196

Chapuis-lardy, L., Wrage, N., Metay, A., Chotte, J. L., & Bernoux, M. (2007). Soils, a sink for N2O? A review. *Global Change Biology*, *13*(1), 1–17. https://doi.org/10.1111/j.1365-2486.2006.01280.x

Charles, A., Rochette, P., Whalen, J. K., Angers, D. A., Chantigny, M. H., & Bertrand, N. (2017). Global nitrous oxide emission factors from agricultural soils after addition of organic amendments: A meta-analysis. *Agriculture, Ecosystems and Environment*, *236*(3), 88–98. https://doi.org/10.1016/j.agee.2016.11.021

Cooper, R. L., Fausey, N. R., & Streeter, J. G. (1991). Yield Potential of Soybean Grown under a Subirrigation/Drainage Water Management System. *Agronomy Journal*, *83*(5), 884–887. https://doi.org/https://doi.org/10.2134/agronj1991.00021962008300050021x

Cowan, N. J., Levy, P. E., Famulari, D., Anderson, M., Drewer, J., Carozzi, M., Reay, D. S., & Skiba, U. M. (2016). The influence of tillage on N2O fluxes from an intensively managed grazed grassland in Scotland. *Biogeosciences*, *13*(16), 4811–4821. https://doi.org/10.5194/bg-13-4811-2016

Crézé, C. M., & Madramootoo, C. A. (2019). Water table management and fertilizer application impacts on CO 2 , N 2 O and CH 4 fluxes in a corn agro-ecosystem. *Scientific Reports*, *9*(1), 1–13. https://doi.org/10.1038/s41598-019-39046-z

Datta, A., Smith, P., & Lal, R. (2013). Effects of long-term tillage and drainage treatments on greenhouse gas fluxes from a corn field during the fallow period. *Agriculture, Ecosystems and Environment*, *171*, 112–123. https://doi.org/10.1016/j.agee.2013.03.014

De Klein, C. a. M., & Harvey, M. (2015). Nitrous Oxide Chamber Methodology Guidelines. In *Global Reserch Alliance on Agricultural Greenhouse Gases* (Issue December).

De Rosa, D., Rowlings, D. W., Biala, J., Scheer, C., Basso, B., McGree, J., & Grace, P. R. (2016). Effect of organic and mineral N fertilizers on N2O emissions from an intensive vegetable rotation. *Biology and Fertility of Soils*, *52*(6), 895–908. https://doi.org/10.1007/s00374-016-1117-5

Delbecq, B. A., Brown, J. P., Florax, R. J. G. M., Kladivko, E. J., Nistor, A. P., & Lowenberg-DeBoer, J. M. (2012). The impact of drainage water management technology on corn yields. *Agronomy Journal*, *104*(4), 1100–1109. https://doi.org/10.2134/agronj2012.0003

Dengel, S., Zona, D., Sachs, T., Aurela, M., Jammet, M., Parmentier, F. J. W., Oechel, W., & Vesala, T. (2013). Testing the applicability of neural networks as a gap-filling method using CH4 flux data from high latitude wetlands. *Biogeosciences, 10*(12), 8185–8200. https://doi.org/10.5194/bg-10-8185-2013

Dentener, F., Stevenson, D., Cofala, J., Mechler, R., Amann, M., Bergamaschi, P., Raes, F., & Derwent, R. (2005). The impact of air pollutant and methane emission controls on tropospheric ozone and radiative forcing: CTM calculations for the period 1990-2030. *Atmospheric Chemistry and Physics*, *5*(7), 1731–1755. https://doi.org/10.5194/acp-5-1731-2005

Drury, C. F., Tan, C. S., Welacky, T. W., Reynolds, W. D., Zhang, T. Q., Oloya, T. O., McLaughlin, N. B., & Gaynor, J. D. (2014). Reducing Nitrate Loss in Tile Drainage Water with Cover Crops and Water-Table Management Systems. *Journal of Environmental Quality*, *43*(2), 587–598. https://doi.org/10.2134/jeq2012.0495

Elmi, A., Burton, D., Gordon, R., & Madramootoo, C. (2005). Impacts of water table management on N2O and N2 from a sandy loam soil in Southwestern Quebec, Canada. *Nutrient Cycling in Agroecosystems*, *72*(3), 229–240. https://doi.org/10.1007/s10705-005-2920-9

Environmental Protection Agency. (2022). *Basic Information about Biosolids*. https://www.epa.gov/biosolids/basic-information-about-biosolids

Falge, E., Baldocchi, D., Olson, R., Anthoni, P., Aubinet, M., Bernhofer, C., Burba, G., Ceulemans, R., Clement, R., Dolman, H., Granier, A., Gross, P., Grünwald, T., Hollinger, D., Jensen, N. O., Katul, G., Keronen, P., Kowalski, A., Lai, C. T., … Wofsy, S. (2001).

Gap filling strategies for defensible annual sums of net ecosystem exchange. *Agricultural and Forest Meteorology*, *107*(1), 43–69. https://doi.org/10.1016/S0168-1923(00)00225-2

Fernández, F. G., Venterea, R. T., & Fabrizzi, K. P. (2016). Corn Nitrogen Management Influences Nitrous Oxide Emissions in Drained and Undrained Soils. *Journal of Environmental Quality*, *45*(6), 1847–1855. https://doi.org/10.2134/jeq2016.06.0237

Firestone, M. K. (1982). Biological Denitrification. In F. J. Stevenson (Ed.), *Nitrogen Agricultural Soils. Agron. Monogr. 22.* (pp. 289–326). American Society Agronomy, Crop Science Society of America and Soil Science Society of American.

Firestone, M. K., & Davidson, E. A. (1989). Micorbiological basis of NO and N2O production and consumption in soil. *Exchange of Trace Gases between Terrestrial Ecosystems and the Atmosphere*, *January 1989*, 7–21.

Fisher, T. R., Fox, R. J., Gustafson, A. B., Koontz, E., Lepori-Bui, M., & Lewis, J. (2021). Localized Water Quality Improvement in the Choptank Estuary, a Tributary of Chesapeake Bay. *Estuaries and Coasts*, *44*(5), 1274–1293. https://doi.org/10.1007/s12237-020-00872-4

Fisher, T. R., Jordan, T. E., Staver, K. W., Gustafson, A. B., Koskelo, A. I., Fox, R. J., Sutton, A. J., Kana, T., Beckert, K. A., Stone, J. P., McCarty, G., & Lang, M. (2010). The choptank basin in transition: Intensifying agriculture, slow urbanization, and estuarine eutrophication. *Coastal Lagoons: Critical Habitats of Environmental Change*, 135–165. https://doi.org/10.1201/EBK1420088304

Foken, T., Göockede, M., Mauder, M., Mahrt, L., Amiro, B., & Munger, W. (2004). Post-Field Data Quality Control. In X. Lee, W. Massman, & B. Law (Eds.), *Handbook of Micrometeorology: A Guide for Surface Flux Measurement and Analysis* (pp. 181–208). Springer Netherlands. https://doi.org/10.1007/1-4020-2265-4_9

Garson, G. D. (1991). Interpreting Neural-Network Connection Weights. *AI Expert*, *6*(4), 46–51.

Goh, A. T. C. (1995). Back-propagation neural networks for modeling complex systems. *Artificial Intelligence in Engineering*, *9*(3), 143–151. https://doi.org/https://doi.org/10.1016/0954-1810(94)00011-S

Groffman, P. M., Butterbach-Bahl, K., Fulweiler, R. W., Gold, A. J., Morse, J. L., Stander, E. K., Tague, C., Tonitto, C., & Vidon, P. (2009). Challenges to incorporating spatially and temporally explicit phenomena (hotspots and hot moments) in denitrification models. *Biogeochemistry*, *93*(1–2), 49–77. https://doi.org/10.1007/s10533-008-9277-5

Grossel, A., Nicoullaud, B., Bourennane, H., Lacoste, M., Guimbaud, C., Robert, C., & Hénault, C. (2016). The effect of tile-drainage on nitrous oxide emissions from soils and drainage streams in a cropped landscape in Central France. *Agriculture, Ecosystems and Environment*, *230*, 251–260. https://doi.org/10.1016/j.agee.2016.06.015

Hagedorn, J. G., Davidson, E. A., Fisher, T. R., Fox, R. J., Zhu, Q., Gustafson, A. B., Koontz, E., Castro, M. S., & Lewis, J. (2022). Effects of Drainage Water Management in a Corn–Soy Rotation on Soil N2O and CH4 Fluxes. *Nitrogen*, *3*, 128–148. https://doi.org/10.1515/intag-2017-0045

Hall, S. J., Reyes, L., Huang, W., & Homyak, P. M. (2018). Wet Spots as Hotspots: Moisture Responses of Nitric and Nitrous Oxide Emissions From Poorly Drained Agricultural Soils. *Journal of Geophysical Research: Biogeosciences*, *123*(12), 3589–3602. https://doi.org/10.1029/2018JG004629

Hargreaves, K. J., Wienhold, F. G., Klemedtsson, L., Arah, J. R. M., Beverland, I. J., Fowler, D., Galle, B., Griffith, D. W. T., Skiba, U., Smith, K. A., Welling, M., & Harris, G. W. (1996). Measurement of nitrous oxide emission from agricultural land using micrometeorological methods. *Atmospheric Environment*, *30*(10–11), 1563–1571. https://doi.org/10.1016/1352-2310(95)00468-8

Hensen, A., Skiba, U., & Famulari, D. (2013). Low cost and state of the art methods to measure nitrous oxide emissions. *Environmental Research Letters*, *8*(2). https://doi.org/10.1088/1748-9326/8/2/025022

Hergoualc'h, K., Mueller, N., Bernoux, M., Kasimir, Ä., van der Weerden, T. J., & Ogle, S. M. (2021). Improved accuracy and reduced uncertainty in greenhouse gas inventories by refining the IPCC emission factor for direct N2O emissions from nitrogen inputs to managed soils. *Global Change Biology*, *27*(24), 6536–6550. https://doi.org/10.1111/gcb.15884

Horst, T. W. (1999). *The footprint for estimation of atmosphere-surface exchange fluxes by profile techniques*. *July 1998*, 171–188.

Horst, T. W., & Weil, J. C. (1994). How far is far enough? The fetch requirements for micrometeorological measurement of surface fluxes. In *Journal of Atmospheric & Oceanic Technology* (Vol. 11, Issue 4 part 1, pp. 1018–1025). https://doi.org/10.1175/1520-0426(1994)011<1018:hfifet>2.0.co;2

Huang, H., Wang, J., Hui, D., Miller, D. R., Bhattarai, S., Dennis, S., Smart, D., Sammis, T., & Reddy, K. C. (2014). Nitrous oxide emissions from a commercial cornfield (Zea mays) measured using the eddy covariance technique. *Atmospheric Chemistry and Physics*, *14*(23), 12839–12854. https://doi.org/10.5194/acp-14-12839-2014

IPCC. (2014). *Climate Change 2014: Synthesis Report. Contribution of Working Groups I, II and III to the Fifth Assessment Report of the Intergovernmental Panel on Climate Change [Core Writing Team, R.K. Pachauri and L.A. Meyer (eds.)]*.

https://doi.org/10.1017/CBO9781139177245.003

IPCC. (2019). N2O Emissions From Managed Soils, and Co2 Emissions From Lime and Urea Application. *2019 Refinement to the 2006 IPCC Guidelines for National Greenhouse Gas Inventories*, 1–48.

Järvi, L., Nordbo, A., Junninen, H., Riikonen, A., Moilanen, J., Nikinmaa, E., & Vesala, T. (2012). Seasonal and annual variation of carbon dioxide surface fluxes in Helsinki, Finland, in 2006-2010. *Atmospheric Chemistry and Physics*, *12*(18), 8475–8489. https://doi.org/10.5194/acp-12-8475-2012

Jones, S. K., Famulari, D., Di Marco, C. F., Nemitz, E., Skiba, U. M., Rees, R. M., & Sutton, M. A. (2011). Nitrous oxide emissions from managed grassland: A comparison of eddy covariance and static chamber measurements. *Atmospheric Measurement Techniques*, *4*(10), 2179–2194. https://doi.org/10.5194/amt-4-2179-2011

Jones, S. K., Rees, R. M., Skiba, U. M., & Ball, B. C. (2007). Influence of organic and mineral N fertiliser on N2O fluxes from a temperate grassland. *Agriculture, Ecosystems and Environment*, *121*(1–2), 74–83. https://doi.org/10.1016/j.agee.2006.12.006

Kljun, N., Calanca, P., Rotach, M. W., & Schmid, H. P. (2015). A simple two-dimensional parameterisation for Flux Footprint Prediction (FFP). *Geoscientific Model Development*, *8*(11), 3695–3713. https://doi.org/10.5194/gmd-8-3695-2015

Kroon, P. S., Hensen, A., Jonker, H. J. J., Zahniser, M. S., Van't Veen, W. H., & Vermeiden, A. T. (2007). Suitability of quantum cascade laser spectroscopy for CH4 and N2O eddy covariance flux measurements. *Biogeosciences*, *4*(5), 715–728. https://doi.org/10.5194/bg-4-715-2007

Kumar, S., Nakajima, T., Kadono, A., Lal, R., & Fausey, N. (2014). Long-term tillage and drainage influences on greenhouse gas fluxes from a poorly drained soil of central Ohio. *Journal of Soil and Water Conservation*, *69*(6), 553–563. https://doi.org/10.2489/jswc.69.6.553

Laubach, J., Barthel, M., Fraser, A., Hunt, J. E., & Griffith, D. W. T. (2016). Combining two complementary micrometeorological methods to measure CH4 and N2O fluxes over pasture. *Biogeosciences*, *13*(4), 1309–1327. https://doi.org/10.5194/bg-13-1309-2016

Laville, P., Jambert, C., Cellier, P., & Delmas, R. (1999). Nitrous oxide fluxes from a fertilised maize crop using micrometeorological and chamber methods. *Agricultural and Forest Meteorology*, *96*(1–3), 19–38. https://doi.org/10.1016/S0168-1923(99)00054-4

Liang, L. L., Campbell, D. I., Wall, A. M., & Schipper, L. A. (2018). Nitrous oxide fluxes determined by continuous eddy covariance measurements from intensively grazed pastures: Temporal patterns and environmental controls. *Agriculture, Ecosystems and Environment*, *268*(May), 171–180. https://doi.org/10.1016/j.agee.2018.09.010

Mauder, M., & Foken, T. (2015). Documentation and Instruction Manual of the Eddy-Covariance Software Package TK3. *Arbeitsergebnisse, Universität Bayreuth, Abt. Mikrometeorologie (ISSN 1614-8916)*, *62*, 62.

Maynard, D. G., Kalra, Y. P., & Crumbaugh, J. A. (1993). Nitrate and Exchangeable Ammonium Nitrogen. In *Soil Sampling and Methods of Analysis* (pp. 25–31). CRC Press: Boca Raton, FL, USA.

McMillan, A. M. S., Harvey, M. J., Martin, R. J., Bromley, A. M., Evans, M. J., Mukherjee, S., & Laubach, J. (2014). The detectability of nitrous oxide mitigation efficacy in intensively grazed pastures using a multiple-plot micrometeorological technique. *Atmospheric Measurement Techniques*, *7*(5), 1169–1184. https://doi.org/10.5194/amt-7-1169-2014

Merbold, L., Eugster, W., Stieger, J., Zahniser, M., Nelson, D., & Buchmann, N. (2014). Greenhouse gas budget (CO2, CH4 and N2O) of intensively managed grassland following restoration. *Global Change Biology*, *20*(6), 1913–1928. https://doi.org/10.1111/gcb.12518

Meredith, L. K., Commane, R., Munger, J. W., Dunn, A., Tang, J., Wofsy, S. C., & Prinn, R. G. (2014). Ecosystem fluxes of hydrogen: A comparison of flux-gradient methods. *Atmospheric Measurement Techniques*, *7*(9), 2787–2805. https://doi.org/10.5194/amt-7-2787-2014

Mishurov, M., & Kiely, G. (2011). Gap-filling techniques for the annual sums of nitrous oxide fluxes. *Agricultural and Forest Meteorology*, *151*(12), 1763–1767. https://doi.org/10.1016/j.agrformet.2011.07.014

Moffat, A. M., Papale, D., Reichstein, M., Hollinger, D. Y., Richardson, A. D., Barr, A. G., Beckstein, C., Braswell, B. H., Churkina, G., Desai, A. R., Falge, E., Gove, J. H., Heimann, M., Hui, D., Jarvis, A. J., Kattge, J., Noormets, A., & Stauch, V. J. (2007). Comprehensive comparison of gap-filling techniques for eddy covariance net carbon fluxes. *Agricultural and Forest Meteorology*, *147*(3–4), 209–232. https://doi.org/10.1016/j.agrformet.2007.08.011

Moncrieff, J. B., Massheder, J. M., De Bruin, H., Elbers, J., Friborg, T., Heusinkveld, B., Kabat, P., Scott, S., Soegaard, H., & Verhoef, A. (1997). A system to measure surface fluxes of momentum, sensible heat, water vapour and carbon dioxide. *Journal of Hydrology*, *188–189*(1–4), 589–611. https://doi.org/10.1016/S0022-1694(96)03194-0

Moncrieff, J., Clement, R., Finnigan, J., & Meyers, T. (2004). Averaging, Detrending, and Filtering of Eddy Covariance Time Series. In X. Lee, W. Massman, & B. Law (Eds.), *Handbook of Micrometeorology* (pp. 7–31). Springer Netherlands.

https://doi.org/10.1007/1-4020-2265-4_2

Mosier, A. R., Halvorson, A. D., Reule, C. A., & Liu, X. J. (2006). Net global warming potential and greenhouse gas intensity. *Journal of Environmental Quality*, *35*(4), 1584–1598. https://doi.org/10.1002/saj2.20152

Mukherjee, S., Sturman, A. P., McMillan, A. M. S., Harvey, M. J., & Zawar-Reza, P. (2014). Assessment of error propagation in measured flux values obtained using an eddy diffusivity based micrometeorological setup. *Atmospheric Environment*, *84*, 144–155. https://doi.org/10.1016/j.atmosenv.2013.10.034

Müller, R. (2021). The impact of the rise in atmospheric nitrous oxide on stratospheric ozone: This article belongs to Ambio's 50th Anniversary Collection. Theme: Ozone Layer. *Ambio*, *50*(1), 35–39. https://doi.org/10.1007/s13280-020-01428-3

Nangia, V., Sunohara, M. D., Topp, E., Gregorich, E. G., Drury, C. F., Gottschall, N., & Lapen, D. R. (2013). Measuring and modeling the effects of drainage water management on soil greenhouse gas fluxes from corn and soybean fields. *Journal of Environmental Management*, *129*, 652–664. https://doi.org/10.1016/j.jenvman.2013.05.040

Nash, P., Motavalli, P., Nelson, K., & Kremer, R. (2015). Ammonia and nitrous oxide gas loss with subsurface drainage and polymer-coated urea fertilizer in a poorly drained soil. *Journal of Soil and Water Conservation*, *70*(4), 267–275. https://doi.org/10.2489/jswc.70.4.267

Neftel, A., Ammann, C., Fischer, C., Spirig, C., Conen, F., Emmenegger, L., Tuzson, B., & Wahlen, S. (2010). N2O exchange over managed grassland: Application of a quantum cascade laser spectrometer for micrometeorological flux measurements. *Agricultural and Forest Meteorology*, *150*(6), 775–785. https://doi.org/10.1016/j.agrformet.2009.07.013

Obi-Njoku, O., Boh, M. Y., Smith, W., Grant, B., Price, G. W., Hussain, N., Whalen, J. K., & Clark, O. G. (2022). Greenhouse gas emissions following biosolids application to farmland: Estimates from the DeNitrification and DeComposition model. *Science of the Total Environment*, *823*, 153695. https://doi.org/10.1016/j.scitotenv.2022.153695

Papale, D., Reichstein, M., Aubinet, M., Canfora, E., Bernhofer, C., Kutsch, W., Longdoz, B., Rambal, S., Valentini, R., Vesala, T., & Yakir, D. (2006). Towards a standardized processing of Net Ecosystem Exchange measured with eddy covariance technique: Algorithms and uncertainty estimation. *Biogeosciences*, *3*(4), 571–583. https://doi.org/10.5194/bg-3-571-2006

Parkin, T. B. (1987). Soil Microsites as a Source of Denitrification Variability. *Soil Science Society of America Journal*, *51*(5), 1194–1199.

Pattey, E., Edwards, G. C., Desjardins, R. L., Pennock, D. J., Smith, W., Grant, B., & MacPherson, J. I. (2007). Tools for quantifying N2O emissions from agroecosystems. *Agricultural and Forest Meteorology*, *142*(2–4), 103–119. https://doi.org/10.1016/j.agrformet.2006.05.013

Pattey, E., Edwards, G., Strachan, I. B., Desjardins, R. L., Kaharabata, S., & Wagner Riddle, C. (2006). Towards standards for measuring greenhouse gas fluxes from agricultural fields using instrumented towers. *Canadian Journal of Soil Science*, *86*(3), 373–400. https://doi.org/10.4141/S05-100

Pelster, D. E., Chantigny, M. H., Rochette, P., Angers, D. A., Rieux, C., & Vanasse, A. (2012). Nitrous Oxide Emissions Respond Differently to Mineral and Organic Nitrogen Sources in Contrasting Soil Types. *Journal of Environmental Quality*, *41*(2), 427–435. https://doi.org/10.2134/jeq2011.0261

Pihlatie, M., Rinne, J., Ambus, P., Pilegaard, K., Dorsey, J. R., Rannik, Ü., Markkanen, T., Launiainen, S., & Vesala, T. (2005). Nitrous oxide emissions from a beech forest floor measured by eddy covariance and soil enclosure techniques. *Biogeosciences*, *2*(4), 377–387. https://doi.org/10.5194/bg-2-377-2005

Rannik, Haapanala, S., Shurpali, N. J., Mammarella, I., Lind, S., Hyvönen, N., Peltola, O., Zahniser, M., Martikainen, P. J., & Vesala, T. (2015). Intercomparison of fast response commercial gas analysers for nitrous oxide flux measurements under field conditions. *Biogeosciences*, *12*(2), 415–432. https://doi.org/10.5194/bg-12-415-2015

Ravishankara, A. R., Daniel, J. S., & Portmann, R. W. (2009). Nitrous oxide (N2O): The dominant ozone-depleting substance emitted in the 21st century. *Science*, *326*(5949), 123–125. https://doi.org/10.1126/science.1176985

Richardson, A. D., Mahecha, M. D., Falge, E., Kattge, J., Moffat, A. M., Papale, D., Reichstein, M., Stauch, V. J., Braswell, B. H., Churkina, G., Kruijt, B., & Hollinger, D. Y. (2008). Statistical properties of random CO2 flux measurement uncertainty inferred from model residuals. *Agricultural and Forest Meteorology*, *148*(1), 38–50. https://doi.org/10.1016/j.agrformet.2007.09.001

Rochette, P. (2011). Towards a standard non-steady-state chamber methodology for measuring soil N2O emissions. *Animal Feed Science and Technology*, *166–167*, 141–146. https://doi.org/10.1016/j.anifeedsci.2011.04.063

Roman-Perez, C. C., Hernandez-Ramirez, G., Kryzanowski, L., Puurveen, D., & Lohstraeter, G. (2021). Greenhouse gas emissions, nitrogen dynamics and barley productivity as impacted by biosolids applications. *Agriculture, Ecosystems and Environment*, *320*(July), 107577. https://doi.org/10.1016/j.agee.2021.107577

Saggar, S., Jha, N., Deslippe, J., Bolan, N. S., Luo, J., Giltrap, D. L., Kim, D. G., Zaman, M., & Tillman, R. W. (2013). Denitrification and N2O: N2 production in temperate grasslands: Processes, measurements, modelling and mitigating negative impacts. *Science of the Total Environment*, *465*, 173–195. https://doi.org/10.1016/j.scitotenv.2012.11.050

Salesky, S. T., & Chamecki, M. (2012). Random errors in turbulence measurements in the atmospheric surface layer: Implications for monin-obukhov similarity theory. *Journal of the Atmospheric Sciences*, *69*(12), 3700–3714. https://doi.org/10.1175/JAS-D-12-096.1

Scanlon, T. M., & Kiely, G. (2003). Ecosystem-scale measurements of nitrous oxide fluxes for an intensely grazed, fertilized grassland. *Geophysical Research Letters*, *30*(16), 2–5. https://doi.org/10.1029/2003GL017454

Schmid, H. P. (2002). Footprint modeling for vegetation atmosphere exchange studies: A review and perspective. *Agricultural and Forest Meteorology*, *113*(1–4), 159–183. https://doi.org/10.1016/S0168-1923(02)00107-7

Schott, L., Lagzdins, A., Daigh, A. L. M., Craft, K., Pederson, C., Brenneman, G., & Helmers, M. J. (2017). Drainage water management effects over five years on water tables, drainage, and yields in southeast Iowa. *Journal of Soil and Water Conservation*, *72*(3), 251–259. https://doi.org/10.2489/jswc.72.3.251

Schuepp, P. H., Leclerc, M. Y., MacPherson, J. I., & Desjardins, R. L. (1990). Footprint Prediction of Scalar Fluxes from Analytical Solutions of the Diffusion Equation. *Boundary-Layer Meteorology*, *50*, 355–373.

Shedekar, V. S., Fausey, N. R., King, K. W., & Brown, L. C. (2020). Agricultural Drainage: Past, Present, and Future. In J. A. Delgado, C. J. Gantzer, & G. F. Sassenrath (Eds.), *Soil and Water Conservation: A Celebration of 75 Years*.

Shurpali, N. J., Rannik, Ü., Jokinen, S., Lind, S., Biasi, C., Mammarella, I., Peltola, O., Pihlatie, M., Hyvönen, N., Räty, M., Haapanala, S., Zahniser, M., Virkajärvi, P., Vesala, T., & Martikainen, P. J. (2016). Neglecting diurnal variations leads to uncertainties in terrestrial nitrous oxide emissions. *Scientific Reports*, *6*(April), 1–9. https://doi.org/10.1038/srep25739

Simpson, I. J., Thurtell, G. W., Neumann, H. H., Den Hartog, G., & Edwards, G. C. (1998). The validity of similarity theory in the roughness sublayer above forests. *Boundary-Layer Meteorology*, *87*(1), 69–99. https://doi.org/10.1023/A:1000809902980

Skaggs, W. R., Fausey, N. R., & Evans, R. O. (2012). Drainage water management. *Journal of Soil and Water Conservation*, *67*(6). https://doi.org/10.2489/jswc.67.6.167A

Skiba, U., Jones, S. K., Drewer, J., Helfter, C., Anderson, M., Dinsmore, K., McKenzie, R., Nemitz, E., & Sutton, M. A. (2013). Comparison of soil greenhouse gas fluxes from extensive and intensive grazing in a temperate maritime climate. *Biogeosciences*, *10*(2), 1231–1241. https://doi.org/10.5194/bg-10-1231-2013

Smith, K. A. (1994). Micrometeorological and chamber methods for measurement of nitrous oxide fluxes between soils and the atmosphere: overview and conclusions. *Journal of Geophysical Research*, *99*(D8), 541–548. https://doi.org/10.1029/94jd00619

Stehfest, E., & Bouwman, L. (2006). N2O and NO emission from agricultural fields and soils under natural vegetation: Summarizing available measurement data and modeling of global annual emissions. *Nutrient Cycling in Agroecosystems*, *74*(3), 207–228. https://doi.org/10.1007/s10705-006-9000-7

Sunohara, M. D., Craiovan, E., Topp, E., Gottschall, N., Drury, C. F., & Lapen, D. R. (2014). Comprehensive Nitrogen Budgets for Controlled Tile Drainage Fields in Eastern Ontario, Canada. *Journal of Environmental Quality*, *43*(2), 617–630.

https://doi.org/10.2134/jeq2013.04.0117

Taki, R., Wagner-Riddle, C., Parkin, G., Gordon, R., & VanderZaag, A. (2019). Comparison of two gap-filling techniques for nitrous oxide fluxes from agricultural soil. *Canadian Journal of Soil Science*, *99*(1), 12–24. https://doi.org/10.1139/cjss-2018-0041

Tallec, T., Brut, A., Joly, L., Dumelié, N., Serça, D., Mordelet, P., Claverie, N., Legain, D., Barrié, J., Decarpenterie, T., Cousin, J., Zawilski, B., Ceschia, E., Guérin, F., & Le Dantec, V. (2019). N2O flux measurements over an irrigated maize crop: A comparison of three methods. *Agricultural and Forest Meteorology*, *264*(January 2018), 56–72. https://doi.org/10.1016/j.agrformet.2018.09.017

Taylor, J. (1997). *Introduction to error analysis, the study of uncertainties in physical measurements*.

Taylor, N. M., Wagner-Riddle, C., Thurtell, G. W., & Beauchamp, E. G. (1999). Nitric oxide fluxes from an agricultural soil using a flux-gradient method. *Journal of Geophysical Research Atmospheres*, *104*(D10), 12213–12220. https://doi.org/10.1029/1999JD900181

Tenuta, M., Amiro, B. D., Gao, X., Wagner-Riddle, C., & Gervais, M. (2019). Agricultural management practices and environmental drivers of nitrous oxide emissions over a decade for an annual and an annual-perennial crop rotation. *Agricultural and Forest Meteorology*, *276–277*(June), 107636. https://doi.org/10.1016/j.agrformet.2019.107636

Thurtell, G. W. (1989). Comments on using K-theory within and above the plant canopy to model diffusion processes. *Estimation of Areal Evapotranspiration*, *177*(177), 81–85. http://itia.ntua.gr/hsj/redbooks/177/hysj_177_01_0081.pdf%0Apapers3://publication/uuid/F6398BE1-A439-49C7-B5E5-8057436E30D2

Tian, H., Yang, J., Xu, R., Lu, C., Canadell, J. G., Davidson, E. A., Jackson, R. B., Arneth, A., Chang, J., Ciais, P., Gerber, S., Ito, A., Joos, F., Lienert, S., Messina, P., Olin, S., Pan, S., Peng, C., Saikawa, E., … Zhang, B. (2019). Global soil nitrous oxide emissions since the preindustrial era estimated by an ensemble of terrestrial biosphere models: Magnitude, attribution, and uncertainty. *Global Change Biology*, *25*(2), 640–659. https://doi.org/10.1111/gcb.14514

Topp, E., & Pattey, E. (1997). Soils as sources and sinks for atmospheric methane. *Canadian Journal of Soil Science*, *77*(2), 167–178. https://doi.org/10.4141/s96-107

Topp, G. C., Davis, J. L., & Annan, A. P. (1980). Electromagnetic determination of soil water content: Measurements in coaxial transmission lines. *Water Resources Research*, *16*(3), 574–582. https://doi.org/10.1029/WR016i003p00574

Tyagi, L., Kumari, B., & Singh, S. N. (2010). Water management - A tool for methane mitigation from irrigated paddy fields. *Science of the Total Environment*, *408*(5), 1085–1090. https://doi.org/10.1016/j.scitotenv.2009.09.010

Van Zandvoort, A., Lapen, D. R., Clark, I. D., Flemming, C., Craiovan, E., Sunohara, M. D., Boutz, R., & Gottschall, N. (2017). Soil CO2, CH4, and N2O fluxes over and between tile drains on corn, soybean, and forage fields under tile drainage management. *Nutrient Cycling in Agroecosystems*, *109*(2), 115–132. https://doi.org/10.1007/s10705-017-9868-4

Verchot, L. V, Davidson, E. a, Cattfinio, J. H., Ackerman, T. M. I. L., Erickson, H. E., & Keller, M. (1999). Land use change and biogeochemical controls of nitrogen oxide emissions from soils in eastern Amazonia. *Global Biogeochemical Cycles*, *13*(1), 31–46.

Wagner-riddle, C., Furon, A., Mclaughlin, N. L., Lee, I., Barbeau, J., Jayasundara, S., Parkin, G., von Bertoldi, P., & Warland, J. (2007). Intensive measurement of nitrous oxide emissions from a corn-soybean-wheat rotation under two contrasting management systems over 5 years. *Global Change Biology*, *13*(8), 1722–1736. https://doi.org/10.1111/j.1365-2486.2007.01388.x

Wagner-Riddle, C., Thurtell, G. W., & Edwards, G. C. (2005). Trace Gas Concentration Measurements for Micrometeorological Flux Quantification. *Micrometeorology in Agricul-Tural Systems, Agronomy Monograph*, *47*, 321–343. https://doi.org/10.2134/agronmonogr47.c14

Wagner-Riddle, C., Thurtell, G. W., King, K. M., Kidd, G. E., & Beauchamp, E. G. (1996). Nitrous Oxide and Carbon Dioxide Fluxes from a Bare Soil Using a Micrometeorological Approach. *Journal of Environmental Quality*, *25*(4), 898–907. https://doi.org/https://doi.org/10.2134/jeq1996.00472425002500040035x

Waldo, S., Russell, E. S., Kostyanovsky, K., Pressley, S. N., O'Keeffe, P. T., Huggins, D. R., Stöckle, C. O., Pan, W. L., & Lamb, B. K. (2019). N2O Emissions From Two Agroecosystems: High Spatial Variability and Long Pulses Observed Using Static Chambers and the Flux-Gradient Technique. *Journal of Geophysical Research: Biogeosciences*, *124*(7), 1887–1904. https://doi.org/10.1029/2019JG005032

Webb, E. K., Pearman, G. I., & Leuning, R. (1980). Correction of flux measurements for density effects due to heat and water vapour transfer. *Quarterly Journal of the Royal Meteorological Society*, *106*(447), 85–100. https://doi.org/https://doi.org/10.1002/qj.49710644707

West, J. J., Fiore, A. M., Horowitz, L. W., & Mauzerall, D. L. (2006). Global health benefits of mitigating ozone pollution with methane emission controls. *Proceedings of the National Academy of Sciences of the United States of America*, *103*(11), 3988–3993. https://doi.org/10.1073/pnas.0600201103

Williams, M. R., King, K. W., & Fausey, N. R. (2015). Drainage water management effects on tile discharge and water quality. *Agricultural Water Management*, *148*, 43–51. https://doi.org/10.1016/j.agwat.2014.09.017

Wutzler, T., Lucas-Moffat, A., Migliavacca, M., Knauer, J., Sickel, K., Šigut, L., Menzer, O., & Reichstein, M. (2018). Basic and extensible post-processing of eddy covariance flux data with REddyProc. *Biogeosciences*, *15*(16), 5015–5030. https://doi.org/10.5194/bg-15-5015-2018

Zhang, X., Lee, X., Griffis, T. J., Andrews, A. E., Baker, J. M., Erickson, M. D., Hu, N., & Xiao, W. (2015). Quantifying nitrous oxide fluxes on multiple spatial scales in the Upper Midwest, USA. *International Journal of Biometeorology*, *59*(3), 299–310. https://doi.org/10.1007/s00484-014-0842-4

Zhao, J., Zhang, M., Xiao, W., Wang, W., Zhang, Z., Yu, Z., Xiao, Q., Cao, Z., Xu, J., Zhang, X., Liu, S., & Lee, X. (2019). An evaluation of the flux-gradient and the eddy covariance method to measure CH4, CO2, and H2O fluxes from small ponds. *Agricultural and Forest Meteorology*, *275*(March), 255–264. https://doi.org/10.1016/j.agrformet.2019.05.032

Zhu, J., Mulder, J., Wu, L. P., Meng, X. X., Wang, Y. H., & Dörsch, P. (2013). Spatial and temporal variability of N2O emissions in a subtropical forest catchment in China. *Biogeosciences*, *10*(3), 1309–1321. https://doi.org/10.5194/bg-10-1309-2013